Dissertation

submitted to the
Combined Faculties of the Natural Sciences and Mathematics
of the Ruperto-Carola University of Heidelberg, Germany
for the degree of
Doctor of Natural Sciences

put forward by

Dipl.-Phys. Daniel Spielmann, M. A.

born in Heidelberg

Oral examination: January 12, 2011

Aspects of confinement in QCD from lattice simulations

Referees: Prof. Dr. Jan M. Pawlowski
Prof. Dr. Michael G. Schmidt

Aspekte des Confinement in der QCD aus Gittersimulationen

Zusammenfassung. Wir untersuchen Confinement (Farbeinschluss) in der Quantenchromodynamik mittels numerischer Simulationen im Rahmen der Gittereichtheorie. In Landau-Eichung ist der Confinement-Mechanismus durch die Gribov–Zwanziger- und Kugo–Ojima-Szenarien mit dem Infrarotverhalten der Geist- und Gluonpropagatoren verbunden. Aus diesen Szenarien folgt ein bestimmtes 'Scaling'-Verhalten der Propagatoren. Funktionale Methoden im Kontinuum ergeben sowohl dieses Verhalten als auch 'Decoupling'-Lösungen, während Gitterrechnungen in drei und vier Dimensionen nur letztere bestätigen. Eine mögliche Erklärung für diese Diskrepanz besteht in Eigenschaften der Eichfixierung. Daher erforschen wir in reiner $SU(2)$-Eichtheorie in zwei, drei und vier Dimensionen mehrere Alternativen zu üblichen Eichfixierungsalgorithmen.

Aus stochastischer Quantisierung erhalten wir ein Infrarotverhalten der Propagatoren im Einklang mit Resultaten üblicher Eichfixierung auf dem Gitter, während das Spektrum des Faddeev–Popov-Operators auf teils unterschiedliche Eigenschaften hinweist. Im Grenzfall starker Kopplung stellen unsere Ergebnisse dagegen das bisherige Bild in Frage. Insbesondere finden wir in einer nichtperturbativen Vervollständigung der Landau-Eichung eine so starke Wirkung der Gribov-Ambiguität, dass kein Infrarotverhalten ausgeschlossen werden kann. Zudem untersuchen wir den Gluonpropagator mit freien Randbedingungen. Erst auf großen Volumina resultiert weitgehend das übliche Verhalten. Zum Vergleich implementieren wir nichtperiodische Eichtransformationen.

Darüber hinaus analysieren wir zwei Themen aus dem Bereich des QCD-Phasendiagramms. Erstens untersuchen wir das Vorzeichenproblem für Fermionen auf dem Gitter, indem wir das dreidimensionale Thirring-Modell mit einer komplexen Langevin-Gleichung simulieren. Der Algorithmus erbringt ein 'Silver Blaze'-Verhalten der Observablen, jedoch nicht die korrekte Position des Übergangs zu einer Phase mit nichtverschwindender Dichte. Zweitens gelingt es uns, Eigenschaften des Deconfinement-Phasenübergangs der reinen $SU(2)$-Eichtheorie in $2+1$ Dimensionen, wie die kritische Temperatur, anhand des Gluonpropagators in Landau-Eichung zu bestimmen.

Aspects of confinement in QCD from lattice simulations

Abstract. We study confinement in quantum chromodynamics via numerical simulations in the framework of lattice gauge theory. In Landau gauge, the mechanism of confinement is related to the infrared behavior of the ghost and gluon propagators via the Gribov–Zwanziger and Kugo–Ojima scenarios. These scenarios entail a scaling behavior. Functional methods in the continuum allow both for this behavior and for decoupling solutions, while lattice simulations in three and four dimensions yield only the latter. A possible explanation for this mismatch is based on limitations of standard lattice gauge fixing methods. Hence, we investigate a number of alternative gauge fixing algorithms in pure $SU(2)$ gauge theory in two, three and four dimensions.

We find that stochastic quantization yields an infrared behavior of the propagators in agreement with the results of standard procedures, even though the Faddeev–Popov operator spectrum indicates some different properties. In the strong-coupling limit, our results challenge the standard picture. In particular, we find in a non-perturbative completion of Landau gauge an enormous effect of the Gribov ambiguity. It entails that no subset of infrared solutions can be excluded yet. Moreover, we study the gluon propagator with free boundary conditions. On large lattices, the results mostly show the standard behavior. We also examine non-periodic gauge transformations.

Furthermore, we analyze two topics related to the phase diagram of QCD. First, we explore the sign problem for fermions on the lattice by simulating the three-dimensional Thirring model with a complex Langevin equation. The algorithm succeeds in yielding a 'Silver Blaze' behavior of observables, but it does not reliably describe the onset to a phase with non-zero density. Second, we determine properties of the deconfinement phase transition of pure $SU(2)$ gauge theory in $2+1$ dimensions, like the critical temperature, by means of the gluon propagator in Landau gauge.

CONTENTS

CHAPTER 1

INTRODUCTION AND OUTLINE

Particle physics and confinement

The search for the fundamental building blocks of matter has been an endeavor of mankind for millennia. After a long history of speculative efforts, it found a solid base with the advent of empirical science, and due to ever more systematic and technically advanced investigations, it has subsequently made remarkable progress. Science has now identified a small number of candidates for elementary particles, and it is able to reduce all interactions occurring at any place and time in nature to the strong, the electromagnetic, the weak and the gravitational interaction. Two of these have been subsumed under the unified theory of the electroweak interaction. Gravity has not been successfully quantized so far. But the interactions most relevant to the physics of elementary particles, sc. the strong and the electroweak interaction, are well described by quantum field theories, more specifically, by gauge theories. Together, these form the standard model of particle physics.

The standard model is a quantum field theory whose predictions have received excellent experimental confirmation. It cannot be the exact fundamental theory of nature since it does not include gravity; it requires modification for non-zero neutrino masses; and it faces a few fine-tuning problems. Still, overall, it has proven to be a supremely successful theory. The elementary fields of the standard model correspond to quarks, leptons and gauge bosons. Put more abstractly, these fields are associated with representations of the Poincaré group and the product $SU(3) \times SU(2) \times U(1)$ of internal symmetry groups.

Ordinary matter is composed of quarks and leptons, which are, according to the standard model, elementary particles. While the electroweak interaction affects both types of particles, quarks are the fundamental fermions that are subject to the strong interaction. Gluons are the gauge bosons mediating this interaction. Both quarks and gluons carry the corresponding charge, 'color charge' [1, 2, 3]. This is in contrast to quantum electrodynamics, whose gauge boson, the photon, is neutral. Quantum chromodynamics (QCD), the theory of the strong interaction, is based on the gauge group $SU(3)$ for the color degree of freedom. The thesis at hand deals with aspects of QCD.

All empirical evidence is consistent with the confinement of quarks and gluons in hadrons, which can be classified into mesons (quark–antiquark pairs) and baryons (quark

triplets), while gluons without quarks are expected to form glueballs. I. e., no free particles with non-vanishing color charge are observed in nature, unless the temperature or density is very high. Free quarks carry a non-integer electric charge, in contrast to all color-neutral particles.

The quark model of hadrons was first motivated by regularities in the charge and strangeness of particles with the same spin and parity, which the hypothesis of particles with fractional electric charge [4], later identified as quarks, was able to explain. Further evidence for the existence of quarks was obtained from deep inelastic scattering experiments [5, 6], which led to the parton model; partons are now referred to as quarks and gluons.

Hadrons account for most of the mass of ordinary matter. But the mass of hadrons cannot be explained by the bare quark masses alone. Rather, the largest part of the hadronic masses is dynamically generated by interactions of quarks and gluons, described by QCD. This effect is larger than the generation of the fermion masses via the interaction with the Higgs field, as it accounts e. g. for the fact that nucleons (protons and neutrons) have masses of almost 1 GeV, despite being composed (in a simple picture) of three 'current quarks' with masses of only a few MeV each. This fact is an instance of another fundamental, non-perturbative feature of QCD, sc. of the dynamical breaking of chiral symmetry.

QCD can be formulated as a renormalizable quantum field theory, more precisely, as a non-Abelian gauge theory. That it is non-Abelian means that the gauge field mediating the interaction interacts with itself, since it carries color charge. Its character as a gauge theory leads to intricacies in the theoretical treatment which will play an important role in the thesis at hand.

Confinement is one of the outstanding properties of QCD. Another one is asymptotic freedom, which is much better understood. 'Asymptotic freedom' refers to the behavior of the strong coupling constant as a function of the energy scale, in particular to the fact that it decreases toward large momenta (i. e., small distances) [7, 8]. This stands in stark contrast to the electromagnetic interaction, whose strength, characterized by the fine structure constant, increases with the energy scale. (It is still reasonable to characterize these quantities as constants, since they are, to the current knowledge, constant in space-time.) Extrapolated to very high energies, the couplings of all fundamental interactions come closer to each other, which may point toward a unified approach; but we do not pursue this topic any further, as we concentrate solely on the strong interaction. Renormalizable theories can exhibit asymptotic freedom only by virtue of non-Abelian gauge fields [9, 10]. Further seminal early work on QCD from a theoretical perspective may be found e. g. in refs. [11, 12, 13, 14, 15].

Confinement still eludes an explanation from first principles, and the search for a theoretical understanding of how exactly it comes about is among the fundamental questions of particle physics. The increase of the coupling constant toward large distances prohibits successful perturbative calculations in the infrared sector of QCD, i. e., at momenta of a few hundred MeV and below. Hence, confinement is a non-perturbative phenomenon, and a non-perturbative method is called for. Among such methods are Dyson–Schwinger equations and the functional renormalization group. Another widely used non-perturbative method is lattice gauge theory, a method from first principles that rests on a discretization of space-time, making the underlying quantum field theory amenable to a numerical treatment. Lattice gauge theory is the method we utilize throughout the present work.

Confinement scenarios, gauge fixing ambiguity, infrared propagators and further aspects of confinement

The thesis at hand deals with a number of aspects of confinement in QCD. A large part of it is devoted to the confinement mechanism and involves problems of gauge fixing. But we also study the deconfinement phase transition at non-zero temperature and the 'sign problem' at non-zero density.[1]

A major topic is the question of the mechanism by which confinement comes about. We focus on the confinement scenarios proposed by Gribov and Zwanziger [16, 17, 18, 19, 20] and by Kugo and Ojima [21, 22]. The character of QCD as a gauge theory plays a crucial role in this context. Notably, the explanations provided by these and other confinement scenarios depend on the chosen gauge. The relevant gauge in our case is Landau gauge. We investigate pure $SU(2)$ Yang–Mills theory, i. e., a theory similar to QCD, but with two colors and without dynamical fermions.

In Landau gauge, these confinement scenarios make specific predictions for the behavior of certain correlations functions, specifically of the ghost and gluon propagators, in the infrared, i. e., at small momenta. These are in line with a 'scaling behavior'. Our investigations are motivated by the fact that previous lattice results in three and four dimensions do not agree with the standard implications of these scenarios. In contrast, functional methods in the continuum allow for a one-parameter family of solutions, which includes the 'scaling solution' as well as 'decoupling solutions'.

The investigations of the infrared propagators are greatly complicated by a gauge fixing ambiguity encountered in Yang–Mills theories in Landau gauge and many other gauges, the 'Gribov ambiguity' [16, 23]. For every physical configuration that satisfies the Landau gauge condition, there is a plethora of gauge copies on the same orbit that do so as well. Since the ghost and gluon propagators are gauge-dependent quantities, their infrared behavior may be severely influenced by the choice of copies with specific properties. Some of our results explicitly confirm this.

We study different possibilities to alter the gauge fixing algorithm on the lattice. This general way to proceed is motivated by the aforementioned apparent mismatch, together with the suspicion that it may come about by systematic differences between standard lattice gauge fixing procedures and their continuum counterparts. More specifically, we explore the following approaches.

First, we consider stochastic quantization as an alternative to standard gauge fixing algorithms. It induces a more local evolution of configurations, and we find evidence that it indeed samples configuration space in a different way from a standard approach, although this statement deserves some qualification. We calculate the ghost and gluon propagators in two, three and four dimensions with stochastic quantization and find agreement with previous results in all dimensions, despite the alternative gauge fixing.

Second, we perform an extensive investigation of a recently proposed non-perturbative completion of Landau gauge. It is based on the insight that the Landau gauge condition does not impose a unique gauge fixing prescription, as it permits a residual gauge freedom. Eliminating this residual freedom amounts to a non-perturbative completion of this gauge. It allows to assess the severity of the Gribov ambiguity of the chosen gauge copy. In Landau

[1] Note that we provide most of the references only in the respective chapters, as we wish to keep this introduction rather concise.

max-B gauge, we find the ghost propagator at small lattice momenta to be dramatically enhanced, such that even an 'over-scaling' behavior of the effective running coupling is obtained on moderate lattice volumes.

These studies are done in the strong-coupling limit. This limit of pure gauge theory on the lattice offers the possibility to assess the infrared behavior of the propagators at all lattice momenta, as has been shown previously in four dimensions. This comes at the cost of enhanced systematic uncertainties, like discretization effects, which we analyze explicitly in addition. In the same limit, we also take a closer look at standard gauge fixing. Our results call for a basic re-evaluation of some statements that have hitherto been advanced, as they may allow in some respects for a more unified picture in all dimensions.

Third, we explore an alternative to the usual periodic boundary conditions of the lattice. Free boundary conditions cause the gluon propagator to vanish exactly at zero momentum (as previously shown), which is not in line with a decoupling behavior. They might lead to a change in global properties of the gauge fixing that could possibly survive in the infinite volume limit. The enlarged computational effort due to a modified gluon propagator definition notwithstanding, we simulate volumes that allow to draw some definite conclusions from our results. These are not consistent with the scaling solution.

Perhaps surprisingly, the deconfinement phase transition at non-zero temperature can also be investigated by means of the infrared gluon propagator in Landau gauge. Even though gauge fixing is required, the problem of the Gribov ambiguity is less pertinent in this case. We perform such an investigation in $2+1$ dimensions, where the transition is of second order in pure $SU(2)$ Yang–Mills theory. We are able to extract gauge-invariant information from the gauge-dependent gluon propagator, as we determine the transition temperature and also find evidence for the expected universality class.

In order to calculate the full phase diagram of QCD, reliable lattice simulations at non-zero density are a major desideratum. However, they face the 'sign problem'. This huge challenge for lattice QCD is a problem that arises once dynamical fermions are included in the simulations. In a nutshell, it consists in the fact that the fermionic action is complex, rendering ordinary Monte Carlo simulations based on importance sampling impossible. We study the sign problem in a fermionic model, the three-dimensional Thirring model, with a complexified version of the method of stochastic quantization, the same general approach also employed for gauge fixing in a part of the present thesis. While no set of criteria is known that would allow to decide a priori whether complex Langevin evolution converges against the correct solution in a specific case, it has yielded some promising results. However, incorrect convergence has also been observed in some models, so care is required.

Outline of the thesis

We now give a brief overview of the structure of the thesis at hand.

In ch. 2, we provide introductory remarks on quantum chromodynamics in general. More specifically, we discuss the Gribov ambiguity as well as the confinement mechanism in Landau gauge according to the Gribov–Zwanziger/Kugo–Ojima scenarios and its connection to the infrared behavior of correlation functions. These functions depend on the chosen gauge, and the question of the adequacy of gauge fixing procedures is a guiding theme throughout much of our studies (in particular, in chs. 4 through 7). We also intro-

duce the non-perturbative method of lattice gauge theory and some related notions, like gauge fixing on the lattice, in ch. 2. Regarding the infrared behavior of the propagators, we elaborate on the discrepancy between continuum and lattice results which may affect the status of the aforementioned confinement scenarios. It motivates our studies in chs. 4, 5, 6 and 7.

Chs. 3 and 4 stand in a close relation to each other, as both of them are devoted to the method of stochastic quantization. In ch. 3, we lay out the basic ideas of stochastic quantization and illustrate them in a toy model that already includes gauge fixing. This serves as a preparation for the application of stochastic quantization as a viable alternative to standard gauge fixing algorithms in non-Abelian gauge theory. This application is the subject of ch. 4, where results obtained with stochastic gauge fixing in the framework of lattice gauge theory are presented. We focus on the infrared ghost and gluon propagators in two, three and four dimensions. In addition, we compare the distributions in configuration space induced by stochastic and by standard gauge fixing.

In chs. 5 and 6, we describe the results of studies in the strong-coupling limit. We study the ghost and gluon propagators in two and three dimensions with standard gauge fixing methods in ch. 5, elucidating their behavior by means of the effective running coupling and of a local analysis. We also put our results in the context of previous results for the four-dimensional case.

In ch. 6, we explore these quantities within a non-perturbative completion of Landau gauge in the strong-coupling limit. This completion is provided by the recently proposed Landau max-B gauge, which is part of a family of gauges that can be related to the one-parameter family of solutions found by functional continuum methods. We discuss the consequences of these findings for the ongoing debate about the infrared behavior of the Landau gauge propagators.

Yet another approach to the infrared properties of the Yang–Mills propagators, besides altering the gauge fixing algorithm (chs. 3 and 4), working in the strong-coupling limit (chs. 5 and 6) and investigating the effect of Gribov copies (ch. 6), is to modify the boundary conditions of the compactified lattices of our simulations. In ch. 7, we employ free boundary conditions instead of periodic ones. We present the first numerical simulations of the gluon propagator with these boundary conditions in various dimensions, both at finite coupling and in the strong-coupling limit. We also investigate two versions of implementing non-periodic gauge transformations.

In ch. 8, we again study pure $SU(2)$ Yang–Mills theory, but now at non-zero temperature. We focus on the Landau gauge gluon propagator in $2+1$ dimensions. Both the transverse and the longitudinal propagator are analyzed at many temperatures around the phase transition, and the magnetic and electric screening masses are extracted from them. The susceptibility of the latter allows to locate the deconfinement phase transition.

Finally, we approximate the full theory of quantum chromodynamics in a different way. In the bulk of this thesis, we explore pure $SU(2)$ gauge theory. In ch. 9, however, we consider the Thirring model in three dimensions. This is a fermionic model that is distinctly different from QCD, but shares with (proper, i. e., three-color) QCD the 'sign problem' at non-zero density. We discuss the promising, though not always reliable method of complex stochastic quantization, which we subsequently apply to the Thirring model at non-zero chemical potential.

We conclude with a summary of our results in ch. 10, where we also indicate possible

directions for future work. The appendix comprises several details, some conventions and also a few miscellaneous results.

Origin and publication of the results

Some results of the present thesis have already been published. In particular, the main results of chs. 3 and 4 have been published in ref. [24], and those of chs. 5 and 6 in ref. [25]. The results of chs. 7, 8 and 9 are still awaiting publication and are presented here for the first time.

Virtually all of the data displayed throughout the present thesis have been produced using our lattice gauge theory code in the programming language C++. This code was written specifically for this purpose by the author of this thesis.

CHAPTER 2

INFRARED QCD AND CONFINEMENT

In this chapter, we do not yet present any new results. Instead, we lay the foundation for the studies described in the subsequent chapters. In sec. 2.1, we introduce some notions of the continuum formulation of quantum chromodynamics. In particular, issues related to gauge fixing and the configuration space that we briefly review here will resurface throughout large parts of the thesis at hand, mostly in chs. 4 through 7. In sec. 2.2, we give an introduction to the relationship between confinement scenarios and the infrared behavior of the ghost and gluon propagators in Landau gauge. Subsequently, we introduce (sec. 2.3) the non-perturbative method that we use, sc. lattice gauge theory, before we elaborate on a discrepancy between continuum and lattice results for the infrared propagators (sec. 2.4), which serves as a motivation for our lattice studies of this subject in chs. 4 through 7. The investigations at non-zero temperature (ch. 8) and density (ch. 9) are separately motivated in the respective chapters.

2.1 Continuum QCD in a nutshell

2.1.1 Action and gauge symmetry

Quantum chromodynamics is the quantum field theory of the strong interaction between quarks and gluons. Its elementary fields are the fermionic quark and antiquark fields ψ, $\overline{\psi}$ and the bosonic gluon field (gauge field) A_μ. The action of a field theory is fixed by the Lagrangian density, or simply Lagrangian, $\mathcal{L}$ via $S = \int d^d x\, \mathcal{L}$. The classical Lagrangian density of QCD is in a Euclidean formulation[1]

$$\mathcal{L}_{\mathrm{QCD}}^{\mathrm{classical}} = \underbrace{\frac{1}{4} F^a_{\mu\nu} F^a_{\mu\nu}}_{\mathcal{L}_{\mathrm{gluon}}} + \underbrace{\sum_f \overline{\psi}^b_f (-\not{D} + m_f)^{bc} \psi^c_f}_{\mathcal{L}_\psi} . \tag{2.1}$$

[1] Further details may be found e. g. in textbooks like [26, 27] and in reviews like [28]. – The action could also contain a CP-violating term, but it is empirically found to be tiny or vanishing.

The indices a, b, c are color indices, which run up to N_c for the fermion (quark) fields living in the fundamental representation of $SU(N_c)$, and to $N_c^2 - 1$ for the gluon fields. N_c is the number of colors; in nature, $N_c = 3$. The index f denotes the quark flavors, and μ and ν run over the space-time directions. See app. A.1 for some relevant conventions.

Only in the limit of vanishing bare quark masses m_f does $L_{\text{QCD}}^{\text{classical}}$ exhibit chiral symmetry. Apart from the explicit breaking for $m_f \neq 0$, chiral symmetry is dynamically broken at not extreme temperatures and densities, which leads to an increase of the quark masses by around $300 - 400\,\text{MeV}$ compared to their bare values. Thus, most of the constituent mass of the three lightest quarks (those with flavors up, down and strange) is generated by this spontaneous breaking, not via the Higgs mechanism.

But this Lagrangian possesses a crucial symmetry, sc. invariance with respect to local gauge transformations. It would be broken by an explicit mass term $\propto m^2 A_\mu^a(x) A_\mu^a(x)$ for the gluon field, which therefore must not exist. Issues related to gauge symmetry, in particular to gauge-equivalent configurations, play an important role in our studies.

The Lagrangian (2.1) is the sum of a term $\mathcal{L}_\psi$ that describes the fermions and their couplings to the gauge field and a term $\mathcal{L}_{\text{gluon}}$ that characterizes the pure gauge sector of the theory. The form of $\mathcal{L}_{\text{QCD}}^{\text{classical}}$ is fixed by the requirements of renormalizability and invariance with respect to parity and time reversal. Note that effects of the quantum nature of the theory, in particular from gauge fixing, are absent in this formulation. For the additional terms which are required, see sec. 2.1.2,[2] eqs. (2.23) and (2.24).

Two important expressions occurring in $\mathcal{L}_{\text{QCD}}^{\text{classical}}$ are the covariant derivative D_μ and the non-Abelian field strength tensor $F_{\mu\nu}$. The former is defined as

$$D_\mu = \partial_\mu + igA_\mu \tag{2.2}$$

with the bare (unrenormalized) coupling g and the gauge field A_μ. It is called 'covariant' due to its behavior under gauge transformations, see eq. (2.9) below. The gauge field is Hermitian and traceless. It is an element of the Lie algebra of the gauge group, i. e., a linear combination of the generators T^a, which share these properties (cp. app. A.2); thus,

$$A_\mu(x) = A_\mu^a(x) T^a \quad (A_\mu^a(x) \in \mathbb{R}). \tag{2.3}$$

The field strength tensor is the quantity governing the gluonic sector of the theory, the pure gauge Lagrangian $\mathcal{L}_{\text{gluon}}$. It reads

$$F_{\mu\nu} = \partial_\mu A_\nu - \partial_\nu A_\mu + ig[A_\mu, A_\nu] \tag{2.4}$$

or in color components, $F_{\mu\nu} = F_{\mu\nu}^a T^a$,

$$F_{\mu\nu}^a = \partial_\mu A_\nu^a - \partial_\nu A_\mu^a - g f^{abc} A_\mu^b A_\nu^c. \tag{2.5}$$

The real numbers f^{abc} are the structure constants of the Lie group (see eq. (A.9)). If the theory is Abelian, i. e., the generators commute, the last term in eq. (2.4) vanishes. On the other hand, in non-Abelian gauge theories, this terms survives. It leads to a self-interaction of the gauge field, as it contains terms that are cubic and quartic in this field. In the language

[2] We refer to sections, subsections and subsubsections alike as 'sections' when giving internal references in this work.

of quantum field theory, there are three- and four-gluon vertices. In contrast, photons, the gauge bosons of the Abelian gauge theory of quantum electrodynamics (QED), do not couple to each other directly (to lowest order). Due to its non-Abelian nature, already $\mathcal{L}_{\text{gluon}}$ describes an interacting field theory, namely pure Yang–Mills theory [29].[3]

The field strength tensor is proportional to the commutator of covariant derivatives (2.2),

$$i[D_\mu, D_\nu] = gF_{\mu\nu} \tag{2.6}$$

Hence, it transforms covariantly under gauge transformations (cp. eq. (2.9) below). It is closely related to a crucial quantity of lattice gauge theory, the Wilson loop, and in particular to the plaquette variable, see sec. 2.3.1.3. The left hand side of eq. (2.6) can be understood as the difference between transformations along different sides of such a plaquette.[4]

We now spell out the gauge invariance of the Lagrangian density of QCD. $\mathcal{L}_{\text{QCD}}^{\text{classical}}$ is invariant under gauge transformations of the gluon field,

$$A_\mu(x) \to A_\mu^V(x) = V(x)A_\mu(x)V^{-1}(x) + \frac{i}{g}V(x)\partial_\mu V^{-1}(x) \tag{2.7}$$

with

$$V(x) = \exp(ig\omega^a(x)T^a). \tag{2.8}$$

V is an element of the gauge group and thus is unitary, $V^{-1} = V^\dagger$. In particular, this entails that the covariant derivative indeed transforms covariantly under gauge transformations,

$$D_\mu(x) \to V(x)D_\mu(x)V^{-1}(x). \tag{2.9}$$

Thus, if D_μ is applied to a field that transforms like

$$\psi(x) \to V(x)\psi(x), \tag{2.10}$$

the covariant derivative of the field transforms in the same way as the field; thus the attribute 'covariant'. The commutator of covariant derivatives again transforms in the same way as the covariant derivative, and so does therefore the field strength, see eq. (2.6).

Gauge fixing is an indispensable component of our studies of QCD. In the following sec. 2.1.2, we lay out some basics of the Faddeev–Popov gauge fixing procedure, which introduces additional terms to the Lagrangian (2.1) and which breaks gauge invariance. It is important to note that a different symmetry remains for the gauge-fixed Lagrangian, sc. the Becchi–Rouet–Stora–Tyutin symmetry [30, 31, 32, 33], in short, BRST symmetry. This provides a way to fix a gauge without recourse to a path integral. We slightly postpone its discussion to sec. 2.2.3.2, where we approach it in the context of confinement scenarios, more specifically, of the Kugo–Ojima confinement criterion. Even though we pursue a gauge fixing approach entirely within the framework of lattice gauge theory, some concepts related to the Faddeev–Popov method and also to BRST symmetry will be important in parts of the thesis at hand.

[3] Alternatively, the gluonic sector is often referred to as 'Yang–Mills theory' simpliciter.

[4] For details, see textbooks like [26].

2.1.2 Gauge fixing and the Faddeev–Popov method

The Lagrangian (2.1) is not the full Lagrangian of QCD as a quantum theory. In particular, the effects of gauge fixing are not yet included. We are specifically interested in Landau gauge. However, most of the following discussion will be rather general. The discussion of the Faddeev–Popov method also gives us the opportunity to briefly review the important concept of the Faddeev–Popov operator resp. the Faddeev–Popov determinant.

Landau gauge is defined by the Lorenz gauge condition on the gauge field,[5]

$$\partial_\mu A_\mu(x) = 0. \tag{2.11}$$

It is a manifestly covariant gauge condition. Most studies of the main subject of our thesis, the infrared behavior of the Yang–Mills propagators, have been performed in this gauge. Another important gauge for this purpose is Coulomb gauge

This discussion takes place in the framework of the path integral formulation of quantum field theory, where expectation values are given by functional integrals over the dynamical fields. In a Euclidean formulation, i. e., after a Wick rotation from Minkowski space, the expectation value of a quantity B reads

$$\langle B \rangle = \frac{1}{Z} \int \mathcal{D}\overline{\psi}\, \mathcal{D}\psi\, \mathcal{D}A\, B[\psi, \overline{\psi}, A] \exp(-S[\psi, \overline{\psi}, A]) \tag{2.12a}$$

$$\text{with } Z = \int \mathcal{D}\overline{\psi}\, \mathcal{D}\psi\, \mathcal{D}A\, \exp(-S[\psi, \overline{\psi}, A]). \tag{2.12b}$$

If issues concerning the consistent definition of path integrals in the continuum are set aside, another problem still remains in the context of gauge theory, namely that of 'overcounting' due to gauge-equivalent configurations. Schematically,[6]

$$\int \mathcal{D}A\, e^{-S} \propto \int \mathcal{D}\tilde{A}\, e^{-S} \int \mathcal{D}V \tag{2.13}$$

with gauge transformations V and gauge-fixed configurations $\tilde{A}$. The action

$$S = \int d^d x\, \mathcal{L}(x) \tag{2.14}$$

is gauge-invariant. Assuming that B is an observable and therefore also gauge-invariant, the path integral over the infinitely many gauge transformations V can be factored out. Hence, each functional integral over a gauge field involves a continuous infinity of gauge-equivalent field configurations, which renders the integral divergent. Thus, both the numerator and the denominator of expressions like eq. (2.12a) are not well-defined. This problem can be avoided by a procedure due to Faddeev and Popov [34]. The crucial idea is to reformulate the path integral by inserting unity in the following form,[7]

$$1 = \int dV\, \delta[\mathcal{F}[A^V]] \Delta_{\mathcal{F}}[A], \tag{2.15}$$

[5] Any possible subtleties arising from differences between this definition of Landau gauge and the definition via the limit $\xi \to 0$ of eq. (2.23) below are not relevant to our discussion.

[6] See e. g. [27] for more details.

[7] The Faddeev–Popov procedure is also treated in standard textbooks like [26, 27].

where $\mathcal{F} = 0$ is the gauge condition and V is a local gauge transformation of the gauge field A, see eq. (2.7). Note that it is assumed here that the gauge condition $\mathcal{F}$ is satisfied for exactly one A^V; this assumption is not valid once gauge copies have to be taken into account, see sec. 2.2.3.3. An essential part of (2.15) is the Faddeev–Popov determinant.

$$\Delta_{\mathcal{F}}[A] = \det M \tag{2.16}$$

It is the determinant of the Faddeev–Popov operator (FPO)

$$M^{ab}_{xy} = \left.\frac{\delta \mathcal{F}^a[A^V(x)]}{\delta \omega^b(y)}\right|_{\omega=0} \tag{2.17}$$

with the spatio-temporal coordinates written as indices for brevity. A sometimes important subtlety is that strictly speaking, the absolute value should be taken in eq. (2.16); as it stands, it is only perturbatively valid.[8] The FPO is the variation (functional derivative) of the gauge condition with respect to gauge transformations, which are given by (2.8). The gauge condition is in turn the variation of the gauge fixing functional

$$E[A] := \|A\|^2 = \frac{1}{2}\int d^d x\, A^a_\mu(x) A^a_\mu(x). \tag{2.19}$$

Hence, the FPO is the second variation, or Hessian matrix, of the gauge fixing functional,[9]

$$\delta^2 E[A] = \int d^d x\, \omega^a(x) M^{ab}_{xy} \omega^b(x), \tag{2.20}$$

see (2.8) for an implicit definition of the gauge transformation parameters ω^a. – We elaborate on this in the context of our lattice studies, see sec. 2.3.2 for the corresponding introduction. In those studies, the Faddeev–Popov operator is of great importance, since the ghost propagator is calculated from the inverse of the FPO, see sec. 2.3.3.2. In fact, the Faddeev–Popov ghosts are introduced in order to write the Faddeev–Popov determinant as a functional integral,

$$\det M^{ab}_{xy} = \int \mathcal{D}c\, \mathcal{D}\bar{c}\, \exp\left(\int dx\, dy\, \bar{c}^a(x) M^{ab}_{xy} c^b(y)\right). \tag{2.21}$$

The ghosts have zero spin. Nevertheless, they are anticommuting fields, obeying Fermi statistics. This is possible despite the spin-statistics theorem [35] since they do not represent physical particles.

In Landau gauge, eq. (2.11), the FPO takes the form

$$M^{ab}_{xy} = -\partial_\mu D^{ab}_\mu(x)\delta(x-y). \tag{2.22}$$

[8] The derivation of the Faddeev–Popov determinant involves an identity analogous to the well-known

$$\delta(f(x)) = \sum_i \frac{1}{\left|\frac{df(x_i)}{dx}\right|}\delta(x - x_i) \tag{2.18}$$

in ordinary calculus, where an absolute value is included.

[9] In the lattice formulation, we say that the FPO is the *negative* Hessian of the corresponding functional, since in that case, it is defined such that it is positive if the lattice gauge fixing functional assumes a maximum. In our continuum conventions, however, the FPO is positive if (2.19) assumes a minimum.

The two factors on the right hand side of eq. (2.15) generate two additional terms in the Lagrangian of QCD. First, the factor $\delta[\mathcal{F}[A^V]]$ corresponds (for linear covariant gauge conditions) to

$$\mathcal{L}_{\text{g. f.}} = \frac{1}{2\xi} \left(\partial_\mu A_\mu\right)^2, \tag{2.23}$$

from which Landau gauge is obtained by taking the limit $\xi \to 0$. Entering via the factor e^{-S} with S from eq. (2.14) into the path integral, this induces a Gaussian distribution for non-zero ξ, which becomes sharp in the Landau gauge limit. Second, from eq. (2.21), the Faddeev–Popov determinant leads to the ghost term

$$\mathcal{L}_{\text{ghost}} = -\int d^d y\, \overline{c}^a(x) M^{ab}_{xy} c^b(y) = \overline{c}^a(x) \left[\partial_\mu D^{ab}_\mu(x)\right] c^b(x). \tag{2.24}$$

Landau gauge is a specific linear covariant gauge. The Faddeev–Popov operator has the same form (2.22) in other such gauges, defined by $\partial_\mu A^a_\mu(x) = \Lambda^a(x)$, but Landau gauge is the only such gauge in which it is Hermitian. This has the valuable consequence that its eigenvalues can be classified exhaustively into positive, negative and vanishing ones.

This leads to a rather straightforward relationship between the Faddeev–Popov operator and different regions in configuration space. We discuss it in sec. 2.2.3.3 below, but a few remarks about it are in order already here. It is instructive to consider the specific case $A = 0$, the origin of configuration space.[10] At the origin, the Faddeev–Popov operator is simply the negative Laplace operator $-\partial_\mu\partial_\mu$, which possesses only positive eigenvalues (note again that we work in Euclidean space). Around the origin, a perturbative expansion can be performed. Hence, there is a region in configuration space around $A = 0$ where the FPO has only positive eigenvalues (except for trivially vanishing ones) and is thus a positive operator. This is the first Gribov region Ω, see sec. 2.2.3.3 below for more details.

The Faddeev–Popov gauge fixing procedure is a perturbative method. In the vicinity of $A = 0$, where the FPO is positive, it is irrelevant whether the absolute value of the right hand side of eq. (2.16) is taken. It faces severe problems in the non-perturbative regime due to the unavoidable existence of an abundance of gauge-equivalent copies [16, 23].

An important symmetry of the gauge-fixed Lagrangian mentioned already in sec. 2.1.1 above, the BRST symmetry, is discussed in sec. 2.2.3.2 below, in the context of the Kugo–Ojima scenario of confinement. See also our remarks in sec. 2.4 in the context of possible discrepancies between gauge fixing in the continuum and its counterpart on the lattice.

In the lattice discretization of gauge theory, the gauge-equivalent configurations contribute merely a constant factor to both the numerator and the denominator of path integrals like eq. (2.12a). Hence, gauge fixing is not in general required on the lattice. But we calculate gauge-dependent quantities throughout this work, so we need to fix a gauge. See sec. 2.3 for more on lattice gauge theory.

2.2 Confinement and infrared Yang–Mills propagators

2.2.1 The notion of confinement

A basic characterization of confinement of quarks and gluons was already provided in the introduction, ch. 1. While it would be premature to define confinement in general as

[10] "$A = 0$" is here a short notation for the trivial configuration which has $A_\mu(x) = 0$ for any space-time point x and any direction μ.

the absence of particles with fractional electric charge or with non-vanishing color charge (counterexamples are given in [36]), these are reasonable statements in QCD as it stands. In particular, an appropriate description of confinement in QCD is the statement that no asymptotic states carry color charge.

An intuitive picture accounting for confinement is that the chromoelectric flux between a quark and an antiquark is squeezed into a narrow region, forming a flux tube, as illustrated in fig. 2.1. This picture is connected to a phenomenological fact, sc. to the 'Regge trajectories' [37] observed in meson resonances. These trajectories describe the relation between the spin and the squared mass of mesons. They turn out to be almost linear, which can be explained in the flux tube picture. In this picture, the potential energy of quark and antiquark is proportional to the distance between them. Evidently, this statement cannot be strictly valid, as the notion of potential is a non-relativistic one. For finite quark masses, there is a finite energy which suffices to create a new quark–antiquark pair at the expense of the potential energy of the first pair, and 'string breaking' occurs. But for infinitely heavy (static) quarks, which are often simulated on the lattice, the potential rises linearly without bonds. A linearly rising potential corresponds to a force that is independent of the distance.

Figure 2.1: Naïve illustration of the color-electric flux tube between a quark and an antiquark.

Confinement via a flux tube between static charges has been demonstrated to occur in numerical simulations in the framework of lattice gauge theory (e. g. [39, 40, 41]), see sec. 2.3.4 below for a brief introduction including references. (At sufficiently strong coupling, confinement has even been rigorously proven in pure Euclidean lattice Yang–Mills theory [42, 43].) – However, while lattice calculations of the static potential verify *that* the non-

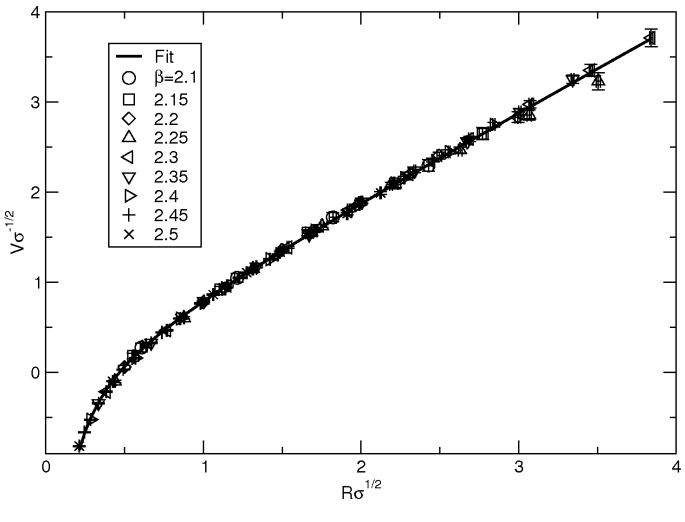

Figure 2.2: Static quark potential in four-dimensional pure $SU(2)$ Yang–Mills theory, from [38]. See sec. 2.3.4 for an explanation, including the definition of the string tension σ, and see eq. (2.68) for the definition of the lattice coupling β.

Abelian gauge theory of QCD exhibits confinement (see fig. 2.2 for an exemplary result in pure $SU(2)$ gauge theory), they do not by themselves offer an explanation for *why* it occurs. The question of how exactly confinement comes about has proven to be very intricate. In fact, a rigorous proof that Yang–Mills theory has a mass gap is part of one of the seven 'millennium prize problems' posed by the Clay Mathematics Institute. The presence of a mass gap means in QCD that massless gluons do not occur as asymptotic states, but instead massive glueballs do so, in which gluons are confined. (We do not always strictly distinguish between the discussion of quark confinement and that of gluon confinement.)

In the present thesis, we are predominantly concerned with the question of the confinement mechanism – not by means of a mathematical proof, but by virtue of numerical simulations. Some approaches aim at explaining the static quark–antiquark potential e. g. in terms of topological defects, see sec. 2.2.3.1. We do not focus on the static potential, which is a gauge-invariant quantity, but instead on the connection of gauge-dependent correlation functions to confinement. Confinement scenarios that postulate such a connection are explained in sec. 2.2.3. Those of our simulations that are directly related to the confinement mechanism pertain to vanishing temperature and density.

At very high temperatures and densities, quarks and gluons are expected to be deconfined. By 'very high', we refer to conditions such as those in the first split seconds after the beginning of the universe (Big Bang). While no entirely uncontroversial signatures of the deconfined state, the quark–gluon plasma, exist yet, indirect evidence has been found at CERN, and afterwards stronger evidence in favor of it has been gathered at the 'Relativistic Heavy-Ion Collider' RHIC [44, 45, 46, 47]. The results so far indicate that it is strongly coupled, behaving more like a liquid than like a gas. It is widely hoped that the 'Large Hadron Collider' (LHC) experiment will improve the empirical knowledge of the quark–gluon plasma. We do not directly address this topic in the present work, but we do perform some simulations concerning the deconfinement phase transition at non-zero temperature (ch. 8) and also explore non-zero density (ch. 9).

2.2.2 Infrared propagators in Landau gauge

We now elaborate on the ghost and gluon propagators in Landau gauge, in particular on their infrared behavior, and also introduce some notations. This infrared behavior provides an important test of confinement scenarios like Gribov–Zwanziger and Kugo–Ojima, as explained in sec. 2.2.3 below. Hence, it potentially offers insight into the mechanism of confinement. In addition to the comprehensive review [28], more concise overviews may be found e. g. in [48, 49, 50].

2.2.2.1 Basics

We have defined Landau gauge above, eq. (2.11). In this gauge, the gluon and ghost propagators, schematically: $\langle A(q)A(-q)\rangle$ resp. $\langle c(q)\bar{c}(-q)\rangle$, have the tensor structures

$$(D_{\mathrm{gl}})^{ab}_{\mu\nu} = \delta^{ab}\left(\delta_{\mu\nu} - \frac{q_\mu q_\nu}{q^2}\right) D_{\mathrm{gl}}(q^2), \tag{2.25}$$

$$(D_{\mathrm{gh}})^{ab} = -\delta^{ab} D_{\mathrm{gh}}(q^2). \tag{2.26}$$

I. e., the gluon propagator is purely transverse (due to the gauge condition (2.11)), and in color space, both the gluon and the ghost propagator are diagonal. Apart from these tensor

structures, the propagators are parametrized by the scalar functions $D_{\mathrm{gl/gh}}(q^2)$. We will mainly calculate these scalar functions; this is discussed in detail in sec. 2.3.3. Sometimes, it is more convenient to explicitly consider the dressing functions, which differ simply by a factor of q^2 from the propagators; they are by definition $q^2\, D_{\mathrm{gl/gh}}(q^2)$. For example, the Gribov–Zwanziger and Kugo–Ojima confinement scenarios (sec. 2.2.3) entail an infrared divergent ghost dressing function in Landau gauge.

2.2.2.2 Continuum results: Scaling and decoupling

The Landau gauge gluon and ghost propagators can be calculated in both the lattice and the continuum formulation of the theory. While we choose the former approach, numerous investigations with functional continuum methods have been performed, sc. with Dyson–Schwinger equations (DSE) [51, 52, 53, 54, 55, 56, 57, 58, 59, 60, 61, 62, 63, 64, 65, 66, 67, 68, 69, 70, 71, 28, 72], the functional renormalization group (FRG) [73, 74, 75, 76, 77, 78, 79, 80, 81] and with a combination of these approaches [82, 83], and also with stochastic quantization in the continuum [84, 85, 20] (related to DSE).[11]

These continuum studies allow for a 'scaling solution', see e. g. [51, 52, 28, 84, 54, 55, 56, 73, 57, 82, 86, 67]. It is explained in sec. 2.2.2.3. Roughly speaking, it is a solution where the ghost propagator is enhanced, which means that its dressing function diverges in the infrared, equivalent to the ghost propagator being more singular than a massless particle pole. The gluon propagator is suppressed in the infrared and vanishes at zero momentum.[12] Crucially, quantitative properties of the infrared behavior of both propagators are connected by a strict relation (eq. (2.28) below) if the scaling solution is realized.

One-parameter family of solutions. The scaling solution is unique[13] [82, 83] (see also [86, 68, 63], and for Coulomb gauge resp. maximal Abelian gauge [87] resp. [88]). 'Unique' means that there is only one scaling solution, not that the scaling solution is the only solution at all.

Indeed, strong arguments have been put forward in favor of a one-parameter family of decoupling solutions where scaling is violated [77, 66]. Related work may be found in [60, 65, 71, 89, 90, 91, 92, 93, 94, 61, 62, 95, 64, 96, 97, 70, 98, 99, 100, 101, 102, 103, 104, 105, 106]. The scaling solution is an endpoint of this one-parameter family of solutions. A decoupling-type solution is characterized by an infrared finite ghost dressing function and an infrared non-zero gluon propagator.[14]

Relation to BRST symmetry. The scaling solution is unique in the specific sense pointed out above: there is only one scaling solution, but it is not the only solution. Rather, it is merely an endpoint of the one-parameter family of solutions. It is singled out, however, by being the one solution that preserves global BRST invariance of the theory [77, 107]. We discuss the notion of BRST symmetry in sec. 2.2.3.2 below. (Note, though, that this

[11] These lists of references are far from exhaustive. – For references to some perturbative results, which are of limited relevance to the infrared behavior, see the remark on stochastic perturbation theory in sec. 4.1.

[12] An infrared non-vanishing, finite gluon propagator is, as a limiting case, not strictly incompatible with scaling. However, an infrared divergent ghost dressing function is required for scaling.

[13] This holds under the assumption of a single mass scale, sc. in four dimensions, Λ_{QCD} (see sec. 2.3.1.5).

[14] In the present context, it goes without saying that the ghost dressing function does not vanish at zero momentum and that the gluon propagator does not diverge there.

statement about the special status of the scaling solution is valid assuming a standard local BRST invariance. Other BRST formulations may be viable for which it does not hold. They remain to be spelled out in detail, see [91] for a promising approach.) Given global BRST invariance, the Kugo–Ojima confinement criterion (sec. 2.2.3.2) entails the scaling solution. – The violation of global BRST symmetry in case of a decoupling solution may severely complicate the construction of a physical state space, as is argued in ref. [77].

2.2.2.3 Infrared exponents

The scaling solution is characterized by a specific infrared power-law behavior of the propagators [51, 52, 84, 54, 73].[15] The infrared exponents $\kappa_{A/C}$ of the gluon resp. ghost propagator (eqs. (2.25) and (2.26)) are implicitly defined via

$$\lim_{q^2\to 0} D_{\mathrm{gl}}(q^2) \propto \frac{1}{(q^2)^{\kappa_A+1}}, \tag{2.27a}$$

$$\lim_{q^2\to 0} D_{\mathrm{gh}}(q^2) \propto \frac{1}{(q^2)^{\kappa_C+1}}. \tag{2.27b}$$

Eq. (2.27) can be used to define infrared exponents in a formal manner also in case that scaling does not hold.[16] For example, $\kappa_{A/C} = -1$ would imply an infrared non-vanishing gluon resp. ghost propagator, and $\kappa_{A/C} = 0$ such a dressing function. However, the scaling solution puts definite restrictions on the values of κ_A and κ_C. Crucially, these values are not independent. The scaling solution entails that the infrared exponents of the ghost and gluon propagator jointly satisfy the scaling relation

$$\kappa_A = -2\kappa_C + \frac{d-4}{2}, \tag{2.28}$$

which depends on the number d of space-time dimensions. In $d = 4$, eq. (2.28) reduces to the particularly simple relation

$$\kappa_A = -2\kappa_C. \tag{2.29}$$

Eq. (2.28) allows to characterize the infrared behavior of the ghost and gluon propagator by just one of the two exponents. Commonly, κ_C is used as this single infrared exponent. It is frequently simply referred to as κ.

The introduction of the unique critical infrared exponent $\kappa := \kappa_C$ also simplifies the statement about the absolute values predicted for κ in case of the scaling solution. It reads

$$\frac{d-2}{4} \leq \kappa < \frac{d}{4}. \tag{2.30}$$

As long as $\kappa > 0$, the ghost propagator in the infrared is enhanced compared to its tree-level behavior, i. e., it diverges more strongly than $1/q^2$ in the limit $q \to 0$. This is strictly implied by the relation (2.30) in three and four dimensions.

Together, eqs. (2.30) and (2.28) entail

$$-2 < \kappa_A \leq -1. \tag{2.31}$$

[15] See also [108, 109] for early confirmation of the result first put forward in [51, 52].

[16] A possible behavior different from a power law is discussed e. g. in [65].

If κ_A takes its maximally allowed value, the gluon propagator assumes a finite and non-vanishing value at zero momentum, as the total power-law exponent in eq. (2.27a) is zero in that case. The usual prediction from scaling, however, is an infrared vanishing gluon propagator at $q = 0$ (see our remarks below eq. (2.33)). An infrared divergent gluon propagator is ruled out in any case, also for solutions of decoupling type.

The derivation of the scaling relation (2.28) rests on non-renormalization of the ghost–gluon vertex in Landau gauge [110, 111], which has been explicitly verified on the lattice [112, 113, 114], also in three [115] and two [116] dimensions, as well as from DSE [58]. Functional continuum methods predict not only the scaling relation between κ_A and κ_C, but also specific values for κ_A and κ_C, subject to the number d of dimensions. By virtue of the scaling relation, it is sufficient to give the values of $\kappa := \kappa_C$ alone. Predictions from DSE for these values read [54, 84], see also [86, 117][17]

$$\kappa = \frac{1}{98}\left(93 - \sqrt{1201}\right) \approx 0.595 \quad \text{in } d = 4, \tag{2.33a}$$

$$\kappa \approx 0.3976 \quad \text{in } d = 3, \tag{2.33b}$$

$$\kappa = 0.2 \quad \text{in } d = 2. \tag{2.33c}$$

The precise values depend on the details of the dressing of the ghost–gluon vertex; the values given here are obtained for a bare vertex [54]. Slightly different values can still be consistent with the scaling solution. The value for $d = 4$ has also been confirmed using the FRG [73, 74], where a possible decrease by 10% is within the regulator dependence; more precisely, the range is $\kappa \in [0.539, 0.595]$, see ref. [73]. Moreover, this range is consistent with the recently found upper bound $\kappa < 23/38$ [118].

We insert here a brief remark about notation. In particular in ch. 5 and also in ch. 6, we frequently use the term 'κ_Z' for the scaling exponent of the ghost propagator as calculated from the gluon propagator assuming the scaling relation (2.28). I. e.,

$$\kappa_Z := \frac{1}{2}\left(\frac{d-4}{2} - \kappa_A\right) \tag{2.34}$$

with κ_A according to eq. (2.27a). This allows to compare the infrared behavior of the ghost and gluon propagators in a particularly transparent manner, since a necessary criterion for the scaling solution in this notation is simply $\kappa_Z = \kappa$ (equivalent to eq. (2.28)).

For decoupling-type solutions, both the gluon propagator and the ghost dressing function are finite, neither divergent nor vanishing, in the infrared. These solutions can be formally characterized by the infrared exponents $\kappa_A = -1$ and $\kappa_C = 0$, see eq. (2.27). In this case, it is not possible to describe the behavior of the ghost and gluon propagator at small momenta by a common infrared exponent, since the gluon decouples at small momenta (below its mass).

[17] The value in three dimensions cannot be given in such a concise form as in the four-dimensional case. Rather, it is obtained as a root of the equation (see [84])

$$\frac{32\alpha(1-\alpha)(1-\cot^2(\pi\alpha))}{(3+2\alpha)(1+2\alpha)} = 1. \tag{2.32}$$

2.2.2.4 Possible relation to experiments

We emphasize that the scaling and decoupling solutions differ only in the infrared regime, i. e., at momenta $q \lesssim \Lambda_{\mathrm{QCD}}$, on the order of a few hundred MeV and below. A precise determination of the scale below which the solutions differ is also impeded by finite volume effects in lattice simulations. At intermediate and large momenta, the solutions agree with each other. Which type of infrared solution is realized is a question of relevance to the theoretical explanation of confinement.

In contrast, experimental results are in general not sensitive to the behavior of the propagators in the deep infrared. This holds not only for the general fact of quark and gluon confinement (see sec. 2.2.4.1 resp. 2.2.4.2 for details) – e. g., quark confinement has been shown to follow from a scaling behavior as well as from a decoupling behavior [119] –, but it holds also for more specific facts. Both the deconfinement phase transition and the chiral phase transition (i. e., the transition at which chiral symmetry is restored) have been investigated in the unquenched [120] and the quenched [121] case,[18] with the result that the influence of the type of infrared solution (scaling vs. decoupling) is tiny. The gauge-dependent propagators of QCD are used as input to certain equations for hadron phenomenology, see the reviews [28, 72, 49] and also the references in [122]. Certain meson properties, the mass and decay constant of the ρ meson, have recently been found to be independent of the infrared behavior of the propagators [123].

On the other hand, it has been argued that for some issues accessible by experiment, a non-vanishing effective gluon mass might be relevant. This was already remarked in the pioneering study [124] of the gluon propagator. In particular, in the early work [125] the view is expressed that a non-vanishing effective gluon mass might be favored by certain properties of J/ψ decays. Further examples of work that aims to relate the behavior of the gluon propagator to experimental data are [126, 127].[19] However, nontrivial assumptions about vertex structures are required in order to establish such statements.

Overall, we do not hold the view that a convincing case for either type of solution could be made based on experimental data. But it is worth stressing again that both scaling and decoupling solutions are consistent with the fact of confinement (see sec. 2.2.4).

2.2.2.5 Running coupling

We have already mentioned the peculiar property of the QCD coupling strength to decrease toward small distances, i. e., large momentum scales. A non-perturbative definition of the running coupling [51, 52] in terms of the gluon and ghost propagators, suitable also for lattice studies, is[20]

$$\alpha_S(q) = \frac{g^2}{4\pi} \left(q^2 D_{\mathrm{gl}}\right) \left(q^2 D_{\mathrm{gh}}\right)^2 , \tag{2.35}$$

This is a gauge-dependent quantity and thus, as it stands, not an observable. If the scaling solution is realized, α_S takes a non-vanishing value in the infrared, in contrast to the

[18] See sec. 2.3.1.1 for the definition of 'quenched'.

[19] For further references, see e. g. ref. 2 in [128] and ref. 93 in [129], and also [130].

[20] A brief overview of alternative definitions of the running coupling in the non-perturbative regime is provided e. g. in [113]. The non-renormalization of the ghost–gluon vertex [110] enters in eq. (2.35) (as its squared renormalization constant would explicitly occur in the denominator if it did not equal unity).

decoupling solution, where $\alpha_S(0) = 0$. In four dimensions and for a regular ghost–gluon vertex, this value is for the gauge group $SU(N_c)$ [54]

$$\alpha_S \approx \frac{9}{N_c} \cdot 0.99, \tag{2.36}$$

hence $\alpha_S \approx 4.46$ for $SU(2)$, which we study here. Note that eq. (2.35) yields a dimensionless quantity only in $d = 4$ dimensions, as the coupling g^2 has mass dimension $d - 4$. Otherwise, additional powers of the momentum have to be introduced in order to render the effective running coupling dimensionless in any dimension d.[21] We further discuss the case $d \neq 4$ in sec. 5.2.3.

The definition (2.35) of the running coupling is not unique, in particular with regard to the infrared behavior. For instance, an alternative which is hardly sensitive to the distinction between scaling and decoupling has been proposed in [77].

2.2.3 Confinement scenarios

The occurrence of confinement cannot depend on the choice of a specific gauge. But its explanation may well be phrased differently for different gauges, i. e., confinement scenarios may depend on the gauge. Some established scenarios ascribe an important role in explaining confinement to the condensation of topological defects, like center vortices or magnetic monopoles. We briefly explain this in the following, since the location of such defects in configuration space may connect them to the Gribov–Zwanziger scenario.[22]

2.2.3.1 Confinement via topological defects

It was suggested in refs. [139, 140, 141, 142, 143, 144] that center vortices could account for confinement of quarks in non-Abelian gauge theories. Roughly speaking, these objects are $d - 2$-dimensional hypersurfaces of finite thickness which carry chromomagnetic flux and contribute a non-trivial center element to a Wilson loop (see sec. 2.3.1.2) when linked to it. Thus, they are named after the center of the gauge group (see app. A.2.5). Center vortices can be identified on the lattice [145], and it has been shown in lattice simulations that removal of the vortices makes the static quark–antiquark potential vanish at long distances, e. g. [146]. This removal also has a significant impact on the gluon propagator [147] and on the ghost propagator [148]. The density of vortices has been shown to exhibit asymptotic scaling in $SU(2)$ [149] and $SU(3)$ [150]. The string tension brought about by them may be evaluated by projecting the configurations to the center subgroup after suitable gauge fixing. For the gauge group $SU(2)$, this procedure often reproduces virtually the full string tension [151, 145, 152, 153, 154], even though the percentage diminishes after more elaborate gauge fixing [155]. The string tension of the full theory is only partially reproduced after

[21] An analogous role is played by the power of the lattice spacing in the definition of the dimensionless lattice coupling β, eq. (2.68), which depends on g^2.

[22] For reviews of the confinement problem including the relevance of center symmetry, see [36, 131] and also [132]. – For the connection between center vortices, the configuration space and the infrared propagators in Coulomb gauge, see e. g. [133, 134], and for lattice results on the propagators in this gauge see e. g. [135, 136, 137, 138].

center projection in larger gauge groups like $SU(3)$ [150], which is realized in nature, and $Sp(2)$ [38].[23]

If an explanation in terms of magnetic monopoles is correct, confinement may be described in a comparatively vivid and intuitive way by means of the 'dual Meißner effect' [158, 159, 160, 161]. This effect resembles the Meißner effect that occurs in ordinary superconductors of type II. But it differs from that effect insofar as the roles of electric and magnetic fields are inverted (thus 'dual'). See e. g. [162, 163] for a partial corroboration of the relevance of Abelian monopoles on the lattice.

Vortices and monopoles are defects in the sense that the action formally becomes infinite. Depending on the gauge, vortices can be located in a specific region of configuration space, sc. in the vicinity of the Gribov horizon in Coulomb and also Landau gauge [164, 134]. This fact provides a connection between the confinement scenarios in terms of topological defects and different, mutually related confinement scenarios, sc. the Gribov–Zwanziger and Kugo–Ojima scenarios, to which we now turn.

2.2.3.2 Kugo–Ojima scenario and BRST symmetry

The gauge-fixed Lagrangian of QCD is invariant with respect to BRST transformations (as mentioned already on p. 9). This symmetry is valuable for the following reason. If global BRST invariance holds, and a corresponding charge is thus conserved, the latter can be used to define the physical state space of a quantum field theory. I. e., it serves to draw the boundary between particles (fields) that occur as asymptotic states and such ones that do not, either because they are unphysical particles with negative norm in the first place, like ghosts, or because they are confined, like gluons. In particular, we discuss BRST symmetry here because it is intimately related to an important criterion for confinement, the Kugo–Ojima criterion. We do not state the BRST transformations explicitly, as they are not directly relevant for our purpose and can be found in various textbooks, e. g. [26, 165, 166]. Instead, we confine ourselves to brief remarks about the essentials of BRST invariance to the extent that they are relevant to the confinement mechanism.

The Kugo–Ojima scenario of confinement, as put forward in [21] and reviewed e. g. in [167], singles out the physical part of state space, the set of states possessing a positive norm. It explains confinement via the BRST quartet mechanism. This mechanism resembles the Gupta–Bleuler mechanism [168, 169] in QED, as both remove unphysical polarizations of the gauge bosons from the spectrum, i. e., such ones that do not appear as asymptotic states in the scattering matrix (S-matrix). The Gupta-Bleuler mechanism ensures that longitudinal and timelike photons cancel in all S-matrix elements. Transverse photons, on the other hand, are asymptotic states.

In QCD, the BRST quartet mechanism faces the task of eliminating also transverse gluons from the spectrum of asymptotic states. All S-matrix states have to be neutral with respect to color, and the ghosts need to vanish from the spectrum. BRST quartets are composed of two BRST exact states (see eq. (2.40) below) and two BRST non-invariant states. For both of these doublets, one state of the doublet is the BRST variation of the other one. Together, the contributions from these four states cancel in all physical observables. All states can be exhaustively classified into members of BRST quartets on the one hand and

[23] Skepticism concerning the relevance of the center for the deconfinement transition is articulated e. g. in [156, 157].

BRST singlet states on the other hand.

Now for a few more formal statements. The BRST operator Q_B is nilpotent, i. e.,

$$Q_B^2 = 0. \tag{2.37}$$

The physical state space is the cohomology of Q_B,

$$W_{\text{phys}} = \frac{\operatorname{Ker} Q_B}{\operatorname{Im} Q_B}. \tag{2.38}$$

We now spell out this statement. The physical state space is the set of states $|\psi\rangle$ which (i) are BRST invariant, i. e., are annihilated by the BRST charge,

$$Q_B|\psi\rangle = 0, \tag{2.39}$$

and (ii) are not BRST exact. For a state $|\psi\rangle$ to be BRST exact is to be the BRST variation of another state $|\phi\rangle$,

$$|\psi\rangle = Q_B|\phi\rangle. \tag{2.40}$$

Since Q_B is nilpotent, eq. (2.37), any BRST exact state is BRST invariant. That physical states are annihilated by the BRST charge means that they are elements of its kernel. That they are not BRST exact means that they are not elements of the image of Q_B. These two statements together add up to (2.38). The states that fulfill this condition are BRST singlet states.

Hence, an unbroken BRST symmetry can be utilized to define the physical part of the state space. The physical state space contains only color-neutral states if a global color charge is well-defined.

We are particularly interested in the implications of the Kugo–Ojima confinement criterion for the infrared behavior of the ghost and gluon propagators. An integral part of this criterion is that a well-defined global color charge exists if and only if the theory has a mass gap and, in Landau gauge, there is an infrared enhanced ghost propagator.

The Kugo–Ojima criterion, which is valid in linear covariant gauges, has in Landau gauge the seemingly simple form[24]

$$u^{ab}(q=0) =: u^{ab} \stackrel{!}{=} -\delta^{ab}. \tag{2.41}$$

The crucial parameters u^{ab} are defined via the asymptotic limit of the covariant derivative of the antighost field. The latter is an important quantity as it enters into the globally conserved current corresponding to the BRST charge. The limit which implicitly defines q^{ab} reads

$$D_\mu^{ab}\bar{c}^b = \left(\partial_\mu\delta^{ab} + g f^{abc} A_\mu^c\right)\bar{c}^b \xrightarrow[x_0\to\pm\infty]{} \left(\delta^{ab} + u^{ab}\right)\partial_\mu\bar{\gamma}^b + \ldots, \tag{2.42}$$

where $\bar{c}^a \xrightarrow[x_0\to\pm\infty]{} \bar{\gamma}^a$. The condition (2.41) eliminates this massless asymptotic state. Defining the single parameter $u := u(q=0)$ in $u^{ab}(q) = \delta^{ab}u(q)$, the Kugo–Ojima criterion may then be succinctly written as

$$1 + u = 0. \tag{2.43}$$

[24] Here, we closely follow the presentation in ref. [49].

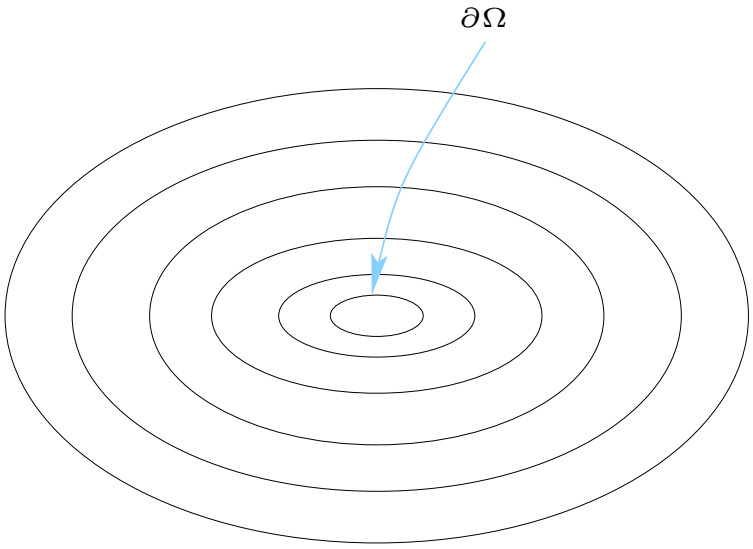

Figure 2.3: Illustration of the various Gribov regions in configuration space. At each of the borders, one eigenvalue of the Faddeev–Popov operator changes its sign. In the following, we are usually concerned with the first Gribov region, the innermost one in this sketch, see fig. 2.4 for a more detailed look.

The parameter u is related [22] to the infrared ghost dressing function as

$$\frac{1}{q^2 D_{\mathrm{gh}}(q=0)} = 1 + u. \tag{2.44}$$

Hence, the Kugo–Ojima criterion of confinement entails that the ghost propagator diverges more strongly than $1/q^2$ at infrared momenta. In short, it predicts ghost enhancement, expressed by a positive infrared exponent of the ghost, $\kappa > 0$.

The parameter u has been explicitly determined on the lattice [170, 171, 172, 173], where values around $-(0.6 - 0.8)$ have been found.

We emphasize that the consequences of the Kugo–Ojima scenario are consistent with the scaling solution under the assumption that a 'standard' global BRST symmetry exists. There is work toward an alternative (non-local) BRST formulation [91] which might eventually break this firm link between the Kugo–Ojima criterion and the scaling solution. However, this remains to be shown.

2.2.3.3 Configuration space and the Gribov ambiguity

In the following, we introduce some notions about configuration space of Yang–Mills theories, with a focus on Landau gauge. This is helpful for the subsequent presentation of the Gribov–Zwanziger scenario of confinement [16, 17, 18, 19, 20]. This scenario starts from a different perspective than the Kugo–Ojima scenario, but it turns out to have similar consequences for the infrared behavior of correlation functions.

Gribov regions and first Gribov region. The configuration space of Yang–Mills theories contains various 'Gribov regions' (illustrated in fig. 2.3), which are distinguished by the

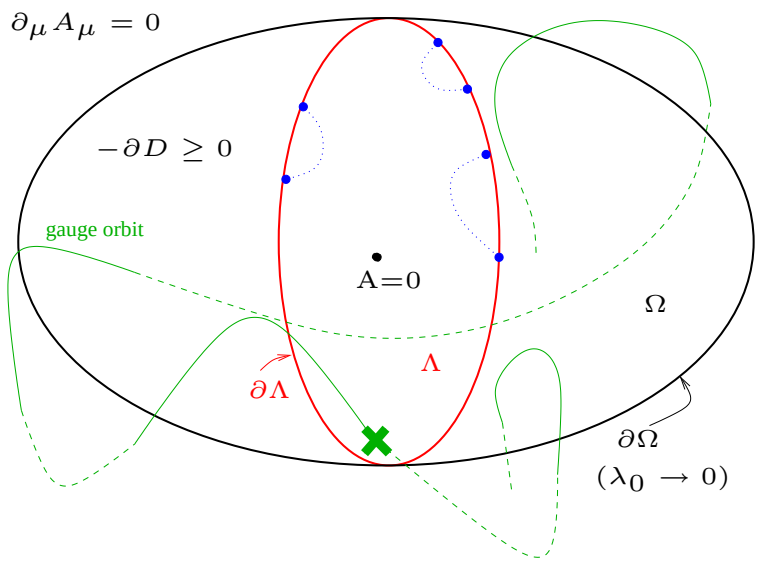

Figure 2.4: Schematic depiction of the first Gribov region Ω (black ellipse) and the fundamental modular region Λ (red ellipse). The plane of projection represents the gauge fixing surface Γ. The green line is a gauge orbit, which pierces Γ many times inside Ω, but only once inside Λ (green cross). Blue dotted lines connect gauge-equivalent configurations on ∂Λ.

sign of the eigenvalues of the Faddeev–Popov operator, defined in eq. (2.17). If Landau gauge fixing has been performed, i. e., the Lorenz gauge condition eq. (2.11) is satisfied, the configurations are situated on the gauge fixing surface

$$\Gamma = \left\{ \{A_\mu(x)\} \,\middle|\, \partial_\mu A_\mu(x) = 0 \right\}. \tag{2.45}$$

At a 'Gribov horizon', which is the border between two Gribov regions, one of the eigenvalues λ_i changes its sign, and so does the Faddeev–Popov determinant[25]

$$\det\left(-\partial_\mu D_\mu\right) = \prod_n \lambda_n. \tag{2.46}$$

In particular, $\lambda_i = 0$ at the respective horizon. After gauge fixing, every eigenvalue of the FPO is positive, i. e., the FPO is a positive operator. (Note that there are $N_c^2 - 1$ zero eigenmodes, which are omitted in these considerations.) This defines the first Gribov region $\Omega \subset \Gamma$,

$$\Omega = \left\{ \{A_\mu(x)\} \,\middle|\, \partial_\mu A_\mu = 0 \wedge -\partial_\mu D_\mu[A] > 0 \right\}. \tag{2.47}$$

The properties of the Gribov region depend on the chosen gauge. We explore it here in Landau gauge.[26] It is convex and bounded in every direction [20]. Moreover, it contains the origin, i. e., the trivial gauge configuration where $\forall x, \mu : A_\mu(x) = 0$.

[25] Note that here and sometimes in the following, the explicit form of the Faddeev–Popov operator which we give is specific to Landau gauge (more precisely, to linear covariant gauges).

[26] See e. g. [174] for Coulomb gauge and [175] for maximal Abelian gauge (with $N_c > 2$ colors).

Gauge orbits. An gauge orbit is a set of gauge copies ('configurations' in a broad sense) which can be obtained from a single configuration ('configuration' in a narrow sense, with fixed values of $A_\mu(x)$ for all μ and x) by virtue of gauge transformations V (see eq. (2.7)),

$$O[A] := \left\{ \{\tilde{A}_\mu\} \,\middle|\, \tilde{A}_\mu = A_\mu^V \right\}. \tag{2.48}$$

Every gauge orbit intersects the gauge fixing surface inside the first Gribov horizon, see e. g. [176]. Crucially, every orbit does so multiple times [177, 178, 176, 179]. I. e., even inside the first Gribov region, many gauge copies of each configuration exist.

Gauge copies of a configuration C are physically equivalent configurations, related to C and thus to each other by local gauge transformations. They are nevertheless clearly distinct from C e. g. for the purpose of calculating gauge-dependent quantities, as we do here. Specifically, for any configuration $C \in \Omega$, there is an abundance of gauge copies $\tilde{C}$ of C which are also in Ω. This ambiguity cannot be resolved by any local condition – hence, not only Landau gauge is not uniquely fixed.[27] It is known as the Gribov–Singer ambiguity [16, 23], reviewed e. g. in [180]. Despite Singer's merit in having proven the generality of this problem, we will usually refer to it simply as the 'Gribov problem' for brevity.

Fundamental modular region. There is a region in configuration space which contains only a single copy of each configuration [179, 176], the fundamental modular region (FMR) Λ,[28] a convex manifold [177] that is a proper subset of Ω. In contrast to the interior of Λ, its border does contain configurations which are gauge copies of each other [179, 182, 183, 181], symbolized by the blue dots on $\partial\Lambda$ in fig. 2.4. Unfortunately, no local criterion is known that allows to determine whether a given configuration is an element of Λ – in contrast to the first Gribov region, where it suffices to calculate the Faddeev–Popov eigenvalues and to check thereby whether the operator is positive.

On the lattice, the fundamental modular region corresponds to the set of global maxima of a gauge fixing functional. But to find this maximum for a given configuration is an optimization problem that de facto eludes a solution, see sec. 2.3.2 for more remarks on this.

According to a conjecture by Zwanziger, the FMR and the Gribov region might be equivalent in the thermodynamic limit [20]. This would entail Gribov copy effects to become weaker with increasing lattice volumes. However, it is a conjecture. And even if it should prove to be true, it implies no definite statement on how large the lattices would have to be in order for Gribov copy effects to become insignificant.

The Gribov region and the fundamental modular region are illustrated, together with a generic gauge orbit, in fig. 2.4.

2.2.3.4 Gribov–Zwanziger scenario

Basic idea. The Gribov–Zwanziger scenario [16, 17, 20] rests on restricting the path integral to the first Gribov region. It may, in a simplifying manner, be characterized by the

[27] There are gauges without Gribov copies, like the axial gauge $n_\mu A_\mu = 0$, but their choice leads to other difficulties (singularities in the propagator).

[28] The fundamental modular region is sometimes also referred to as 'fundamental domain', e. g. in [181]. We stick with the former terminology.

statement that configurations in the vicinity of $\partial\Omega \cap \partial\Lambda$ account for confinement [20]. Intuitively, the accentuated role of $\partial\Omega$ is related to the idea that entropy favors $\partial\Omega$ due to the high dimensionality of configuration space (in lattice simulations, on the order of the number of lattice sites). This is because in spaces of high dimensionality, almost all of the volume of a hypersphere is close to its surface, as the volume measure $r^{d-1}dr$ is peaked at $r \approx 1$ for large d. While this is a general proposition and prima facie not directly related to confining properties of the theory, e. g. connections to the location of topological defects in other confinement scenarios (see sec. 2.2.3.1) exist.

Implications for the infrared propagators. Again, we are in particular interested in the consequences for the infrared behavior of the propagators. The Gribov–Zwanziger scenario implies

(i) that the ghost propagator is infrared enhanced, i. e., that the ghost dressing function diverges for infrared momenta $q^2 \to 0$ [17, 18] ('ghost enhancement'), and

(ii) that the gluon propagator vanishes in the infrared limit [19], see also [184, 185].

The first implication, sc. ghost enhancement, amounts to the horizon condition, which at the same time serves to restrict the functional integral to the first Gribov region. While the Kugo–Ojima scenario also predicts ghost enhancement, the second implication of the Gribov–Zwanziger scenario, i. e., the one concerning the gluon propagator, is stronger than the corresponding statement of the Kugo–Ojima scenario (which merely entails an infrared non-divergent gluon propagator). In this regard, the Gribov–Zwanziger scenario makes the more restrictive (more informative, logically stronger) statement than the Kugo–Ojima scenario. This can be seen by considering its implications for κ, the infrared exponent of the ghost propagator, see sec. 2.2.2. While the Kugo–Ojima scenario simply predicts $\kappa > 0$ overall, the Gribov–Zwanziger scenario entails $\kappa > 0$ for the ghost and $\kappa_A < -1$ for the gluon. The latter statement entails $\kappa > 1/2$ if the scaling relation, eq. (2.29), is invoked.[29]

Discussion. These statements can be realized by virtue of the Gribov–Zwanziger action [16, 186] already at the perturbative level. This action restricts the field configurations entering into the path integrals to the first Gribov region. This breaks global BRST invariance. A possible alternative BRST formulation [91] might be more in line with the Gribov–Zwanziger action approach (see e. g. [187, 188] for relatively recent work within the Gribov–Zwanziger action approach). In particular, there have been efforts [89, 90, 189, 93] to reconcile the Gribov–Zwanziger action with the lattice results, which are at odds with scaling in three and four dimensions (see [190] for the two-dimensional case), as we review in sec. 2.4 below. This has led to the 'refined Gribov–Zwanziger action' (which still exhibits a soft breaking of the BRST symmetry, see [90, 191]). See also [192] for a recently proposed alternative, which may again permit a scaling solution in a modification of the Gribov–Zwanziger theory, and [193, 194, 195] for recent work on the relation between the Gribov–Zwanziger theory and BRST symmetry.

As noted, the Gribov–Zwanziger and the Kugo–Ojima scenarios make similar predictions for the infrared behavior of the gluon propagator, and identical ones for the ghost.

[29] With regard to eq. (2.29), note again that we refer to the infrared ghost exponent κ_C also as κ.

This is so even though they start from quite different perspectives. For recent work on the relation between the two frameworks, see e. g. [196].

All in all, it is fair to say that the debate about the precise status of the two confinement scenarios is not settled from a theoretical point of view. We take an agnostic stance here and concentrate on the relation of the standard formulation of the confinement scenarios to the lattice results.

2.2.3.5 Early results on the gluon propagator

The predictions of the Gribov–Zwanziger/Kugo–Ojima confinement scenario render the old idea of 'infrared slavery' obsolete, which involves an infrared behavior of the gluon propagator proportional to $1/q^4$ [197] (see e. g. [198, 199, 200, 201] for work along the same lines), leading to an area law for the Wilson loop (see eq. (2.104) in sec. 2.3.4 below) and thus to a linear confining potential [202].

The results of ref. [197] are based on certain momentous approximations. In particular, essentially all ghost contributions to the gluon DSE of pure QCD were neglected (see e. g. [28]). Due to a plethora of results gathered in the meantime, it is now uncontroversial that these approximations are misleading and that, instead, the ghost propagator plays a crucial role in infrared Yang–Mills theory in Landau gauge [51, 52], see also [83, 57, 63], and that in fact the gluon propagator does not diverge in the infrared.

However, this insight did not unambiguously resolve the question of the true infrared behavior of the gluon propagator. In addition to an infrared vanishing gluon propagator, in line with the scaling solution, a massive infrared behavior of the gluon propagator, with a dynamically generated mass, was obtained in [98] from a self-consistent solution to the corresponding DSE.

We stress once again that the behavior of both the ghost and the gluon propagators needs to be taken into account when assessing which type of infrared solution is realized, as the scaling solution entails an exact relation between the respective infrared exponents, eq. (2.28). Both scaling- and decoupling-type solutions are part of the one-parameter family of solutions found with functional methods. The scaling solution stands out among this family since it is in line with global BRST symmetry.

2.2.4 More on the relation of the infrared behavior to confinement

2.2.4.1 Relation of color confinement to quark confinement

In Landau gauge, the Gribov–Zwanziger/Kugo–Ojima scenarios of confinement make predictions for the infrared behavior of the ghost and gluon propagators, as laid out in detail in sec. 2.2.3.In this sense, confinement implies a certain infrared behavior of the propagators. It has also been shown that a converse type of statement holds, sc. that ghost and gluon propagators with a sufficiently large infrared suppression of the gluon and an infrared enhancement of the ghost lead to quark confinement [119] (see also [203] for further analysis of the relation between quark confinement and color confinement for a variety of gauge groups). The order parameter for confinement, related to center symmetry, is the Polyakov loop (strictly so in the limit of infinitely heavy quarks).[30] To be more specific,

[30] See sec. 8.1 below.

it has been shown that in case scaling is realized, a sufficiently large value of the infrared ghost exponent, sc.

$$\kappa_C \equiv \kappa > \frac{d-3}{4}, \tag{2.49}$$

entails confinement in this sense. In the same ref. [119], it has been demonstrated that a decoupling-type solution has the same consequence.

2.2.4.2 Violation of reflection positivity

There is a different way to see that both scaling-type and decoupling-type solutions are confining (now in the sense of gluon confinement). This simply rests on the fact that for both of them, reflection positivity of the gluon propagator is violated, even though it is maximally violated only for the scaling solution. We briefly introduce the notion of reflection positivity here; a detailed account is given e. g. in the review [28].

Positivity is an important property of Euclidean two-point functions, since they possess a Källén–Lehmann representation if and only if reflection positivity holds, and since the absence of such a representation entails that it is not possible to interpret the respective field in terms of stable particle states. E. g. for gluons, this impossibility amounts to confinement. The Källén–Lehmann representation of a propagator is of the form

$$D(q) = \int_0^\infty dm^2 \frac{\rho(m^2)}{q^2 + m^2} \tag{2.50}$$

with the crucial condition that the spectral density is non-negative, $\rho(m^2) \geq 0$. This can be formulated in terms of the Euclidean correlator

$$\begin{aligned} \tilde{D}(t, \vec{q}^2) &= \int_{\vec{q}^2}^\infty d\omega \, \rho\left(\omega^2 - \vec{q}^2\right) e^{-\omega t} \\ \text{with } \omega &:= \sqrt{\vec{q}^2 + m^2}. \end{aligned} \tag{2.51}$$

Evidently, if $\tilde{D}(t, q^2)$ takes negative values anywhere, then $\rho(m^2) < 0$ for some m^2. Hence, the temporal correlator $\tilde{D}$ provides a formal confinement criterion.

Positivity violation has been explicitly confirmed in lattice simulations of four-dimensional pure $SU(3)$ gauge theory [173, 204, 205] as well as of three-dimensional pure $SU(2)$ gauge theory [206] and also of unquenched $SU(3)$ [173, 205].[31] – From $D(t, \vec{0})$, an effective mass may be defined as

$$m_{\text{eff}}(t) = -\frac{d \log D(t, \vec{q}^2 = \vec{0})}{dt}, \tag{2.52}$$

which was found to grow with increasing t already in the early simulation of ref. [124]. This result was subsequently confirmed, see e. g. [211, 212, 173]. – Positivity violation is obtained also in a DSE approach [213]. On the lattice, where the gluon propagator is finite and non-zero at $q = 0$ in three and four dimensions, positivity is non-maximally violated, which still entails gluon confinement. An infrared vanishing gluon propagator means that reflection positivity is maximally violated. – For the ghost propagator, the situation is simpler than for the gluon. It is negative (eq. (2.26)), so positivity is violated in any case.

[31] See also [207, 208, 209, 210]. – The concept 'quenched' is defined in sec. 2.3.1.1.

2.3 Lattice gauge theory

2.3.1 Generalities

2.3.1.1 Path integrals and lattice formulation

Lattice gauge theory [214] is a method from first principles that allows for a numerical treatment and solution of gauge theories like QCD. Reviews may be found in many textbooks, e. g. [215, 216, 217, 218, 219]. The basic idea is, starting from the path integral quantization of a quantum field theory, to replace the (formal) path integrals (e. g. (2.12)) over an infinite number of degrees of freedom by well-defined integrals in a large, but finite number of dimensions. This is done by defining the gauge and fermion fields on a hypercubic lattice in Euclidean space-time with a non-vanishing lattice spacing a. Since this induces a $2\pi/a$-periodicity of the Fourier transforms of functions defined on the lattice, it leads to a momentum cutoff π/a. Thereby, an ultraviolet regulator is introduced into the respective quantum field theory without compromising gauge invariance. Of course, certain space-time symmetries, like Euclidean rotational resp. Lorentz invariance, are broken by this procedure. It permits a numerical evaluation of expectation values without encountering divergences, in contrast to continuum path integrals. This is since the full gauge group is simply the product of the a compact group (the gauge group in the narrow sense), like $SU(2)$ or $SU(3)$, at all lattice sites, whose number is of course finite. The effect from 'overcounting' due to various gauge copies amounts simply to multiplication by the same number in the numerator and in the denominator of eq. (2.56). Hence, these factors cancel, and no problem of divergences arises, in contrast to continuum methods.

Therefore, gauge fixing on the lattice is obsolete in many cases where it is required in continuum calculations. However, for our purposes, gauge fixing is indispensable, since we study gauge-dependent quantities. And it often occupies the focus of our attention because the Gribov ambiguity plays a crucial role for central quantities of interest, see sec. 2.2.3.3. This ambiguity entails that gauge fixing is far from unique. This can exert a possibly large influence on the results, as we will demonstrate by virtue of numerical results in ch. 6. See e. g. [220] for a review of lattice gauge fixing procedures.

The basic quantities of lattice gauge theory are the link variables $U_\mu(x)$, which represent the gauge field and are explained in sec. 2.3.1.2 below, and the fermion and antifermion fields ψ, $\overline{\psi}$. Fermion fields are defined on the lattice sites, and gauge fields on the links between these sites, as illustrated in fig. 2.5. The calculation of expectation values in lattice gauge theory is based on integrals of the form (see also eq. (2.12) above)

$$\langle B\rangle = \frac{1}{Z}\int \mathcal{D}U\,\mathcal{D}\psi\,\mathcal{D}\overline{\psi}\,e^{-S_G[U]-S_F[\psi,\overline{\psi},U]}B[\psi,\overline{\psi},U], \tag{2.53}$$

with the gauge resp. fermion action S_G resp. S_F, and formally with the partition function

$$Z = \int \mathcal{D}U\,\mathcal{D}\psi\mathcal{D}\overline{\psi}\,e^{-S_G[U]-S_F[\psi,\overline{\psi},U]}, \tag{2.54}$$

but de facto, mostly either an independent normalization is given (see e. g. sec. 2.3.4), or ratios of expectation values are considered such that Z cancels. The integral over the fermion and antifermion field may be absorbed in the determinant of the fermion matrix M, yielding

$$\langle B\rangle = \frac{1}{Z}\int \mathcal{D}U\ \det M[U]B[U]e^{-S_G[U]}. \tag{2.55}$$

If dynamical fermions are included in the simulations, the generation of configurations requires the frequent inversion of the fermion determinant (see ch. 9). We work in the quenched approximation, in which the fermion determinant $\det M$ is set to unity. This amounts to omitting effects from vacuum quark loops. Hence, it suffices to consider

$$\langle B \rangle = \frac{1}{Z} \int \mathcal{D}U \, e^{-S[U]} B[U] \tag{2.56}$$

with

$$Z = \int \mathcal{D}U \, e^{-S[U]}, \tag{2.57}$$

where the pure gauge action S_G is now simply denoted by 'S'; $\mathcal{D}U$ is the Haar measure of the gauge group (see app. A.2.1).

The method of choice for numerically evaluating the integral (2.56), which is of high, but finite dimensionality, is Monte Carlo integration with importance sampling. Essentially, the expectation values can be calculated from N uncorrelated configurations via

$$\langle B \rangle = \frac{1}{N} \sum_c B_c[U], \tag{2.58}$$

where c counts the configurations and B_c is the value on a specific configuration. For any implementation, it must be specified how the N configurations are generated. We give some details on the Markov chain Monte Carlo approach in app. B.1.

Note that eq. (2.56) pertains only to gauge-invariant quantities in a straightforward way, since in these cases it is insignificant whether there is any bias regarding which gauge copies on each orbit are sampled. A large part of our work in the thesis at hand (especially chs. 4 and 6) revolves around the possible significance of such a bias for gauge-dependent quantities.

2.3.1.2 Link variables

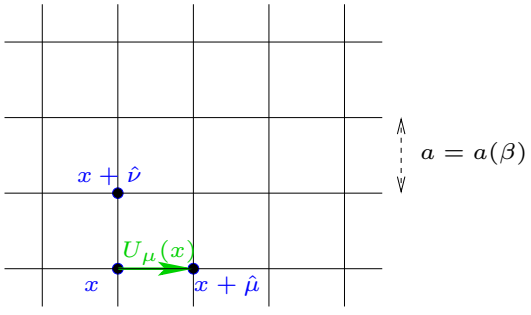

Figure 2.5: Two-dimensional illustration of a hypercubic lattice with link variables $U_\mu(x)$.

For calculations in lattice gauge theory, the gauge fields are not introduced as variables $A_\mu(x)$ from the Lie algebra of the gauge group, but rather as link variables $U_\mu(x)$ which take values in the gauge group itself. They are defined on the links between the sites on the hypercubic Euclidean space-time lattice, see fig. 2.5 for an illustration. For a numerical treatment, the lattice must, of course, be of finite size. Periodic boundary conditions are the standard choice for the gauge fields (a slight difference arises for fermions, where antiperiodic b. c. in the temporal direction are required, but we simulate fermions only in ch. 9). Thus, these fields are defined on a torus. See, however, ch. 7 for a deliberately different choice of boundary conditions. The link variable $U_\mu(x)$ is defined

on the link emanating from the site x and pointing in direction $\hat{\mu}$. Each link variable is oriented, i. e.,

$$U_{-\mu}(x) = U_\mu^\dagger(x - \hat{\mu}). \tag{2.59}$$

The link variables $U_\mu(x)$ are analogous to parallel transporters, i. e., they constitute the lattice version of the path-ordered exponential of the gauge field along a contour, see e. g. [26, 219]. They are related to the algebra-valued lattice gauge field $A_\mu(x)$ via[32]

$$U_\mu(x) = \exp\left(iaA_\mu(x)\right). \tag{2.60}$$

But they are taken to be the basic variables of quenched lattice theory, not derived quantities. From eq. (2.60),

$$U_\mu(x) = \mathbb{1} + iaA_\mu(x) + \mathcal{O}(a^2). \tag{2.61}$$

As this relation involves terms of higher order in the lattice spacing (discretization effects), the determination of the lattice gauge field from the link variables is not unique, see app. C.1 for different possibilities. The standard definition is

$$A_\mu(x) = \left[\frac{U_\mu(x) - U_\mu^\dagger(x)}{2ia}\right]_{\text{traceless part}}. \tag{2.62}$$

Since $A_\mu = A_\mu^a T^a$ with the generators $T^a = \sigma^a/2$ of $SU(2)$ (cp. app. A.2), the components of the lattice gauge field are simply given by

$$aA_\mu^a(x) = 2u_\mu^a(x), \tag{2.63}$$

where the Cayley–Klein parametrization (2.72) of the $SU(2)$ link variables has been used.[33] In practice, we sometimes omit the factor of the lattice spacing when the lattice gauge field A is concerned.

A general gauge transformation of a configuration $\{U_\mu(x)\}$ is on the lattice given by

$$U_\mu(x) \to \Omega(x)U_\mu(x)\Omega^\dagger(x + \hat{\mu}) \tag{2.64}$$

for all sites x and directions μ, where $\Omega(x)$ is an arbitrary, independent element of the gauge group for all x.

Closed loops of link variables are invariant under gauge transformations of the form specified in (2.64).[34] They are called 'Wilson loops'. A general rectangular Wilson loop is a path-ordered product of link variables along a (typically) rectangular contour $\mathcal{C}$. Often, the term 'Wilson loop' is used to denote the normalized trace of such a holonomy,

$$W_\mathcal{C}[U] := \frac{1}{N_c}\mathrm{Re}\,\mathrm{tr}\left(\mathcal{P}\prod_{l\in\mathcal{C}} U_l\right), \tag{2.65}$$

[32] Here, 'A' denotes the lattice gauge field, not the continuum gauge field. This change in notation also justifies the absence of a factor of g in the exponential in eq. (2.60), as we change the continuum convention in this respect when passing over to the lattice notation.

[33] See e. g. [221] for further details regarding the notation.

[34] A terminological remark: Sometimes, the Wilson loop is referred to as 'Wegner–Wilson loop' due to Wegner's contribution [222]. For brevity and in compliance with common convention, we simply use the term 'Wilson loop' throughout the present thesis, without any intention to downplay the importance of Wegner's work on this subject.

where '$\mathcal{P}$' refers to path-ordering of the subsequent product.

It is straightforward to see that Wilson loops are gauge-invariant. Evidently, the gauge transformation matrices Ω cancel pairwise in the combinations $\Omega^\dagger(x)\Omega(x) = \mathbb{1}$, due to the unitarity of the gauge group $G \ni \Omega$. A crucial gauge-invariant quantity, the static quark–antiquark potential, is entirely determined by them, see sec. 2.3.4 below.

2.3.1.3 Lattice action

The lattice discretization of the usual Yang–Mills gauge action, which reads in the continuum[35]

$$S_G[A] = \frac{1}{2}\int d^d x \,\mathrm{tr}\,\left[F_{\mu\nu}(x)F_{\mu\nu}(x)\right], \tag{2.66}$$

is not unique. Throughout this work, we employ the standard Wilson plaquette action [214] for the gauge sector[36]

$$S_G[U] = \beta \sum_x \sum_\mu \sum_{\nu>\mu} \mathrm{Re}\,\mathrm{tr}\,(\mathbb{1} - U_{\mu\nu}(x)) \tag{2.67}$$

with the important dimensionless number β, which is commonly used to characterize the coupling on the lattice. Inevitably, any discretization of the continuum action introduces errors which vanish only in the limit of zero lattice spacing, $a \to 0$. The Wilson action for the gauge sector has discretization errors of $\mathcal{O}(a^2)$. Hence, improvements are less important than for the Wilson fermion action, whose errors are of $\mathcal{O}(a)$ and which we do not discuss here. In order for the continuum limit $a \to 0$ of (2.67) to equal the continuum action, the lattice coupling β in d (Euclidean) space-time dimensions needs to take the value

$$\beta = \frac{2N_c}{g^2 a^{4-d}}. \tag{2.68}$$

The factor a^{4-d} in the denominator of eq. (2.68) is required since the coupling g^2 has mass dimension one in three dimensions resp. two in two dimensions, and since β is bound to be dimensionless. The expression '$U_{\mu\nu}$' in eq. (2.67) refers to the plaquette variable, often simply called 'plaquette'. (In terms such as 'plaquette' and 'Wilson loop', there is an ambiguity of reference between a holonomy and its (normalized) trace. Usually, the reference is clear from the context.) A plaquette is a minimal Wilson loop, sc. one of extension 1×1. Formally,[37]

$$U_{\mu\nu}(x) = U_\mu(x)U_\nu(x+\hat{\mu})U_\mu^\dagger(x+\hat{\nu})U_\nu^\dagger(x). \tag{2.69}$$

It is the exponential of the lattice field strength tensor $\hat{F}_{\mu\nu}$, which agrees in the continuum limit $a \to 0$ with $F_{\mu\nu}$ as given by (2.4),

$$U_{\mu\nu} = \exp\left(iga^2\hat{F}_{\mu\nu}\right). \tag{2.70}$$

[35] The trace is understood over the color indices and taken in the fundamental representation.
[36] The additive constant in (2.67) possesses no physical relevance and is often omitted.
[37] Note eq. (2.59) for the Hermitian conjugate of any link variable.

Often, it is helpful to refer not to the holonomy $U_{\mu\nu}$, but simply to its trace, a real number in the case of $SU(2)$. When averaged over the entire lattice and normalized such that its absolute value is no larger than 1, it reads

$$U_P := \frac{1}{V} \sum_x \left\{ \frac{1}{n_p} \sum_\mu \sum_{\nu>\mu} \left[\frac{1}{N_c} \mathrm{Re}\,\mathrm{tr}\, U_{\mu\nu}(x) \right] \right\}, \tag{2.71}$$

with N_c again denoting the number of colors, V the number of lattice sites, and n_p the number of plaquettes per site, $n_p = 1, 3, 6$ in $d = 2, 3, 4$, respectively. This is of course just the special case of eq. (2.65) for a 1×1 contour, now averaged over all of its instances on the lattice.

2.3.1.4 Pure $SU(2)$ lattice gauge theory

Throughout most of this work (the exception being ch. 9), we simulate quenched $SU(2)$ gauge theory. Choosing the gauge group $SU(2)$ instead of the physical case of $SU(3)$ is justified since the question we are mainly interested in does not crucially depend on the number of colors, see the respective remarks in sec. 2.4.1. Since $SU(2)$ is a smaller gauge group than $SU(3)$, this (common) choice allows to simulate larger lattices, which is very helpful for investigations of the infrared sector of the theory. – The restriction to the quenched limit is also justified, because dynamical fermions are not decisive for the quantities of our interest, see again sec. 2.4.1 for references.

We work in the pseudoreal[38] fundamental representation of $SU(2)$, which we always refer to when speaking about $SU(2)$ without explicitly specifying a representation. Its pseudoreality entails that while the matrices representing the group elements have complex entries, their trace is invariably real. For $SU(2)$, the link variables $U_\mu(x)$ can be conveniently parametrized in a quaternionic representation by four real numbers $u^i_\mu(x)$, the Cayley–Klein parameters, as

$$U_\mu(x) = u^0_\mu(x) + i u^a_\mu(x) \sigma^a, \tag{2.72}$$

where σ^a are the standard Hermitian Pauli matrices, $a \in \{1, 2, 3\}$, see app. A.2.6. Moreover, the condition

$$\det U_\mu(x) = \left(u^0_\mu(x) \right)^2 + \sum_{i=1}^{3} \left(u^i_\mu(x) \right)^2 = 1 \tag{2.73}$$

is required to hold in order for $U_\mu(x)$ to be an element of $SU(2)$. Hence, the absolute value of any Cayley–Klein parameter is at most 1. Of course, this condition is also the reason why the number of Cayley–Klein parameters is larger by one than the number of generators of the gauge group $SU(2)$.

2.3.1.5 Lattice spacing and running coupling

The finite extension of the periodic lattice and its discrete structure lead to systematic errors in the results of lattice simulations. Hence, the predictive power of such simulations depends, inter alia, on two facts: on how large the lattices are, and on how coarsely grained they are. The answer to the latter question is the lattice spacing a. Its value is typically

[38] See app. A.2.4.

considerably smaller than the Sommer parameter $r_0 \approx 0.5\,\mathrm{fm}$ [223], since the latter characterizes the extension of a quark–antiquark pair. The answer to the former question is simply the product of the lattice spacing and the number of lattice points for each direction, L_μ.

The lattice spacing depends on the value of the lattice coupling β, defined in eq. (2.68). We briefly elaborate on this in the following.[39]

That an observable f possesses a well-defined continuum limit may be succinctly put as the statement that the quantity

$$f_{\mathrm{phys}} := \lim_{a\to 0} f(g(a), a) \tag{2.74}$$

is finite, where g denotes the coupling. The observable is related to its continuum counterpart via

$$f(g(a), a) = \left(\frac{1}{a}\right)^{d_f} \hat{f}(g). \tag{2.75}$$

Here, d_f is the mass dimension of f, and $\hat{f}$ is the dimensionless lattice value of f. The Callan-Symanzik equation [224, 225]

$$\frac{df}{d\ln a} = \left(\frac{\partial}{\partial \ln a} + \frac{\partial g}{\partial \ln a}\frac{\partial}{\partial g}\right) f = 0 \tag{2.76}$$

expresses that the observable f is independent of the chosen scale. It contains the β-function

$$\beta(g) := -\frac{\partial g}{\partial \ln a} = -a\frac{\partial g}{\partial a}, \tag{2.77}$$

which must not be confused with the dimensionless lattice coupling β, eq. (2.68). From a perturbative expansion, the β-function can be approximately determined, thus fixing the mutual dependence of the running coupling and the lattice spacing. For QCD, it is found [7, 8] that the lattice spacing decreases toward smaller couplings. This behavior holds true unless the number of flavors N_f of approximately massless quarks is at least $(11/2)N_c$, which is not the case in nature ($N_f = 6$, $N_c = 3$). For all sufficiently small N_f, the antiscreening by the gluons dominates the screening effect of the quarks. This behavior of the coupling is called 'asymptotic freedom', as mentioned in the introduction (ch. 1).

A quantity commonly used to characterize the interaction strength of QCD is the running coupling

$$\alpha_S := \frac{g^2}{4\pi}, \tag{2.78}$$

which is analogous to the fine-structure constant of QED. Experiments confirm that its dependence on the momentum scale μ is in line with asymptotic freedom, see [226] for a recent compilation of results. From perturbative calculations,

$$\alpha_S(\mu) \propto \left(\log(\mu/\Lambda_{\mathrm{QCD}})\right)^{-1} \tag{2.79}$$

with the important scale Λ_{QCD}, which cannot be computed from first principles and has empirically found to be around 200 MeV. It characterizes the distance of around $1/\Lambda_{\mathrm{QCD}} \approx 1\,\mathrm{fm}$ beyond which the strong interaction becomes non-perturbative. This appearance of

[39] See also standard textbooks like [218, 219].

a physical scale in a theory with a dimensionless coupling constant, like four-dimensional QCD, is called 'dimensional transmutation' [227]. For the non-perturbative definition of the running coupling which we employ in our lattice studies and which is gauge-dependent, see sec. 2.2.2.5 and also sec. 5.2.3.

2.3.2 Gauge fixing

2.3.2.1 Basic concepts

Fixing to Landau gauge, eq. (2.11), amounts on the lattice to finding a local maximum of the gauge fixing functional [228, 124]

$$R[U] := \frac{1}{N_c V d} \sum_x \sum_{\mu=0}^{d-1} \mathrm{Re}\,\mathrm{tr}\, U_\mu(x). \tag{2.80}$$

It is normalized such that it takes values in the range $[0,1]$. The lattice volume V entering into eq. (2.80) is simply the number of lattice points,

$$V = L_s^{d-1} L_t. \tag{2.81}$$

By construction, R is extremal at gauge copies[40] which satisfy the discretized gauge condition

$$\Delta^a(x) = \sum_{\mu=0}^{d-1} \left[A^a_\mu(x) - A^a_\mu(x-\hat{\mu}) \right] = 0 \tag{2.82}$$

with the lattice gauge field $A_\mu(x)$ defined from the link variables $U_\mu(x)$ according to eq. (2.62).

The continuum functional corresponding to $R[U]$ is $E[A]$ as defined in eq. (2.19). It is extremal if the Lorenz gauge condition (2.11) is satisfied. Both for the continuum functional (2.19) and for the lattice functional (2.80) it holds true that minimizing (in the continuum) resp. maximizing (on the lattice) the functional is slightly stronger than the respective gauge condition, (2.82) resp. (2.11). – The functionals (2.80) and (2.19) are equivalent only up to terms of $\mathcal{O}(a)$, see e. g. [220] and references therein for details and alternatives. Thus, there is room for discretization effects, see e. g. app. C.1.

Global maximization of the functional R means that the gauge copies which are 'optimized' in this way come closer to the fundamental modular region (FMR), which is defined as the set of global maxima of the gauge fixing functional, see sec. 2.2.3.3. However, finding the FMR in gauge-fixed lattice simulations poses an NP-hard problem, which is equivalent to finding the ground state of a spin glass [229, 230]. 'NP-hard' means non-deterministic polynomial-time hard. The computer time required to find the global maximum of R increases roughly exponentially with the lattice volume, and a search for the exact global maximum is futile even on rather small lattices. See sec. 6.1.1 for a discussion of global maximization approaches; note also that Landau max-B-gauge, discussed at length in ch. 6, serves as a different type of global maximization approach. As a side note, we remark that there is a case where all gauge copies have recently been determined [231], but this

[40] We sometimes refer to such copies as 'configurations', even though we use at other places the term 'configuration' to denote an entire gauge orbit. We take care to use the word 'configuration' such that its proper disambiguation is evident from the context.

pertains so far only to tiny lattices for compact $U(1)$ in one and two dimensions, thus further illustrating the severity of the numerical problem one faces here.

Regardless of how close the local maximum of R found in gauge fixing is to the global maximum, it is indispensable to approximate the local maximum to good precision in order to fix the gauge accurately. To this end, the quantity Δ^2 is helpful and will be frequently invoked throughout this work. It is calculated from the lattice version of the Landau gauge fixing condition, which can be easily deduced for the gauge group $SU(2)$ by inserting (2.63) in (2.82). The lattice version of the gauge condition reads in this case[41]

$$\Delta^a(x) = \sum_{\mu=0}^{d-1} \operatorname{Im}\operatorname{tr}\left(\frac{\sigma^a}{2}(U_\mu(x) - U_\mu(x-\hat{\mu}))\right) = \sum_{\mu=0}^{d-1}\left(u^a_\mu(x) - u^a_\mu(x-\hat{\mu})\right) = 0. \tag{2.83}$$

This formulation uses the Cayley–Klein parameters (2.72). The quantity Δ^2 is the spatio-temporal average of

$$\Delta^2(x) = \Delta^a(x)\Delta^a(x), \tag{2.84}$$

i. e.,

$$\Delta^2 = \frac{1}{Vd}\sum_x \Delta^a(x)\Delta^a(x). \tag{2.85}$$

As a general rule, we impose as a numerical gauge condition $\Delta^2 < 10^{-15}$ in simulations on lattices of less than huge size. An even safer approach is to terminate a series of gauge fixing sweeps only if the spatio-temporal maximum $\max_x \Delta^2(x)$ is below some small value, which is typically chosen to be somewhat larger than the stopping criterion on Δ^2. This procedure is obviously designed to handle possible large local fluctuations in the gauge fixing conditions. Such a measure of precaution can be taken, although we have found no actual evidence of significant such fluctuations in our simulations. In parallelized simulations on huge lattices, we still do so, i. e., we take $\max_x \Delta^2(x) < 10^{-15}$ as the criterion for sufficient gauge fixing.

We numerically compare these two criteria (average vs. maximum) and yet another candidate criterion for sufficient gauge fixing in app. B.2.2. It is important to note that by 'sufficient', we mean in this context merely whether the gauge fixing condition (2.83) is satisfied. The possibility that the gauge fixing algorithm itself can be improved upon is left open. One way to do so is to search for the global maximum of the gauge fixing functional. We explore alternative approaches of changing and possibly improving the gauge fixing algorithm. 'Improvement' can here be understood in the sense of the algorithm being able to find a larger set of infrared solutions for the propagators. In particular, chs. 4 and 6 are devoted to such explorations (employing stochastic gauge fixing and Landau max-B gauge, respectively).

2.3.2.2 Note on lattice BRST symmetry

Any lattice gauge fixing that proceeds as described above restricts the path integral measure to the first Gribov problem, where the lattice Faddeev–Popov operator, as the negative second variation of the gauge fixing functional $R[U]$, is positive. Note that this restriction

[41] Note the sometimes slightly unconventional range of our indices, and for the following also the fact that we use the Einstein summation convention, see app. A.1.1.

pertains also to functional methods like FRG and DSE. A lattice analog of BRST symmetry would be obtained if it were possible to sample all Gribov copies (in particular, not just those inside the first Gribov horizon), weighted by the sign of the Faddeev–Popov determinant at the respective intersection of the given orbit with the gauge fixing surface, as was initially proposed [232]. This is prohibited, however, since the sum of the signs obtained from all Gribov copies cancels exactly. Therefore, the expectation values of gauge-invariant observables vanish, and indeed already the partition function is zero. This fact is referred to as the Neuberger $0/0$ problem[42] [233, 234].

A first idea might be to simply include the absolute value of the Faddeev–Popov determinant $\Delta_{\mathcal{F}}$. But this is hardly feasible on the lattice, where gauge fixing proceeds by extremizing some functional. A promising path to a solution has recently been proposed [235, 236, 107, 237]. It rests on stereographic projection of the gauge field. For compact $U(1)$, it has indeed been proven that this approach solves the Neuberger $0/0$ problem [235]. It constitutes significant progress toward a lattice BRST formulation. (See [238] for an earlier approach regarding a toy model, and [239] for yet another effort.) But a satisfactory numerical implementation remains to be formulated. It will be very interesting to see whether such a formulation is able to resolve the apparent mismatch between lattice and continuum results for the infrared propagators (sec. 2.4.1), or at least to shed new light on it.

2.3.3 Propagators

The correlation functions that are of crucial importance throughout this work are the gluon propagator and the ghost propagator, which we always consider in Landau gauge. We now discuss their definitions in the framework of lattice gauge theory.

2.3.3.1 Gluon propagator

The severe gauge fixing ambiguity encountered in Yang–Mills theories, see sec. 2.3.2 and 2.2.3.3, introduces considerable conceptual complications. But the actual calculation of the Landau gauge gluon propagator on the lattice, once a gauge has been fixed, is rather straightforward.

The gluon propagator in Landau gauge is transverse, as mentioned in sec. 2.2.2.1. It has the continuum tensor structure (already given in (2.25) above)

$$(D_{\mathrm{gl}})^{ab}_{\mu\nu}(q(k)) = \delta^{ab}\left(\delta_{\mu\nu} - \frac{q_\mu q_\nu}{q^2}\right) D_{\mathrm{gl}}(q(k)). \tag{2.86}$$

The relation between continuum momenta q and lattice momenta k (understood here as momentum vectors) is given in components by (see e. g. [240])

$$q_\mu = \frac{2}{a(\beta)} \sin\left(\frac{\pi k_\mu}{L_\mu}\right). \tag{2.87}$$

The periodicity of the lattice restricts meaningful choices for k_μ to values no larger than half the linear lattice extension in the respective direction, $k_\mu \leq L_\mu/2$. The momentum

[42] It is called '$0/0$ problem' since both the numerator and the denominator in expressions like (2.12a) resp. (2.56) vanish thereby.

definitions q^2 and k^2 are proportional to each other in the continuum limit. They differ by terms of second and higher order in the lattice spacing.[43]

We are interested in the scalar gluon propagator function

$$D_{\mathrm{gl}}(q(k)) = \frac{1}{N_c^2-1}\frac{1}{d-1}(D_{\mathrm{gl}})^{aa}_{\mu\mu}(q(k)) \tag{2.88a}$$

$$\text{with } (D_{\mathrm{gl}})^{ab}_{\mu\nu}(q(k)) = \left\langle A^a_\mu(k)A^b_\nu(-k)\right\rangle. \tag{2.88b}$$

The normalization of the propagators stems from the requirement that they assume their tree-level form for the trivial link configuration, i. e., the configuration with $U_\mu(x) = \mathbb{1}$ for all x and μ, see e. g. [221]. At finite coupling, the proper normalization in this sense is not essential, since the propagators are multiplicatively renormalized anyway, see sec. 2.3.4. In the strong-coupling limit ($\beta = 0$), however, it is indispensable for a quantitative determination of the effective running coupling, as explained in sec. 5.2.3.

In order to calculate $D_{\mathrm{gl}}(q(k))$, we use

$$\begin{aligned}\left\langle A^a_\mu(k)A^a_\mu(-k)\right\rangle &= \frac{1}{V}\left\langle\left(\sum_x A^a_\mu(x)e^{ik\cdot x}\right)\left(\sum_y A^a_\mu(y)e^{-ik\cdot y}\right)\right\rangle \\ &= \frac{1}{V}\sum_{x,y}\left\langle A^a_\mu(x)A^a_\mu(y)\right\rangle e^{ik\cdot(x-y)},\end{aligned} \tag{2.89}$$

where V is the number of lattice points. Thus, of course, the gluon propagator may be determined from a Fourier transform of the spatial correlator. An alternative calculation, directly in momentum space, is possible (see [19, 242] and also e. g. [147]), since (2.89) is equivalent to

$$\left\langle A^a_\mu(k)A^a_\mu(-k)\right\rangle = \frac{1}{V}\sum_{a,\mu}\left[\left(\sum_x A(x)\cos(k\cdot x)\right)^2 + \left(\sum_y A(y)\sin(k\cdot y)\right)^2\right]. \tag{2.90}$$

The expectation value $\langle\cdots\rangle$ is understood as an average (see (2.58)) over uncorrelated copies from different orbits, on which gauge fixing has to be performed in order to calculate the propagators.[44] The inner product is defined as

$$k\cdot x := \sum_{\mu=0}^{d-1} 2\pi\frac{k_\mu x_\mu}{L_\mu}, \tag{2.91}$$

where L_μ is the linear lattice extension (number of points) in $\hat{\mu}$-direction.

Now we combine the above expressions. The full definition of the $SU(2)$ gluon propagator on the lattice, exploiting the standard definition (2.63) of the gauge field and the Cayley–Klein parametrization (2.72) and also including the proper normalization factor, reads (for $q \neq 0$)

$$D_{\mathrm{gl}}(q(k)) = \frac{4}{N_c^2-1}\frac{1}{d-1}\frac{1}{V}\sum_{\mu,a}\left\langle\left(\sum_x u^a_\mu(x)\cos(k\cdot x)\right)^2 + \left(\sum_x u^a_\mu(x)\sin(k\cdot x)\right)^2\right\rangle. \tag{2.92}$$

[43] The terms by which they differ are proportional to certain invariants under the isometry group of hypercubic lattices, see e. g. [241].

[44] See app. B.1 for Monte Carlo methods, sec. 4.2 specifically for stochastic gauge fixing and app. B.2 for gauge fixing algorithms.

The normalization of the gluon propagator given in eq. (2.92) is not valid at vanishing momentum. In this case, the factor $d-1$ in the denominator of this equation is to be replaced by d. This is because for $q \neq 0$, the Lorenz gauge condition in momentum space entails that only $d-1$ of the d Lorentz[45] components of the gauge field are independent of each other, see e. g. [244].

In practice, the implementation of the gluon propagator can proceed either directly by virtue of eq. (2.90) or via a fast Fourier transform of the correlator in position space, see eq. (2.89). Since the gluon propagator calculation is not the most expensive part of most simulations, not much hinges on this choice. De facto, we use eq. (2.90). Note that the Fourier transform implicit in the definition of the scalar gluon propagator function presupposes a periodic lattice. For our studies of a case where this condition is violated and the definition of the gluon propagator needs to be modified accordingly, see ch. 7.

2.3.3.2 Ghost propagator

The ghost propagator is diagonal in color space, as already stated in eq. (2.26) above,

$$D^{ab}_{\mathrm{gh}}(q) = -\delta^{ab} D_{\mathrm{gh}}(q). \tag{2.93}$$

The bulk of the calculation of the ghost propagator in momentum space,

$$D^{ab}_{\mathrm{gh}}(q(k)) = \frac{1}{V}\left\langle \sum_{x,y} \left(\mathbb{M}^{-1}\right)^{ab}_{xy} e^{ik\cdot(x-y)} \right\rangle, \tag{2.94}$$

consists in the inversion of the matrix $\mathbb{M}$. This crucial quantity is the lattice discretization of the Faddeev–Popov operator (FPO), here in Landau gauge. We denote it as '$\mathbb{M}$' in order to distinguish it from its continuum counterpart $M = -\partial D$, see sec. 2.1.2. From eq. (2.93), the scalar ghost propagator function reads

$$D_{\mathrm{gh}}(q(k)) = \frac{1}{N_c^2-1} D^{aa}_{\mathrm{gh}}(q(k)). \tag{2.95}$$

The FPO is the negative Hessian of the gauge fixing functional R (2.80),

$$\frac{\partial^2}{\partial\tau^2} R\Big|_{\tau=0} = \frac{\partial}{\partial\tau} \sum_x F(x)\Big|_{\tau=0} = -\sum_{x,y,a,b} \omega^c_x \mathbb{M}^{a,b}_{x,y} \omega^b_y. \tag{2.96}$$

$F(x) = \partial_\mu A_\mu(x) = 0$ is the Landau gauge condition for the lattice gauge field A (cp. eq. (2.82)), i. e., the lattice version of the continuum condition $\mathcal{F}$, cp. p. 11, and ω^a_x and τ are real parameters of a gauge transformation, see app. C.1. R is not unique. Hence, neither is the lattice FPO, see again app. C.1. In any case, the latter is a real and symmetric $(N_c^2-1)V \times (N_c^2-1)V$ matrix. Although it is sparsely populated, its inversion does pose a certain numerical challenge on large lattices. This challenge is particularly big since an accurate calculation of the ghost propagator requires a new inversion for each momentum value, see the discussion of plane-wave source vs. point source below and in app. B.3.

[45] Note, by the way, that neither spelling of "Loren(t)z" here is a typo, as the gauge condition derives its name from Ludvig Lorenz [243], while the relativistic space-time transformations are named after Hendrik Lorentz.

We assume the standard gauge fixing functional R, see eq. (2.80), and thereby the standard Faddeev–Popov operator $\mathbb{M}$ throughout most of this work, with the exception of app. C.1 where we present and numerically explore some alternatives. Immediately specializing to the gauge group $SU(2)$, the lattice FPO is given by the following expression:[46]

$$\begin{aligned}\mathbb{M}^{ab}_{xy} = \sum_{\mu} \Bigg\{ & \delta^{ab} \left[u^0_\mu(x) + u^0_\mu(x-\hat{\mu}) \right] \delta(x-y) - \\ & - \left[\delta^{ab} u^0_\mu(x) + \varepsilon^{abc} u^c_\mu(x) \right] \delta(x+\hat{\mu}-y) + \\ & + \left[-\delta^{ab} u^x_\mu(x-\hat{\mu}) + \varepsilon^{abc} u^c_\mu(x-\hat{\mu}) \right] \delta(x-\hat{\mu}-y) \Bigg\}.\end{aligned} \tag{2.97}$$

A sketch of the derivation is provided in app. C.1, eq. (C.17). A more general form of the Faddeev–Popov operator, not specific to $SU(2)$, may be found explicitly e. g. in [173], see also [246].

A note regarding the implementation. There are at least two common ways to calculate the ghost propagator from the inversion of the lattice FPO $\mathbb{M}$, sc., first, the plane-wave source method [242] and, second, the point source method [247, 248]. Both of them derive their names from the type of source on which $\mathbb{M}$ is inverted.

The point source method is relatively fast, since it requires $\mathbb{M}$ to be inverted only once per individual ghost propagator measurement, regardless of the number of momenta. However, it suffers from the drawback of producing rather pronounced 'wiggles' in the propagator, especially at intermediate and large lattice momenta (we explicitly compare the results on several occasions in chs. 4, 5 and 6).

The plane-wave source method has the advantage that the result is much more precise even with a small number of measurements (like a few dozen), since an averaging over the lattice is inherent in this method. Its drawback is that it requires an inversion of the FPO for each single momentum, which may be cumbersome in practical applications. Note that it is of course feasible to apply the plane-wave source method only to a subset of all momenta, as we sometimes do in ch. 4 when we are interested specifically in the *infrared* behavior of the ghost propagator.

The calculation of the ghost propagator, including the conjugate gradient algorithm, and the difference between the plane-wave source and the point source method are spelled out in more detail in app. B.3.

2.3.3.3 Choice of lattice momenta

It is advisable to choose a specific subset of all possible lattice momenta as those momenta at which to evaluate the propagators and related quantities, since this reduces lattice artifacts. Usually, we have chosen the cylinder cut [240], which reduces in particular errors at large momenta that stem from discretization effects due to an inevitably non-zero lattice spacing. The cylinder cut is defined such as to allow only for limited deviations of the

[46] See also e. g. [245].

momenta from the diagonal. More specifically, the condition on the momentum vector $\hat{q}$ reads[47]

$$|\Delta\hat{q}| \leq 1, \tag{2.98}$$

where

$$\Delta\hat{q} = |\hat{q}| \sin\theta_{\hat{q}} \tag{2.99}$$

with

$$\cos\theta_{\hat{q}} = \frac{\hat{q}\cdot\hat{n}}{|\hat{q}|}. \tag{2.100}$$

On a symmetric lattice (i. e., one of equal extension in the temporal and all spatial directions, $L_s = L_t$) in d dimensions, the normalized vector $\hat{n}$ is

$$\hat{n} = \frac{1}{\sqrt{d}}\underbrace{(1,\ldots,1)}_{d \text{ times}}. \tag{2.101}$$

Exploiting the relation $\sin\arccos x = \pm\sqrt{1-x^2}$, one arrives at

$$|\hat{q}|^2 - (\hat{q}\cdot\hat{n})^2 \leq 1 \tag{2.102}$$

as the cylinder cut condition.[48]

Another cut, the cone cut [240], is mainly useful for small volumes and asymmetric lattices. Since we do not focus on these cases, we have not used this cut.

There are two cases in the present work where we choose momenta differently from the cylinder cut. First, we perform some studies of discretization effects in the strong-coupling limit for which the choice of momenta along face diagonals resp. space diagonals ('face-diagonal resp. space-diagonal momenta') in contrast to on-axis momenta is purposive, see sec. 5.2.4. Second, we employ on-axis momenta for the studies at non-zero temperature, see ch. 8.

2.3.4 Physical units and the quark–antiquark potential

2.3.4.1 The static quark–antiquark potential

The key to assign physical units to lattice quantities, like the propagators, is to obtain values of the lattice spacing a, which depends on the coupling. This is done by combining values of the string tension (cp. sec. 2.2.1) in lattice units, σa^2, with the scale $\sigma = (440\,\text{MeV})^2$ approximately obtained from Regge trajectories (see e. g. [249]). An alternative possibility, which we do not pursue here, is to utilize the Sommer parameter [223]. As a side note, the value of σ can be equivalently expressed as being on the order of $1\,\text{GeV/fm}$ (by way of eq. (2.108) below), which permits a simple physical picture of the energy required to separate a quark and an antiquark by some distance.

In any case, a calculation of the static quark–antiquark[49] potential as a function of distance is required. 'Static' means here that the quarks are taken to be infinitely heavy.

[47] Here, we denote the momentum vector as $\hat{q}$ in order to clearly distinguish it from its norm; at most other places, we do not do so, since the disambiguation is evident from the context.

[48] See e. g. [173] for the corresponding relation on asymmetric lattices.

[49] Note that in $SU(2)$, there are no antiquarks, strictly speaking. This is because its fundamental representation, which describes quarks, is pseudoreal (app. A.2.4), not complex, and thereby unitarily equivalent to its complex conjugate, which describes antiquarks..

Indeed, the very concept of potential is void in quantum field theory, unless this limit is considered, in which virtual quark–antiquark pairs are suppressed. The dimensionless potential $\hat{V} := Va$ as a function of the distance in lattice units R/a can be parametrized in the form

$$Va = \sigma a^2 \frac{R}{a} - \alpha \frac{a}{R} + c + \mathcal{O}\left(\frac{a^2}{R^2}\right) \tag{2.103}$$

with dimensionless parameters α, c and, crucially, $\sigma a^2 =: \hat{\sigma}$. (The symbol $\hat{}$ indicates dimensionless quantities.) The Coulombic force proportional to α is relevant only at small distances and can be explained by one-gluon exchanges. For large distances, a linear potential dominates, corresponding to a force that is independent of distance. Its slope, i. e., the coefficient of the linear term, is the string tension σ, with dimension $[\sigma] = \mathrm{GeV}^2$, i. e., mass dimension two. It has been proven that the potential cannot grow stronger than linearly at large distances [250, 251].

It is the term proportional to σ that accounts for confinement. A linear increase of the potential at asymptotically large distances entails an area law [214] for the Wilson loop along a rectangular contour $\mathcal{C}$ with large spatial resp. temporal extension $\hat{R} := R/a$ resp. $\hat{T} := T/a$,

$$W := \langle W_{\mathcal{C}} \rangle \propto \exp\left(-\hat{\sigma}\hat{R}\hat{T}\right). \tag{2.104}$$

An immediate consequence of this is the important relation

$$\sigma a^2 = \lim_{\hat{R},\hat{T}\to\infty} \frac{1}{\hat{R}\hat{T}} \ln W\left(\mathcal{C}_{\hat{R},\hat{T}}\right) \tag{2.105}$$

between the string tension and large Wilson loops.

In practice, the potential between static color charges can be calculated by considering, for any positive integer $\hat{R} \leq L_\mu/2$ (for a direction μ),

$$-\ln W = \hat{V}\hat{T} + \tilde{c}. \tag{2.106}$$

The value of $\hat{V}$ at a specific $\hat{R}$ can be determined from a fit of the data (possibly omitting the lowest values of $\hat{T}$) to this function. It is very helpful to apply a 'smearing' algorithm [252] to the link variables in spatial directions before calculating the string tension from them. This serves to enhance the overlap between operators calculated from the link variables and the flux tube state of lowest energy. It improves the linear behavior of $\hat{V}\hat{T}$ as a function of $\hat{T}$. For $SU(2)$, smearing is performed by 'mixing' links pointing in spatial directions (loosely speaking, 'spacelike links') with the 'spacelike' staples surrounding them,

$$\begin{aligned} U_\mu(x) \to \alpha U_\mu(x) + (1-\alpha) \sum_{\substack{\nu=1 \\ 0\neq\mu\neq\nu}}^{d-1} \Big[& U_\nu(x) U_\mu(x+\hat{\nu}) U_\nu^\dagger(x+\hat{\mu}) \\ & + U_\nu^\dagger(x-\hat{\nu}) U_\mu(x-\hat{\nu}) U_\nu(x+\hat{\mu}-\hat{\nu}) \Big], \end{aligned} \tag{2.107}$$

with a parameter $\alpha \in [0, 1[$.

In addition to the values of σa^2 and σ, the standard relation

$$197\,\mathrm{MeV} \cdot \mathrm{fm} \approx 1 \tag{2.108}$$

is employed in order to obtain a value of the lattice spacing a.

The values of σa^2 are usually, i. e. here in three and four dimensions, obtained from lattice simulations of the quark–antiquark potential, see sec. 2.3.4.4. This stands in marked contrast to the two-dimensional case, where the lattice gauge theory can be solved analytically [253, 254, 255]. In particular, in this case it can be shown that the Wilson loop obeys an area law, and the string tension can be calculated exactly [254], see sec. 2.3.4.3.

2.3.4.2 Renormalization

The general definitions of the gluon and ghost propagator on the lattice are given in sec. 2.3.3 above. They are to be understood in lattice units and yield dimensionless quantities. But the propagators have mass dimension -2. In order to introduce the proper units and to enable a comparison between propagator results obtained at different lattice couplings β, the data are multiplicatively renormalized at some momentum μ such that, after multiplication by an appropriate factor,

$$D_{\mathrm{gl}}(q=\mu) = D_{\mathrm{gh}}(q=\mu) = \frac{1}{\mu^2}. \tag{2.109}$$

I. e., the dressing functions equal unity at the renormalization scale μ, which is typically between 2 and 3 GeV. It is constrained by two requirements: On the one hand, the value of μ must be large enough to be outside the non-perturbative domain. On the other hand, it must be below the largest lattice momentum at all values of the lattice coupling β employed in the specific case.[50] E. g., the propagators from stochastic quantization, ch. 4, have been renormalized at $\mu = 2.5\,\mathrm{GeV}$, and the propagators at non-zero temperature, ch. 8, at $\mu = 2.3\,\mathrm{GeV}$.

As the propagators are calculated at a discrete set of momenta, some interpolation needs to be performed to determine the unrenormalized value at $q = \mu$, and thus via the condition eq. (2.109) the renormalization constant. Usually, it is sufficient to interpolate the respective propagator linearly, based on its values at the momenta right above and below μ. For the finite-temperature studies in ch. 8, where we use a fine temperature grid, we construct instead a spline interpolation, see sec. 8.2.1.3.

We now discuss explicit values of the string tension in two, three and four dimensions.

2.3.4.3 The two-dimensional case

The string tension is related to the values of rectangular Wilson loops via eq. (2.105); thus, values of the latter imply values of the former. In $d = 2$, the Wilson loop is given by [254]

$$W(\mathcal{C}_{\hat{R},\hat{T}}) = d_j \cdot \left(\frac{c_j(\beta)}{c_0(\beta)}\right)^{|f|}, \tag{2.110}$$

where $|f| = \hat{R}\hat{T}$ is the area of the region bounded by the contour $\mathcal{C}$ and the index j characterizes the representation of the gauge group. For the gauge group $SU(2)$, $j = 1/2$, and $d_{1/2} = 2$. Moreover [254],

$$\lim_{a\to 0}\left(\frac{c_j(\beta(a))}{c_0(\beta(a))}\right) = e^{-j(j+1)g^2|f|}, \tag{2.111}$$

[50] The largest lattice momentum is $2/a$ per direction, see eq. (2.87). Hence, $(qa)_{\max} = 2\sqrt{d}$ in d dimensions.

which evaluates in our case to

$$\lim_{a\to 0}\left(\frac{c_j(\beta(a))}{c_0(\beta(a))}\right) = \exp\left(-\frac{3}{4}g^2|f|\right) \underset{SU(2)}{=} \exp\left(-\frac{3}{\beta}\hat{R}\hat{T}\right), \tag{2.112}$$

such that

$$W\left(\mathcal{C}_{R,T}\right) = 2\exp\left(-\frac{3}{\beta}\hat{R}\hat{T}\right). \tag{2.113}$$

Consequentially,

$$a = \sqrt{\frac{3\ln 2}{\beta\sigma}}, \tag{2.114}$$

i. e. for $\beta = 10$,

$$a = \sqrt{\frac{3\ln 2}{10}}\frac{197\,\text{MeV}}{440\,\text{MeV}}\text{fm} \approx 0.204\,\text{fm}. \tag{2.115}$$

In two dimensions, the lattice spacing can thus easily be obtained at all β. We choose $\beta = 10$ when working at finite coupling in two dimensions.

2.3.4.4 The three- and four-dimensional cases

In three and four dimensions, no analytic expressions such as eq. (2.110) for the Wilson loop exist, and lattice data for σa^2 need to be utilized, in our case for $SU(2)$. Such data can be found e. g. in [256, 257, 258, 259] ($d = 3$) resp. in [260, 261] ($d = 4$), see also the references in [262].

When studying the case of finite coupling ($\beta \neq 0$) and zero temperature (as in chs. 4 and 7), we perform simulations in three dimensions mostly at $\beta = 4.2$, and in four dimensions at $\beta = 2.2$. The corresponding values of the string tension in lattice units and of the lattice spacing (with $\sqrt{\sigma} = 440\,\text{MeV}$) read as follows.

d	β	$\sqrt{\sigma}a$	source	a
3	4.2	0.387(3)	[258]	0.173 fm
4	2.2	0.4690(100)	[260]	0.21 fm

For our studies at non-zero temperature, values of $\sqrt{\sigma}a$ at many different β are needed. We elaborate on this in sec. 8.2.1.2.

2.4 Lattice and continuum results for the infrared propagators

Lattice results for the infrared behavior of the ghost and gluon propagators in Landau gauge form only a proper subset of the one-parameter family of solutions found with functional continuum methods [77, 66], as already mentioned in sec. 2.2.2, where we also give many references to continuum studies. Specifically, the scaling solution, which constitutes an endpoint of this family, is not observed on the lattice in three and four dimensions. Rather, both the gluon propagator and the ghost dressing function are generally held to be neither divergent nor vanishing in the infrared according to lattice simulations in these cases. We now elaborate on this apparent mismatch. – The exploration of possible approaches to resolve it forms a major part of this work. We present and discuss the corresponding results in chs. 4, 5, 6 and 7.

2.4.1 Previous lattice results

2.4.1.1 Infrared gluon propagator

An unequivocal result of lattice studies of the gluon propagator has always been to rule out an infrared divergent propagator, and thereby the scenario of 'infrared slavery' (see sec. 2.2.3.5). Another question is whether the gluon propagator at $q = 0$ vanishes or takes a positive value. This pertains in particular to four dimensions, but also to three dimensions.

The earliest lattice study of the gluon propagator of pure $SU(3)$ Yang–Mills theory in Landau gauge[51] can be found in [124]. The work on the lattice gluon propagator was continued in studies like [264, 212, 209], and also in more refined approaches to the infrared behavior including the studies of possible artifacts,[52] see e. g. [207].

The question of whether $D_{\mathrm{gl}}(0)$ equals zero was initially not seen as fully resolved, see e. g. [265]. However, various more recent studies both of $SU(2)$ and $SU(3)$ in four dimensions [208, 147, 113, 266, 267, 268, 269, 204, 173, 270, 271, 272, 273, 274, 275, 276, 277, 278, 279, 122, 280] indicate with increasing reliability an infrared non-vanishing gluon propagator. See also our own results in ch. 4, published in [24].

Whether the simulations are done for the gauge group $SU(2)$ or $SU(3)$ is not decisive for the qualitative question of scaling vs. decoupling behavior. Explicit comparisons of $SU(2)$ and $SU(3)$ [281, 282, 271] show a good agreement and no qualitative difference. (See also e. g. [273, 283] for $SU(3)$ results.) This is in line with results from calculations in the Dyson–Schwinger framework.

The infrared gluon propagator $D_{\mathrm{gl}}(q = 0)$ decreases with increasing lattice extension. There is still no unanimous consensus on its infrared behavior, as there are also recent claims of the exponent κ (see p. 16) being slightly above 0.5 from a finite volume analysis of data for the infrared gluon propagator in four dimensions [284, 285, 286]. This would entail $D_{\mathrm{gl}}(0) = 0$. But most of the work on this subject supports an infrared non-zero propagator, see the references above.

The long list of references comprises also some simulations on especially large lattice volumes of up to $(27\,\mathrm{fm})^4$. Such studies have been performed both for $SU(3)$ [273] and $SU(2)$ [272]. We present an own result in the latter case for a huge $(34\,\mathrm{fm})^4$ lattice, obtained with parallel computing, in ch. 7 (fig. 7.6).[53]

The lattice volume is by necessity finite, and the extrapolation to infinite volume is nontrivial. Indeed, a natural suggestion to explain the discrepancy could at first glance be that the simulated volumes are not large enough to allow to extract information about the true infrared behavior. It is helpful to have a criterion for whether a lattice is large enough for the true infrared behavior to be visible. Such a criterion has been provided by studies of Dyson–Schwinger equations on a torus, i. e., in a finite geometrical setting that closely resembles the compactified lattices employed in numerical simulations. Some studies in such a setting were performed in [55, 287]. A closer look led to the suggestion that volumes above $(10\,\mathrm{fm})^4$ could suffice for the correct infinite volume behavior of correlation functions in Landau gauge to be visible [288]. As the simulated lattice volumes extend up to approx.

[51] While we concentrate here on Landau gauge, note that recently a simple relation has been found between the lattice gluon propagators in Landau gauge and in Coulomb gauge [263].

[52] Among the possibilities to reduce some artifacts is the choice of specific momenta, like the cylinder cut, which we have adopted, see sec. 2.3.3.3.

[53] Contrary to the main subject of ch. 7, this is a result for the usual periodic boundary conditions.

$(30\,\mathrm{fm})^4$, DSE studies on a torus and recent lattice simulations jointly provide evidence that the discrepancy between continuum and lattice results is not an effect of finite (lattice) volume.

Alongside the influence of the volume and of the number of colors, another systematic error of lattice studies consists in the fact that dynamical fermions are often not included, as they render the already very demanding simulations even more expensive. Lattice studies beyond the quenched approximation yield clear quantitative effects especially on the gluon propagator, but they show that unquenching does not change the infrared behavior of correlation functions in a large, qualitative manner [269, 289, 171, 290].

At issue is not simply whether the gluon propagator vanishes in the deep infrared, but also its functional form at small momenta, related to the question of a (dynamically generated) gluon mass. See e. g. [240] for different model functions and [147, 127, 122, 130] concerning attempts to extract a value of an infrared mass scale.

In three dimensions, the lattice results for the Landau gauge gluon propagator also point toward a decoupling behavior, see e. g. [258], even on lattices as large as $(85\,\mathrm{fm})^3$ [272]. Although a peak at a momentum of around 350 MeV is clearly visible here [244] below which the gluon propagator decreases toward $q = 0$, the zero momentum value of the propagator remains positive in the infinite volume extrapolation. Our own results with stochastic quantization are presented in ch. 4.

The two-dimensional case, which lacks dynamics [291] and where quantities like the string tension can be calculated analytically [254] (see sec. 2.3.4.3), probably constitutes an exception. Here, the gluon propagator does go to zero at $q = 0$ for large volumes [116, 275]. Our results for this case in the strong-coupling limit confirm this, but they also cast some doubt on the existence of a clear distinction between this case and its higher-dimensional counterparts, see ch. 5.

2.4.1.2 Infrared ghost propagator

In order to ascertain whether a set of solutions for the infrared propagators exhibits scaling behavior, it is indispensable to take the ghost propagator into account, in addition to the gluon. This is because the scaling relation (2.28) between the infrared exponents κ_A and $\kappa_C \equiv \kappa$ is a necessary condition for this type of solution to be realized.

Computationally, the ghost propagator calculation is considerably more demanding than the one of the gluon propagator (see sec. 2.3.3). A pioneering investigation of the Landau gauge ghost propagator on the lattice was performed in [247]. Among the numerous recent lattice studies aimed at exploring its infrared behavior are [292, 113, 267, 268, 173, 204, 273, 272, 276, 293, 277, 278]. For our own results, see ch. 4 (mainly published in [24]) and chs. 5 and 6 (mainly published in [25]).

The infrared gluon propagator tends to decrease with increasing lattice volume, as noted in sec. 2.4.1.1 above. The same holds for the ghost propagator and hence for the ghost dressing function $q^2 D_{\mathrm{gh}}$, but the meaning of this effect is just the opposite one, as the ghost propagator thereby tends away from a scaling behavior. In this case, it is useful to discuss explicitly the dressing function, as the distinction between a scaling-type and a decoupling-type behavior corresponds to a clear qualitative difference between an infrared divergent ghost dressing function and an infrared finite one. Its apparent infrared divergence on smaller lattices becomes weaker as the lattice volume is increased. On large

lattices, it approaches a plateau in the infrared, which is at odds with a scaling behavior.

Again, in two dimensions, qualitatively different results have been obtained [116]. In this case, the infrared exponent κ is consistent with the infrared behavior of the gluon propagator according to the scaling relation, i. e., the sum rule (2.28).

The Gribov copy dependence of the ghost propagator was found to be much stronger than the one of the gluon propagator. We discuss it in the following and in ch. 6, where we also give further references.

2.4.2 Gauge fixing problem and relation to continuum results

As demonstrated in sec. 2.4.1 (lattice) and sec. 2.2.2 (continuum), lattice gauge theory and functional continuum methods do not yield the same set of results for the infrared ghost and gluon propagators in Landau gauge. This might be related to properties of the gauge fixing.

A priori, the relationship between gauge fixing on the lattice and in the continuum is far from obvious. There is no simple argument which rules out that both procedures sample configuration space in different ways. Gauge-dependent quantities like the propagators may well be sensitive to this. In particular, it might be speculated that standard lattice gauge fixing methods introduce a bias, e. g., against the Gribov horizon $\partial\Omega$ or against the fundamental modular region Λ. The first type of bias would hurt the prospects of corroborating the predictions of the Gribov–Zwanziger scenario. The impact of the second type of bias is less obvious. There have been simulations aimed specifically at approaching the *global* maximum of the gauge fixing functional R, as defined in eq. (2.80), to a better precision by employing sophisticated optimization methods like simulated annealing combined with global $\mathbb{Z}_2$ flips [277, 122]. This means that the algorithm comes closer to the FMR Λ, although the exact global optimization is an NP-hard problem, see sec. 2.3.2.1. These simulations result in a ghost propagator that is less enhanced in the infrared than the ghost propagator obtained from standard gauge fixing. To be more specific, the ghost propagator at small momenta has been found to be smaller by about 10% than after invoking a standard method. This indicates that this type of approach to the fundamental modular region does not support the Gribov–Zwanziger scenario. See [242, 294, 292, 266, 267, 268, 277, 274, 295, 221, 296, 297, 278, 279] for further investigations of the Gribov–Singer ambiguity, which all lead to 'mere' quantitative effects.

If the path integral is restricted to the first Gribov region, global BRST invariance is broken. Standard lattice methods inevitably impose this restriction, and so does the stochastic gauge fixing method we present in chs. 3 and 4, indicating the generality of this problem. As the construction of a physical state space is difficult without global BRST [77], see sec. 2.2.2.2, it would be highly desirable to have a variant of lattice gauge fixing that possibly evades the Neuberger $0/0$ problem and is able to sample gauge-fixed configurations from all Gribov regions. Such a variant has in fact been proposed [235, 236, 107, 237], see sec. 2.3.2.2. This provides evidence that the scaling solution, which is in line with global BRST invariance, should exist also on the lattice. It creates the genuine possibility that a numerical implementation of BRST invariance on the lattice might resolve the discrepancy between lattice and continuum results, see sec. 2.3.2.2. It should be noted, however, that the actual numerical realization is far from trivial. More generally, the recent progress toward a lattice BRST formulation backs up the view that it is reasonable and important to search

for a realization of an infrared scaling behavior of the propagators on the lattice, which is also consistent with the Kugo–Ojima/Gribov–Zwanziger scenarios of confinement (sec. 2.2.3).

In the thesis at hand, we pursue several different approaches related to modifying the gauge fixing procedure, sc. stochastic quantization (chs. 3 and 4), a closer look at the Gribov ambiguity in the strong-coupling limit (ch. 6), and a change of boundary conditions (ch. 7). We now turn to the first of these approaches, the method of stochastic quantization, whose application in the framework of lattice gauge theory is preceded by a more general introduction in the following chapter.

CHAPTER 3

STOCHASTIC QUANTIZATION AND A TOY MODEL

In the present and the next chapter, we pursue the approach of stochastic quantization. Our aim is to use it as an alternative gauge fixing method. By means of this alternative method, we strive to explore the gauge dependence of the infrared behavior of the Landau gauge ghost and gluon propagators in a rather novel way. Before we do so (ch. 4), we outline the basic ideas of stochastic quantization (sec. 3.1), and we employ a simple toy model in order to illustrate some properties of the application of this method to gauge fixing (sec. 3.2).

3.1 Introduction to stochastic quantization

3.1.1 Basic concepts and Langevin equation

3.1.1.1 Origin of the idea

Stochastic quantization goes back to Parisi and Wu [298] (see also [299]), who proposed it as a method to obtain quantum mechanics as the equilibrium of a stochastic process. This process is taken to evolve in a fictitious time, a 'fifth coordinate', which we denote here by the variable θ and which is distinct from the physical time that may be a parameter of the simulated system – such as e. g. in lattice gauge theory, where the link variables in the full Euclidean space-time may evolve according to the Langevin equation, see ch. 4. This sharply distinguishes the approach of Parisi and Wu from its predecessors, like the endeavor to describe quantum mechanics by stochastic processes in the ordinary time [300]. Moreover, stochastic quantization is usually formulated in Euclidean space-time. Otherwise, a complex Langevin evolution is required instead of a real one. The latter is also necessary for other applications like QCD at non-zero density, see ch. 9. For early reviews and overviews of stochastic quantization, see [301, 302, 303]. In our simulations, the 'fictitious time' simply corresponds to computer time. In contrast to many usual Monte Carlo simulations, it is reasonable to distinguish between the 'Langevin time' θ and the number n of steps, since the Langevin approach to simulations involves a non-zero step

size, which may in principle vary, giving rise to 'adapted step size' approaches. (However, we have not found this to be required in our applications.)

3.1.1.2 Langevin equation

Stochastic quantization is based on the Langevin equation. This is a stochastic differential equation, typically used to describe physical processes that involve random fluctuations, such as Brownian motion. We discuss it here first briefly for real physical processes that take place in ordinary time, before we turn to its application as an alternative to standard Monte Carlo methods.

The Langevin equation for the velocity v of a particle undergoing Brownian motion, taking place in real time t, reads

$$m\frac{d}{dt}v(t) = -\gamma v(t) + K(t). \tag{3.1}$$

The term $-\gamma v$ describes a friction force, which is proportional to the velocity, following Stokes' law. The coefficient γ is proportional to the viscosity of the fluid in which the particle is immersed. In contrast to this deterministic term, K is a stochastic force.

The physical process that, by virtue of its modern discoverer, gave Brownian motion its name is the floating of colloidal particles, like pollen grains or tiny pieces of stone, in liquids like water. Such particles were observed [304] to move randomly in all directions with zero net momentum. This was later quantitatively explained [305, 306] in terms of very frequent collisions (occurring on the order of every 10^{-10} s) with the considerably smaller molecules of the surrounding liquid, which are in thermal motion. This allowed to relate the macroscopic diffusion constant to microscopic properties of matter. Thus, in this case, the random fluctuations are a phenomenological description of microscopic collisions, which can be considered as deterministic and which are simply too frequent to be described individually.

In our applications of the Langevin equation, the noise does not serve as a statistical description of microscopic events. Instead, it is a helpful tool, sc. an ingredient in a method to calculate observables as statistical averages of stochastic processes. We now elaborate on this.

3.1.1.3 An alternative to standard Monte Carlo approaches

In the present work, we employ the Langevin equation as an alternative to usual Monte Carlo simulations in order to generate a Markov process (see app. B.1). Stochastic processes can fulfill this task, and in addition, they are more general in the sense that their formulation can start directly from the equation of motion and does not, in principle, require an action, even though the existence of a real action (bounded from below) ensures convergence.[1] In the present thesis, we treat only cases where there is an action. On the negative side, the precise value against which the Langevin evolution converges depends on the step size. But this can usually be controlled well, as we demonstrate in sec. 4.2.1 below.

[1] For a comprehensive overview of the theory of stochastic processes, see e. g. [307], which we sometimes follow.

In a rather general form, the Langevin equation for variables $x_i(\theta)$, with the discrete index $i \in \{1, 2, \ldots, n\}$, reads

$$\frac{dx_i}{d\theta} = c(\vec{x}, \theta) + b(\vec{x}, \theta)\eta_i(\vec{x}, \theta). \tag{3.2}$$

The terms c and b^2 describe drift and diffusion, respectively. η is Gaussian white noise. This means that it is characterized by a normal distribution and by possessing only local correlations,

$$\langle \eta_i(\vec{x}, \theta) \rangle = 0, \tag{3.3}$$

$$\langle \eta_i(\vec{x}, \theta)\eta_j(\vec{x}', \theta') \rangle = \sigma^2 \delta_{ij} \delta(\vec{x} - \vec{x}')\delta(\theta - \theta'). \tag{3.4}$$

σ^2 is the variance of the corresponding probability distribution.

The fact that $\eta(\theta)$ is Gaussian white noise can be understood in physical terms, since the joint effect of a large number of fluctuating forces on a system amounts to a Gaussian distribution, by virtue of the central limit theorem. It is called 'white' since all frequencies occur with equal probability, due to the absence of temporal correlations.

Unless mentioned otherwise, we take the variables in the Langevin equation to be real. However, a complex Langevin equation has also been demonstrated to be useful in certain cases. But care is required, as a convergence of the *complex* stochastic process to the correct result is not in general assured, in contrast to the real case, where mild conditions suffice; see [301] and also the remarks in sec. 9.1.2. See ch. 9 for our studies of a fermionic model with the complex Langevin equation, as well as for references regarding this case.

As remarked above, eq. (3.2) is a comparatively general form of the Langevin equation. In fact, it is more general than the formulation we use in this work. If the prefactor of the random noise η, the function b, actually depends on the stochastic variables $\vec{x}$, the noise is 'multiplicative noise'. This type of noise may be useful e. g. in order to describe fluctuations of external parameters, and it may induce a phase transition, see [307] for any details. For our purposes, however,

$$b(\vec{x}(\theta), \theta) = \sigma = \text{const.} \tag{3.5}$$

holds. This means that the noise is additive.

If the drift term c is proportional to the negative gradient of a real-valued action $S(\vec{x})$, the equilibrium distribution of this stochastic process is

$$\rho(\vec{x}) \propto \exp\left(-\frac{2}{\sigma^2} S(\vec{x})\right), \tag{3.6}$$

see e. g. [303]. In our applications, we combine a drift derived from an action – typically, from the Yang–Mills gauge action – with an additional drift term for gauge fixing that is not derived from an action, see ch. 4 and also sec. 3.2. – Sometimes, a diffusion constant $\alpha := \sigma^2/2$ is defined, slightly simplifying eq. (3.6). In order to reproduce the path integral measure $\propto \exp(-S/\hbar)$, $\alpha = \hbar$ is required.[2] Since moreover $\hbar = 1$ in natural units, see app. A.1.2, we impose $\sigma^2 = 2$ such that configurations are sampled according to the Gibbs measure.

[2] E. g. in biological applications of the Langevin equation, $\alpha = k_B T$ with the Boltzmann constant k_B.

3.1.2 Formulations and applications

3.1.2.1 Fokker–Planck equation

There is a close relation between the Langevin equation, which is formulated in terms of the dynamical variables, and the Fokker–Planck equation. The latter equation is the equation of continuity for the corresponding probability density, which we denote here by ρ in order to avoid confusion with the plain probability p of updates in a random walk process (e. g. eq. (3.14) below). For simplicity, we restrict the following presentation to the case of one spatial dimension, thus replacing $\vec{x}$ by the single real variable x; the generalization to the higher-dimensional case is obvious. The Fokker–Planck equation reads

$$\frac{\partial}{\partial\theta}\rho(x,\theta) = \left(-\frac{\partial}{\partial x}a_1(x) + \frac{1}{2}\frac{\partial^2}{\partial x^2}a_2(x)\right)\rho(x,\theta), \tag{3.7}$$

where $a_1(x)$ and $a_2(x)$ are drift and diffusion terms, respectively, and it is important to note that the spatial derivatives act on ρ as well as on a_1 and a_2. Without perfect mathematical rigor, the Fokker–Planck equation and the Langevin equation can be seen as mutually equivalent. In particular, if the drift in the Langevin equation is the gradient of a real action with a lower bound, the resulting probability distribution satisfies the Fokker–Planck equation. The coefficients in eqs. (3.2) (with additive noise, (3.5)) and (3.7) are related via $a_1 = c$ and $a_2 = 2\sigma^2$.

The Fokker–Planck equation (3.7) can be written as a continuity equation, sc. simply as

$$\frac{\partial}{\partial\theta}\rho(x,\theta) = -\frac{\partial}{\partial x}\left(a_1(x)\rho(x,\theta) - \frac{1}{2}\frac{\partial}{\partial x}a_2(x)\rho(x,\theta)\right). \tag{3.8}$$

From this, the stationary distribution can be determined, i. e., the distribution for the case $\partial_\theta p = 0$. If the drift term is the gradient of an action and the noise is additive, $\partial_x a_2 = 0$, the stationary distribution is proportional to $\exp(-S/a_2)$.

In practice, we use not the Fokker–Planck equation, but the Langevin equation, as the latter is a differential equation formulated directly in terms of the dynamical variables. Its implementation is, after discretization, conceptually straightforward. We also employ a random walk approach as a de facto equivalent alternative to the Langevin equation.

3.1.2.2 Wiener process and random walk

If the Fokker–Planck equation holds for the probability density of some stochastic process, it holds a fortiori for the transition probability between two states separated by a tiny time interval Δt. If this transition probability takes the simple Gaussian form

$$p_2(x', \theta + \Delta\theta | x, \theta) = \frac{1}{\sqrt{2\pi\Delta\theta}}\exp\left(-\frac{(x'-x)^2}{2\Delta\theta}\right), \tag{3.9}$$

the drift term vanishes, and the stochastic process reduces to a pure diffusion process, called ‘Wiener process’.

The Wiener process can be understood as the continuum limit of a random walk process (see e. g. [308]), which describes a particle moving in discrete steps of a fixed size. The direction in which the particle moves is determined in a stochastic manner (‘stochastic jumps’) – in the simplest case, with equal probability for each direction. However, the

probability can be modified such that it depends on the action. This renders the random walk process equivalent to the Langevin and the Fokker–Planck equation (up to discretization effects). This is formulated as follows. A fixed step size η is used as an input, and the (here, simply one-dimensional) variable x is updated either to $x + \eta$ or to $x - \eta$, with the probability

$$p(x \to x \pm \eta) = \frac{1}{2}\left[1 \pm \tanh\left(\frac{\eta}{2} \cdot \left(-\frac{dS}{dx}\right)\right)\right]. \tag{3.10}$$

The tanh is introduced in order to ensure $p \in [0, 1]$. We have implemented several applications of the random walk process. We discuss such applications in sec. 3.2 for a toy model, in ch. 4 for stochastic quantization of $SU(2)$ gauge theory and in ch. 9 for complex stochastic quantization. In the latter two cases, we use it alongside a Langevin procedure as an additional test, fortifying the evidence that the results are no discretization artifacts.

3.1.2.3 Sketch of applications to gauge fixing and to the sign problem

In the context of Yang–Mills theory, we employ stochastic quantization for two joint purposes. The first of these purposes is the generation of configurations which are distributed according the path integral measure of this theory. This allows the calculation of expectation values of quantum field theoretical operators based on importance sampling, see app. B.1. The second of these purposes is gauge fixing, the necessity and complications of which we have laid out in detail in ch. 2. Of course, both can be done with standard methods. This means to employ usual Monte Carlo methods for updating, and some optimization algorithm for gauge fixing.

But we also employ stochastic quantization for a reason. This reason is that standard approaches do not reproduce the scaling solution, as laid out in sec. 2.2.2 and 2.4. Since this is a valid solution obtained from functional continuum methods, and the lattice should also be able to see it, an alternative to standard lattice algorithms is called for – in particular, an alternative gauge fixing algorithm. In stochastic gauge fixing, the dynamics and the gauge fixing are not separated, but intertwined, such that the algorithm samples configuration space in a more local way. This might induce a different sampling of configurations inside the Gribov region.

In addition, we perform a study that involves stochastic quantization in a different context, sc. in the context of the sign problem. At non-zero chemical potential, the action of QCD is complex, rendering usual Monte Carlo methods inapplicable, as they are based on importance sampling and a real probability measure. Complex Langevin evolution may provide a way out, as described in ch. 9.

The application of stochastic gauge fixing in pure $SU(2)$ Yang–Mills theory on the lattice is the subject of ch. 4, where it is discussed more extensively. But as a preparation, we first digress to describe our studies of a simple toy model that exemplifies important properties of stochastic quantization.

3.2 A toy model

3.2.1 Motivation

A simple toy model for stochastic gauge fixing has already been proposed and studied in [309]. We generalize it to a higher number of dimensions. This generalization is useful in order to study the effect of the 'entropy'. By this, we refer to the increasing tendency of configurations to accumulate close to the Gribov horizon as the number of dimensions grows. Since such configurations should account for confinement in QCD according to the Gribov–Zwanziger scenario (see sec. 2.2.3.4), it is worthwhile exploring the 'entropy effect'.

A different toy model for stochastic gauge fixing has been investigated in [310]. It is concerned with a force that moves configurations not only toward the Gribov region, but even toward the fundamental modular region. In this deliberately modified toy model, it was observed that a standard heat-bath technique is more efficient than stochastic gauge fixing [310]. But this insight cannot be transferred directly to the case of Yang–Mills theory, where a local criterion for the fundamental modular region (see sec. 2.2.3.3) is absent, making it difficult to benefit from the insights obtained from the toy model of ref. [310].

We resume the discussion of the toy model simulated by us. In addition to the effect of the entropy, we can clearly distinguish between dynamical effects and gauge fixing effects. This is because we have chosen the sign of the action differently from [309].

3.2.2 Details and numerical results

3.2.2.1 Details

In the toy model, the variables $x_i \in \mathbb{R}$, where $i \in \{1, \ldots, n\}$, and $y \in \mathbb{R}$ are subject to two forces. In addition to a force derived from an action, i. e., a force of the type familiar from the preceding introduction in sec. 3.1.1.3, there is a gauge fixing force. We start with presenting the latter. It reads

$$\begin{pmatrix} \dot{y} \\ \dot{x}_i \end{pmatrix} = \begin{pmatrix} K_0^g \\ K_i^g \end{pmatrix} = -\frac{1}{\alpha} \begin{pmatrix} (1-x^2)y \\ 2x_i y^2 \end{pmatrix}, \tag{3.11}$$

where $x^2 := \sum_{i=1}^n x_i^2$, $\dot{f} := df/d\theta$, and α is a gauge fixing parameter, which is bound to be positive. This gauge fixing force cannot be written as the gradient of an action. Hence, its curl does not vanish. It drives the configurations toward the gauge fixing surface, which in case of this toy model is the set of points $(y, \vec{x})$ with $y = 0$.

The limit $\alpha \to 0$ is the limit of perfect gauge fixing. In this limit, the asymptotic distribution of the scalar variables $x = |\vec{x}|$ and y is

$$d\rho(x, y) \propto x^{n-1}(1-x^2)\theta(1-x^2)\delta(y)dx\, d\Omega\, dy, \tag{3.12}$$

where $d\Omega$ is the differential solid angle in n dimensions. This implies that in the limit of perfect gauge fixing, all configurations are elements of the set

$$\Omega = \left\{ \begin{pmatrix} y \\ \vec{x} \end{pmatrix} \middle| \, y = 0, \; x < 1 \right\}, \tag{3.13}$$

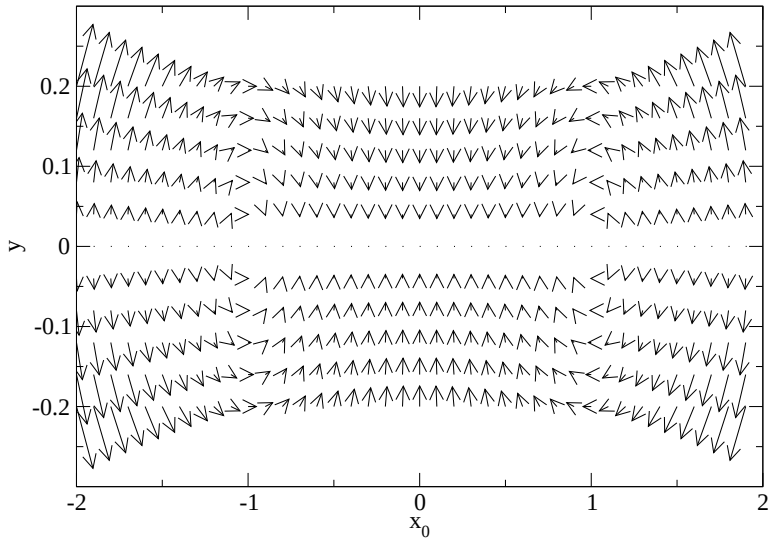

Figure 3.1: The gauge fixing force of the toy model for $n = 1$ and $\alpha^{-1} = 0.15$.

which therefore serves as the 'Gribov region' of this model. This terminology, in analogy to the case of Yang–Mills theories, is sensible because the Gribov region is where all configurations are located if the gauge is fixed to optimal accuracy (see eq. (2.47) for its general definition).

The 'Faddeev–Popov operator' h of the toy model is obtained from the linearization $\frac{d}{dt}v = hv$, where $v = 0$ is the gauge condition, thus here $v = y$. Therefore, from the first component of eq. (3.11), the 'Faddeev–Popov determinant' of this model is $-\alpha^{-1}(1 - x^2)$. It is proportional to (3.12) only in the special case $n = 1$ (investigated in [309] with a different sign of the action) and vanishes, like (3.12), linearly in the vicinity of the horizon $x = 1$.

The asymptotic distribution (3.12) is maximal at $x = \sqrt{\frac{n-1}{n+1}}$. Obviously, this maximum approaches the 'Gribov horizon' $\partial\Omega$ as n, the dimensionality of $\vec{x}$, increases. It is a priori possible that stochastic gauge fixing supports this effect, although such a support could only come about in an indirect manner. This is because the gauge fixing force is obviously orthogonal to the gauge fixing surface in the immediate vicinity of the latter (see fig. 3.1), since this surface is the equilibrium of the gauge force. Hence, very close to the gauge fixing surface, the gauge force can induce no movement parallel to this surface.

This equilibrium is stable only inside the bounded 'Gribov region' Ω (eq. (3.13)). Fig. 3.1 illustrates this region where the gauge fixing force is attractive to the gauge fixing surface.

3.2.2.2 Numerical simulation

A numerical simulation of this toy model is straightforward. A method that suggests itself is a random walk algorithm (see sec. 3.1.2.2), which has been applied to simulations of gauge theories and models thereof e. g. in early works like [311, 312, 313]. Its continuum limit is equivalent to the Langevin approach (see textbooks like [308]). A characteristic quantity of a random walk process is the fixed step size η. The probability of a local

update is

$$p(x_\nu \to x_\nu \pm \eta \hat{e}_\nu) = \frac{1}{2}\left[1 \pm \tanh\left(\frac{\eta}{2} K_\nu(\{x_\mu\})\right)\right]. \tag{3.14}$$

Here, we have introduced the joint notation x_ν for $\vec{x}$ and y, with $\nu \in \{0, 1, \ldots, n\}$, simply by virtue of defining $x_0 := y$.

A gauge-invariant dynamics may be derived from the orbits

$$u_i = x_i \exp\left(-\frac{x^2}{2} - y^2\right) (= \text{const.}), \quad i = 1, \ldots, n \tag{3.15}$$

as

$$S = \beta u^2, \quad u^2 = \sum_{i=1}^{n} u_i^2. \tag{3.16}$$

The parameter β plays the role of the inverse coupling, analogously to lattice gauge theory (eq. (2.68)). The action S increases monotonically for $0 \leq x \leq 1$. Thus, it drives the configurations toward $x = 0$. In this regard, our change of the sign of the action compared to [309] has a noticeable effect; with the old sign, the configurations are driven in the opposite direction, i. e., toward $x = 1$. The latter direction is also favored by the gauge fixing force. The pure gauge fixing force leads to a maximum of the distribution at $x = \sqrt{\frac{n-1}{n+1}}$ (see sec. 3.2.2.1), which approaches 1 for large n. Hence, the change of sign permits a clear distinction between effects from dynamics and from gauge fixing.

The dynamical part of the force is given by[3]

$$K_\nu^a = -\frac{dS}{du}\frac{du}{dx_\nu}. \tag{3.17}$$

This yields explicitly

$$K_0^a = 4\beta y x_0 u^2, \tag{3.18a}$$

$$K_i^a = -2\beta x_i (1 - x^2) \exp(-x^2 - 2y^2). \tag{3.18b}$$

It enters into the drift force of the random walk algorithm, eq. (3.14), which reads

$$K_\nu = K_\nu^a + K_\nu^g. \tag{3.19}$$

For the second component of the drift force, i. e. the gauge fixing force K^g, see eq. (3.11) above.

In the following figures, we show the distribution of gauge-fixed configurations, $\rho(x)$. Fig. 3.2 depicts the situation at $\beta = 0$, i. e., at vanishing action. It illustrates that the expected 'entropy effect' occurs, since the configurations move closer to the Gribov horizon as the dimensionality n grows. The effect of the pure gauge fixing force is as expected, since the numerical results follow the distribution (3.12). Since the gauge fixing parameter is non-zero, although small, gauge fixing is not perfect, and some configurations outside the Gribov region are sampled (the 'tails' at $x > 1$ in fig. 3.2).

It is interesting to study the interplay of the parameters n, α and β, i. e., of the respective sizes of the 'entropy' (dimensionality), of the gauge fixing force and of the action. The

[3] Note that 'a' in eq. (3.17) is not an index, but an abbreviation for 'action'.

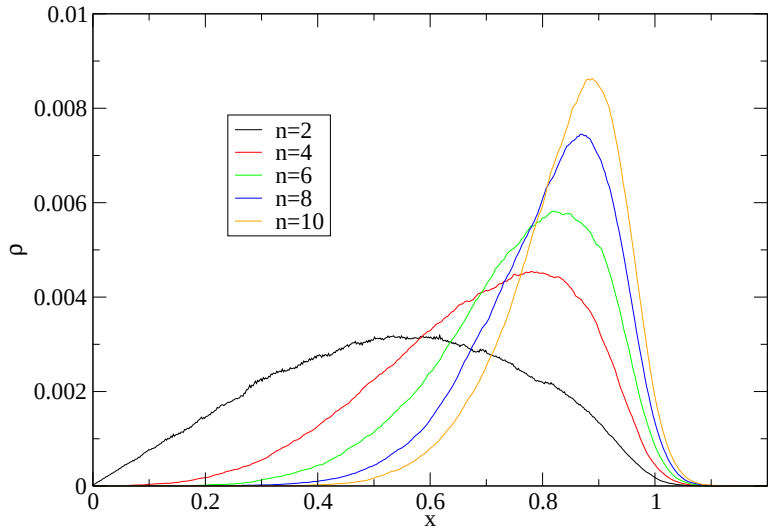

Figure 3.2: 'Entropy effect' for the (not gauge-invariant) distribution of values of x at the parameters $\alpha = 5 \cdot 10^{-5}$, $\beta = 0$, step size $\eta = 0.001$. Note that the distributions we give are generally not normalized.

distributions at fixed $n = 500$, but for varying gauge fixing parameter α, are depicted in the four plots of fig. 3.3 for four different values of β. If n is kept fixed, the action has little effect up to some value of β (compare figs. 3.3a and 3.3b), and then suddenly starts driving the configurations toward the interior of the Gribov zone, see figs. 3.3c and 3.3d. From fig. 3.3c, which shows the distributions at $\beta = 1650$, it is clearly visible that this effect depends on α. If α is larger, the gauge fixing force, which is proportional to α^{-1}, is weaker, hence the configurations tend to be closer to the minimum of the action. For $\alpha = 10^{-4}$, there is only a single peak, sc. the one around $x \approx 0.5$. For all other values of α, this peak is virtually indistinguishable, and an additional peak close to the 'Gribov horizon' emerges. At $\beta = 1800$ (fig. 3.3d), in contrast, the distributions for all values of α that we study coincide. In this case, β is sufficiently large for the action to be dominant compared to the gauge fixing force. – Moreover, we have found that the action starts to dominate at smaller values of β for lower n. This is also expected, already from the fact that the influence of the 'entropy' decreases toward small n. – Finally, it is evident from all plots in fig. 3.3 that the number of gauge-fixed configurations outside the Gribov horizon decreases monotonically with the gauge fixing parameter α, since the limit $\alpha \to 0$ corresponds to perfect gauge fixing, i. e., to the case in which all gauge-fixed configurations are inside the Gribov region.

The upshot of our brief discussion of this toy model is that while non-linear effects occur, there is no aspect of the behavior that comes unexpected. In fact, the non-linearity is obviously built into the model by virtue of the non-linear dependence of the drift force on the variables $\vec{x}$ and y. In contrast, 'a priori' statements about the resulting distribution of configurations are hardly possible in the more realistic case of lattice gauge theory – regardless of whether they would draw justification from the toy model or from other sources. Naturally, extensive numerical simulations are required. We present the 'a posteriori' results of such simulations with stochastic gauge fixing in ch. 4, before we go on to study and compare other methods for Yang–Mills theory.

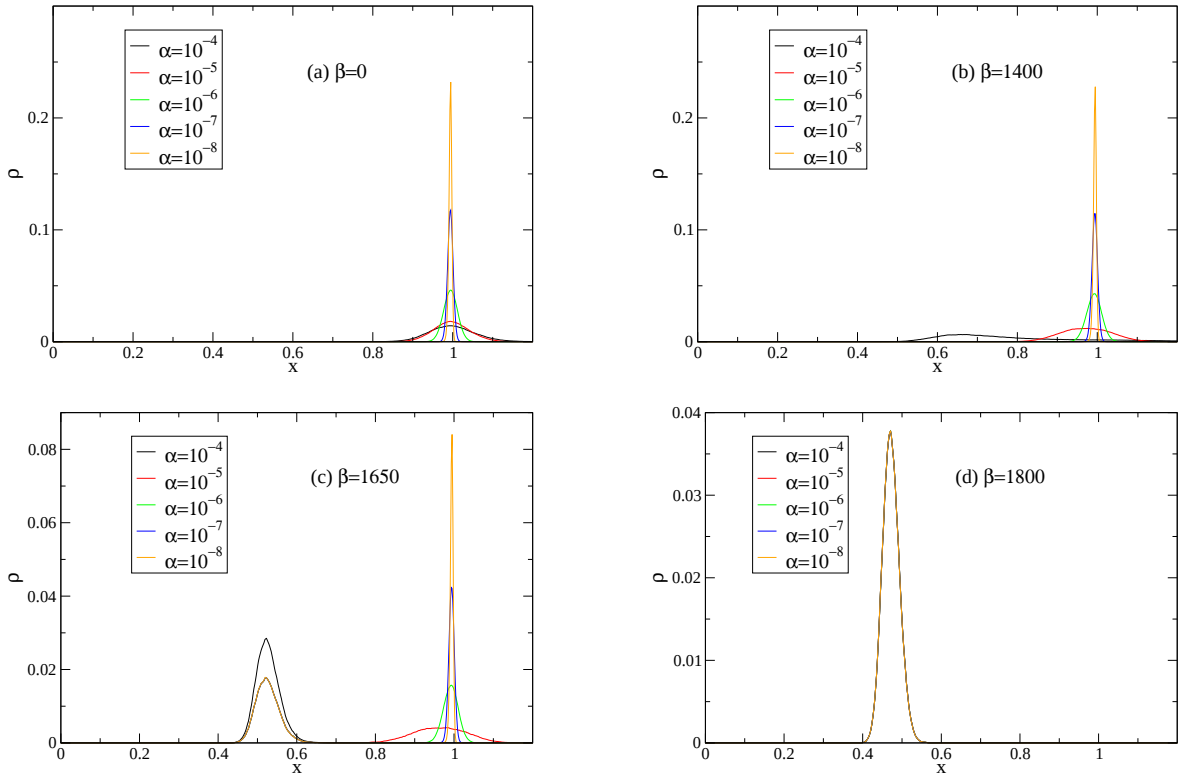

Figure 3.3: Change of the distribution $\rho(x)$ of gauge-fixed configurations when increasing β, the strength of the gauge action, at $n = 500$ for $\alpha = 10^{-4}, \ldots, 10^{-8}$. Values of β indicated in the plots. Step size $\eta = 10^{-4}$.

3.3 Summary

Stochastic quantization is based on the Langevin equation, a stochastic differential equation for the respective field in an additional, fictitious time, which corresponds in numerical applications to computer time. If the drift force is the negative gradient of a real action, the Langevin evolution of configurations defined in Euclidean space-time converges against an equilibrium in which configurations are sampled with a distribution according to the Gibbs measure, i. e., proportional to $\exp(-S)$. Hence, it is a feasible alternative to standard Monte Carlo methods.

For our purposes, it is important to note that stochastic quantization can also be used for gauge fixing. The Langevin equation can be supplemented by a gauge fixing term. In a toy model for stochastic gauge fixing, a non-linear interplay of the effects of the action, the gauge fixing force and the number of dimensions is observed. This concurs with a priori expectations. In the following chapter, these investigations are extended to the considerably more involved case of Yang–Mills theory, where justified a priori expectations are much more difficult to obtain.

CHAPTER 4

LATTICE LANDAU GAUGE WITH STOCHASTIC QUANTIZATION

We start our numerical investigations of the infrared properties of the gluon and ghost propagators of pure $SU(2)$ Yang–Mills theory by using the method of stochastic quantization for gauge fixing. It serves as an alternative to standard methods. A basic introduction to stochastic gauge fixing was already provided in the preceding chapter. But the application to Yang–Mills theory is both conceptually (due to the issues raised in ch. 2) and computationally much more demanding. We first motivate this approach (sec. 4.1) and introduce its application to lattice gauge theory (sec. 4.2), before we present results especially for the propagators in various dimensions (sec. 4.3.1), whose infrared properties are among our main interests, and also for the spectrum of the Faddeev–Popov operator (sec. 4.3.2), which is relevant for an analysis of how the different gauge fixing methods sample configuration space.

4.1 Introduction and motivation

There is a discrepancy between lattice and continuum results regarding the infrared behavior of correlation functions in Landau gauge, as laid out in sec. 2.4. In three and four dimensions, lattice simulations result only in decoupling-type solutions, in contrast to functional continuum methods, which also yield the scaling solution. We emphasize once again that all of these solutions are confining (see sec. 2.2.4) and that observables are generally insensitive to their difference (2.2.2.4). But we also emphasize that the status of prominent confinement scenarios (sec. 2.2.3), like the Gribov–Zwanziger and Kugo–Ojima scenarios, is at stake. I. e., the difference between scaling-type and decoupling-type solutions for the infrared propagators (sec. 2.2.2) concerns the question of how confinement comes about. Unraveling its mechanism is among the central desiderata of fundamental particle physics, even though it depends on the chosen gauge.

The discrepancy may well stem from a difference between the gauge fixing methods in the continuum, on the one hand, and on the lattice, on the other hand. In particular,

different parts of configuration space might be preferably sampled by lattice gauge fixing as compared to its continuum counterpart. Other proposals, like a finite volume effect, are not supported by the data, see the discussion in sec. 2.4. In particular, it is a priori possible that lattice gauge fixing exhibits a bias e. g. against the first Gribov horizon or against the fundamental modular domain. The first type of bias might explain the mismatch between lattice results and the predictions of the Gribov–Zwanziger scenario for the propagators, since according to this scenario, configurations close the first Gribov horizon account for confinement (cp. sec. 2.2.3.4). The second type of bias would be complementary to approaches aiming at a global maximization of the gauge fixing functional, see sec. 6.1 for some discussion. Obviously, these ideas are rather speculative, and it is desirable to either back them up with more specific data than the general mismatch concerning the infrared propagators, or to refute them at least partially.

Therefore, we have utilized a gauge fixing procedure which serves as a viable alternative to standard numerical gauge fixing algorithms, sc. gauge fixing via stochastic quantization [314, 312, 311, 313, 309, 315, 316, 317, 210, 318, 319, 320]. It rests on a stochastic differential equation for the gauge field, namely on the Langevin equation, which was explained in the previous chapter, ch. 3. This equation can be extended to contain a gauge fixing term, which does not affect expectation values of gauge-invariant observables. An intuitive idea behind this approach is that it induces a more 'local' evolution of configurations, see fig. 4.1. Let us briefly explain this idea.

In standard gauge fixing, dynamics and gauge fixing are completely separated. Uncorrelated configurations are produced according to the standard path integral measure, forming a Markov chain (see app. B.1). They are not gauge-fixed at all, i. e., their distance to the gauge fixing surface Γ (see (2.45)) is large. We have already introduced a measure for this distance, sc. the quantity Δ^2, eq. (2.85). If gauge-dependent quantities are to be calculated, an initially identical copy of each of these uncorrelated configurations is generated. To every copy, an optimization algorithm is applied which iteratively performs a number of gauge transformations (we describe a standard method in app. B.2 and use it also in chs. 5 through 8). This serves to reach a local maximum the gauge fixing functional R, eq. (2.80). Expectation values are then calculated from these gauge-fixed copies.

Stochastic gauge fixing of course also locally maximizes R. In fact, the values of R we obtain are within errors consistent with those from standard gauge fixing (see sec. 4.3.1.3 for a quantitative statement). But it proceeds in a different manner. The most striking difference is that the 'thermalization' process that generates uncorrelated configurations is not separated from the gauge fixing. Instead, the distance to the gauge fixing surface, as measured by Δ^2 (eq. (2.83)), is kept small during the entire stochastic process.

The present study is the first systematic non-perturbative investigation of the infrared properties of Landau gauge Yang–Mills propagators with stochastic quantization. Earlier, there have been a few gluon propagator calculations utilizing this method, e. g. [317, 210]. The Coulomb gauge gluon propagator in four dimensions has been calculated with stochastic gauge fixing [321]. Screening mass calculations within stochastic quantization are reported on in [320, 319, 322]. Stochastic gauge fixing has also been applied to Abelian projection [323], which demonstrates the versatility of this method. Moreover, the framework of numerical stochastic perturbation theory [324, 325, 326] can be used to calculate the Landau gauge gluon and ghost propagators [327, 328, 329, 330, 331].

In order to understand the properties of this alternative method, we use it not only

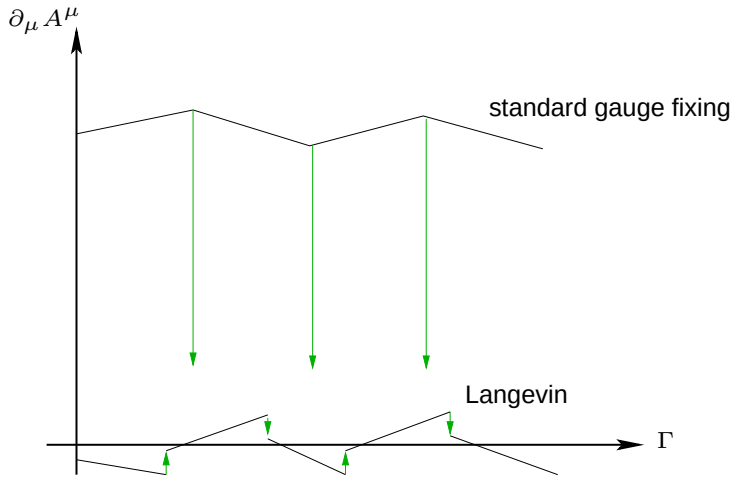

Figure 4.1: Qualitative illustration of a difference between stochastic and standard gauge fixing. The green arrows denote gauge fixing steps, the black lines connecting them denote dynamic updates. A similar picture appeared already in [320].

to calculate the propagators, but we also look at the distribution in configuration space brought about by the stochastic gauge fixing algorithm. The respective results are presented in sec. 4.3.2.

4.2 Stochastic gauge fixing on the lattice

We have introduced general properties of Langevin evolution in sec. 3.1. Here, we discuss its application to gauge fixing in Yang–Mills theories in the continuum formulation in sec. 4.2.1, before we review the implementation in the framework of lattice gauge theory in sec. 4.2.2.

4.2.1 Preliminaries and continuum formulation

We intend to apply the Langevin equation (3.2) to non-Abelian gauge theories, in particular to $SU(2)$ Yang–Mills theory. To this end, the Langevin equation may prima facie be formulated either in terms of the algebra-valued non-Abelian gauge field $A^a_\mu(x)$ or in terms of the lattice representation of the gauge field, i. e., the link variables $U_\mu(x)$, see sec. 2.3.1. The link variables are essentially the 'exponential of the gauge field', see eq. (2.60). We discuss these two approaches in turn. The second one is in line with the usual lattice discretization of gauge theories, and it is the one we actually choose to implement. In doing so, we follow most previous realizations of stochastic quantization on the lattice. We present the second approach in more detail in the following sec. 4.2.2.

Conceptually, the formulation directly in terms of the gauge field is straightforward. It has been studied numerically e. g. in [312]. In this case, the drift force in the generic Langevin eq. (3.2) is the negative gradient of the Yang–Mills gauge action S_{YM}. Hence, the Langevin equation for the non-Abelian gauge field A^a_μ, which is defined in Euclidean space

with d-dimensional coordinate vectors x and evolves in the 'additional time' θ, reads

$$\frac{\partial A^a_\mu(x,\theta)}{\partial\theta} = -\frac{\delta S_{\mathrm{YM}}[A]}{\delta A^a_\mu(x,\theta)} + \eta^a_\mu. \tag{4.1}$$

This equation implements the 'dynamics', i. e., it serves to produce configurations which are distributed according to $\rho \propto \exp(-S_{\mathrm{YM}})$ (see app. B.1). Standard Monte Carlo approaches do the same. For our purposes, gauge fixing is required. In contrast to standard approaches, it is introduced in a manner that is closely intertwined with the dynamical updates of the gauge field, instead of as an optimization procedure separated from the dynamics. To this end, eq. (4.1) may be supplemented by a gauge fixing term $D^{ac}_\mu v^c$ such that it reads

$$\frac{\partial A^a_\mu}{\partial\theta} = -\frac{\delta S_{\mathrm{YM}}}{\delta A^a_\mu} + D^{ac}_\mu v^c + \eta^a_\mu(x,\theta), \tag{4.2}$$

following a proposal by Zwanziger [314] (see also e. g. [85]). The equivalence of the stochastic gauge fixing approach to the Faddeev–Popov procedure has been proven, inter alia, for covariant gauges [332]. The newly introduced gauge fixing force $D^{ac}_\mu v^c$ is the covariant derivative of the Landau gauge condition (2.11), rescaled by the real and positive gauge parameter[1] α, i. e., the covariant derivative of

$$v^c = \frac{1}{\alpha}\left(\partial_\mu A_\mu\right)^c. \tag{4.3}$$

Thus, the gauge fixing force is tangential to a gauge orbit.[2] Expectations values of gauge-invariant quantities are therefore not affected by the addition of Zwanziger's gauge term. Due to the specific choice of v, which gives the direction of steepest descent with respect to the 'continuum gauge fixing functional' (2.19), the force is restoring along gauge orbits. The gauge fixing force is not conservative and cannot be written as a gradient of an action, thus its curl does not vanish.

The Langevin equation including the gauge fixing term is equivalent to the modified Fokker–Planck equation for the probability density ρ,

$$\frac{d\rho}{d\theta} = \int d^dx\, \frac{\delta}{\delta A^a_\mu(x)}\left(\frac{\delta\rho}{\delta A^a_\mu(x)} - \underbrace{\left[-\frac{\delta S_{\mathrm{YM}}}{\delta A^a_\mu(x)} + \frac{1}{\alpha}D^{ac}_\mu\partial\cdot A(x)\right]}_{=K^a_\mu(x)}\rho\right). \tag{4.4}$$

The equilibrium configurations of the gauge force alone, viewed in isolation from the dynamics and the noise, are obviously (cp. eq. (4.3)) just the gauge-fixed configurations. They

[1] It is sometimes stated that the choice $\alpha = 0$ corresponds to Landau gauge, e. g. in [84]:

> "for finite gauge parameter α, the gauge fixing is soft in the sense that no particular gauge condition is imposed"

or also in [320]. From a numerical point of view, the situation is not so straightforward, since $\alpha = 0$ does not lead to a minimal distance from the gauge fixing surface, see e. g. fig. 4.26 below and the associated discussion. We rather say that a small value of α corresponds to an approximate (numerical) implementation of Landau gauge.

[2] See [333, 334, 335] for a generalization of stochastic gauge fixing in which the gauge force is not in general tangential to an orbit, but the expectation values of gauge-invariant observables still remain unchanged.

lie on the gauge fixing surface Γ, as defined in eq. (2.45). Moreover, the equilibrium is stable exactly if the Faddeev–Popov operator is positive, i. e., inside the first Gribov region Ω (eq. (2.47)), as can easily be proven by evaluating the derivative of the norm of the Landau gauge condition with respect to Langevin time explicitly, see e. g. [303, 85]. In contrast, outside of Ω, the gauge fixing force possesses repulsive directions. In the limit of large computer time, we therefore expect this gauge force to bring the gauge field configurations not only onto the gauge fixing surface Γ, but, more specifically, into Ω.

However, this is by itself not a specific property of *stochastic* gauge fixing, since any method which fixes a gauge by locally maximizing the gauge fixing functional (2.80) inevitably brings the gauge copies into the first Gribov region Ω. The reason is simply that Ω is the set of all gauge-fixed configurations with positive Faddeev–Popov operator, which is in turn the negative Hessian of the gauge fixing functional, see e. g. sec. 2.3.3.2.

Although some characterizations of the equilibrium distribution brought about by stochastic gauge fixing are possible – indeed, we have just given some –, it is not feasible to derive the full equilibrium distribution a priori.[3] Thus, extensive numerical simulations are indispensable. For these, however, we utilize the second formulation of stochastic gauge fixing, to which we now turn.

4.2.2 Closer look at the lattice formulation

4.2.2.1 Dynamics

The second formulation of stochastic gauge fixing directly involves the link variables, not the algebra-valued gauge field. There are two different possibilities for the precise implementation of this formulation, sc. first, a Langevin equation transferred to the level of the link variables and, second, a random walk approach. Both of them serve to produce configurations distributed according to the measure $\exp(-S)$, assuming that the finite step size is chosen appropriately small. We implement both of them.

Langevin dynamics. The first method, the lattice Langevin method, amounts to choosing an individual link update as [336] (see also [337] for a review on the dynamics of Langevin simulations)

$$U_\mu(x) \to \exp(i\sigma^a R^a_{\mu x}) U_\mu(x), \tag{4.5}$$

where R is composed of a stochastic term and the dynamical drift force F, which is the Lie derivative of the standard Wilson plaquette action $S[U]$ [214] (eq. (2.67)),[4]

$$R^a_{\mu x} = \varepsilon F^a_{\mu x} + \sqrt{\varepsilon}\,\eta^a_{\mu x} \tag{4.7}$$

$$\text{with } F^a_{\mu x} = i\nabla^a_{\mu x} S[U]. \tag{4.8}$$

This update corresponds to a first-order (Euler) method. A Runge–Kutta scheme was sometimes also used [336, 338], but it proves to be not necessary for our purposes.

[3] Remarks on the conditions to derive the full equilibrium distribution a priori can be found e. g. in [335]. These conditions are violated in Yang–Mills theory.

[4] The differentiation in group space is defined as

$$\nabla^a_{x\mu} f(U_\mu(x)) = \frac{\partial}{\partial\alpha} f\left(e^{i\alpha T^a} U_\mu(x)\right)\Big|_{\alpha=0}. \tag{4.6}$$

We write the Wilson action in a slightly simplified notation compared to eq. (2.67), denoting the plaquette holonomy $U_{\mu\nu}$, eq. (2.69), by $U_\square$ and also omitting the additive constant,

$$S[U] = -\frac{\beta}{2N_c}\sum_\square \mathrm{tr}\,(U_\square + U_\square^\dagger) \underset{SU(2)}{=} -\frac{\beta}{2}\sum_\square \mathrm{tr}\,U_\square. \tag{4.9}$$

"$\sum_\square$" refers to a sum over the individual plaquette variables $U_\square$. The Lie derivative of the Wilson action amounts for $SU(2)$ to[5]

$$\nabla^a_{x\mu} S[U] = -\frac{i\beta}{2}\sum_{U_\square \supset U_\mu(x)} 2iu^a_\square = \beta \sum_{U_\square \supset U_\mu(x)} u^a_\square(x), \tag{4.10}$$

which completes the prescription for a Langevin update of an individual link variable on the lattice. In a full updating sweep, an update of the form (4.5) is performed for each link variable.

Random walk dynamics. A viable alternative to the lattice Langevin algorithm is to perform local random walk updates (see secs. 3.1.2.2 and 3.2.2.2) of the link variables,

$$U_\mu(x) \to \exp\left(iA^a_\mu(x)\sigma^a\right) U_\mu(x), \tag{4.11}$$

where for fixed lattice site x and direction μ, the three numbers $A^a_\mu(x)$ are, starting from zero, updated by fixed steps

$$A^a_\mu(x) \to A^a_\mu(x) \pm \eta \tag{4.12}$$

with the probability

$$p = \frac{1}{2}\left[1 \pm \tanh\left(\frac{1}{2}\eta F^a_{\mu x}\right)\right], \tag{4.13}$$

respectively. Eq. (4.13) is analogous to the corresponding prescription in the toy model studied in ch. 3, eq. (3.14).

Step size dependence. Both methods, Langevin and random walk, obviously involve a non-zero step size, sc. ε resp. η, whose effect needs to be controlled and tested. As a general statement, the random walk step size is larger than the Langevin step size, given that both are chosen appropriately (so as to ensure correct convergence while avoiding overly large autocorrelation times). More quantitatively, $\eta \in \mathcal{O}(\sqrt{\varepsilon})$. Intuitively spoken, the reason is that η is the discretization step size of the dynamical variable x, ε is the discretization step size of the time θ, and $x \propto \sqrt{\theta}$ in stochastic processes like Brownian motion. (See e. g. [311] for a more detailed reasoning.)

We have performed a basic test of our stochastic algorithms. This test simply consists in comparing the expectation value of the plaquette variable U_P, eq. (2.71), with the result from a standard algorithm, like 'heat-bath' [39], see app. B.1.4. The heat-bath algorithm does not involve a step size. The average plaquette $\langle U_P \rangle$ equals the Wilson action (2.67) up to additive and multiplicative constants. In the limits of strong and weak coupling, the

[5] Note that $\mathrm{tr}\,[\sigma^a U_\mu(x)] = 2iu^a_\mu(x)$, cp. the Cayley–Klein parametrization, eq. (2.72). – The relation "$\supset$" in (4.10) denotes the inclusion of the respective link in the plaquette contour.

results of heat-bath simulations may themselves be compared to analytic approximations,[6] but of course, a plethora of independent numerical results exists in addition and can be used to test new algorithms. In any case, the comparison yields an unambiguously positive result already for moderately small step sizes, sc. $\eta \in \mathcal{O}(10^{-2})$ and $\varepsilon \in \mathcal{O}(10^{-4})$, see fig. 4.2. This is merely a test of our implementation of the algorithm and not a new result, as stochastic quantization of $SU(2)$ was compared with the Metropolis algorithm (a simpler alternative to heat-bath, see app. B.1.3) already in [339]. The different thermalization behavior for varying step sizes is illustrated in fig. 4.3. Clearly, if the step size is too large, the stochastic process converges against a significantly wrong value. However, this potential problem can be controlled well by (i) choosing a sufficiently small step size, which leads to the correct equilibrium,[7] and (ii) monitoring the thermalization process carefully, i. e., ensuring that expectation values have 'equilibrated'.

In fig. 4.4, we compare the thermalization behavior of the random walk algorithm at two values of the step size for different couplings and volumes. Naturally, the fluctuations of the plaquette are less pronounced on larger lattices, as U_P is a volume-averaged quantity. The influence of the coupling on the thermalization time (thus, on the autocorrelation time) is not large.

We now turn to the inclusion of Zwanziger's additional gauge fixing force by means of gauge transformations. This is independent of the method used for the dynamic updates (Langevin or random walk).

4.2.2.2 Gauge fixing

In order to calculate quantities like the gluon and ghost propagator, it is indispensable to fix the uncorrelated configurations, which obey the distribution $\rho[U] \propto \exp(-S[U])$, to Landau gauge, eq. (2.11), see sec. 2.3.2 for remarks on lattice gauge fixing. Here, we employ a lattice version of the stochastic gauge fixing procedure [315, 316, 317]. More specifically, it is a procedure for compact lattice gauge theory, in contrast to the non-compact version investigated e. g. in [313]. After every single dynamical link update by the lattice Langevin (4.5) or random walk (4.11) algorithm (see sec. 4.2.1), gauge transformations of those link variables that are affected by the change of the respective link are performed according to the standard lattice formula, eq. (2.64), with the local gauge transformation matrices

$$\Omega(x) = \exp\left(-i\frac{\beta}{2N_c}\Delta^a\sigma^a\frac{\varepsilon}{\alpha}\right). \tag{4.16}$$

[6] In the limit of strong coupling, i. e., for small β (see eq. (2.68) for the def. of β),

$$\langle U_P\rangle \xrightarrow[\beta\to 0]{} \frac{\beta}{N_c^2} \tag{4.14}$$

for gauge group $SU(N_c)$. In the opposite limit, the one of weak coupling, $\beta \to \infty$,

$$\langle U_P\rangle = 1 - \frac{n_g}{4\beta} + \mathcal{O}\left(\frac{1}{\beta^2}\right) \tag{4.15}$$

with n_g the number of generators, $n_g = N_c^2 - 1$ for $SU(N_c)$. See e. g. [218, 215].

[7] Naturally, in cases where the correct result is not known, it is a reasonable criterion for a sufficiently small step size that the results are not susceptible to further changes of the step size.

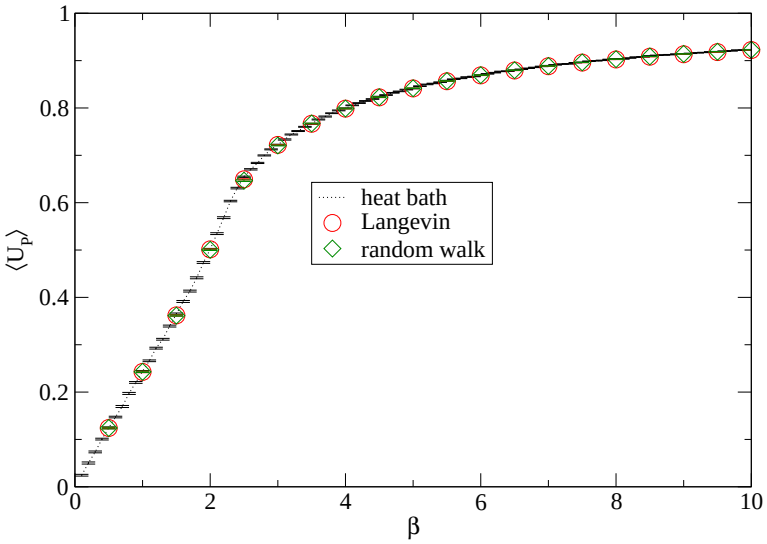

Figure 4.2: Comparison of the plaquette values (see eq. (2.71) for the def. of U_P) from Langevin and random walk (here, both without gauge fixing) vs. the standard heat-bath algorithm at various β. Results from a 12^4 lattice. Step size: $\varepsilon = 0.001$ for Langevin, $\eta = 0.03$ for random walk.

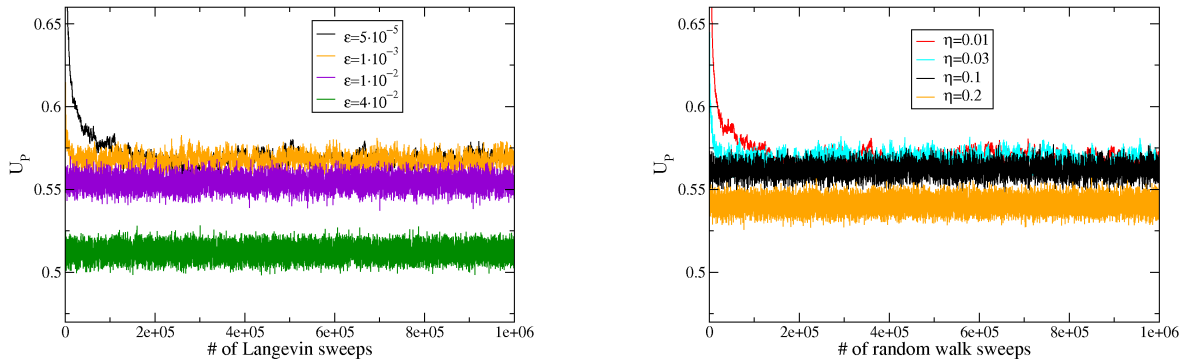

Figure 4.3: Comparison of the evolution in computer time ('thermalization') of the plaquette variable for different step sizes on a 8^4 lattice at $\beta = 2.2$. *Left (a):* Langevin algorithm (step size ε). *Right (b):* Random walk algorithm (step size η).

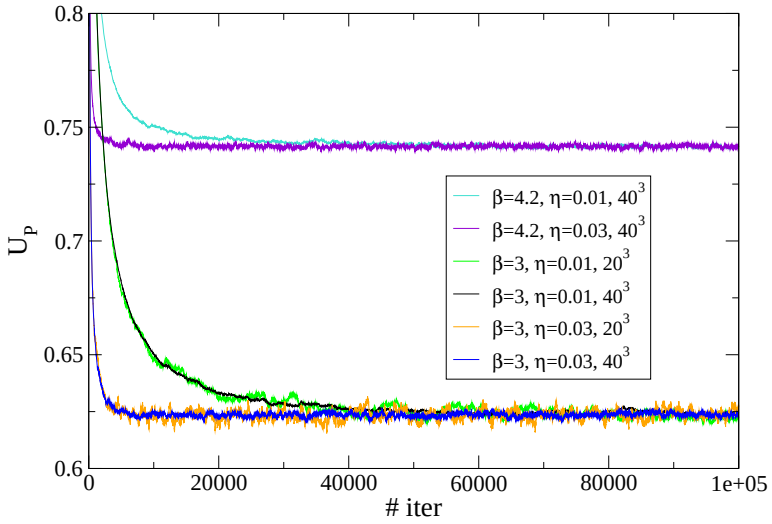

Figure 4.4: Computer time history for the thermalization of the plaquette variable with the random walk algorithm for different volumes, couplings and step sizes.

The number of affected link variables is $4d - 1$ in d dimensions, as is illustrated for the three-dimensional case in fig. 4.5.

An important quantity that enters the gauge transformation matrix (4.16) is the lattice version Δ^a of the Landau gauge fixing condition, defined in eq. (2.83). See sec. 2.3.2 for further details on lattice gauge fixing in general, where we have also defined the space-time averaged square of $\Delta^a(x)$, Δ^2 (2.85), which we will frequently encounter in the following.

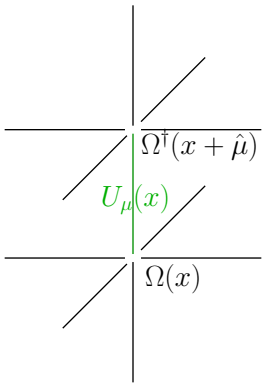

Figure 4.5: A link variable $U_\mu(x)$ together with its gauge transformation matrices Ω and the links they affect ($d = 3$).

Performing such a gauge transformation after each single link update obviously requires a higher numerical effort than the simple alternative of doing so only after an entire sweep of 'dynamical' updates. But choosing the 'more local' procedure proves to be worth the additional effort, since Δ^2 is significantly diminished by this procedure, as is illustrated in fig. 4.6. Hence, we employ the more local version. We do so in order to maximize the difference to standard gauge fixing methods, which are non-local in the sense that the distance to the gauge fixing surface becomes very large due to the dynamical updates between gauge fixing steps. If stochastic gauge fixing should be able to yield a different distribution in configuration space than standard gauge fixing, this would probably be brought about by the local nature of the evolution it induces.

We consider the value of Δ^2, the average of $\Delta^2(x)$, as a measure of distance of a gauge copy from the gauge fixing surface. Thus, it is desirable to minimize it during thermalization. To this end, the gauge fixing parameter α may be suitably adapted, see fig. 4.26. (Note for the interpretation of fig. 4.26 that the Langevin step size enters into the gauge transformations (4.16) via the ratio ε/α.) However, it is numerically very expensive and impracticable to obtain a value of Δ^2 small enough for precise calculations of Landau gauge propagators on lattices of reasonable size, if the strict requirement is imposed that the algo-

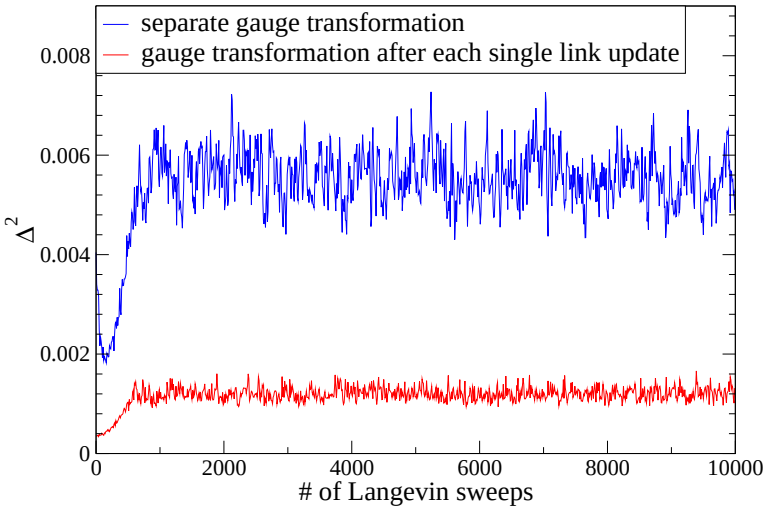

Figure 4.6: Influence of the frequency of stochastic gauge fixing steps during updates on the distance from the gauge fixing surface (see main text for explanation). These data merely serve the purpose of qualitative illustration and have been produced on a 6^4 lattice at $\beta = 1$ with the Langevin algorithm.

rithm stays completely within the scheme of stochastic gauge fixing. Therefore, in practice, we amend stochastic gauge fixing by stochastic overrelaxation steps designed in order to bring Δ^2 from e. g. 10^{-6} down to 10^{-15}.[8] That is, stochastic gauge fixing is performed as long as this is feasible, and only the fine-tuning is done with a standard approach.

4.3 Results

We have discussed our studies of a toy model with stochastic quantization in sec. 3.2. The present section contains the much more extensive results for stochastic quantization applied as a gauge fixing procedure in Yang–Mills theory.

We have studied both the gluon and ghost propagator in two, three and four dimensions with stochastic quantization. The results in different dimensions have been produced with the same C++ code, changing only the value of a single integer variable. For the ghost propagator, we have employed the plane-wave source method, see app. B.3, unless mentioned otherwise. This ensures a high precision of the data.

4.3.1 Gluon and ghost propagators

We are particularly interested in the *infrared* behavior of the gluon and ghost propagators. This behavior can be characterized by infrared power-law exponents, as defined via eqs. (2.27a) and (2.27b). The definitions of the propagators on the lattice are given in sec. 2.3.3.

[8] It might be argued that such a procedure could in principle compromise the 'locality' of stochastic gauge fixing, where the latter is understood in the sense that is illustrated in fig. 4.1. I. e., it could lead to the copies traveling large distances in configuration space. However, since stochastic overrelaxation is utilized only for fine-tuning, such a movement is at least limited.

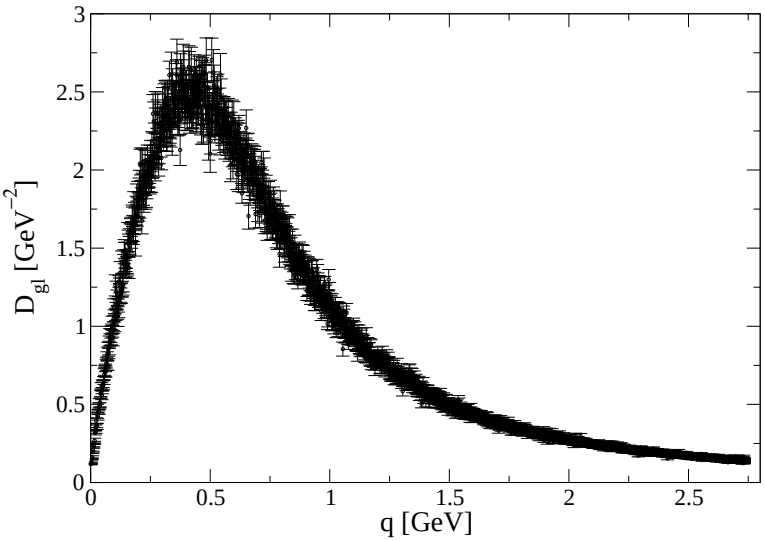

Figure 4.7: A result from *standard* gauge fixing: Gluon propagator in two dimensions on a huge lattice, sc. one of 'volume' 2560^2 at $\beta = 10$, corresponding to a lattice extension in physical units of $(520\,\mathrm{fm})^2$ (see sec. 2.3.4.3). Individual momenta can hardly be distinguished here, since they number more than 2500.

The method to extract estimates for these exponents from discrete data sets obtained on finite volumes is clearly not unique. We follow the procedure of ref. [116], i. e., we discard the propagator values at the two lowest non-vanishing momenta and perform a power-law fit to the data at the next five ones. We do so for both the gluon and the ghost propagator.

The infrared fit to the ghost propagator yields the infrared exponent $\kappa \equiv \kappa_C$ by means of eq. (2.27b). Similarly, the corresponding fit to the gluon propagator directly gives the infrared gluon exponent κ_A (eq. (2.27a)). From this quantity, the ghost exponent from the gluon data, called κ_Z, can easily be deduced via the scaling relation, eq. (2.28).[9]

4.3.1.1 Two dimensions

Pure Yang–Mills theory in two dimensions has special properties compared to its higher-dimensional counterparts. In this case, the theory lacks dynamics [291] and can be solved exactly [253, 254, 255]. Confinement may be referred to as a 'trivial' phenomenon in this case, since on the classical level, the degrees of freedom of the gauge field are eliminated already by imposing e. g. the Landau gauge condition, see [190] for a brief discussion.

It is part of the 'standard lattice scenario' that the propagators in two dimensions are consistent with the scaling solution [116], see also [275] for gluon data. We have calculated the gluon propagator on one of the largest two-dimensional lattices simulated so far, sc. a 2560^2 lattice, employing parallel code (app. B.4), see fig. 4.7. This result shows a very pronounced decrease toward the infrared, consistent with a vanishing value at zero momentum. We emphasize that this figure is an exception in the present chapter, as the data presented therein have been obtained after standard gauge fixing, as opposed to stochastic gauge fixing like all following ones in the present chapter.

[9] To this end, κ is calculated from κ_A via (2.28) and subsequently referred to as κ_Z.

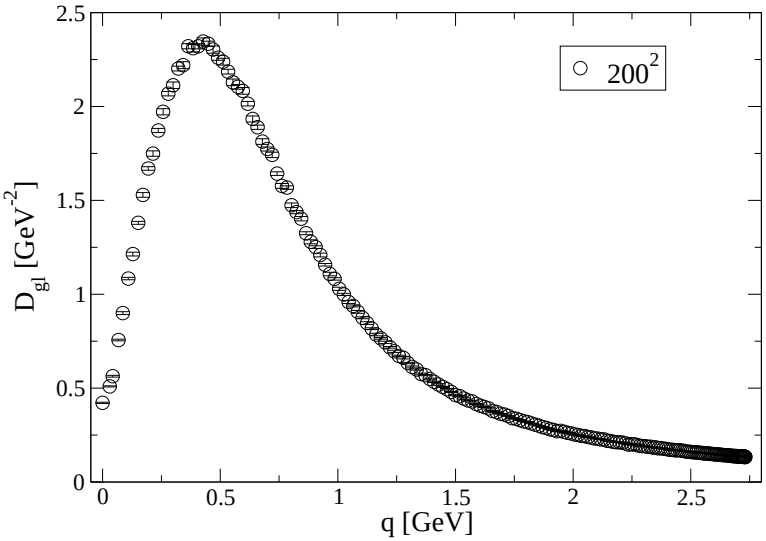

Figure 4.8: Gluon propagator in two dimensions with stochastic quantization.

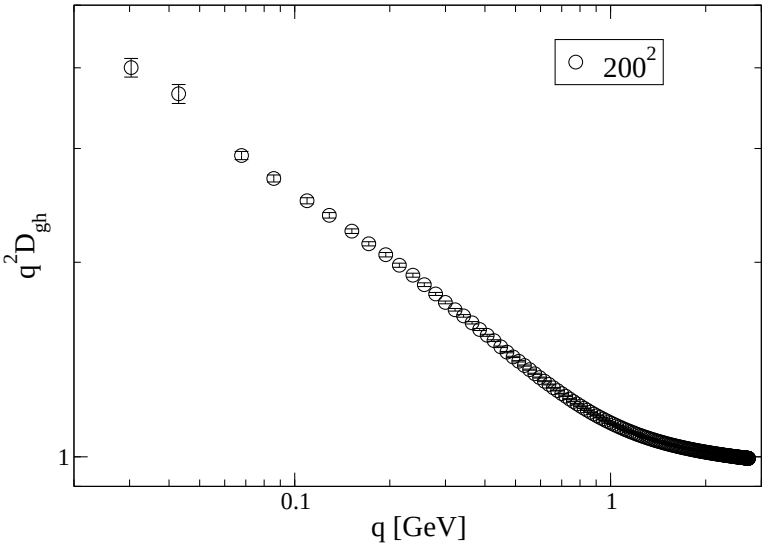

Figure 4.9: Ghost dressing function in two dimensions with stochastic quantization. Note the logarithmic scales.

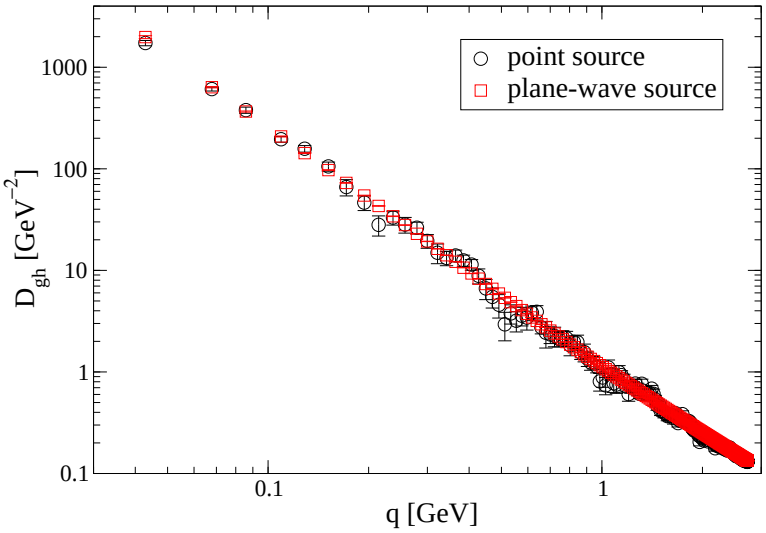

Figure 4.10: Point source vs. plane-wave source method for the ghost propagator with stochastic gauge fixing on a 200^2 lattice at $\beta = 10$ (random walk, $\eta = 0.03$ for the point source data resp. $\eta = 0.01$ for the plane wave source data). In order to facilitate a comparison, the same number N of measurements is used in both cases, sc. $N = 50$.

Our results from stochastic gauge fixing in two dimensions confirm the standard lattice scenario. I. e., they are consistent with a scaling behavior, like those in [116, 275]. The gluon propagator on a 200^2 lattice is depicted in fig. 4.8. At the chosen value of the coupling, $\beta = 10$, this corresponds to a linear lattice extension of about 40 fm (cp. sec. 2.3.4.3). While we have not pursued an extensive finite volume study in this case (but see sec. 5.2.2.1 for a finite volume analysis in the strong-coupling limit), our results are compatible with those of ref. [116], which were obtained with standard gauge fixing and which point to $D_{\mathrm{gl}}(q = 0) = 0$ for $V \to \infty$.

The ghost dressing function $q^2 D_{\mathrm{gh}}$ obtained after stochastic gauge fixing is shown in fig. 4.9. It is already visible by the naked eye that this appears consistent with a power-law behavior at small and intermediate momenta (straight line with logarithmic scales on both axes). We have employed the plane-wave source method, which is numerically much more expensive (by a factor of the number of momenta), but greatly reduces fluctuations, as explained in app. B.3 and illustrated in fig. 4.10.[10] A further illustration of this difference is provided in sec. 5.2.2.2 below.

We emphasize again that for the scaling solution, the values of the infrared ghost exponent from the gluon data, called κ_Z, and from the gluon data, called κ, agree exactly. The values we obtain, sc. $\kappa_Z = 0.19$ (from $\kappa_A = 1.37$ and eq. (2.28)) and $\kappa = 0.17$, are indeed close to each other. Moreover, they resemble the expectation based on the scaling solution, which predicts $\kappa = \kappa_Z = 0.2$ [54]. Note that the precise values of κ predicted by functional continuum methods depend on certain assumptions resp. approximations, see sec. 2.2.2. But that the equation $\kappa = \kappa_Z$ holds is a strictly necessary condition for scaling behavior.

However, our studies at $\beta = 0$ (ch. 5) with high statistics cast doubt on any overly

[10] The slightly different random walk step sizes employed, as explained in the caption to fig. 4.10, do not make any decisive difference.

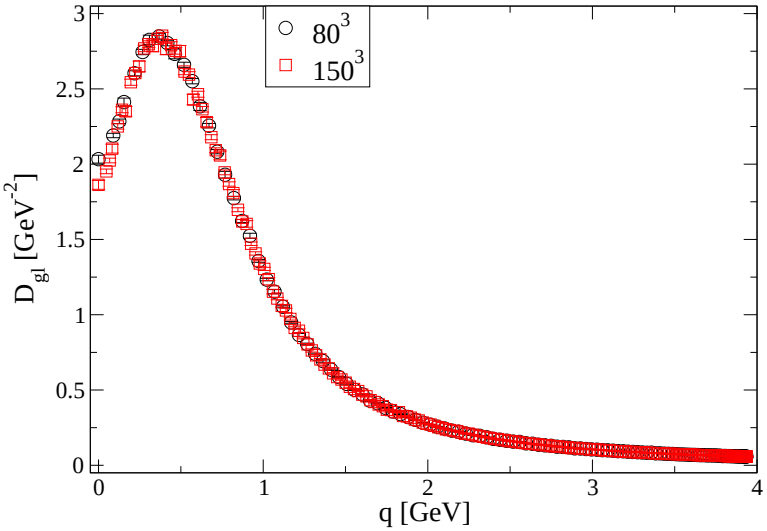

Figure 4.11: Gluon propagator in three dimensions with stochastic quantization for two different lattice volumes. See fig. 4.12 for a blowup at small momenta.

straightforward interpretation of the present result for in two dimensions. They may be interpreted as evidence for a more unified picture in two, three and four dimensions, see in particular sec. 5.2.2.1.

4.3.1.2 Three dimensions

The gluon propagator from stochastic quantization in three dimensions is shown in fig. 4.11 for two different lattice sizes, sc. 80^3 and 150^3, corresponding to a linear lattice extension of 14 fm resp. 26 fm in physical units. A closer look at small momenta is provided in fig. 4.12. The gluon propagator shows a significant peak at a non-zero momentum value, sc. at $q \approx 350\,\mathrm{MeV}$, which agrees well with a previous result obtained by standard gauge fixing [258]. At vanishing momentum, the gluon propagator assumes a non-zero value, $D_{\mathrm{gl}}(0) \neq 0$. Finite volume effects are apparently not strong enough to change this behavior. This immediately implies $\kappa_A = -1$ (cp. the definition of κ_A, eq. (2.27a)), which entails for the ghost exponent from the gluon data (assuming the scaling relation, eq. (2.28)) $\kappa_Z = 0.25$.

The ghost dressing function in three dimensions is presented in fig. 4.13.[11] While we have pursued an extensive finite volume analysis only in the strong-coupling limit (see sec. 5.2.2.2), the behavior of the ghost propagator at finite coupling, which is presented here, unambiguously exhibits qualitative differences from the two-dimensional case: At small momenta, a deviation from a pure power-law behavior is observed, i. e., κ decreases toward the infrared. On an 80^3 lattice at $\beta = 4.2$, κ drops to 0.2, down from 0.25 on the smaller 40^3 lattice. We have included a power-law fit to the data from which κ is extracted on the smaller lattice in fig. 4.13.

[11] On large lattices in three and four dimensions, we have calculated the ghost propagator with stochastic quantization only for the relevant infrared momenta. This restriction is lifted in our simulations presented in the subsequent chapters, the reason simply being that the latter simulations were carried out later, when we had access to significantly more computing resources.

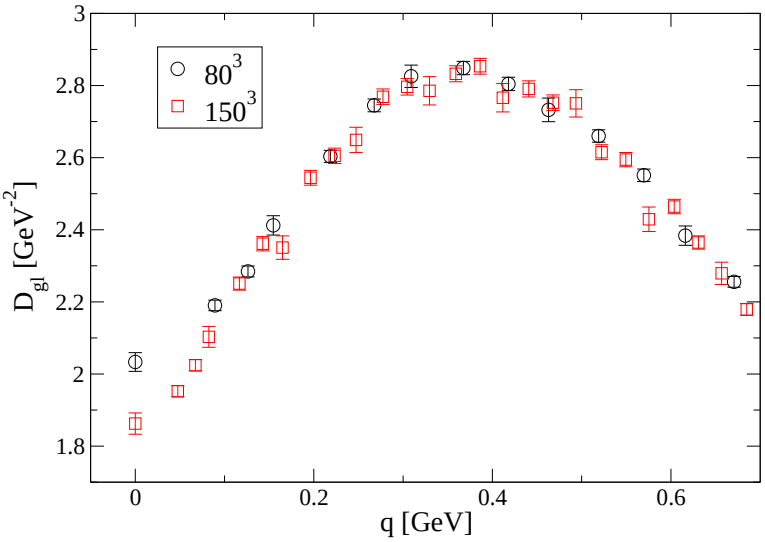

Figure 4.12: Blowup of fig. 4.11 at small momenta.

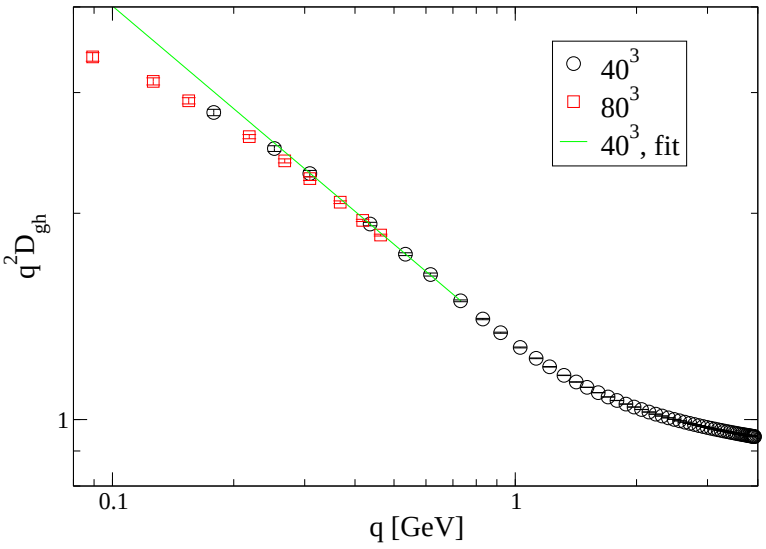

Figure 4.13: Ghost dressing function in three dimensions with stochastic quantization for two different lattice volumes. On the larger volume, the Faddeev–Popov operator was inverted only on selected infrared momenta. The fit is an extrapolation of the procedure described in the text to extract the infrared exponent κ. Fit result included here for the smaller lattice.

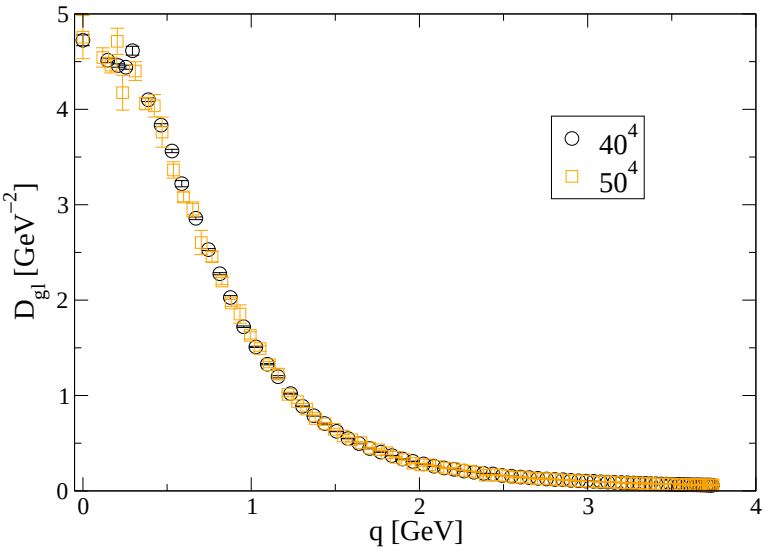

Figure 4.14: Gluon propagator in four dimensions, calculated with our usual stochastic quantization procedure as described in the text (here, random walk dynamics).

Naturally, the larger lattice allows to obtain more information about the infrared behavior, because smaller momenta are accessible. Since stochastic gauge fixing is less readily parallelized than a standard algorithm (see app. B.4 for parallelization issues in the latter case) and since the picture is already quite unambiguous, we postpone an investigation of even larger lattices to our studies of standard gauge fixing at strong coupling, see sec. 5.2.2.2 (and also at finite coupling, like in fig. 7.6).

4.3.1.3 Four dimensions

Gluon propagator. The gluon propagator in four dimensions from stochastic quantization is shown in fig. 4.14. Like in three dimensions, it does not vanish in the infrared. Hence again $\kappa_A = -1$, but this entails $\kappa_Z = 0.5$, differently from the three-dimensional case (note that the scaling relation (2.28) depends on the number d of dimensions). The values $\kappa_Z = 0.25$ and 0.5 in three and four dimensions, respectively, are important because they represent the border between an infrared vanishing and non-zero gluon propagator.

In contrast to the three-dimensional case, the gluon propagator does not even possess a peak at non-zero momenta. Rather, it is virtually constant in the infrared. This is not only generically rather in line with a decoupling-type solution than with a scaling behavior, but in addition, it provides evidence that the difference between the lattice data and the scaling solution is even larger than in lower dimensions, in line with previous lattice results.

Ghost propagator. For a conclusive statement about the type of infrared solution, it is again indispensable to consider the ghost propagator in addition to the gluon. The exponent κ extracted from the ghost dressing function decreases toward the infrared, again like in three dimensions and quantitatively slightly stronger, now from 0.26 (20^4) to 0.19 (40^4). On the larger lattice in four dimensions, the infrared behavior of the ghost as obtained with a plane-wave source and depicted in fig. 4.16 cannot be fitted with $\chi^2/\mathsf{ndf} \lesssim 1$. The value

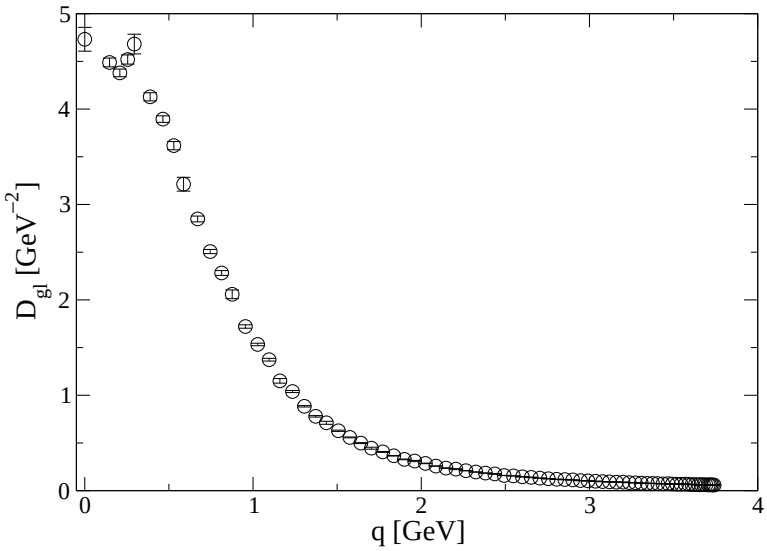

Figure 4.15: Gluon propagator on a 40^4 lattice, differing from fig. 4.14 insofar as even the 'fine-tuning' is performed by stochastic gauge fixing. This requires that the accuracy of gauge fixing is deliberately lower, sc. only $\Delta^2 < 10^{-8}$. See main text.

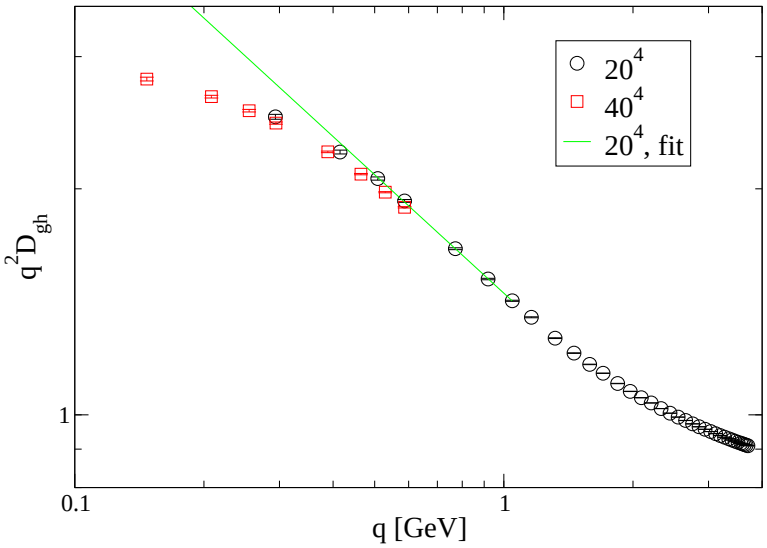

Figure 4.16: Ghost dressing function in four dimensions with stochastic quantization. On the larger lattice, calculation only at infrared momenta. Green line: power-law fit to 20^4 data at 3rd through 7nd non-vanishing momentum.

of 0.19 is obtained from data that have been produced with the point source method; in all other cases, a plane wave source is used (see sec. 2.3.3.2 and app. B.3.1). The decrease is even consistent with a vanishing κ in the $V \to \infty$ limit, corresponding to a decoupling-type solution.

Discussion. The results for both the ghost and gluon propagator are fully in line with previous lattice results like e. g. [273, 276, 278, 272, 293], which also include studies on even larger lattices. That the gluon propagator does not vanish in the infrared is currently widely agreed upon, with a few exceptions [285, 286] (see sec. 2.4.1.1 for a more extensive overview of results and references). Regarding the ghost propagator (see also sec. 2.4.1.2), the conclusions drawn from the data range from the cautious statement that the ghost propagator is much weaker divergent in the infrared than expected from functional methods, e. g. [269, 276], to the claim that no singular behavior can be seen at small momenta, e. g. [272, 293, 278].[12] However, the issue is rather intricate since in addition to the volume dependence, the Gribov copy dependence of the infrared propagators needs to be taken into account. Naturally, this poses an even larger numerical challenge. We discuss this effect in ch. 6, where we also give further references.

The fact that κ does not vanish in three and four dimensions may well be due to the finite lattice extension [278, 293] or also to choosing the first instead of the 'best' Gribov copy [277]. Here, 'best' is understood in the sense of an approximate *global* maximization of the gauge fixing functional R, eq. (2.80). Our value of $R = 0.82795(1)$ in four dimensions on a 40^4 lattice from stochastic gauge fixing (with more than 1000 measurements) is close to the values typically obtained from standard gauge fixing, while it is significantly lower than the value after the 'globally optimizing' gauge fixing [274] (e. g., $R = 0.82843(1)$ from a 'best copy' approach on a 32^4 lattice).

Note again that we usually amend stochastic gauge fixing by a standard method for fine-tuning, sc. stochastic overrelaxation, as described in app. B.2.1.2. But in order to confirm that this does not introduce a bias, we have also investigated a procedure where the fine-tuning is done via stochastic gauge fixing, sc. by gradually decreasing the step size η in the random walk algorithm. Because this is numerically expensive, as the decrease of Δ^2 by this method turns out to be far from monotonic, we merely impose the condition $\Delta^2 < 10^{-8}$, which is much weaker than the usual condition of $\Delta^2 < 10^{-15}$. The result is shown in 4.15. It is virtually identical to the result of the procedure we employ otherwise, fig. 4.14. This is some evidence that our fine-tuning method does not lead to a significant bias.

4.3.1.4 Miscellaneous results on the gluon propagator

In fig. 4.17, we compare the gluon propagator in two dimensions for different gauge fixing algorithms at deliberately not sufficiently small Δ^2. In fig. 4.17a, it is shown that the gluon propagator improves (i. e., approaches its true shape, see fig. 4.8) as the value of Δ^2 continuously obtained during stochastic gauge fixing becomes smaller, i. e., as the Markov chain of configurations fluctuates around a smaller distance from the gauge fixing surface. Surprisingly, stochastic overrelaxation with deliberately high Δ^2 yields a considerably better gluon

[12] In giving these references, we generally do not distinguish between the cases of $SU(2)$ and the $SU(3)$. See e. g. [281, 282] for an explicit comparison of these two cases, see also sec. 2.4.

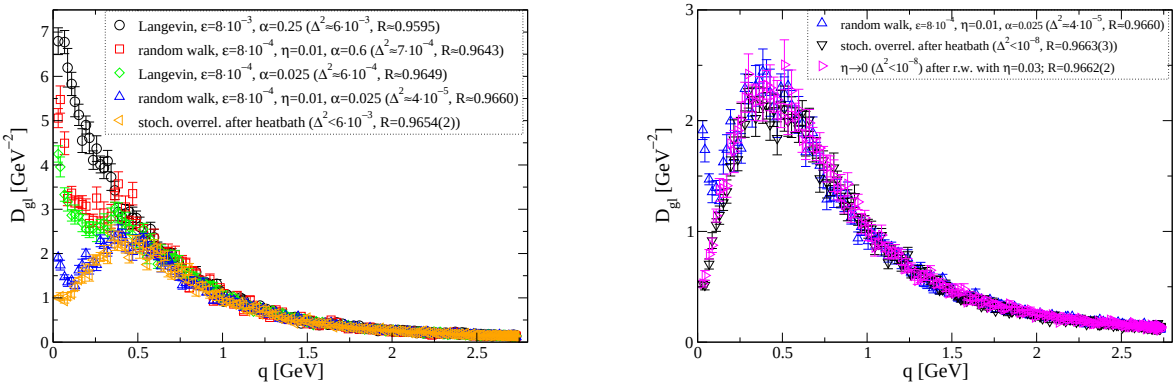

Figure 4.17: Gluon propagator at deliberately not fully sufficient gauge fixing. The average values of Δ^2 and R for the various sets of configurations are given explicitly in the legends. *Left (a):* larger Δ^2, *right (b):* smaller Δ^2; one data set (random walk, $\Delta^2 \approx 4 \cdot 10^{-5}$) is shown in both plots in order to facilitate a comparison. Note the different scales on the y-axis.

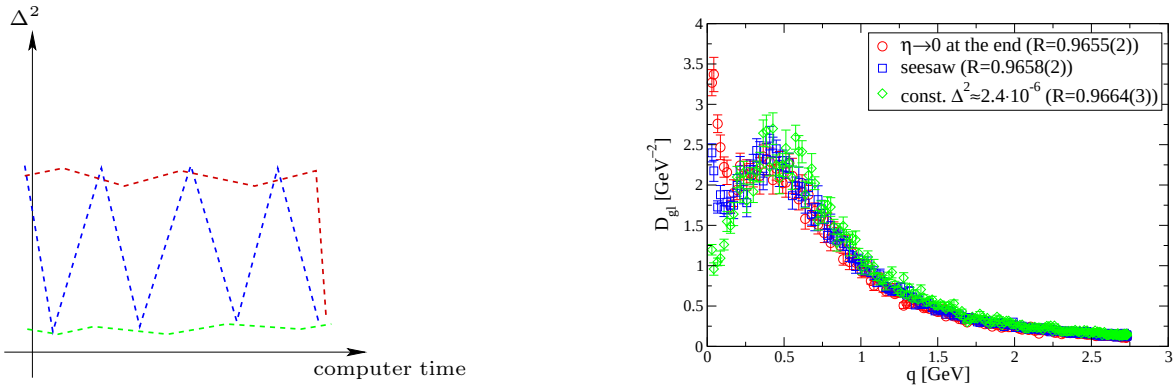

Figure 4.18: Comparison of three different gauge fixing methods with the same final value of Δ^2. All of these methods are variants of stochastic gauge fixing, see main text for details. *Left (a):* Illustration. *Right (b):* Results on a 200^2 lattice at $\beta = 10$.

propagator. This underlines that the dependence on Δ^2 is significantly less pronounced for standard gauge fixing, such as stochastic overrelaxation, than for stochastic gauge fixing.[13] This is additional evidence for a difference between these methods.

Fig. 4.17b shows a comparison of stochastic and standard gauge fixing, by means of its effects on the two-dimensional gluon propagator, for a smaller distance from the gauge fixing surface, $\Delta^2 < 10^{-8}$, with one set of data from fig. 4.17a included so as to facilitate comparison with those data. The algorithm '$\eta \to 0$ after random walk' means that after a usual random walk version of stochastic gauge fixing, the step size η is gradually decreased. This is a much less efficient way of obtaining a low Δ^2 than e. g. stochastic overrelaxation, but it stays more strictly within the scheme of stochastic gauge fixing. At $\Delta^2 < 10^{-8}$, the result of this method is virtually indistinguishable from the result of standard gauge fixing, as is apparent from fig. 4.17b.

Moreover, we note that the values of the gluon propagator at zero momentum and of the gauge fixing functional R are uncorrelated, also for suboptimal stochastic gauge fixing, sc. for $\Delta^2 \in \mathcal{O}\left(10^{-3}\right)$, as well as for $\Delta^2 \in \mathcal{O}\left(10^{-8}\right)$. This is largely in line with our results for the gluon propagator in Landau max-B gauge (ch. 6), where the infrared gluon propagator changes only slightly between different gauge copies.

In addition, we have also probed a version of stochastic gauge fixing during which the distance in configuration space is restricted to be small when the descent to the gauge fixing surface is performed. The gluon propagator in two dimensions is insensitive to this restriction, which is implemented naïvely with regard to the changes in the Cayley–Klein parameters of the link variables at all lattice sites.

Finally, we have implemented yet another variant of stochastic gauge fixing, which we refer to as the 'seesaw algorithm', and have tested whether it affects the infrared behavior in an interesting way. The 'seesaw' method is designed to interpolate between stochastic gauge fixing at relatively large Δ^2 and the very time-consuming method of thermalizing with a very small Δ^2. In the latter case, a particularly small step size is required, leading to a higher autocorrelation time. An illustration of the 'seesaw procedure' is provided in fig. 4.18a. The idea is to perform after each updating sweep a number of pure gauge transformations, which serve to decrease Δ^2 by a factor of γ, e. g. $\gamma = 0.01$, before another regular updating sweep is performed which brings Δ^2 back to a larger, but still small value ('small' compared to $\Delta^2 \in \mathcal{O}(1)$, i. e., to copies that are not gauge-fixed at all). We compare its results for the gluon propagator with those of the pure stochastic gauge fixing method fluctuating around $\Delta^2 \in \mathcal{O}(10^{-6})$ throughout the entire Langevin evolution, and with those of a method where Δ^2 is at first larger and then decreases toward the same intermediate value. The results for the gluon propagator in two dimensions demonstrate that the 'seesaw' method is indeed an interpolation between these two cases, see fig. 4.18b.

4.3.1.5 Summary of the infrared propagators from stochastic quantization

We summarize here the results for the infrared exponents of the gluon and ghost propagators from stochastic quantization, as presented in secs. 4.3.1.1 through 4.3.1.3. We give the ghost exponent from the ghost data, κ, and the ghost exponent obtained from the gluon data via the scaling relation (2.28), κ_Z. The statement '$\kappa = \kappa_Z$' is equivalent to this relation.

[13] We emphasize again that stochastic gauge fixing is unrelated to stochastic overrelaxation; in this context, the latter method's name may be slightly confusing.

The column 'continuum' refers to the prediction from functional continuum methods, which do not uniquely fix the values of κ and κ_A, although they do fix their scaling relation (2.28), as reviewed in sec. 2.2.2. Note that we deliberately do not give explicit error estimates for the infrared exponents, since it is reasonable to assume that the systematic errors, which are hard to quantify, are larger than the mere error of the power-law fit. These systematic effects stem from the finiteness of the volume, the non-zero lattice spacing and also the procedure of extracting the exponent (choice of infrared momenta, see p. 69).

As is again apparent, our results from stochastic quantization point toward a scaling solution in two dimensions, but rather toward a decoupling-type behavior in three and four dimensions. The discrepancy between the results and an infrared scaling behavior is significantly larger in four than in three dimensions. Our strong-coupling studies (ch. 5) shed some more light on the dependence of the behavior on the number of dimensions.

d	κ	κ_Z	continuum [54, 84]	consistent with scaling?
2	0.17	0.19	0.2	✓
3	0.25 (40^3) / 0.2 (80^3)	0.25	$\approx$0.398	✗
4	0.26 (20^4) / 0.19 (40^4)	0.5	$\approx$0.595	✗

Regarding the number of measurements, for the ghost propagator with the plane-wave source, already around 50 uncorrelated configurations are sufficient for a clear picture. The corresponding numbers of the gluon propagator are summed up in the following table.

lattice size	200^2	80^3	150^3	40^4 (fig. 4.14)	40^4 (fig. 4.15)	50^4
no. of meas.	4800	1280	874	1145	242	50

Note that most of the results in this chapter are results of serial code from comparatively early stages of this work,[14] during which the available computing resources were limited. In further studies of the propagators (beyond stochastic quantization), we employ sometimes several orders of magnitudes more measurements or significantly larger lattices, as presented in chs. 5, 6, 7 and 8.

4.3.2 Faddeev–Popov operator spectrum

4.3.2.1 Introductory remarks

The lowest nontrivial eigenvalue λ_0 of the Faddeev–Popov operator $-\partial_\mu D_\mu^{ab}$ serves as a measure of the distance to the first Gribov horizon (often referred to as 'Gribov horizon' simpliciter), as mentioned in sec. 2.2.3.3. This is because the first Gribov horizon is where $\lambda_0 = 0$ (and $\lambda_i > 0$ for $i \neq 0$). Our studies of the FPO spectrum in the framework of stochastic quantization are motivated by the working hypothesis that this alternative gauge fixing method may bring about a different distribution in configuration space than standard methods do. In particular, it might be speculated that the failure of standard lattice gauge fixing methods to confirm the Gribov–Zwanziger scenario could be related to a hypothetical bias that these gauge fixing procedures implicitly introduce, e. g., against the fundamental modular region Λ or against the Gribov horizon $\partial\Omega$.

[14] This holds with the exception of the data from standard gauge fixing on a large two-dimensional lattice shown in fig. 4.7, which have been produced with a parallel code.

For these studies, we employ the standard lattice discretization of the Faddeev–Popov operator, see e. g. [17, 247, 245, 173], which is explicitly given in sec. 2.3.3.2. This is not a unique choice in any case, and it comes with a specific caveat when applied to imperfect gauge fixing, i. e., to the case of a higher Δ^2 than usual.[15] The reason is that the lattice Landau gauge condition, eq. (2.83), is implicitly assumed in the derivation of the standard lattice Faddeev–Popov operator (see app. C.1, especially eq. (C.17)). Still, this should not impede drawing qualitative conclusions from the following results. We briefly explore an alternative discretization that may be more appropriate at significantly non-zero Δ^2 in app. C.2.

4.3.2.2 Results

Stochastic gauge fixing. When performing stochastic gauge fixing, we may adjust the parameters, sc. α and the step size ε resp. η, such that the gauge fixing is deliberately of merely intermediate accuracy, e. g. $\Delta^2 \in \mathcal{O}\left(10^{-3}\right)$.[16] We have done so on a rather small lattice, which allows us to calculate the *entire* FPO spectrum and thereby the *exactly* lowest nontrivial eigenvalue of the FPO, called 'λ_0'. It is the distribution of λ_0 which we are interested in, since $\lambda_0 > 0$ characterizes the first Gribov region Ω.

Stochastic gauge fixing leads to a prima facie surprising distribution of configurations, see the upper left plot in fig. 4.19, with a peak close to the Gribov horizon $\partial\Omega$ as an outstanding property. However, this peak is located slightly outside of $\partial\Omega$, signaling that the gauge has not been fixed to sufficient accuracy here, since the FPO is the negative Hessian of the gauge fixing functional R and is thus a positive operator in a local maximum of R. Still, this result provides some evidence that stochastic gauge fixing avoids a possible reason for a failure of the Gribov–Zwanziger scenario, namely a bias against $\partial\Omega$.

Standard gauge fixing. The situation with standard gauge fixing is less unambiguous, due to the fact that the stochastic overrelaxation method contains an additional parameter p, which fixes the probability of deliberately suboptimal gauge transformations, see app. B.2.1.2. The results for three different values of p are depicted in the lower left plot of fig. 4.19. At small and large values of p, the results differ considerably from the results of stochastic quantization, which are shown in the upper left plot of the same figure. Most notably, standard gauge fixing does not lead to a peak close to $\partial\Omega$. But such a peak can be brought about by suitably adjusting p. As a side note, the value of p that has this effect is close to the 'optimal' value, where 'optimal' is understood in the sense that the respective value leads to the fastest decrease of Δ^2 toward small values, which arerequired for e. g. propagator calculations.

This difference regarding the lowest Faddeev–Popov eigenvalue is reflected in a significant effect on the gluon propagator, see fig. 4.20a. For the value of p at which much more configurations have a negative lowest FPO eigenvalue ($\lambda_0 < 0$), the gluon propagator is considerably higher at infrared momenta, thus deviating more strongly from its value at fully sufficient gauge fixing (i. e., sufficiently small Δ^2). Note again that cum grano

[15] We thank Daniel Zwanziger for emphasizing this caveat in discussion with us.

[16] For comparison, typical values are $\Delta^2 \in \mathcal{O}(1)$ for configurations to which no gauge fixing has been applied and $\Delta^2 < 10^{-12}$ or even lower for a good quality of gauge fixing.

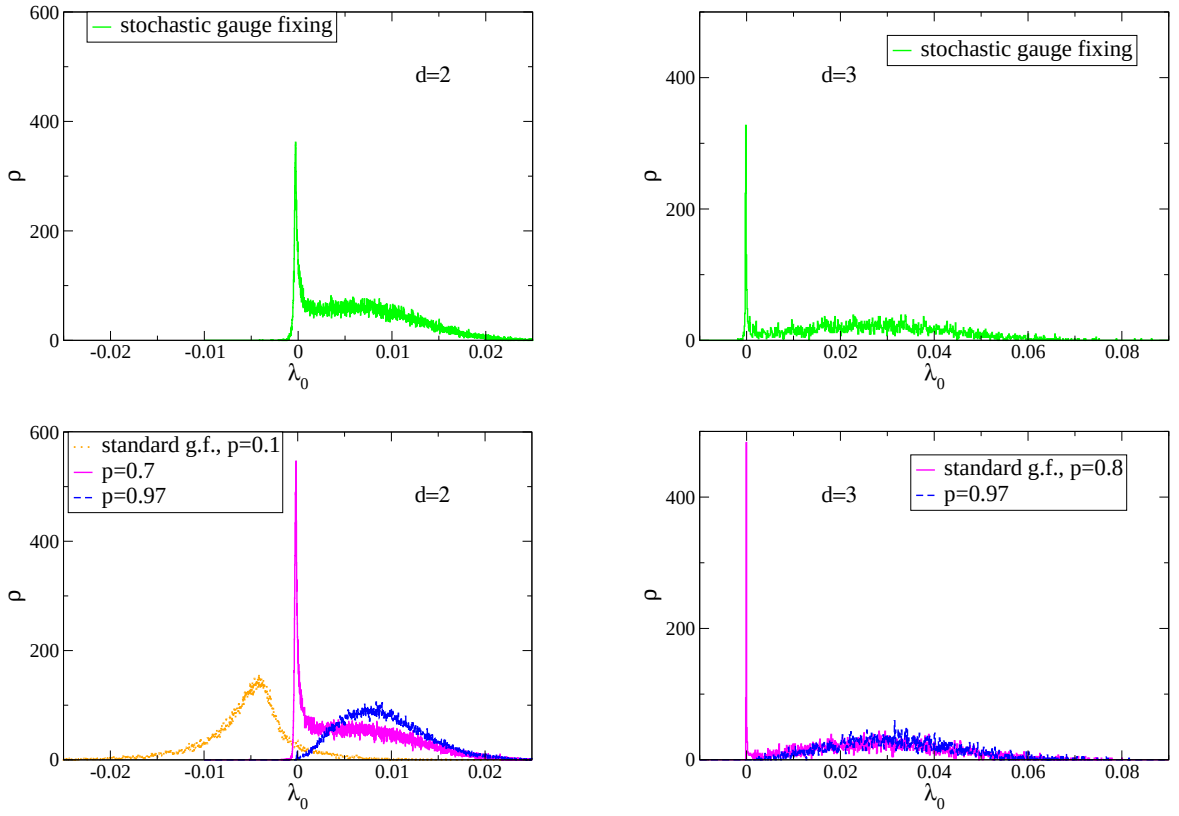

Figure 4.19: Histograms of the lowest nontrivial FPO eigenvalue λ_0 in two resp. three dimensions with stochastic *(top)* and standard gauge fixing *(bottom)*. *Left:* 24^2 lattice, $\beta = 10$, $\Delta^2 \approx 8 \cdot 10^{-4}$. *Right:* 12^3, $\beta = 4.2$, $\Delta^2 \approx 7 \cdot 10^{-4}$.

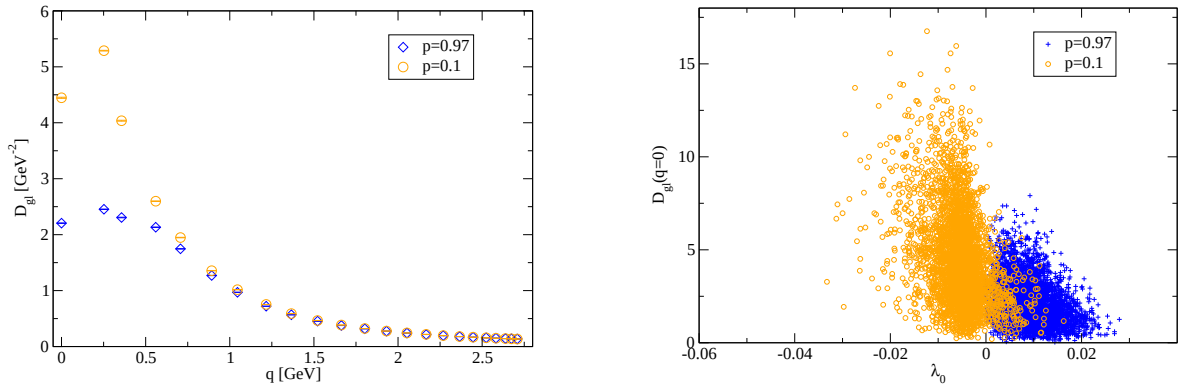

Figure 4.20: Further aspects of the data at intermediate Δ^2 and different overrelaxation parameters p presented in the lower left plot of fig. 4.19 (see the caption of that fig. for details). *Left (a):* Gluon propagators at $p = 0.1$ and $p = 0.97$. *Right (b):* Scatter plot of lowest FPO eigenvalue vs. gluon propagator at $q = 0$. Correlation coefficient: $\rho = -0.40$ ($p = 0.1$, $N = 36000$ configurations) resp. $\rho = -0.29$ ($p = 0.97$, $N = 48000$). For clarity, only 10% of data points are shown in the scatter plot.

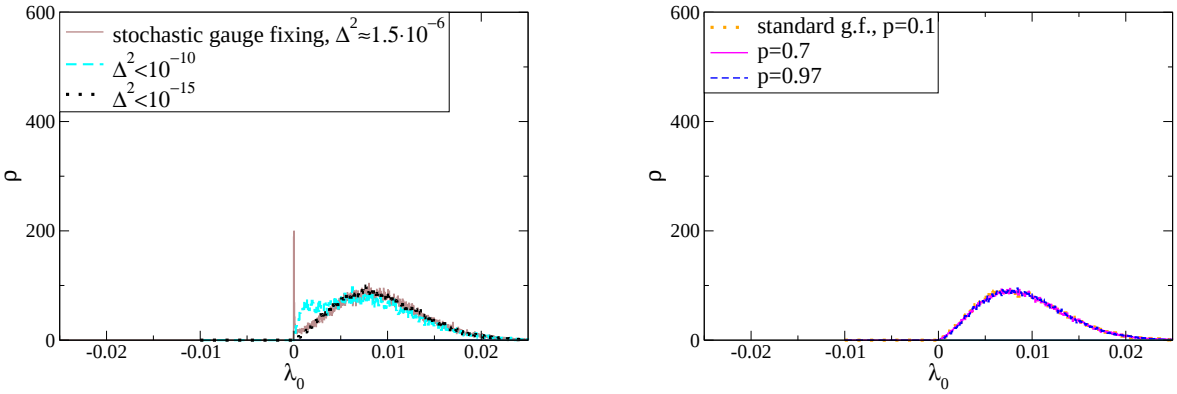

Figure 4.21: Histograms of λ_0 on a 24^2 lattice at $\beta = 10$. *Left (a):* Stochastic gauge fixing with increasing accuracy by choosing a small step size during the entire stochastic process ($\Delta^2 \approx 1.5 \cdot 10^{-6}$) resp. decreasing the step size for fine-tuning ($\Delta^2 < 10^{-10}$ and $\Delta^2 < 10^{-15}$). *Right (b):* Standard gauge fixing with $\Delta^2 < 10^{-10}$ for different values of p.

salis,[17] configurations with a negative lowest FPO eigenvalue lie outside the first Gribov horizon. In compliance with this observation, a further analysis shows that the lowest FPO eigenvalue and the gluon propagator at $q = 0$, are significantly correlated, see fig. 4.20b.

Stochastic gauge fixing at increasing accuracy. It is well known from previous investigations, e. g. [340, 173], that for adequately small Δ^2, no such peak in the vicinity of $\partial\Omega$ is obtained after standard gauge fixing. This is readily confirmed by our numerics. Given this knowledge, the interesting question remains whether stochastic gauge fixing induces any such effect also at sufficiently small Δ^2, e. g. $\Delta^2 \in \mathcal{O}(10^{-15})$. The answer is that it does not; when Δ^2 is gradually decreased by appropriate choices of the step size and the gauge fixing parameter α, the peak 'melts away', see fig. 4.21a. The adjacent fig. 4.21b shows the distribution at $\Delta^2 < 10^{-10}$ after standard gauge fixing (i. e., stochastic overrelaxation). In contrast to stochastic gauge fixing at this accuracy (see the turquoise curve in fig. 4.21a), standard gauge fixing results in a smooth distribution with no sign of a peak close to the Gribov horizon, regardless of the value of the stochastic overrelaxation parameter employed.

Summary regarding the Faddeev–Popov eigenvalues. We sum up the main results for the FPO spectrum. While we find interesting differences between the ways stochastic quantization and generic standard gauge fixing sample configurations at deliberately suboptimal gauge fixing quality, the results from both methods converge against the same result once Δ^2 is sufficiently small. This provides further support for the hypothesis obtained from our studies of the propagators with stochastic gauge fixing, sc. that the lattice gauge fixing problem may be more general than previously assumed. In particular, it confirms the suspicion that the configuration space is ultimately (i. e., for very accurate gauge fixing) sampled in a very similar way by stochastic and standard gauge fixing, while a different

[17] The grain of salt is here the fact that the configurations have a significant distance from the gauge-fixing surface, see sec. 4.3.2.1.

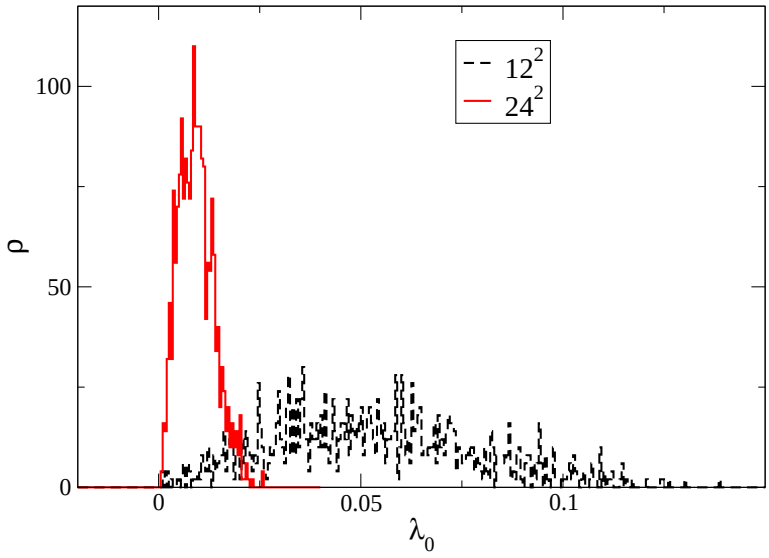

Figure 4.22: Histogram of the lowest nontrivial FPO eigenvalue λ_0 in two dimensions for two different lattice sizes. Data have been produced at $\beta = 10$ with usual random walk amended by decreasing the step size $\eta \to 0$ in order to diminish Δ^2 until $\Delta^2 < 10^{-10}$ (see the discussion of fig. 4.17 in the main text).

sampling would be required in order to obtain a scaling behavior in compliance with the Gribov–Zwanziger scenario of confinement.

Additional results on the FPO spectrum. We conclude the remarks about the Faddeev-Popov operator spectrum after stochastic gauge fixing with two further brief observations. These are less original than much of the foregoing, but rather serve to corroborate that properties of the spectrum known from standard gauge fixing carry over to the case of stochastic gauge fixing.

First, we are able to confirm the well-known volume effect [340, 341, 116] for the lowest FPO eigenvalue λ_0, namely the fact that λ_0 gets smaller as the volume increases. (This effect is even stronger in Coulomb gauge [342].) This translates to the statement that the configurations approach the first Gribov horizon (from inside). See fig. 4.22. This effect is expected already from geometrical resp. 'entropy' considerations, see also the corresponding discussion in ch. 3 regarding the toy model.

Second, the infrared ghost propagator and the lowest FPO eigenvalue are strongly anticorrelated, as is apparent from the results at varying lattice volumes shown in fig. 4.23 (for quantitative statements, see the caption to that fig.).[18] The same fact has been found in [341, 340, 173] with standard gauge fixing, where it has also been analyzed further using the spectral representation of the ghost propagator in terms of eigenmodes and eigenvalues, demonstrating that despite the correlation, a very small lowest eigenvalue of the FPO is not strictly sufficient to obtain a large infrared ghost propagator.

A technical commentary is in order here. The lattices investigated in fig. 4.23 have vol-

[18]The ghost propagator data in fig. 4.23 have not been renormalized. The correlation coefficient is of course insensitive to this.

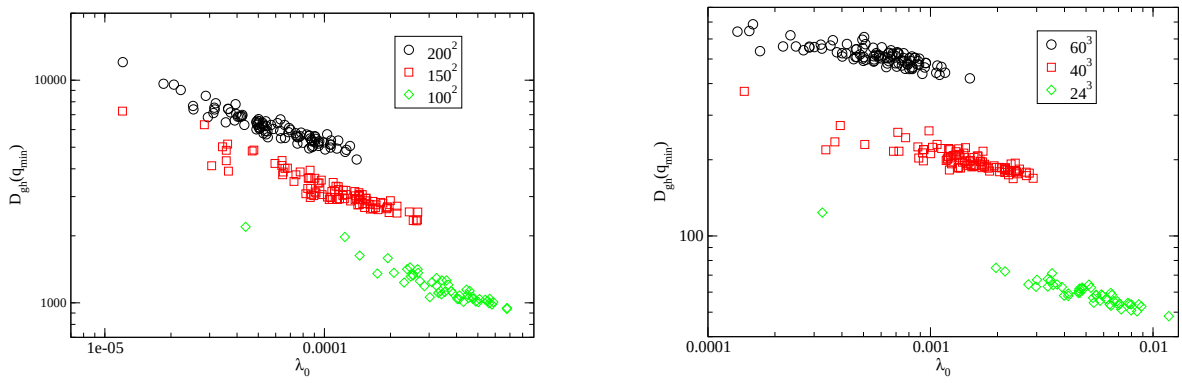

Figure 4.23: Scatter plot of ghost propagator at lowest non-vanishing momentum vs. approximate smallest nontrivial FPO eigenvalue (see text for remarks on the Lanczos algorithm). *Left (a):* $d = 2$. Correlation coefficient $r = -0.82$ resp. -0.83 in all three cases. *Right (b):* $d = 3$. $r = -0.74$ resp. -0.79 in all three cases. Between 50 and 100 configurations per lattice size.

umes V (in lattice units) that are not tiny. It is impracticable to calculate all $3V$ eigenvalues of the FPO on these lattices. Instead, we have utilized a method described in ref. [343]. This method draws on a connection between the conjugate gradient method and the Lanczos algorithm. We use the conjugate gradient method anyway to invert the FPO and thus to calculate the ghost propagator. As laid out e. g. in [343] and app. B.3.3, we can use this to approximately calculate a subset of the eigenvalues of the Faddeev-Popov operator, sc. as many as there are iterations in the conjugate gradient method before it converges. In short, 'λ_0' in fig. 4.23 does not denote the strictly lowest eigenvalue, but the smallest one found by the Lanczos procedure.

4.3.2.3 Return cycles

Stochastic quantization induces 'return cycles' which bring configurations back into the Gribov region while the distance from the gauge fixing surface temporarily increases. This was already noted in early numerical work on stochastic quantization as a gauge fixing mechanism, sc. [312, 313, 309] (investigating non-compact gauge theory). The existence of such cycles is based on the fact that the stochastic gauge fixing force is purely attractive only inside the first Gribov region and possesses repulsive directions outside of it, i. e., that only gauge-fixed configurations *inside* the first Gribov region are *stable* equilibrium configurations, combined with the fact that the Langevin evolution proceeds in a local way. The first of these two facts is not a special property of the gauge force, as it is shared by every algorithm that performs numerical gauge fixing. But a priori, it is possible that such return cycles might help to bring about a distribution in configuration space that deviates from the usual distribution on the lattice. The property of the gauge force to drive configurations into the first Gribov region is also illustrated by our studies of the toy model in the previous chapter, see e. g. fig. 3.1.

The distribution after stochastic gauge fixing at intermediate Δ^2 can be seen in relation to a hypothetical scenario involving 'return cycles'. We emphasize that this relation is rather speculative; nevertheless, we briefly present it here. In an intuitive picture, the Langevin evolution might lead to an accumulation of the gauge-fixed configurations at

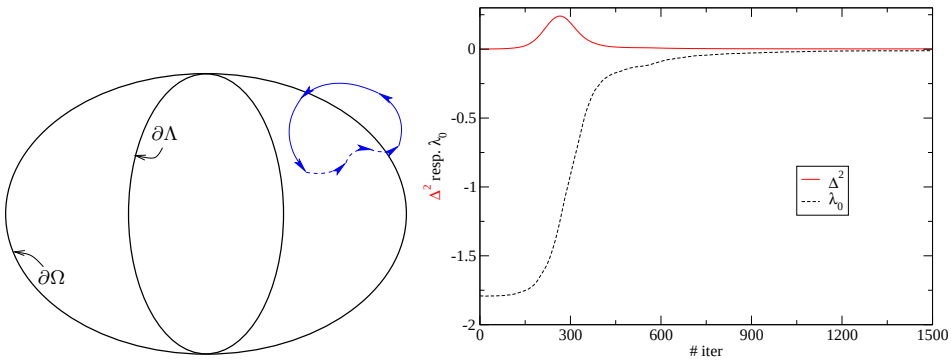

Figure 4.24: *Left (a):* Qualitative illustration of a return cycle. *Right (b):* Numerical data. Approach to Ω during a return cycle with the Langevin algorithm (24^2). Black: Lowest nontrivial FPO eigenvalue ($\hat{=}$ distance to $\partial\Omega$), red: distance to gauge fixing surface.

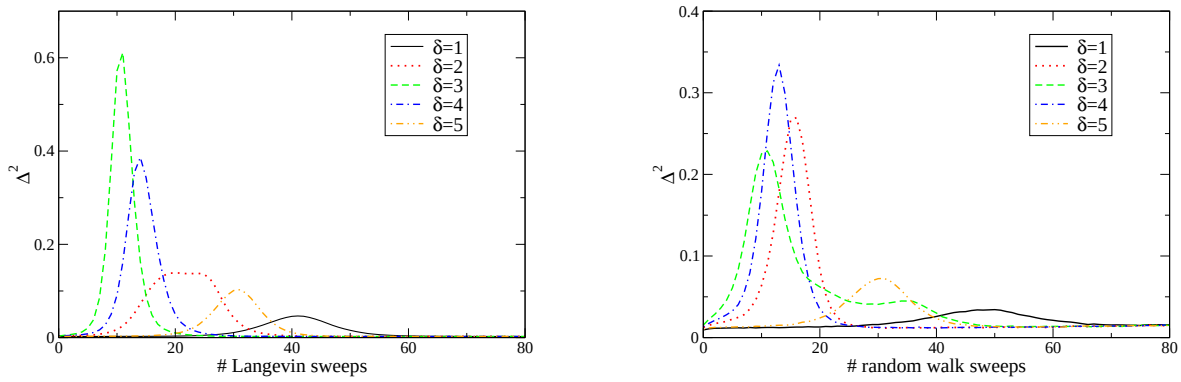

Figure 4.25: Evolution of Δ^2 under stochastic algorithms with gauge fixing after start from a configuration of type (4.17) at $\beta = 0.01$ on a 6^4 lattice at $\alpha = 5 \cdot 10^{-4}$. δ is a measure of the distance of the initial configuration to the origin of configuration space (cp. eq. (4.17)). *Left (a):* Langevin algorithm, $\varepsilon = 10^{-4}$. *Right (b):* Random walk algorithm, $\eta = 0.03$.

the Gribov horizon, due to a combination of two facts, sc. the occurrence of cycles as sketched in fig. 4.24a and the fact that the Gribov horizon acts as a barrier. There is a certain tension inherent in this picture, since the return cycles come about for non-zero gauge parameter α [313], but the horizon strictly acts as a barrier only in the limit of perfect gauge fixing. Hence, it does not come a a surprise that we fail to observe a specific accumulation of configurations close to the horizon with stochastic gauge fixing if the latter is highly accurate (sec. 4.3.2.2).

Still, our numerics readily confirm the existence of trajectories directed back toward the gauge fixing surface, associated with such cycles, see fig. 4.24b. This plot may be understood as follows. The lowest nontrivial eigenvalue λ_0 of the lattice FPO serves as a measure of the distance to the Gribov horizon $\partial\Omega$, where it vanishes. Since $\lambda_0 > 0$ only inside Ω, the configuration whose evolution is depicted in fig. 4.24b starts outside the first Gribov region and approaches it during the Langevin evolution. Simultaneously, the distance from the gauge fixing surface Γ increases temporarily. It is measured by the quantity Δ^2, see eq. (2.85). It is maximal when the approach to Ω is fastest. This is consistent with the intuitive picture of return cycles as depicted in fig. 4.24a. However, as mentioned, the importance of such cycles ought not to be overestimated, also in light of the fact that the distributions after stochastic and standard gauge fixing agree at sufficiently small Δ^2, and even at intermediate Δ^2 for specific choices of the stochastic overrelaxation parameter p related to the standard gauge fixing procedure, see the preceding sec. 4.3.2.2.

For the numerical experiments with return cycles in four space-time dimensions, we have chosen as initial configuration the constant gauge field (see [312, 313])

$$\forall x : \; A^a_\mu(x) = \delta \cdot \delta_{\mu 3}\delta_{a3} \tag{4.17}$$

with a positive real parameter δ that measures the distance of this configuration from the origin of configuration space, where $\forall x, \mu : \; A_\mu(x) = 0$. The origin is in the first Gribov region Ω. For sufficiently large δ, the configuration (4.17) with a spatio-temporally constant gauge field is outside of Ω.[19]

In fig. 4.25, we compare return cycles starting from configurations of the form (4.17) at different values of δ. As δ is increased, a larger distance from the gauge fixing surface is reached during the return cycle. (The property of the results at large values of δ to resemble those at small ones may be due to the periodicity of the link variables in δ.) In addition, we observe that the return to the first Gribov region occurs slower for smaller step sizes (not shown in a figure), as expected. Moreover, it is evident from fig. 4.25 that the Langevin and the random walk algorithm behave in similar ways also in this respect.

4.3.3 Further observations

In this section, we collect a few further results obtained from stochastic gauge fixing, and remarks pertaining to it.

[19] We can make some further statements even without explicitly calculating the FPO eigenvalues, as we have done for fig. 4.24b. This can be done by calculating $\langle v, \mathbb{M}v\rangle$ for random vectors $v \in \mathbb{R}^{3V}$. For the configuration

$$\forall x, \mu : \; A^a_\mu(x) = \delta \cdot \delta_{a3}, \tag{4.18}$$

we observe a change of $\langle v, \mathbb{M}v\rangle$ from 1 to 0 and back at $\delta = (n + 1/2)\pi$, $n \in \mathbb{Z}$. – Starting from (4.18) with e. g. $\delta = 2$, we observe that $\langle v, \mathbb{M}v\rangle$ changes from 0 to 1 just when Δ^2 drops again after its peak, indicating a return to the Gribov region, where the discretized FPO $\mathbb{M}$ is positive-definite.

4.3.3.1 Details on precise gauge fixing

At fixed step size ε resp. η and fixed gauge fixing parameter α, the distance Δ^2 from the gauge fixing surface (eq. (2.85)) fluctuates around a value which is typically small, but not small enough for the gauge to be fixed to sufficient accuracy. One may ask how 'sufficient accuracy' is defined here. A necessary condition for sufficient accuracy is, of course, that the propagators do not change significantly when further decreasing the value of Δ^2.

A smaller gauge parameter α prima facie means that the gauge fixing condition is better implemented, as we have already seen for the toy model in ch. 3. But de facto, Δ^2 cannot be brought to an arbitrarily small value by choosing a very small α. This is because at a fixed step size, Δ^2 does not behave monotonically as a function of α, see fig. 4.26. Therefore, the statement that the limiting case $\alpha = 0$ corresponds to Landau gauge, see e. g. [84, 320], must be qualified from a numerical point of view (as stated in fn. 1).

This behavior may stem from an 'overshooting' effect. By this, we refer to the fact that at small distances and overly small α, the gauge fixing force becomes so large compared to the distance from the gauge fixing surface that, intuitively spoken, the motion induced by this force 'overshoots' the gauge fixing surface. Some numerical evidence for this explanation is provided in fig. 4.27. This figure is a histogram of the size of single gauge transformations during stochastic gauge fixing. This size is measured by the parameter b, which is essentially the size of the parameters in a gauge transformation matrix (see eq. (4.16))

$$\Omega = \exp(i\vec{b}\cdot\vec{\sigma}) = \cos|\vec{b}| + i\sin\vec{b}\frac{\vec{b}}{|\vec{b}|}\cdot\vec{\sigma}, \tag{4.19}$$

with[20]

$$b^a = -\frac{\beta\varepsilon}{\alpha}\sum_{\mu=0}^{2d-1} u_\mu^a(x), \tag{4.20}$$

sc. $b := |\vec{b}|$. Note that '$\mu + d$' denotes here the negative $\hat{\mu}$-direction. The quantity b is a measure of the size of the gauge transformation; it suddenly changes close to the value of α below which Δ^2 becomes large (see fig. 4.27).

As a side note, if the Langevin equation is utilized, α enters via the ratio α/ε. Thus, in this case, lowering α can be balanced by simultaneously lowering ε. The random walk step size η, on the other hand, does not enter via such a combination. However, ε cannot be lowered arbitrarily, as this would render the number of updating sweeps required for subsequent 'measurements' to be uncorrelated so large that simulations would become utterly impractical.

4.3.3.2 Comparison to the heat-bath algorithm

One might ask a simple question about stochastic gauge fixing, sc. why the Langevin equation is employed at all. Instead, one could a priori suggest to consider local interchanges of gauge fixing steps with *standard* dynamic updates of the link variables, which likewise produce ergodic ensembles of $SU(2)$ link configurations. We have also implemented this hypothetical, speculative suggestion. We find it to be unsuccessful. While the average

[20] The factor $(2N_c)^{-1}$ from eq. (4.16) is here omitted. Except for this normalization, (4.16) and (4.19) are equivalent, since $u^b_{\mu+d}(x) = -u^b_\mu(x-\hat{\mu})$ (due to (2.59) and the Cayley–Klein parametrization (2.72)).

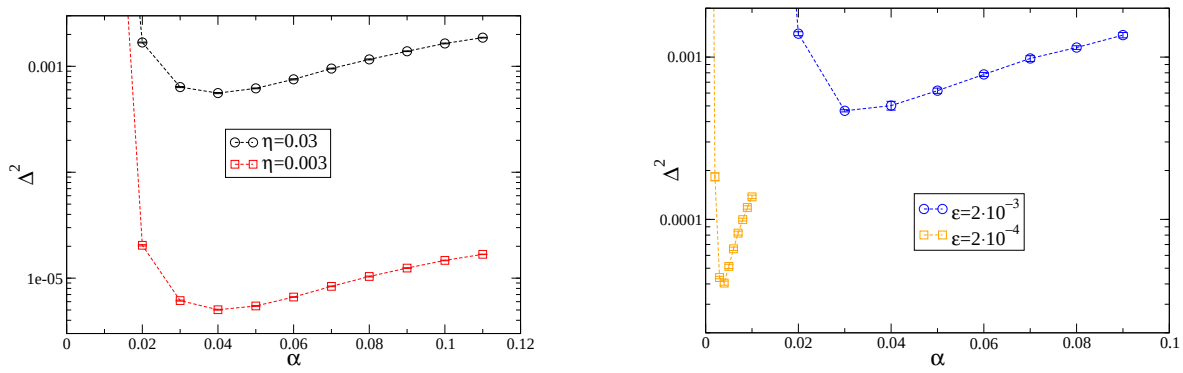

Figure 4.26: Illustration of the dependence of Δ^2 (understood here as the statistical average over independent configurations) on the gauge fixing parameter α. *Left (a):* On a 48^2 lattice at $\beta = 10$ for two different random walk step sizes. *Right (b):* On a 8^4 lattice at $\beta = 2.2$ for two different Langevin step sizes.

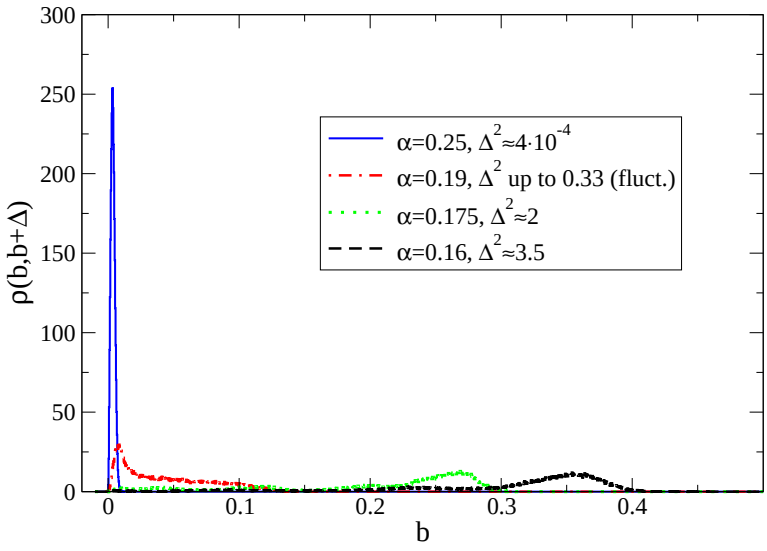

Figure 4.27: Histogram of the size of the gauge transformations (quantified by b) above and below the 'critical' α below which Δ^2 gets large. See eq. (4.20) in the main text for the precise definition of b.

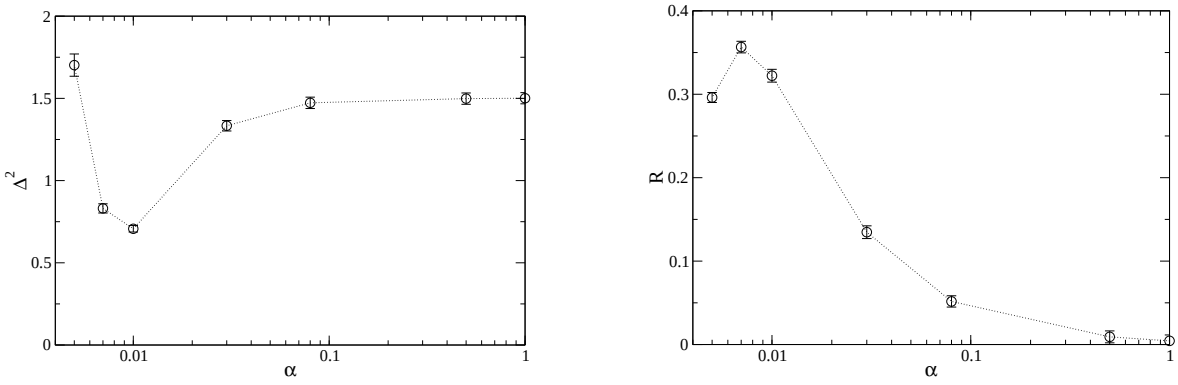

Figure 4.28: An analysis of a heat-bath procedure including gauge fixing at different values of the gauge fixing parameter α, superficially mimicking the stochastic gauge fixing procedure (as explained in the main text), but with a very different outcome. Lattice volume 6^4, $\beta = 2.2$. *Left (a):* Gauge fixing accuracy Δ^2. *Right (b):* Gauge fixing functional R.

value of Δ^2 does exhibit at least a mild dependence on the gauge fixing parameter α also in this case,[21] Δ^2 does not become smaller than $\mathcal{O}(1)$ for any value of α, see fig. 4.28a. This is in stark contrast to stochastic gauge fixing (fig. 4.26). Fig. 4.28b shows in addition that R is far below the values obtained from accurate gauge fixing, which is around 0.828 in four dimensions at $\beta = 2.2$, see p. 76. (The difference between the values of R resulting from standard and from improved gauge fixing is typically of order $\mathcal{O}\left(10^{-4}\right)$.)

4.3.3.3 Alternative: Gauge fixing included in the force

Idea and implementation. It may seem natural to implement gauge fixing along the way sketched in sec. 4.2.2, i. e., with eq. (4.16) (and (2.83)). But it is not a unique choice to do so. In fact, we have also investigated a possible different lattice implementation, where Zwanziger's gauge fixing term $D^{ac}_{\mu} v^c$, see eqs. (4.2) and (4.3), is directly included in the force term F, cp. eqs. (4.5) and (4.7).

To this end, a lattice version of the covariant derivative must be specified. Since it is defined on a lattice site, as opposed to on a link, it needs to transform as

$$D_\mu \phi(x) \to \Omega(x) D_\mu \phi(x) \tag{4.21}$$

under a lattice gauge transformation $\{\Omega(x)|\}$ with independent matrices from the gauge group for each lattice site x. A definition that satisfies (4.21) is

$$D_\mu \phi(x) = U_\mu(x) \phi(x + \hat{\mu}) - \phi(x). \tag{4.22}$$

That it does so follows from $\phi(x) \to \Omega(x)\phi(x)$ under a gauge transformation together with the gauge transformation law (2.64) for link variables. Alternatively,

$$D_\mu(x) \phi(x) = \phi(x) - U^\dagger_\mu(x - \hat{\mu}) \phi(x - \hat{\mu}) \tag{4.23}$$

[21] By 'mild dependence', we mean here, for instance, a variation by a factor of around 3.

is possible as well (see furthermore e. g. [17]). In our application, i. e., when using the covariant derivative in the gauge fixing force, D_μ acts on v, see eq. (4.3). Using the quaternionic parametrization (2.72) of $SU(2)$ elements, we find, with the first definition,

$$(D_\mu v(x))^a = u_0(x)v^a(x+\hat{\mu}) - v^a(x) - \varepsilon^{abc}u_\mu^b(x)v^c(x+\hat{\mu}). \tag{4.24}$$

Results. The results of some numerical tests are not encouraging. With different lattice definitions of the covariant derivative, the procedure fails a very simple test, as the value of the plaquette variable $\langle U_P \rangle$, eq. (2.71), significantly deviates from its true value. We have performed systematic tests for various values of β, from close to zero up to $\beta = 5$, always comparing with results of the heat-bath algorithm (app. B.1.4) which we have produced at many values of β. As an example, in four-dimensional pure $SU(2)$ Yang–Mills theory at $\beta = 1$, applying the pure gauge fixing force to thermalized configurations yields $\langle U_P \rangle \approx 0.19$, while the true value is $\langle U_P \rangle \approx 0.244$.

It is not obvious how such large an effect may be explained, but the most natural reasoning is that an update of the proposed form deviates systematically from a gauge transformation and is thus not tangential to a gauge orbit. Moreover, we observe this effect not only for different lattice definitions of the covariant derivative, but also both for the Langevin and the random walk procedure.

As noted, not even with a pure gauge fixing force is the plaquette value correct. While this may point toward an error in the implementation, the generality of the erroneous results appears to indicate that there is rather a problem of principle. This might stem from the fact that an update of the proposed form deviates systematically from a gauge transformation and is thus not tangential to a gauge orbit. We have currently no explanation, however, for why these deviations occurring in single steps should add up to such a huge, apparently uniform effect on the gauge-invariant plaquette variable. Naïvely, one would rather expect them to cancel on average. In addition, it is puzzling that according to our findings, the deviations hardly depend on the Langevin step size. – In any case, since a working implementation exists which faces no such problems, we have not traced this problem to its very roots and have discarded this algorithm.

4.4 Summary

We have calculated the ghost and gluon propagators with stochastic gauge fixing in two, three and four dimensions. In two dimensions, the results are consistent with the scaling solution. In three and four dimensions, scaling is violated, and the infrared behavior of the propagators is best described as being of decoupling type. These outcomes of studies with an alternative gauge fixing algorithm corroborates the standard lattice scenario.

At the same time, we have found that stochastic gauge fixing does sample the configuration space differently from standard gauge fixing – as long as the gauge is fixed only to intermediate accuracy, and except for specific overrelaxation parameters. Very close to the gauge fixing surface, this difference disappears. Still, this partial difference underlines that stochastic gauge fixing is an algorithm that shows properties distinct from standard gauge fixing. Hence, our main results of this chapter, those for the propagators in various dimensions, carry nontrivial information beyond previous results and complement the latter in an illuminating way.

A possible explanation of the fact that lattice studies do not yield the scaling solution in three and four dimensions is the presence of a gauge fixing problem. This might be understood in the sense of a bias in the numerical gauge fixing procedure that favors certain regions of configuration space and disfavors others, which could lead to a systematic difference between gauge fixing on the lattice and in the continuum. From this perspective, one can conclude from the results of this chapter that the gauge fixing problem may be more general than is often assumed. We explore this line of thought further in particular in ch. 6, and also in ch. 7.

CHAPTER 5

STRONG-COUPLING LIMIT

We continue the investigations of the ghost and gluon propagators of pure $SU(2)$ Yang–Mills theory, but we turn now to the strong-coupling limit $\beta = 0$ and use standard gauge fixing methods. The main results are again those for the gluon and ghost propagators (sec. 5.2.2), now in two and three dimensions, which we examine in the context of previously obtained results in four dimensions. In the limit $\beta = 0$, where the lattice spacing is infinitely large, the behavior at all lattice momenta can shed light on the type of infrared solution. We explicitly discuss the effective running coupling (sec. 5.2.3) calculated from the propagators and also some discretization effects (sec. 5.2.4).

5.1 Introduction

5.1.1 Motivation

The strong-coupling limit of lattice Yang–Mills theory serves as a valuable alternative to standard lattice calculations at finite coupling. This holds especially if one is concerned with the infrared behavior of correlation functions. The reason is that no absolute scale exists in the strong-coupling limit, where $\beta \equiv 2N_c/g^2$ (eq. (2.68)) vanishes and the lattice spacing a, which grows with decreasing lattice coupling β (see sec. 2.3.1.5), is infinitely large. This can be seen from a strong-coupling expansion of the Wilson loop, which yields for the Wilson loop along a quadratic contour $\mathcal{C}$

$$\langle W_{\mathcal{C}}[U] \rangle \xrightarrow[\beta \to 0]{} \left(\frac{\beta}{N_c^2} \right)^{\hat{A}}, \tag{5.1}$$

where $\hat{A} = \hat{R} \cdot \hat{T}$ is the area enclosed by $\mathcal{C}$ (dimensionless, i. e., in lattice units). By way of eq. (2.104), one arrives at

$$\sigma a^2 \approx -\ln(\beta/4) \tag{5.2}$$

for very small β [39]. Hence, formally '$a \to \infty$',[1] and all momenta q and masses are infinitely small relative to the physical scale of the theory. As a consequence of this fact, the infrared behavior of momentum-dependent quantities, like the ghost and gluon propagator, should be visible already at large lattice momenta aq. This has the valuable implication that more data are at our disposal, allowing to determine a possible power-law behavior with greatly improved accuracy. This benefit comes, naturally, at a cost. Here, the considerable cost consists in strong systematic effects of taking this unphysical limit, which are difficult to assess quantitatively.

Previous investigations in four dimensions have resulted in evidence for a possible scaling behavior at large aq [295, 221, 296]. In particular, the gluon propagator has been found to exhibit a power-law behavior in this region. The value of the ghost power-law exponent from the gluon data, see eq. (2.34), was identified as $\kappa_Z \approx 0.55$. This agrees rather well with the prediction $\kappa \approx 0.595$ extracted from functional continuum methods [84, 54], see sec. 2.2.2 and sec. 2.4 for the latter. While an accurate quantitative extraction of κ from the ghost data proved to be considerably harder, it was concluded that the behavior of the ghost propagator at large aq could be consistent with the one of the gluon [295, 221, 296]. In [345], data in three and four dimensions were interpreted in a different way, sc. they were utilized in order to argue in favor of decoupling-type solutions in both cases. An early strong-coupling investigation can be found in [265].

We present results in two and three dimensions for the ghost and gluon propagator. We have been able to obtain a much improved statistical accuracy compared to e. g. [345]. In addition, we study possible discretization effects. The impact of the Gribov ambiguity on the propagators in the strong-coupling limit is presented in a separate chapter, ch. 6.

5.1.2 Method

5.1.2.1 Trivial dynamics

Going to the strong-coupling limit $g^2 \to \infty$ of pure Yang–Mills theory on the lattice amounts to setting $\beta = 0$, see eq. (2.68) for the definition of β. This implies that the influence of the action on the probability distribution of configurations disappears completely. Instead, the configurations are randomly determined simply according to the Haar measure, cp. app. B.1.4.2. Any initial 'thermalization' sweeps and any 'dummy' sweeps between gauge-fixed measurements thereby become obsolete, except for a single one in each case. However, this does not greatly reduce the numerical effort, which is anyway mostly due to the gauge fixing and especially to the accurate ghost propagator calculation with the plane-wave source, see sec. 2.3.3.2 and app. B.3.

The random generation of link variables whose distribution obeys the Haar measure is straightforward. The procedure is a special case of the heat-bath algorithm, app. B.1.4, of course in a simplified form due to $\beta = 0$.

5.1.2.2 Gauge fixing

At $\beta = 0$, there is no motivation to use stochastic quantization for gauge fixing. This is because the dynamics (sec. 5.1.2.1) does not at all depend on the previous step, i. e., subse-

[1] An alternative choice of a (finite, though large) is proposed in [344] and discussed in [345], see in particular also the reply to [345] in [221].

quent configurations are entirely uncorrelated by default. (In addition, at finite coupling, it generally yields similar results as standard gauge fixing, as shown in ch. 4.) Hence, we fix the gauge here by a standard method.

We have used the stochastic overrelaxation algorithm [346], see also e. g. [347]. A brief explanation of this method is given in app. B.2.1.2. The overrelaxation parameter p is adapted for fast convergence toward $\Delta^2 < 10^{-15}$, the optimal value depending on the lattice size and dimensionality. In practice, $p \gtrsim 0.99$ for large linear lattice extensions. This means that on such lattices, suboptimal updates are deliberately chosen in more than 99% of updating steps. See again app. B.2.1.2 for more details and examples.

We emphasize that stochastic overrelaxation bears no relation to stochastic gauge fixing, despite its name; rather, it is a standard method.

5.2 Results

5.2.1 Preliminaries

We have determined the gluon and ghost propagators in two and three dimensions on various lattice sizes. From these, we have calculated the running coupling (see sec. 2.2.2.5) in order to compare it with predictions from functional continuum methods. For such a quantitative comparison, the propagators need to be normalized correctly, see sec. 2.3.3.[2] We also compare our findings with previously obtained results in four dimensions.

5.2.1.1 Bounds on the propagators

In addition to calculating the propagators, we have implemented the definition of upper and lower bounds on the gluon propagator as put forward in [275],

$$V\langle M(0)\rangle^2 \leq D_{\mathrm{gl}}(q=0) \leq Vd(N_c^2-1)\langle M(0)^2\rangle \tag{5.3}$$

with the lattice volume d, the numbers d of dimensions and N_c of colors and

$$M(0) \equiv \frac{1}{d(N_c^2-1)} \sum_{\mu,b} \left| A_\mu^b(q=0) \right| = \frac{1}{d(N_c^2-1)} \sum_{\mu,b} \left| \frac{1}{V} \sum_x A_\mu^b(x) \right| . \tag{5.4}$$

Employing these bounds in addition to the propagator has been compared to considering the magnetization of a spin system in addition to its susceptibility [275]. The bounds have been taken to confirm the finite volume behavior of the gluon propagator at zero momentum, in particular that $D_{\mathrm{gl}}(0)$ vanishes in the limit $V \to \infty$ in two dimensions and assumes a non-zero value in this limit in three and four dimensions [275].

Moreover, bounds on the ghost propagator have been proposed [293]. But for their exact calculation, the lowest eigenvalue of the Faddeev–Popov matrix is needed, whose determination is expensive on large lattices.[3] We do not calculate the bounds on the ghost propagator, since we do not pursue an explicit finite volume study of the ghost propagator at small momenta.

[2] Naturally, a multiplicative renormalization at a momentum scale μ, see sec. 2.3.4.2, is not feasible in the strong-coupling limit, where all momenta are formally infinitely large in physical units.

[3] In fact, the bounds on the ghost propagator have been calculated only approximately in [293], by virtue of the eigenvalues determined approximately e. g. in [115]. We explain a method for approximate determination of eigenvalues in app. B.3.3, where we also show a few results.

5.2.1.2 Local exponents

The behavior of the ghost and gluon propagator at all momenta may be compared by considering local power-law exponents. This is advantageous as it permits an easily accessible representation of whether the behavior of both of them at any lattice momentum is consistent with the scaling relation (2.28), and thus with a scaling behavior. In the strong-coupling limit, such a behavior is prima facie expected to be visible also at large lattice momenta in case it is realized at all.

We calculate the ghost power-law exponent κ_Z from the gluon data, see eq. (2.34), from adjacent or at least nearby momenta q_i and $q_{i+\delta}$, where the index i simply counts the norms of the momenta surviving the cylinder cut (see sec. 2.3.3.3) ordered by size. The increment δ is chosen as small as possible to obtain a clear picture.[4] In an analogous manner, the power-law exponent κ is determined from the ghost data.

To be specific, the local exponents are extracted from the ghost resp. gluon propagator via

$$(\kappa_Z)_{\text{local}} = \frac{1}{4}\left[\frac{\log D_{\text{gl}}(q_{i+\delta}) - \log D_{\text{gl}}(q_i)}{\log q_{i+\delta} - \log q_i} + (d-2)\right], \tag{5.5a}$$

$$(\kappa)_{\text{local}} = \frac{1}{2}\left[\frac{\log D_{\text{gh}}(q_i) - \log D_{\text{gh}}(q_{i+\delta})}{\log q_{i+\delta} - \log q_i} - 2\right]. \tag{5.5b}$$

These equations are justified simply by the definition of the infrared exponents, eq. (2.27). They are valid for all numbers of dimensions treated here. For the scaling relation (2.28) to hold, $\kappa_Z = \kappa$ is required. Cp. also the discussion around eq. (2.34). A very similar calculation has been done in [345], but our results are much more accurate and allow for definite conclusions in cases where those of [345] do not, as we show in the subsequent sections 5.2.2.1 and 5.2.2.2.

5.2.2 Gluon and ghost propagators

5.2.2.1 Two dimensions

We have emphasized some specific properties of two-dimensional Yang–Mills theory already in sec. 4.3.1.1 and sec. 2.3.4. The received view (cp. sec. 2.4) is that in two dimensions, the ghost and gluon propagator jointly confirm the scaling solution, as explicitly found at finite coupling [116, 275] and with stochastic gauge fixing, see our results in ch. 4 (sec. 4.3.1.1), published in [24]. See [84, 54, 293, 190] for further examples of such expectations. Here, we present, to our knowledge, the first investigation of the behavior of the ghost and gluon propagator at strong coupling in two dimensions.

Gluon propagator. The gluon propagator is shown in fig. 5.1 for different lattice sizes. Power-law fits, following eqs. (2.27a) and (2.34), yield a value of $\kappa_Z \approx 0.19$ at intermediate lattice momenta aq around 1, which resembles the scaling prediction of 0.2. At large momenta aq, the result of the fit tends to decrease toward a value of ≈ 0.16.

The finite volume behavior of the gluon propagator at zero momentum is consistent with $D_{\text{gl}}(0) = 0$ in the $V \to \infty$ limit, as shown in fig. 5.2 (the logarithmic plot, fig. 5.2b,

[4] Of course, δ is unrelated to the variable of the same name used in the preceding chapter, eq. (4.17).

makes the exponential decrease even clearer). As $D_{\mathrm{gl}}(0)$ continues to decrease with the inverse linear lattice extension, only a lower bound on a possible mass at zero momentum can be given. For completeness, both plots in fig. 5.2 include the bounds on the gluon propagator as defined in [275] and explained in sec. 5.2.1. Only the propagator data possess immediate relevance for the present purposes. The bounds are very strongly correlated with $D_{\mathrm{gl}}(0)$, see fig. 5.7 below for an example on a large lattice in three dimensions. This might be taken to mean that they do not represent essential information that is not already contained in the gluon propagator data.

In summary, the gluon propagator results at $\beta = 0$ in two dimensions appear to be largely consistent with the scaling solution, like previously concluded at finite coupling [116, 275]. While, strictly speaking, the data deviate from an exactly uniform scaling behavior, this deviation is not large. We turn now to the ghost propagator, which will result in a much less unambiguous picture.

Ghost propagator. In calculating the ghost propagator, we generally employ the plane-wave source method for greatly improved statistical accuracy, see app. B.3. We do so also in three dimensions, sec. 5.2.2.2, in contrast to [345]. (For contrast and illustration, we intersperse the following presentation also with some results obtained from a point source.) This choice causes this part of the simulation to consume the bulk of the computer time, but the precise data are worth the effort. The dressing function thus obtained is contrasted in fig. 5.3 with a result using a point source. The former result is much more accurate, even though only 76 independent configurations have been used, in contrast to approx. $37,000$ in the latter case. From the plane-wave source ghost propagator data, we extract a value of around $\kappa \approx 0.37$ with a power-law fit according to eq. (2.27b) at intermediate and large momenta.[5] This is significantly larger than the expected value of 0.2 [84, 54, 116] and than the corresponding value κ_Z from the gluon data found by us in this momentum range (sc. between 0.16 and 0.19, cp. the preceding paragraph). Moreover, κ grows as larger lattice momenta are included in the fit, or smaller ones excluded from it. The fit to the point source data, obeying the criteria stated in fn. 5, extends over a larger momentum range due to the sizable fluctuations in the point source data.

Comparison of local exponents. The growth of κ as a function of the lattice momentum can be illustrated in a useful way by the locally extracted, 'effective' exponent (sec. 5.2.1.2). Here, the advantage of the plane-wave source method becomes even more apparent. The results for the local exponents, as defined in eq. (5.5), are shown in fig. 5.4a for a plane-wave source resp. fig. 5.4b for a point source, in both cases comparing the local ghost exponent κ from the ghost data with its counterpart obtained from the gluon data, sc. κ_Z. For a point source (which was also used in ref. [345]), the ghost data are compatible with a wide range of interpretations due to the large error bars, stemming from the very local procedure and the 'wiggles' in the ghost propagator at large aq due to the point source method. But the plane-wave source result is unambiguous and surprising. As visible from fig. 5.4a, the local κ increases monotonically as a function of momentum, except for the smallest values of aq. There is only a very narrow region where $\kappa(aq)$ and $\kappa_Z(aq)$ intersect within error bars,

[5] We impose the criterion on this fit that it (i) extends up to the largest lattice momenta and (ii) starts at the smallest momentum that still allows for $\chi^2/\mathsf{ndf} < 1$.

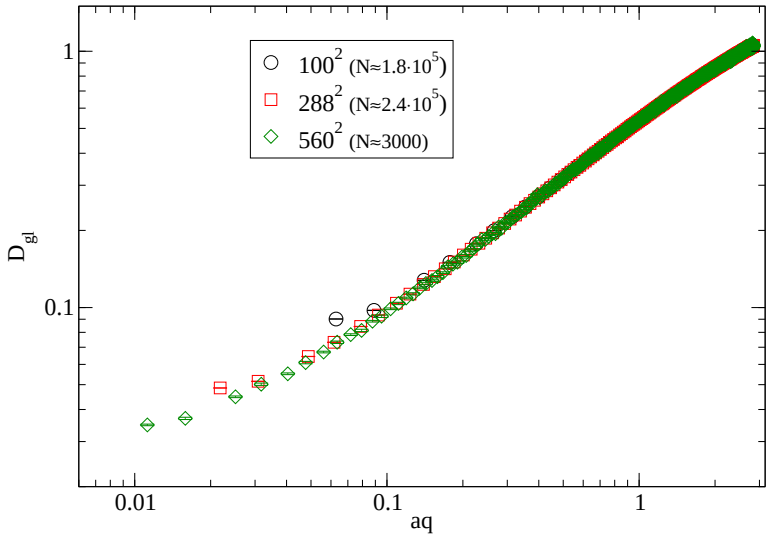

Figure 5.1: Gluon propagator in two dimensions at $\beta = 0$ for different lattice sizes. The numbers N of independent configurations are given in the legend.

essentially just a point. Thus, no stable scaling region can be identified. If anywhere, the local ghost exponent is approximately constant in a region around relatively small lattice momenta $aq \approx 0.1$. In this region, its value is significantly below the local gluon exponent. – The statistical errors in fig. 5.4, as well as those in fig. 5.9, have been estimated with a bootstrap analysis [348], see app. B.1.5.

The local exponent κ_Z from the gluon data shows, strictly speaking, no stable scaling region either, but it comes closer to such a behavior. At intermediate momenta, the value of κ_Z is not far from the scaling prediction [54]. But for the scaling scenario to hold, κ_Z must equal κ. This is unambiguously ruled out by the data at almost all momenta, see again fig. 5.4. The intersection point of κ and κ_Z is necessarily at that lattice momentum at which the effective running coupling assumes an extremum, see sec. 5.2.3.

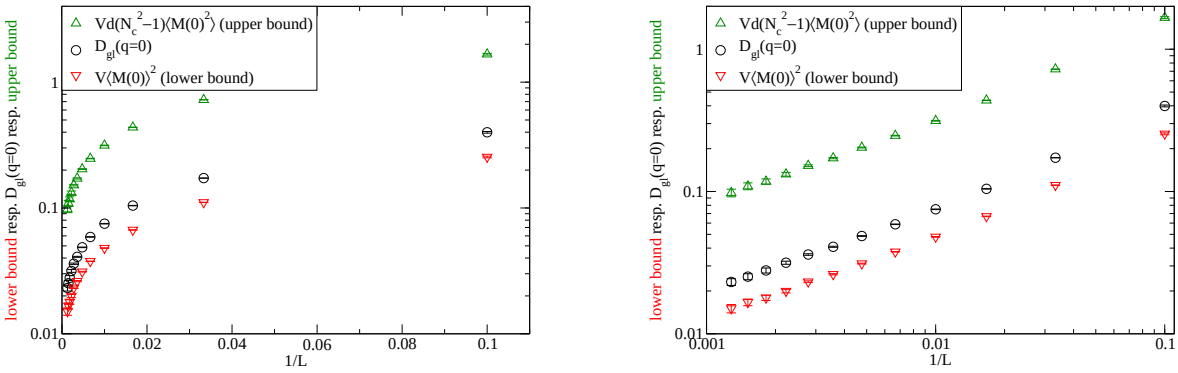

Figure 5.2: Finite volume behavior of the gluon propagator and the bounds [275] (eqs. (5.3), (5.4)) at vanishing momentum in the strong-coupling limit in two dimensions. The linear lattice extension L is given in lattice units. *Left (a):* Linear plot. *Right (b):* Same data in a logarithmic plot.

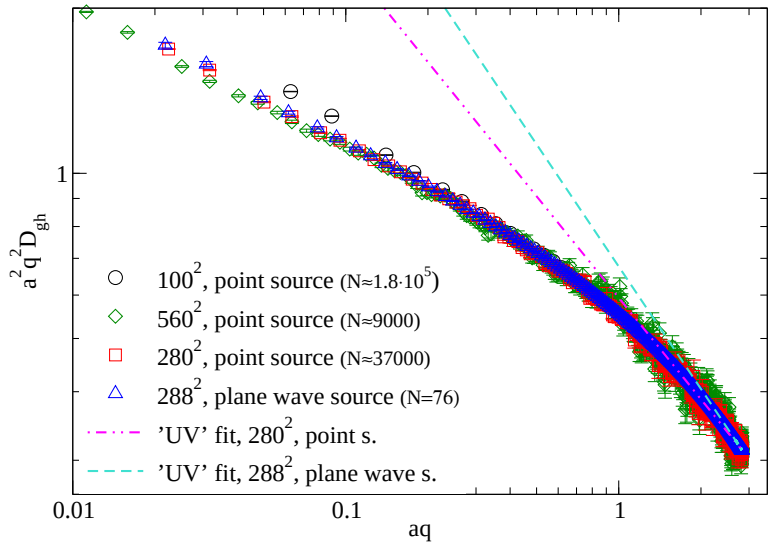

Figure 5.3: Ghost dressing function in two dimensions in the strong-coupling limit, contrasting two different methods for inverting the Faddeev–Popov operator. The broken line corresponds to the local power-law exponent $\kappa \approx 0.37$ at large aq, illustrating the rise of the local exponent toward large aq. Numbers N of independent configurations are given in the legend.

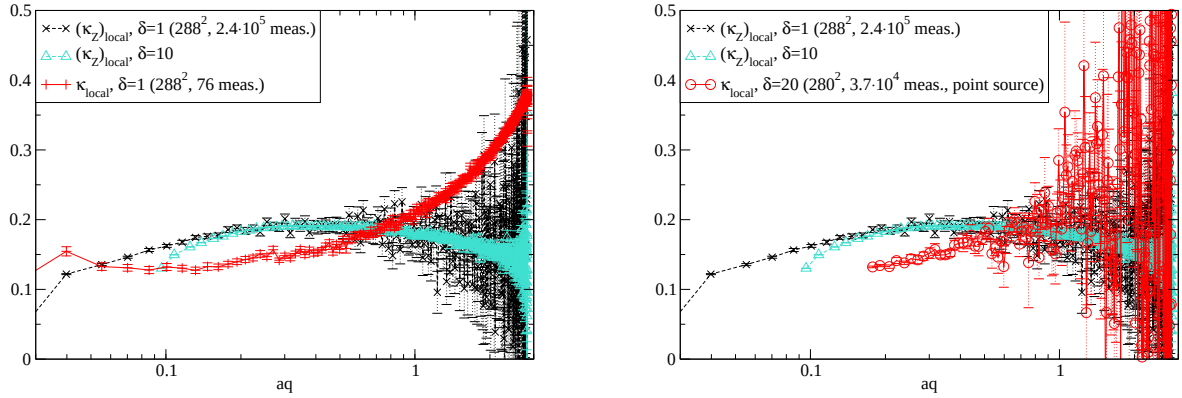

Figure 5.4: Local ghost exponent from the ghost data (κ) resp. from the gluon data (κ_Z) in two dimensions. *Left (a):* Plane-wave source method. *Right (b):* Point source method. Note the far larger number of measurements and the far larger value of δ (see eq. (5.5)) for the point source method.

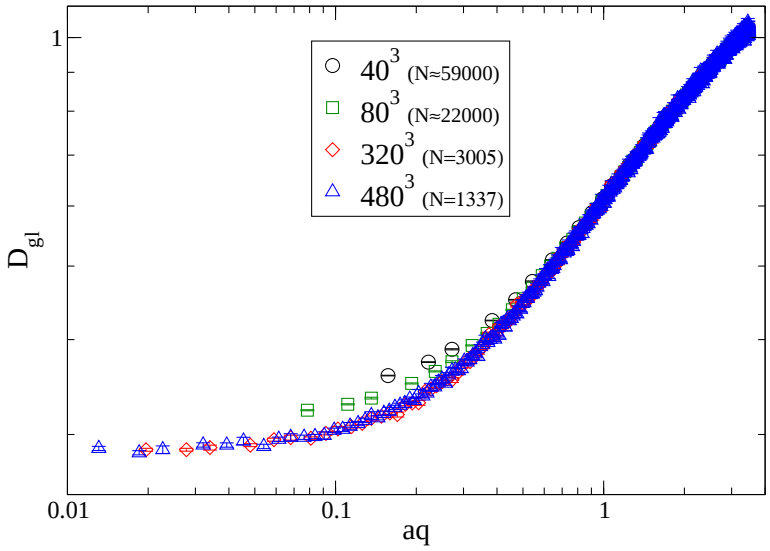

Figure 5.5: Gluon propagator in three dimensions for various lattice sizes. Numbers N of independent configurations given in the legend.

5.2.2.2 Three dimensions

Gluon propagator and local exponent. We start our discussion of the results for three-dimensional pure Yang–Mills theory at $\beta = 0$ by presenting the results for the gluon propagator at different lattice volumes, fig. 5.5. The gluon propagator shows a decoupling branch at small lattice momenta aq and a behavior resembling a scaling branch at large aq (note the logarithmic scales, in which a power-law behavior is represented by a straight line). From fig. 5.5, it is already evident that the decoupling branch shows a significant finite volume effect, but also that there is a qualitative difference to the two-dimensional case. Namely, the finite volume effect is not strong enough to yield a vanishing gluon propagator at zero momentum in the $V \to \infty$ limit. This is confirmed by an analysis of $D_{\mathrm{gl}}(0)$ vs. the inverse linear lattice extension, fig. 5.6. The statement '$0 < D_{\mathrm{gl}}(0) < \infty$' at $\beta = 0$ was already inferred in [345] from significantly smaller lattices (up to 100^3, while our largest lattice has the volume 480^3). It is consistent with results at finite coupling, cp. sec. 4.3.1.2.

A technical note: The data on the largest lattices, e. g. 480^3 and 320^3, have been produced with a fully parallelized version of the code, due to the large memory requirements of such volumes. This version includes parallel routines for heat-bath thermalization, which are obsolete at $\beta = 0$ but have been used for some other simulations,[6] as well as for gauge fixing. See app. B.4 for some details concerning the parallelization procedure.

The locally extracted exponent κ_Z from the gluon data in three dimensions behaves qualitatively similar to its counterpart in the two-dimensional case, see fig. 5.9 (and cp. with the corresponding data for $d = 2$ in fig. 5.4). Quantitatively, both the local analysis and more extended power-law fits[7] at intermediate and large aq show that the branch of the

[6] See, e. g., figs. 4.7 (2560^2 lattice at $\beta = 10$) and 7.6 (160^4 lattice at $\beta = 2.2$).

[7] We have performed power law fits to the gluon data on different volumes, extending up to the largest momenta and choosing as a lower limit a lattice momentum such that $\chi^2/\mathrm{ndf} \lesssim 1$. They yield $\kappa_Z \approx 0.34$. This lower limit depends on the lattice size and also mildly on the statistics.

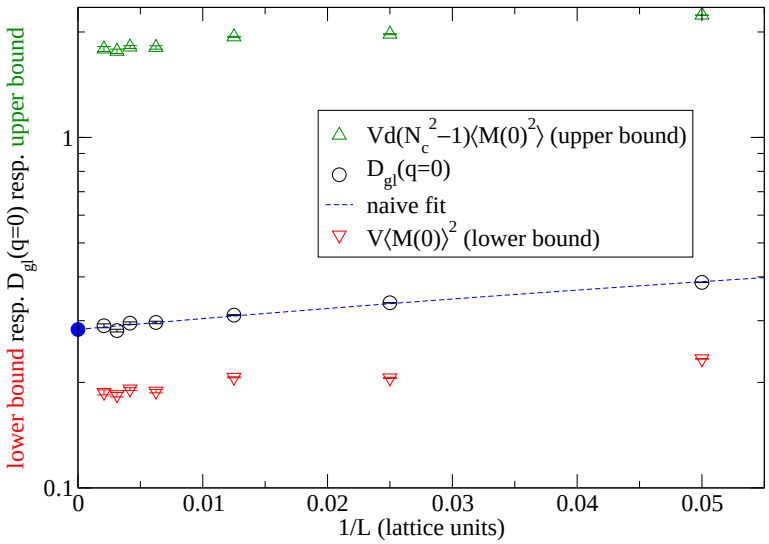

Figure 5.6: Finite volume analysis of the gluon propagator at vanishing momentum in three dimensions in the strong-coupling limit, including the corresponding bounds and a naïve linear fit to $D_{\mathrm{gl}}(0)$ for all $1/L$. Note the linear scale on the abscissa, a crucial difference compared to the depiction of the $d = 2$-data in fig. 5.2b, which otherwise appears similar at first glance.

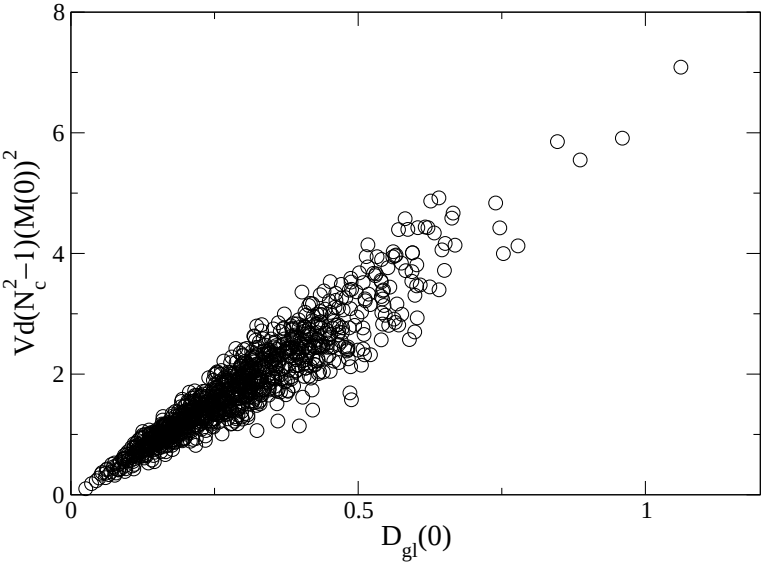

Figure 5.7: Scatter plot of the gluon propagator at vanishing momentum and its upper bound from 1067 measurements on a 480^3 lattice. The correlation coefficient is $\rho \approx 0.94$, obviously describing a very strong correlation.

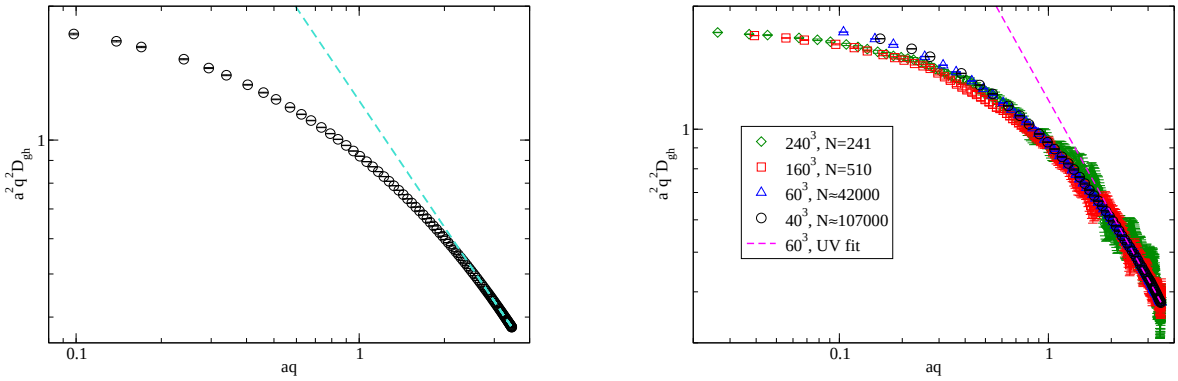

Figure 5.8: Ghost dressing function in the strong-coupling limit in three dimensions. *Left (a):* From the plane-wave source method, $V = 64^3$ ($N = 57$ configurations). Included in the plot is a power-law fit at large aq (broken line), obeying the condition $\chi^2/\mathsf{ndf} \leq 1$. *Right (b):* Same quantity from the point source method, for different lattice volumes.

gluon propagator at large aq is consistent with an exponent κ_Z close to the value predicted by functional continuum methods, i. e., $\kappa_Z \approx 0.35$ found by us compared to the prediction of 0.3976 [84, 54]. This value also agrees with the finding of the other strong-coupling study of three-dimensional pure Yang–Mills theory, sc. [345].

Ghost propagator and local exponent. Fig. 5.8a shows the ghost dressing function and the corresponding power-law fit to the maximal set of largest momenta with the condition that $\chi^2/\mathsf{ndf} \leq 1$. It is obtained from a plane-wave source with only 60 measurements. For comparison, fig. 5.8b shows results obtained with a point source, where much more measurements have been collected. Still, the results are considerably less accurate. In particular, heavy fluctuations at large momenta are noticeable. These are explained in ref. [115].

In fig. 5.9, the locally extracted κ from the data of fig. 5.8a is presented together with the data for κ_Z. Much like in two dimensions, κ_Z and κ (fig. 5.9) intersect only at a single point, entailing that scaling is in general violated. In this case, this is more in line with expectations based on previous lattice studies than in the two-dimensional case. Note that the intersection point, where scaling locally holds, is shifted toward larger aq compared to the two-dimensional case (fig. 5.4). This is apparent as well from the effective running coupling, see sec. 5.2.3.

The ghost propagator data in fig. 5.8b also exhibit a clear finite volume effect at small lattice momenta. On large volumes, the ghost dressing function is virtually flat at small momenta. At these momenta, the fluctuations induced by the point source method are much less notable than at large aq.

Moreover, we comment on a possible fit of the ghost propagator data, proposed in [64], that has been taken to support a decoupling behavior in [345]. It is of the form

$$f(x) = \frac{a - b\log(q^2 + c^2)}{q^2}, \tag{5.6}$$

where the parameter c can be interpreted as a gluon mass [64]. Note that at $\beta = 0$, we replace q by aq in eq. (5.6). We directly fit this function to the data for the ghost dressing

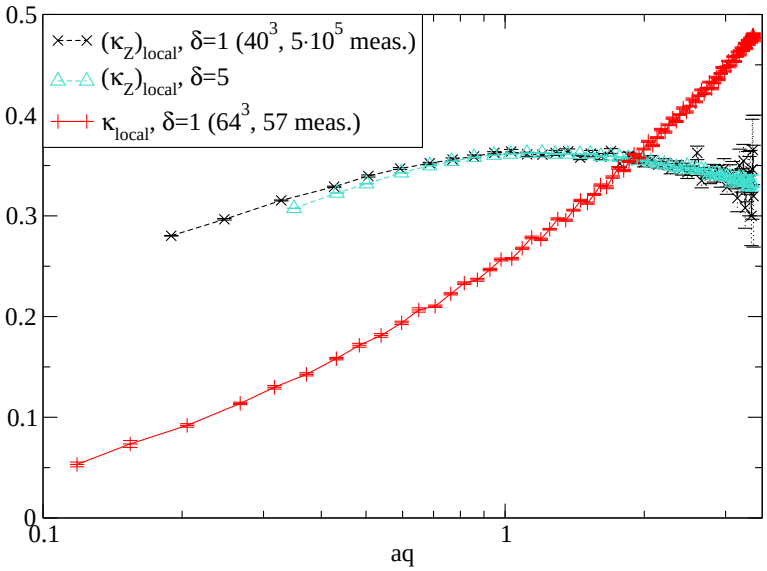

Figure 5.9: Local ghost exponent from the gluon data (κ_Z) and from the ghost data (κ) in three dimensions.

function, thus omitting q^2 in the denominator of eq. (5.6). In [345], this fit was found to be successful in the three- and four-dimensional case, sc. with $\chi^2/\mathsf{ndf} < 1$. Our data shown in fig. 5.8, however, have been produced with a different, more accurate method (fig. 5.8a) resp. with much more configurations (fig. 5.8b). We find that the fit function (5.6) is not in general adequate for the data. We mention three cases, summed up in the following table.

V	method	momenta	χ^2/ndf	a	b	c
240^3	point source	all aq	0.82	0.920(2)	0.215(1)	0.154(2)
60^3	point source	$aq \lesssim 0.72$ all aq	0.95 10.6	0.943(2) 0.936(1)	0.233(2) 0.229(1)	0.153(2) 0.143(3)
64^3	plane-wave source	$aq \lesssim 0.74$ $aq \lesssim 2$ all aq	0.51 11.7 1048	0.933(1) 0.927(1) 0.878(3)	0.240(2) 0.235(1) 0.201(1)	0.166(4) 0.143(7) $5 \cdot 10^{-4} \pm 8$

Note that the 240^3 data rest on 241 configurations, but the 60^3 data on around 42,000 ones, while for the plane-wave source used for the 64^3 lattice, already 60 measurements suffice for a high accuracy. We conclude that the adequacy of a fit of the data according to the function (5.6) worsens considerably as the statistical accuracy improves. Hence, in this respect, our data do not support the claim made in [345] that the strong-coupling data provide evidence for a decoupling solution. However, more generally, we agree that a finite volume analysis of the zero-momentum behavior of the gluon propagator also at $\beta = 0$ results in evidence for a decoupling solution in three and four dimensions, as we have demonstrated ourselves, e. g. figs. 5.5 and 5.6. Still, as we have argued, this is not the whole story.

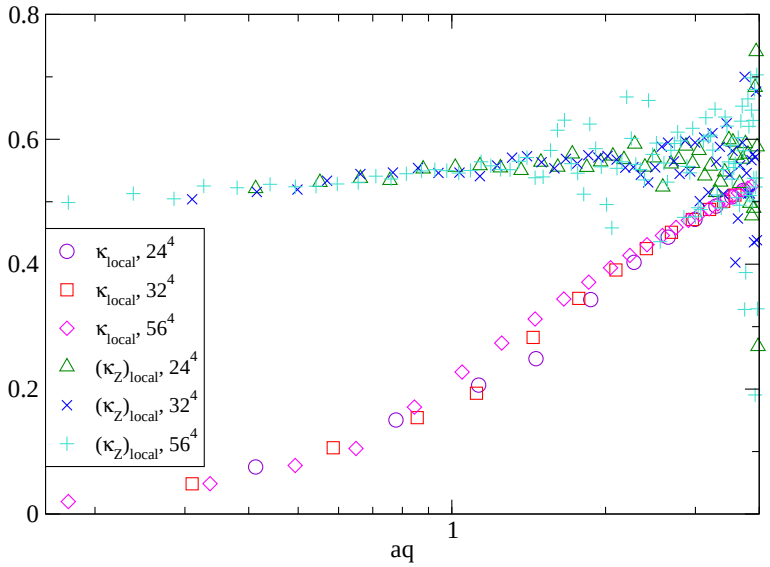

Figure 5.10: Local ghost exponent from gluon data (κ_Z) resp. ghost data (κ) in four dimensions. These data are courtesy of André Sternbeck and have been calculated from the configurations from which also the running coupling in four dimensions was calculated [295, 221, 296].

Upshot. First, the quantitative agreement of the values of κ and κ_Z with predictions from functional continuum methods for the scaling solution is rather good in the 'scaling window', but not at all lattice momenta. Second, the infinite volume limit of $D_{\rm gl}(q=0)$ is zero in two dimensions and non-zero in three-dimensions. Third, the qualitative resemblance of the two- and three-dimensional cases is a surprising finding. It is at odds with the standard lattice scenario according to which the scaling solution is seen in two dimensions, but a decoupling behavior in three and four dimensions, see sec. 2.4.

5.2.2.3 Comparison with four dimensions

For the strong-coupling limit in four dimensions, a thorough investigation has already been carried out in [295, 221, 296]. These data have been re-analyzed by André Sternbeck so as to extract the local exponents κ_Z and κ. Hence, it was not necessary for us to perform production runs to obtain strong-coupling data in four dimensions with our C++ code, although it would have been straightforward.

The results for the local exponents are shown in fig. 5.10.[8] An increase of κ toward large lattice momenta is again apparent from these data, like from the data in two and three dimensions presented in secs. 5.2.2.1 and 5.2.2.2. But unlike in the latter cases, the ghost exponent from the ghost data, κ, does not rise above its counterpart from the gluon data, κ_Z. In line with the observation made in sec. 5.2.2.2, the intersection point of κ_Z and κ in fig. 5.10 is shifted even further toward large lattice momenta, indeed toward the largest accessible lattice momenta. We comment on the relation to previous results for the running

[8] I thank André Sternbeck for sharing these results of his analysis. – Error bars on the data for the effective exponents in fig. 5.10 are absent since the Monte Carlo history of the measurements was not accessible at the time the analysis was performed. This history is required to obtain the error bars of the local exponents via the bootstrap algorithm, see app. B.1.5.

coupling in four dimensions in the following sec. 5.2.3, where we also perform this analysis to lower dimensions.

5.2.3 Effective running coupling in various dimensions

5.2.3.1 Four-dimensional case

The behavior of the local exponents in four dimensions, fig. 5.10, explained in sec. 5.2.2.3, is related to the behavior of the running coupling. The latter can be calculated from the Landau gauge correlation functions [349, 350, 351], sc. as the product of the gluon dressing function $q^2 D_{\mathrm{gl}}$ and the square of the ghost dressing function $q^2 D_{\mathrm{gh}}$ (see also sec. 2.2.2.5),

$$\begin{aligned} \alpha_S &= \frac{g^2}{4\pi} \left(q^2 D_{\mathrm{gl}}\right) \left(q^2 D_{\mathrm{gh}}\right)^2 \\ &= \frac{g^2}{4\pi} D_{\mathrm{gl}} D_{\mathrm{gh}}^2 q^6, \end{aligned} \tag{5.7}$$

Evidently, this is itself a gauge-dependent quantity. As found in [295, 221, 296], in four dimensions at $\beta = 0$ the running coupling approaches a maximum at the largest lattice momenta. We explain the connection between the local exponents and the running coupling below, eq. (5.12). Moreover, the value of α_S at its maximum agrees well with the value predicted from functional continuum methods [54]; to be specific, $(\alpha_S^{\mathrm{eff}})_{\mathrm{max}}$ has been found to equal approx. 90% of the prediction. We include the results for the running coupling in $d = 4$ from [221] in fig. 5.11.

5.2.3.2 General case

For $d \neq 4$, the coupling g^2 is not dimensionless, but has mass dimension $4 - d$ (cp. eq. (2.68)), and eq. (5.7) needs to be generalized in order to yield a dimensionless value. Thus, the effective running coupling is defined as

$$\alpha_S^{\mathrm{eff}} = \frac{g^2}{4\pi} D_{\mathrm{gl}} D_{\mathrm{gh}}^2 q^{d+2}. \tag{5.8}$$

This equation entails that the results for the effective running coupling, fig. 5.11, are a direct consequence of the gluon and ghost propagators. The additional kinematic factor q^{d-4} compared to (5.7) entails an infrared fixed point for α_S^{eff} in case of the scaling solution.

Expectations. In the strong-coupling limit,[9] this infrared fixed point should be seen also at large momenta if the scaling solution is realized. The precise values of α_S^{eff} at this fixed point in two, three and four dimensions, calculated with functional continuum methods (Dyson–Schwinger equations), depend on the ghost exponent κ (note that scaling is assumed here, so there is only one independent exponent) and on the number d of space-time dimensions. The values are, as derived in ref. [54],

$$\alpha_c^{(d)}(\kappa) = \frac{2^{d-2}\pi^{d/2-1}}{N_c I_G^{(d)}} \tag{5.9}$$

[9] In this limit, it is understood regarding eqs. (5.7) and (5.8) that $q \to aq$ and that $D_{\mathrm{gl/gh}}$ are dimensionless.

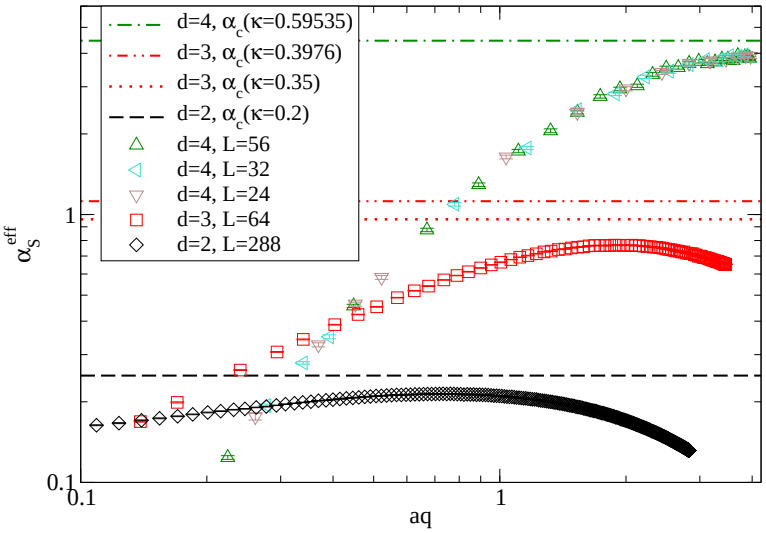

Figure 5.11: Effective running coupling in the strong-coupling limit in two, three and four dimensions. The data in four dimensions are courtesy of André Sternbeck and have been published in [221]. They are shown here for comparison with our data.

with

$$I_G^{(d)}(\kappa) = -\frac{d-1}{2}\frac{\Gamma(\frac{d}{2}-\kappa)\Gamma(1+2\kappa)\Gamma(-\kappa)}{\Gamma(\frac{d}{2}-2\kappa)\Gamma(1+\kappa)\Gamma(\frac{d}{2}+1+\kappa)}, \tag{5.10}$$

which entails for $N_c = 2$ in 4, 3 and 2 dimensions, respectively (assuming the standard values of κ, stated in eq. (2.33))

$$\alpha_c^{(4)} = \frac{4\pi}{N_c I_G^{(4)}\left(\frac{1}{98}\left(93 \mp \sqrt{1201}\right)\right)} \approx \frac{4\pi}{2 \cdot 1.40956} \approx 4.45756, \tag{5.11a}$$

$$\alpha_c^{(3)} = \frac{2\sqrt{\pi}}{N_c I_G^{(3)}(0.3976\ldots)} \approx \frac{2\sqrt{\pi}}{2 \cdot 1.57963} \approx 1.122, \tag{5.11b}$$

$$\alpha_c^{(2)} = \frac{1}{N_c I_G^{(2)}(0.2)} \approx \frac{1}{2 \cdot 1.99569} \approx 0.25054. \tag{5.11c}$$

Results. We turn to our numerical results. In order to facilitate insight into the dependence of the behavior of α_S^{eff} on the dimensionality of the theory, our results in two and three dimensions are shown together with previous results [221] in four dimensions in fig. 5.11. The effective running coupling is not constant in any dimension. Thus, it does not exhibit a uniform scaling behavior. Beside this fact, two features of fig. 5.11 are particularly noteworthy. These are the value and the position of the maximum of the effective running coupling.

Quantitatively, the maximum of α_S^{eff} amounts to approx. 85% of the predicted constant value of α_c in $d = 2$, $\approx 70\%$ in $d = 3$ and, as mentioned above, $\approx 90\%$ in $d = 4$. As is apparent from eq. (5.9), the predicted value of α_c depends on the value of κ. In fig. 5.11, we have included $\alpha_c(\kappa = 0.35)$ in addition to $\alpha_c(\kappa = 0.3976)$ for $d = 3$. We have chosen

these specific values of κ because the numerical data indicate $\kappa_Z \approx 0.35$, as laid out above, while $\kappa = 0.3976$ is the usual scaling prediction [84, 54]. The statement that the maximum of $\alpha_S^{\text{eff}}(aq)$ is around 70% of α_c holds for $\alpha_c(\kappa = 0.3976)$. Inserting the value of κ actually obtained from the gluon data ($\kappa_Z \approx 0.35$, cp. fig. 5.9) slightly improves the situation, cp. the dotted red line in fig. 5.11.

The second notable feature of fig. 5.11 is that the peak moves toward larger lattice momenta as the number of dimensions of the system is increased. It is not at all a coincidence that this mirrors the behavior of the intersection of κ and κ_Z, which was discussed in . This is because the exponents are connected to the effective running coupling α_S^{eff} in a simple way. More precisely, α_S^{eff} is related to the difference of the exponents via

$$\alpha_S^{\text{eff}} \propto (q^2)^{2(\kappa_Z - \kappa)}. \tag{5.12}$$

This follows directly from the definitions of α_S^{eff} (eq. (5.8)) and of the infrared exponents (see eqs. (2.27) and (2.34)) together with the scaling relation (2.28).

The shift in the maximum of $\alpha_S^{\text{eff}}(aq)$ described above follows the pattern observed at non-zero β, see e. g. ch. 4. Namely, the range of momenta in which a scaling-like behavior can be observed at $\beta > 0$ extends to much smaller momenta in two dimensions than in three. Still, at least a peak of the gluon propagator at non-zero q is visible in three dimensions. In four dimensions, finally, this range becomes so small that scaling cannot be observed at all. Hence, one might speculate that at finite coupling and at $\beta = 0$, it is the same mechanism that shifts the maximum to smaller values of aq as d grows. But despite this possible analogy, we do not wish to conceal the fact that our results for α_S^{eff} in two and three dimensions are surprising and not amenable to an immediate explanation.

We stress again that for the scaling solution, a constant value of $\alpha_S^{\text{eff}}(aq)$ is predicted in the strong-coupling limit, as the infrared fixed point should be visible at all momenta in this case. This behavior is not seen. From the perspective of a proponent of this solution, it might be possible to explain the actual results for the running coupling by invoking discretization effects at large aq and Gribov copy effects at small aq. We examine a subset of possible discretization effects in the following sec. 5.2.4, before we devote an entire chapter, ch. 6, to the study of a certain class Gribov copy effects.

5.2.4 Discretization effects

In the strong-coupling limit, significant discretization effects are to be expected, since the lattice spacing is formally divergent (see sec. 5.1.1, also for caveats). Some studies exist that investigate how a change in the lattice discretization of the gauge field resp. of the gauge fixing condition affects the behavior of the gluon and ghost propagators at $\beta = 0$ at small lattice momenta aq [295, 221, 296]. It changes the 'decoupling tail' at small lattice momenta while leaving the 'scaling branch' at large aq unaffected. However, with none of the discretizations explored in these references does the decoupling behavior at small aq disappear. The *qualitative* behavior was thus found not

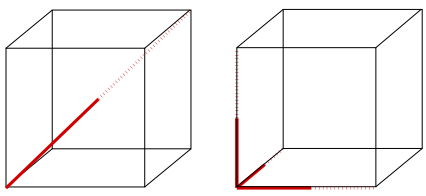

Figure 5.12: Illustration of space-diagonal momenta *(left)* vs. on-axis momenta *(right)*, $d = 3$.

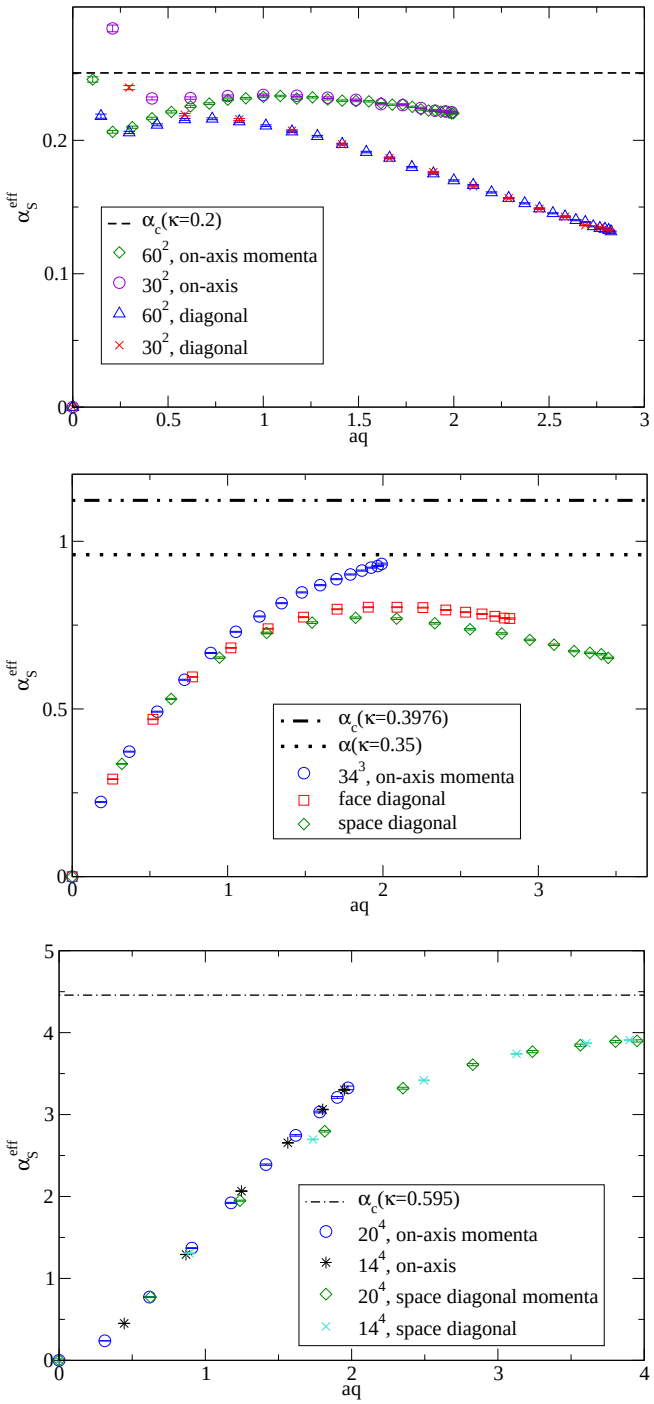

Figure 5.13: Effect of a discretization artifact, sc. the breaking of rotational invariance, on the effective running coupling in the strong-coupling limit. *Top (a):* $d = 2$, *middle (b):* $d = 3$, *bottom (c):* $d = 4$.

to depend on the discretization, to the extent of the variations that were considered in refs. [295, 221, 296].

Here, we study a different discretization effect, sc. the effect of breaking of Euclidean rotational resp. Lorentz invariance, the $O(d)$ symmetry in d dimensions. Usually, we have applied a cylinder cut to the momenta, which selects momenta close to a space diagonal, see sec. 2.3.3.3. We present results for the effective running coupling α_S^{eff}, where the propagators entering into α_S^{eff} have been evaluated either at on-axis momenta or at diagonal momenta. On-axis momenta are defined as $k_i = k\delta_{ij}$ for all fixed j. They constitute the opposite case to the cylinder cut. Momenta along space diagonals resemble the cylinder cut. Momenta along face diagonals constitute an interpolating case, but naturally, they are not an independent option in two dimensions, where they coincide with space-diagonal momenta. A simple illustration is provided in fig. 5.12.

The results for these discretization effects in two, three and four dimensions are depicted in fig. 5.13. Notably, the tendency of the effective running coupling to decrease toward large lattice momenta is within the systematic uncertainty due to the discretization effects. This is apparent in particular from the data in two dimensions, fig. 5.13, where the running coupling from on-axis momenta is much closer to a constant α_S^{eff} in line with continuum predictions than the results from the standard choice of momenta. In the higher-dimensional cases, in particular for $d = 4$, the discretization effects become notably weaker. Definite conclusions, though, are impeded by the fact that the largest on-axis momentum is relatively small compared to the largest space-diagonal one; of course, this difference increases with the number of dimensions, which is a simple geometric effect. This situation cannot be improved by going to larger lattices, as the upper limit on admissible lattice momenta in d dimensions is $(aq)_{\max} = 2\sqrt{d}$ if aligned along a space diagonal, or similarly according to the cylinder cut, and simply 2 if aligned along an axis. (These statements follow from eq. (2.87).) In any case, these discretization effects are still considerably weaker than the effects of the Gribov ambiguity. The subsequent chapter, ch. 6, is concerned with the latter effects.

5.3 Summary

We have studied the strong-coupling limit of pure $SU(2)$ Yang–Mills theory on the lattice in two and three dimensions in standard Landau gauge. This limit potentially allows to assess the infrared behavior at all lattice momenta. When combining our results with previous findings in four dimensions, an interesting picture emerges that casts some doubts on the received lattice scenario of a clear distinction between scaling in two dimensions and decoupling in three and four dimensions. Still, the infinite volume limit of the gluon propagator at zero lattice momentum is zero only in two dimensions.

We have calculated the effective running coupling from the ghost and gluon propagator. From this, we infer that the behavior of the correlation functions resembles a scaling behavior at most in a small region of momenta. This 'scaling window' shifts toward larger lattice momenta as the number of dimensions is increased. But neither are the results unequivocally in line with a decoupling-type solution, although we have obtained some evidence for such a behavior.

The calculation of local ghost and gluon exponents further underlines this picture. The local ghost exponent strongly grows with the lattice momentum, so the ghost propagator

it is by itself sufficient to violate a uniform scaling behavior.

In addition, we have studied discretization effects due to breaking of rotational symmetry, which are found to be significant in particular at large lattice momenta, but to decrease with increasing number of dimensions. The violation of a scaling behavior at small lattice momenta is independent of these effects.

In sum, the results of this chapter constitute evidence that the behavior of the Yang–Mills ghost and gluon propagator, at least in the strong-coupling limit, may be less well understood than is sometimes stated. This is due to the absence of a uniform scaling behavior in two dimensions, and because a more unified picture in two, three and four dimensions than previously assumed might emerge. In the following chapter, we turn to a possibly even more surprising piece of evidence, which stems from the effects of Gribov copies.

CHAPTER 6

GRIBOV AMBIGUITY AT STRONG COUPLING

We continue to study the propagators in the strong-coupling limit in two and three dimensions. Unlike in the previous chapter, ch. 5, however, we now explicitly consider the influence of the chosen gauge copy. This is done in a way that could potentially change in particular the behavior of the effective running coupling at small lattice momenta observed in the previous chapter. We motivate our approach and recapitulate the definition of a recently proposed non-perturbative completion of Landau gauge in sec. 6.1, and we present a number of results especially for the propagators and the effective running coupling in sec. 6.2. We turn our attention in particular to the dependence of these quantities on the number of Gribov copies taken into account.

6.1 Introduction

6.1.1 Motivation

It is an important task to assess the impact of the Gribov ambiguity, see sec. 2.2.3.3, on the quantities we study. This is because, first, the gluon and ghost propagator depend on the chosen gauge, and, second, there is a residual gauge freedom in Landau gauge, such that a unique gauge fixing is an NP-hard problem, see sec. 2.3.2. In other words, instead of a global optimization of the gauge fixing functional R, eq. (2.80), de facto only a local one is performed. This is virtually inevitable. A priori, there is no reliable estimate of how large the effect of choosing a different copy might be.

An additional complication is introduced by the following consideration. It is not evident why the proper choice of a unique gauge copy for calculating correlation functions should be the choice of the copy with the globally maximal value of R, i. e., the copy inside the fundamental modular region Λ, see sec. 2.2.3.3. While this would be evidently be a very consequential choice if one could show that BRST symmetry would be restored by such a choice (see sec. 2.1.2 and 2.2.3.2), arguments to this end are lacking.

Earlier studies of lattice Gribov copies may be found e. g. in [352, 353, 229, 354, 355, 356], see also [220] for further references. We are interested in their influence on correlation functions in Landau gauge. Such investigations were carried out initially with regard to randomly generated gauge copies [242], subsequently also employing global maximization approaches, but only evaluating the gluon propagator [147, 357, 266]. From most of these investigations, it was concluded that the effects on the gluon propagator are not large, although sometimes statistically significant, e. g. [266], and that the ghost propagator is more sensitive to the Gribov ambiguity than the gluon propagator, see [242, 292, 358] and in particular [267].

There have been elaborate efforts toward a better global maximization of R [274, 277, 122]. They employ simulated annealing [359, 360], which is a versatile global optimization algorithm, and global $\mathbb{Z}_2$ flip transformations [268].[1] These studies are motivated by the experience that a similar procedure is required in order to obtain the correct photon propagator in compact $U(1)$ lattice gauge theory [361, 362], see also [363], and additionally by a gauge fixing approach put forward by Parrinello, Jona-Lasinio and Zwanziger [364, 365] as an alternative to the standard Faddeev–Popov path integral.

The 'global maximization' investigations involve a number of Gribov copies of each configuration. In every case, the 'best copy', i. e. here the one with the largest value of the gauge fixing functional R, is selected for calculating the ghost and gluon propagator and other gauge-dependent quantities. This approach results in an effect of about 10% on the ghost propagator [277]. More precisely, the infrared ghost propagator is lowered by this percentage. This prima facie corroborates that the lattice ghost data are in line with the decoupling solution, since it renders the ghost less infrared divergent. The ghost dressing function approaches a plateau in the infrared if calculated from the best copy [277].

The gluon propagator calculated in this way assumes lower values than from the 'first copy' [274] (see also [268]), which might seem to indicate a slow approach toward a zero value, in line with a scaling-type behavior. A thorough analysis reveals that its behavior in the joint limit of many gauge copies and large volumes is probably still of decoupling type with this improved gauge fixing procedure [277, 122]. However, the authors of these studies explicitly "do not yet consider the Gribov copy problem to be finally resolved" [277]. This statement draws additional support from the fact that the number of Gribov copies grows exponentially with the lattice volume, i. e., with the number of lattice sites.

6.1.2 Non-perturbative completions of Landau gauge

In the thesis at hand, we pursue a different path to exploit the residual gauge freedom of Landau gauge. In a nutshell, our method is a 'best gauge copy' approach that strives to maximize not the gauge fixing functional, but the infrared ghost propagator. It has been suggested first in [104] and is based on an analogy to the one-parameter family of solutions for the infrared ghost and gluon propagator found from functional methods in the continuum [77, 66], see sec. 2.2.2. The functional equations need to be supplemented by a boundary condition. The respective parameter can be chosen as the value of the ghost dressing function at zero momentum.

In fact, an entire class of non-perturbative completions of lattice Landau gauge has been proposed in [104]. The parameter governing them is the ratio of the ghost propagator at

[1] Another possibility are genetic algorithms, see e. g. [297] and references therein.

the smallest accessible lattice momentum q_{min} and at a large momentum Q,

$$B := \frac{D_{\mathrm{gh}}(q_{\mathrm{min}})}{D_{\mathrm{gh}}(Q)}. \tag{6.1}$$

The general prescription to implement Landau-B gauge is, for each configuration,

1. to generate a number n_{copy} of gauge copies,
2. to calculate the ghost propagator from each of these copies and
3. to select the gauge copy for which the value of B is closest to a target value specified in advance.

All other gauge-dependent quantities are then calculated from this designated copy as well. The procedure is repeated for each independent configuration.

Choosing different values of B may correspond to choosing different values of the free parameter in calculations with functional continuum methods. Naturally, there is a statistical element inherent in the definition of the Landau-B gauges, since n_{copy} is by necessity finite and hardly ever sufficient to cover even remotely all gauge copies of a configuration.

6.1.3 Landau max-B gauge

The non-perturbative completion of Landau gauge which we implement is max-B gauge. Here, the parameter B and thereby the infrared ghost propagator are chosen to be as large as possible, sc. for each configuration as the maximum of the values on all n_{copy} gauge copies. Formally, this may be expressed as '$B = \infty$'. In practice, we calculate $D_{\mathrm{gh}}(q_{\mathrm{min}})$ as the average of the ghost propagator evaluated at all momentum vectors q_i with $q_i = \delta_{ij}$. I. e., we average over all representations of the lowest lattice momentum. We do so in order to reduce artifacts from breaking of rotational symmetry.[2]

A plethora of other Landau-B gauges is possible by tuning the parameter B to a different value, like e. g. 'min-B gauge', or even choosing yet another parameter. Therefore, the Gribov copy effects on which we report in the following are by no means to be understood as exhaustive. Rather, they represent a lower bound on the impact of the Gribov ambiguity. However, this fact can only strengthen our finding, which is that Gribov copy effects are stronger and less under control than is frequently assumed, as we will lay out in detail in the present chapter.

We stress that fixing to Landau max-B gauge is numerically rather expensive, since the evaluation of the ghost propagator is required for each single copy of each configuration (gauge orbit). First results in this gauge on small three-dimensional lattices at finite coupling have shown strong effects, sc. an increase of the infrared ghost propagator on the order of 100%, already from 20 gauge copies per orbit [104].[3] Here, we perform a more extensive investigation with up to 600 copies in both two and three dimensions. Another advantage of our studies is that we implement the plane-wave source method for the ghost

[2] In the first study of Landau max-B gauge, ref. [104], only one on-axis momentum was chosen when determining $D_{\mathrm{gh}}(q_{\mathrm{min}})$.

[3] In [104], a point source was used for the ghost propagator calculation. This enhances the effect of max-B gauge, but also leads to large statistical fluctuations. See sec. 6.2.2.1.

propagator instead of the point source method (see sec. 2.3.3.2 and especially app. B.3), yielding much more precise data. This further increases the numerical effort per configuration considerably (sc. by a factor of the number of momenta). Our studies, whose results we present in the following sec. 6.2, are the first calculations in Landau max-B gauge at $\beta = 0$.

6.2 Results

6.2.1 Main results

We have restricted our analysis to relatively modest lattice sizes like 48^2 and 20^3. However, as pointed out above, since a ghost propagator with the plane-wave source method needs to be calculated for up to 600 copies for each single orbit, it is a numerically expensive enterprise. We also explore the question whether the dependence of the number of gauge copies can be controlled, i. e., whether a saturation of the results as a function of the number of Gribov copies can be observed.

6.2.1.1 Ghost propagator

The impact of max-B gauge with up to 550 Gribov copies on the ghost dressing function $q^2 D_{\mathrm{gh}}$ on a 20^3 lattice is shown in fig. 6.1. Results from first copies (i. e., standard Landau gauge) are included in this figure, among them such ones that have been obtained on a larger lattice, cp. the legend. We also show results at various smaller values of n_{copy}. The Gribov copy effect on the ghost dressing function at small momenta is evidently strong and on the order of 100% for the numbers of copies we have investigated (note the logarithmic scale). Already 20 copies induce an effect that is far stronger than the volume effect when going from a 20^3 to a 64^3 lattice. This is qualitatively in line with first results at finite coupling [104]. It is not surprising that the ghost propagator increases due to the Gribov copy effect, contrary to the volume effect, since this is inherently built into max-B gauge. But it is a rather unexpected result that the effect is so strong.

The number of independent configurations for the data in fig. 6.1 decreases with the number of copies, which is partly an effect of the numerical procedure.[4] We have used $N \approx 7000$ configurations for $n_{\mathrm{copy}} = 20$ (meaning that $140,000$ ghost propagator calculations were required in this case), $N \approx 2000$ for $n_{\mathrm{copy}} = 80$, and $N \approx 400$ for $n_{\mathrm{copy}} = 300$ and 550.

Note on the inversion method. The ghost propagator would be generically even larger if a point source instead of a plane-wave source was employed for the FPO inversion, since the statistical fluctuations are larger in this case. (We describe and characterize both methods in sec. 2.3.3.2 and app. B.3.1.) However, this would exert an very unfavorable influence on the accuracy, and the extraction of a local scaling exponent would be virtually impossible, as illustrated already in the preceding chapter 5 (fig. 5.4) by the results from

[4] The main effect here is that we initially investigated only a smaller number of copies, expanding the investigation up to 600 copies only when it became clear that the ghost propagator wouldn't saturate (stop growing). In addition, a fixed maximal runtime of the jobs made it necessary to terminate the measurements for some gauge orbits before the full number of 600 copies was generated.

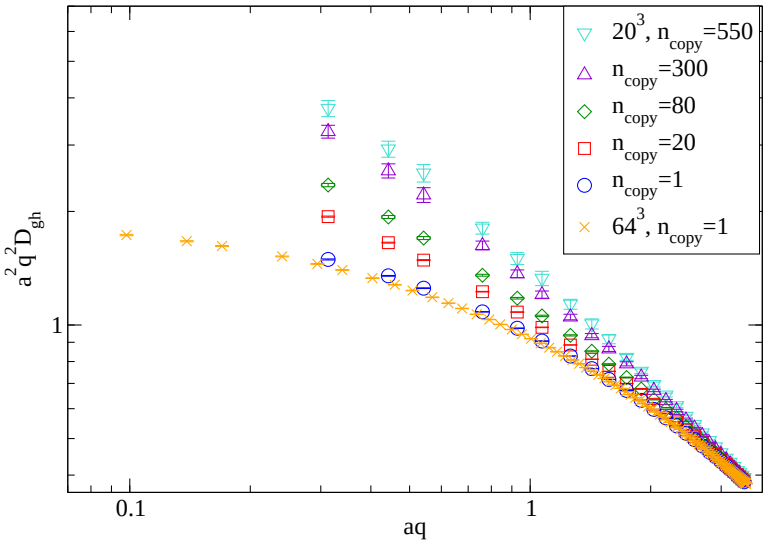

Figure 6.1: Effect of Landau max-B gauge with increasing number of copies on the ghost dressing function in three dimensions ($V = 20^3$), contrasted with first-copy results on 20^3 and 64^3 lattices.

a 'first copy' method, and also by the results of ref. [345]. We show results from a point source in sec. 6.2.2.1.

The ghost propagator enters quadratically into the effective running coupling, eq. (5.8), which is the quantity that best sums up our results. This quadratic dependence further increases the demand for ghost propagator data with small statistical errors. Moreover, the point source method introduces especially pronounced wiggles at large lattice momenta. At finite coupling, these momenta are not relevant to the infrared behavior, but in the strong-coupling limit, information about the infrared behavior of the theory is encoded also in the data at large aq (see sec. 5.1.1).

6.2.1.2 Faddeev–Popov eigenspectrum

As the infrared ghost propagator increases when Landau max-B gauge with a growing number of copies is employed, the spectrum of the Faddeev–Popov operator changes accordingly. In particular, the lowest[5] eigenvalue λ_0 moves toward smaller values, i. e., 'closer to the Gribov horizon', as visible in fig. 6.2 and as can be expected for a ghost propagator that is stronger enhanced in the infrared [20]. This was investigated more closely using the spectral representation of the ghost propagator in terms of eigenmodes and eigenvalues [341, 340, 173], as remarked already in sec. 4.3.2.2. Note that we have chosen a rather small lattice volume in order to corroborate the expected behavior of the lowest eigenvalue. This choice facilitates finding the entire eigenspectrum of the Faddeev–Popov operator (FPO), including its exactly lowest nontrivial eigenvalue. Fig. 6.3 explicitly shows the strong negative correlation between the infrared ghost propagator and the lowest FPO eigenvalue in Landau max-B gauge.

[5]The trivial zero eigenmodes, which number $N_c^2 - 1 = 3$, are again excluded.

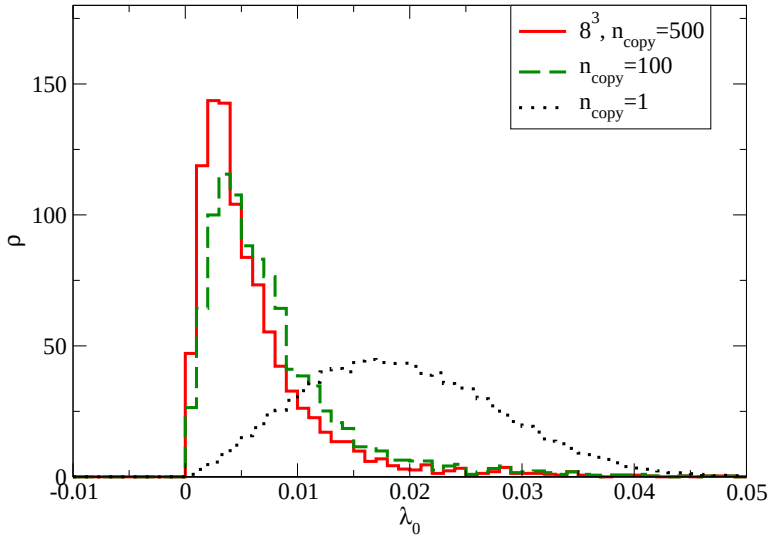

Figure 6.2: Effect of Landau max-B gauge on the lowest nontrivial FPO eigenvalue λ_0 as a function of included Gribov copies. Entries in the histogram correspond to λ_0 on different configurations, in each case calculated from the Gribov copy with the infrared most divergent ghost propagator.

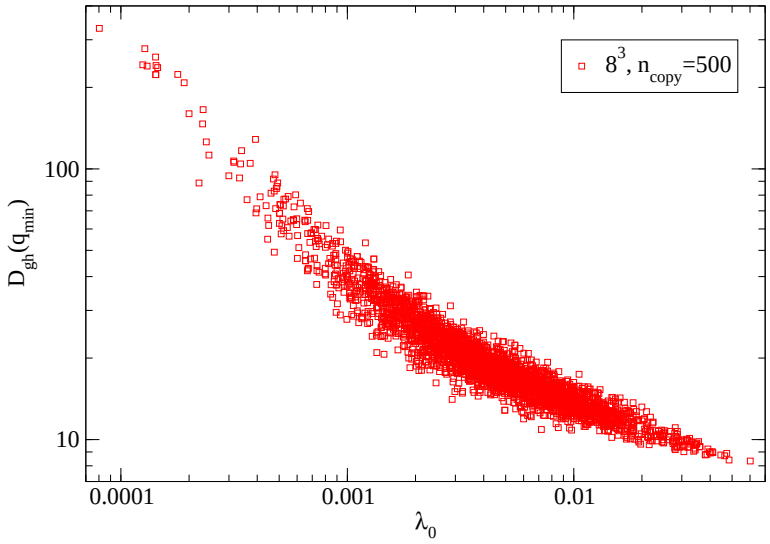

Figure 6.3: The infrared ghost propagator and the lowest nontrivial FPO eigenvalue are strongly anticorrelated (correlation coefficient $\rho \approx -0.37$ from 3120 configurations).

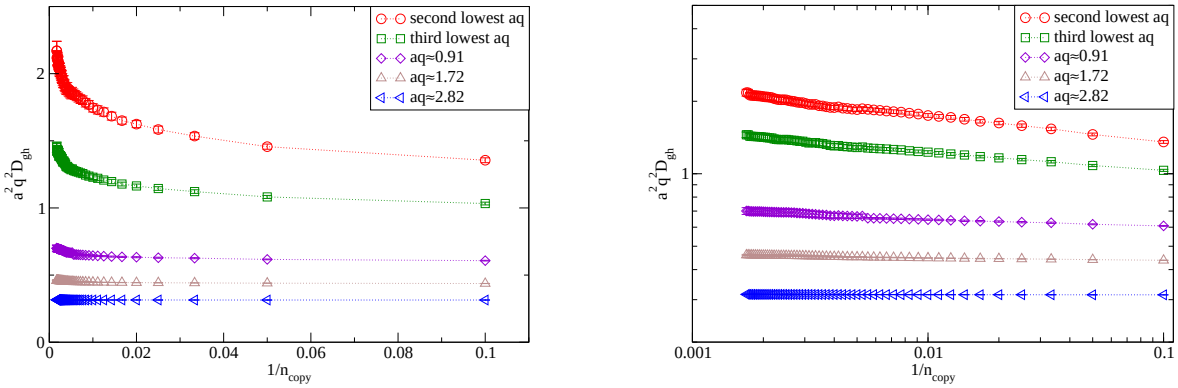

Figure 6.4: Effect of increasing the number n_{copy} of Gribov copies on the ghost dressing function at selected lattice momenta in two dimensions. Lowest lattice momentum omitted here due to exceptional configurations (see main text). *Left (a):* Linear scales. *Right (b):* Same data on logarithmic scales.

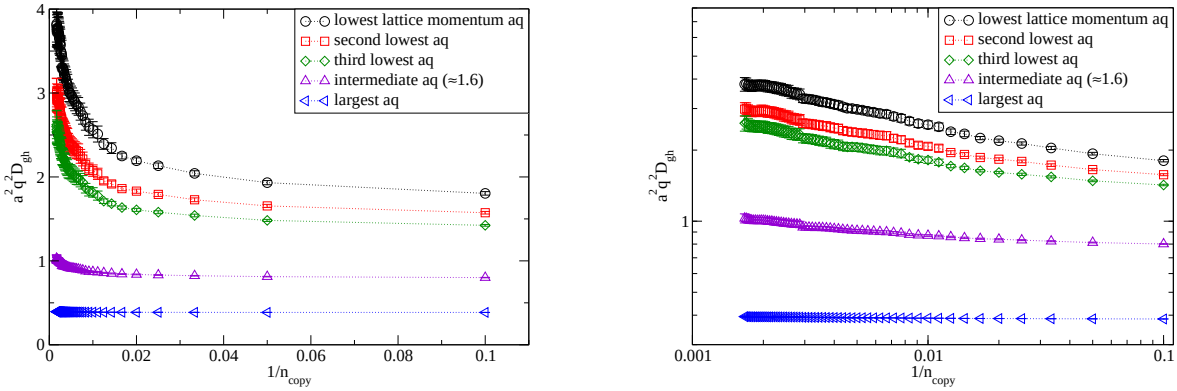

Figure 6.5: Effect of increasing n_{copy} on the ghost dressing function at selected lattice momenta in three dimensions. *Left (a):* Linear scales. *Right (b):* Same data on logarithmic scales.

6.2.1.3 Extrapolation to infinite number of copies

We have demonstrated that Gribov copies exert a dramatic influence on the infrared ghost propagator by virtue of Landau max-B gauge. It is desirable to extrapolate this behavior to the limit $n_{\text{copy}} \to \infty$,[6] i. e., to obtain a reliable estimate of how strongly the ghost propagator can be enhanced by choosing its largest value among *all* Gribov copies of the respective orbit.

While the computational effort caused by the Landau max-B gauge with hundreds of copies and by the precise ghost propagator calculation is large, the lattices we have mainly investigated are not huge (48^2 in $d = 2$ resp. 20^3 in $d = 3$). Due to the exponential growth of the total number of Gribov copies with the lattice volume, it should be easier to observe

[6]Strictly speaking, the number of Gribov copies on a finite lattice is of course not infinite, but it is still so large that in practice only a tiny subset of all copies can be investigated. See [231] for a method to find all copies in simple models on very small lattices. The exponential growth of the number of Gribov copies with the number of lattice sites prohibits a similar procedure on any lattice that is of interest for the calculation of the infrared propagators.

a 'saturation' in these cases than on larger lattices. We have used up to 600 copies per orbit. However, this number does not suffice to see a saturation, see figs. 6.4 ($d = 2$) and 6.5 ($d = 3$), both on linear scales and on logarithmic scales. The logarithmic scales elucidate that the ghost dressing function grows exponentially as n_{copy}^{-1} decreases. In these plots, only a selection of lattice momenta is shown for clarity. The increase is much stronger at infrared momenta than it is at intermediate and large ones; at the largest accessible lattice momentum, the increase from $n_{\text{copy}} = 1$ to 600 amounts to only 2% in $d = 3$ (statistically insignificant) and to merely 0.5% in $d = 2$.

As a side note, with regard to fig. 6.5b, small 'leaps' in the values of $q^2 D_{\text{gh}}$ at some values of n_{copy}^{-1} are clearly visible. They stem simply from the fact that the results for different numbers of copies are not uncorrelated, since they are always the first n_{copy} ones out of (up to) 600. Thus, a particularly large infrared ghost propagator on the mth copy on a single one of the gauge orbits entering the average will induce such a 'leap' of the average between $n_{\text{copy}} = m - 1$ and $m + 1$.

As the volume is finite, a bound on the growth of the ghost propagator is expected to become noticeable at some point. But we have no evidence to conclude that we are anywhere near it. Instead, we infer from the data that an enormous Gribov copy effect is present. In addition, we stress again that our results represent 'only' a lower bound on this effect for the respective volumes, and that an entire family of solutions may be generated by tuning B to other, finite values. On the other hand, the volume effect is just opposite to the Gribov copy effect in max-B gauge, as the former tends to lead to a lower ghost propagator in the infrared. The results in the joint limit $n_{\text{copy}} \to \infty$ and $V \to \infty$ are impossible to anticipate a priori, and very hard to evaluate numerically.

6.2.1.4 Gluon propagator

Both from previous investigations of Gribov copy effects and from the definition of max-B gauge via the ghost propagator, one should naïvely expect the impact of this completion of Landau gauge on the gluon propagator to be smaller than the one on the ghost. This expectation is indeed fulfilled, see fig. 6.6. From the data in fig. 6.6a, the effect of max-B gauge on the gluon propagator is smaller than the finite volume effect.[7] Qualitatively, the infrared propagator increases in the infrared. Like for the ghost, this contrasts with the results of 'global maximization' approaches, which yield an infrared smaller gluon propagator compared to standard gauge fixing (in four dimensions at finite coupling) [274, 277, 122]. So, roughly speaking, while those approaches result at small momenta in a ghost propagator that changes toward decoupling and a gluon propagator that changes in the direction of scaling as the number of copies increases, we find just the opposite behavior in Landau max-B gauge at $\beta = 0$. In another similarity to the ghost propagator, the gluon propagator at large aq remains unaffected by max-B gauge.

But there is also a stark contrast to the behavior of the ghost propagator. Remarkably, the gluon propagator at zero momentum saturates quickly as a function of the inverse number of gauge copies taken into account per orbit, see fig. 6.6b. Thus, the Gribov copy effect for the gluon propagator is better under control – facilitated of course by the fact that

[7] For the result at $n_{\text{copy}} = 550$ in fig. 6.6a, ≈ 5000 gauge orbits have been used. – Much more data for the finite volume effect of the gluon propagator in standard Landau gauge in three dimensions are shown in fig. 5.5 above.

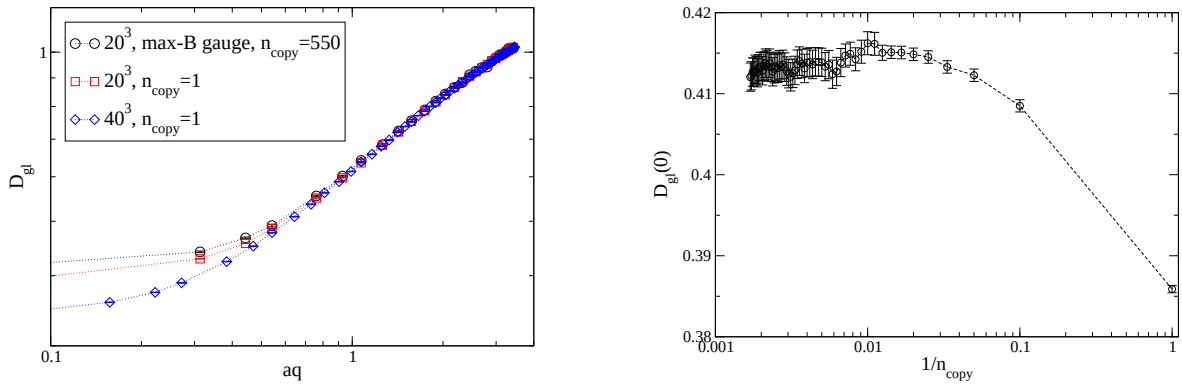

Figure 6.6: *Left (a):* Gluon propagator in max-B gauge vs. standard Landau gauge ($n_{\text{copy}} = 1$) in three dimensions, including comparison with volume effect. *Right (b):* Gluon propagator at zero momentum in max-B gauge vs. number of Gribov copies taken into account. Here, max-B gauge implemented with point source; see main text for reasons and details.

the very definition of Landau max-B gauge explicitly involves only the ghost propagator.

A remark concerning the implementation is in order here. When calculating the gluon propagator in max-B gauge, there is a slight technical difference to our implementation of this gauge explained above (sec. 6.1.3) and used for obtaining expectation values of the ghost propagator. In max-B gauge, regardless of which correlations functions are eventually measured, a ghost propagator calculation for each copy on each orbit is required. Most of these results for the ghost propagator do not enter into the expectation value, since only the maximal one per orbit does so. This is inherent in the definition of max-B gauge. When aiming at obtaining expectation values of the ghost propagator, we have inverted the Faddeev–Popov operator on a plane-wave source, as laid out above. But here, in order to sample a good statistics for the gluon propagator, we have used a point source, see sec. 6.2.2.1 and also sec. 2.3.3.2 and app. B.3. This is because the statistical fluctuations for the gluon propagator are much larger than for the ghost with a plane-wave source. Hence, much more measurements are desirable. On a 20^3 lattice, we use typically $\mathcal{O}(10^4) - \mathcal{O}(10^5)$ measurements for the gluon. For comparison, we have also evaluated the gluon propagator after the usual procedure for the ghost propagator calculation (with a plane-wave source method) and have found that it agrees within errors with our results shown in fig. 6.6.

6.2.1.5 Effective running coupling

As we have shown in the preceding sec. 6.2.1.4, the large influence of the Gribov ambiguity in max-B gauge on the ghost propagator is accompanied by a comparatively small influence on the gluon propagator. By virtue of the definition of the effective running coupling α_S^{eff}, eq. (5.8), it is straightforward to conclude that the effect on the ghost propagator translates into a very strong effect on α_S^{eff}.

We show the results for the effective running coupling in max-B gauge for varying number of gauge copies in fig. 6.7 for the two-dimensional case, and in fig. 6.8 for the three-dimensional case. In both cases, a dramatic over-scaling at small and intermediate lattice momenta is evident for larger n_{copy}. This is very surprising, as such a behavior is prohibited in the continuum by the uniqueness proof put forward in [82, 86, 83]. Indeed, a satisfactory

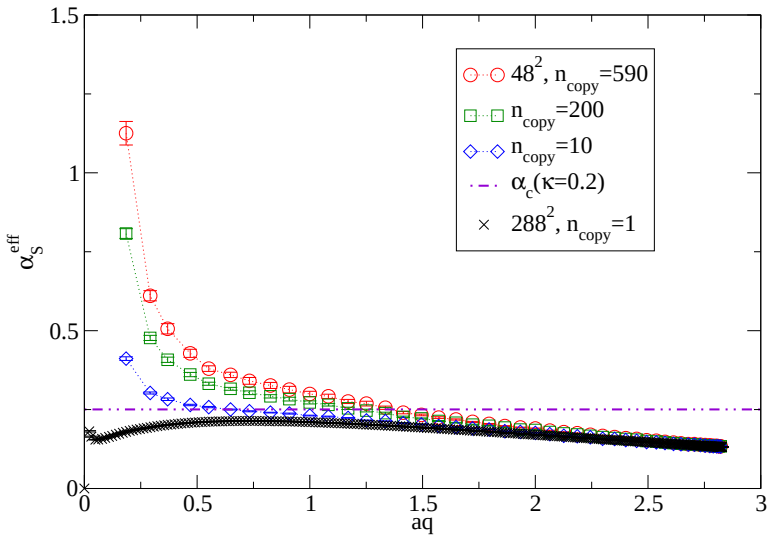

Figure 6.7: Effective running coupling for max-B gauge with increasing number of copies, compared to standard Landau gauge (i. e., $n_{\text{copy}} = 1$) on a larger lattice, in two dimensions. (The lowest lattice momentum is not shown in max-B gauge, since the value here is dominated by a few 'exceptional configurations', see also the caption to fig. 6.4 and the main text.)

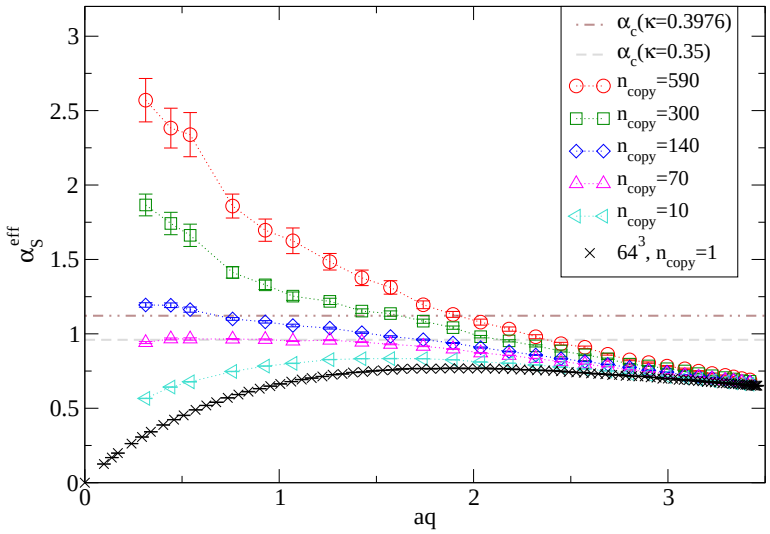

Figure 6.8: Effective running coupling for max-B gauge with increasing number of copies, compared to standard Landau gauge, in three dimensions.

explanation for this over-scaling is lacking. It is bound to disappear in the infinite volume limit, in which the running coupling is expected in decrease in the infrared. However, our results indicate that it is an open question whether Gribov copy effects may be strong enough for a scaling behavior to survive in the joint limit of $V \to \infty$ and $n_{\text{copy}} \to \infty$.

As mentioned and shown already in sec. 5.2.4, the behavior at large momenta might be related to discretization effects which we expect to be particularly strong at $\beta = 0$. Regarding the effective running coupling in max-B gauge, we have studied some such effects related to the momentum definition, see sec. 6.2.2.2 below.

A note on exceptional configurations. In the two-dimensional case, the lowest-momentum value of the ghost propagator resp. the effective running coupling, which is partially determined by the ghost propagator via eq. (5.8), is not included in the figures. This pertains to figs. 6.4 and 6.7. The reason for this exclusion is the occurrence of 'exceptional configurations' in this case. These are configurations on which the ghost propagator takes values which surpass the usual ones (at the specific momentum) by orders of magnitude. A similar observation, albeit at finite coupling, has already been made in [292], see also [267, 341, 340, 115]. We emphasize that we do not exclude these configurations from the average. Their inclusion does not impede plots of the ghost propagator at all lattice momenta above the smallest non-vanishing one (like figs. 6.4 and 6.7), because at all such momenta, the effect is much weaker.[8]

6.2.1.6 Local exponents

We extend the calculation of effective local exponents from the propagator data, as performed in ch. 5 in standard Landau gauge (see sec. 5.2.1.2 for an introduction), to the case of Landau max-B gauge. This allows to further elucidate the statements made hitherto about the behavior of the propagators and the running coupling, e. g. pertaining to the 'over-scaling' at small aq.

Extracting the local κ from the ghost propagator in max-B gauge with increasing n_{copy}, we again observe a considerable 'over-scaling' at small aq for a sufficiently large number of gauge copies, fig. 6.9. The gluon data are included only for the case of $n_{\text{copy}} = 1$ (which, of course, amounts to standard Landau gauge), since the effect of max-B gauge on the gluon data is comparatively weak, see sec. 6.2.1.4 and especially fig. 6.6 above. As we have seen in sec. 5.2.3, the local exponents are intimately related to the effective running coupling, cp. especially eq. (5.12). Hence, fig. 6.9 conveys, to a large extent, similar information as fig. 6.8. Still, it is useful to represent this information also in this way. Inter alia, it nicely illustrates that primarily the ghost, not the gluon, is the reason of the over-scaling behavior which we have inferred from the effective running coupling. From fig. 6.9, it is apparent that at about 70 gauge copies for the given lattice size, the scaling solution is almost realized over a larger momentum range around $aq \approx 1$, with $\kappa \approx 0.35$. But this fact is not at all stable with respect to a further increase of n_{copy}. As explained in sec. 5.2.3.2, this proposition can

[8] To be specific, our numerical simulations on a 48^2 lattice have found three exceptional configurations out of $\mathcal{O}(1000)$ total configurations. This means that in these three cases, at least one Gribov copy of the respective configuration out of 600 copies yielded a ghost propagator larger than the average by at least three orders of magnitude.

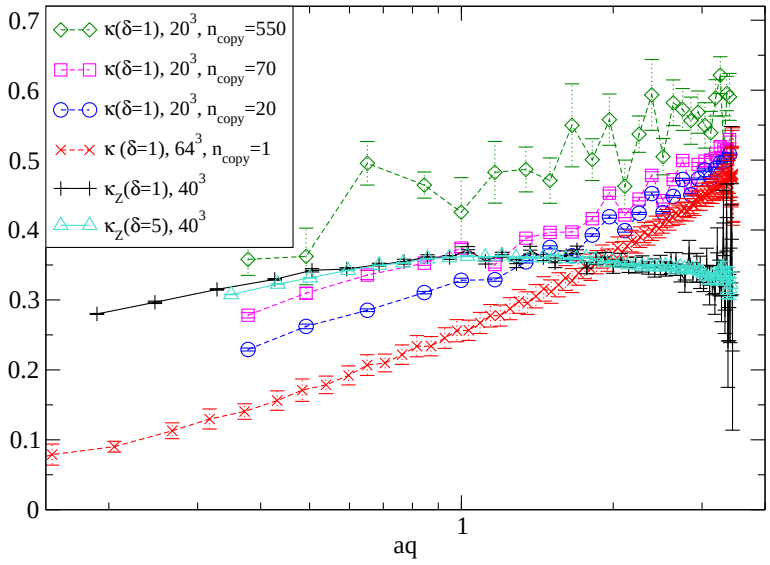

Figure 6.9: Effect of Landau max-B gauge with increasing n_{copy} on the local ghost exponent κ from the ghost data in three dimensions. The local ghost exponent κ_Z obtained from the gluon data, eq. (2.34), from the first copy is shown for comparison.

also be read off from the effective running coupling. The approximate identity $\kappa = \kappa_Z$ at $n_{\mathrm{copy}} \approx 70$ translates via eq. (5.12) to an approximately constant α_S^{eff}, see fig. 6.8.

6.2.2 Further issues

6.2.2.1 Inversion method and volume effects

The choice of the method used to invert the Faddeev–Popov matrix exerts a huge influence on the statistical accuracy of the ghost propagator, as we have shown already in chs. 4 and 5. All results presented in this chapter have been obtained with the plane-wave source method. The sole exception to this rule is fig. 6.10. Before we comment on this figure, we discuss what is to be expected.

The increase of fluctuations when using the point source method as compared to a plane-wave source should have a straightforward effect on the result in max-B gauge. Since the variation in the values of the ghost propagator within the respective ensemble of n_{copy} copies is larger in the former case, the choice of the copy with the largest infrared ghost propagator should generically also yield a larger result. This is indeed the outcome, as is evident from comparing fig. 6.10 to fig. 6.1 above. For example, for 550 gauge copies per orbit, we obtain $q^2 D_{\mathrm{gh}} = 3.75 \pm 0.18$ for the plane-wave source ($\approx$ 400 orbits) vs. $q^2 D_{\mathrm{gh}} = 5.35 \pm 0.05$ for the point source ($\approx$ 12,000 orbits).

In fact, we have explicitly considered the difference between the average and the median of the infrared ghost propagator among various gauge copies used for Landau max-B gauge. It is much larger for the point-source method than for the plane-wave source method. In line with this observation, the results from both methods would become more similar when the median instead of the average was used, which is of course not done for any final results.

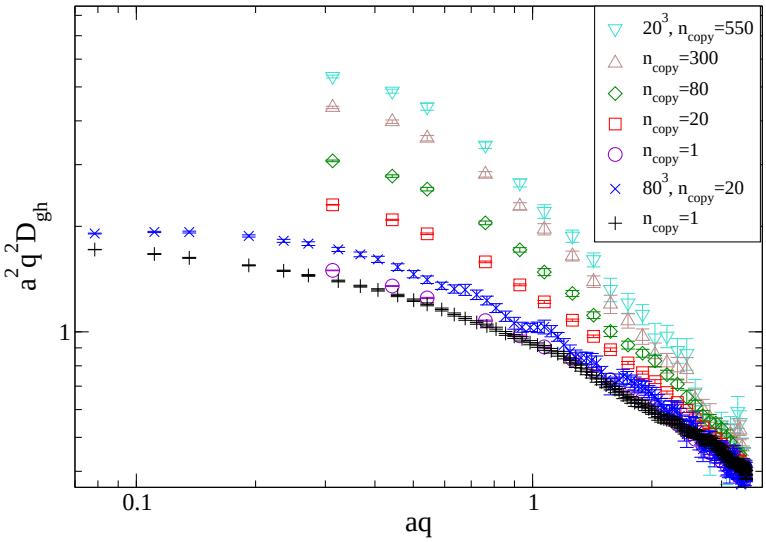

Figure 6.10: Finite volume effect for minimal Landau gauge and for max-B gauge with various numbers of copies. Point source method.

Another aspect of fig. 6.10 is noteworthy. Namely, the volume effect is much stronger for max-B gauge than for standard Landau gauge (i. e., max-B gauge with $n_{\text{copy}} = 1$), given that the number of copies is held fixed when increasing the lattice volume. In fact, the ghost dressing function obtained with 20 copies per orbit in max-B gauge on an 80^3 lattice is virtually flat in the infrared. This illustrates the severe tension between the two limits $n_{\text{copy}} \to \infty$ and $V \to \infty$. The total number of gauge copies exhibits a strong (exponential) growth with the volume. So, certainly, much more copies per orbit are needed on larger lattices in order to possibly obtain the same effect.[9] The prospects to investigate this in practice are evidently limited.

But we are able to infer from our extensive results that none of the infrared solutions can be ruled out, as we obtain even 'over-scaling' on relatively small lattices in max-B gauge. This is a highly interesting statement, as previous lattice studies have frequently been interpreted as decisive evidence in favor of a decoupling-type solution.

6.2.2.2 Discretization effects

We have already studied some aspects of possible discretization artifacts in the strong-coupling limit in sec. 5.2.4. Another estimate of the magnitude of discretization effects may be obtained as follows.

The standard relation between continuum and lattice momenta, eq. (2.87), is not unique. As mentioned in sec. 2.3.1, they differ by terms of $\mathcal{O}(a^2)$ in the lattice spacing, which could obviously become arbitrarily large in the strong-coupling limit. We investigate the effect of

[9] Thus, a comparison at the same number of copies per orbit does not evidently lend support to Zwanziger's conjecture [20], according to which the influence of Gribov copy effects diminishes with increasing lattice volumes (see sec. 2.2.3.3).

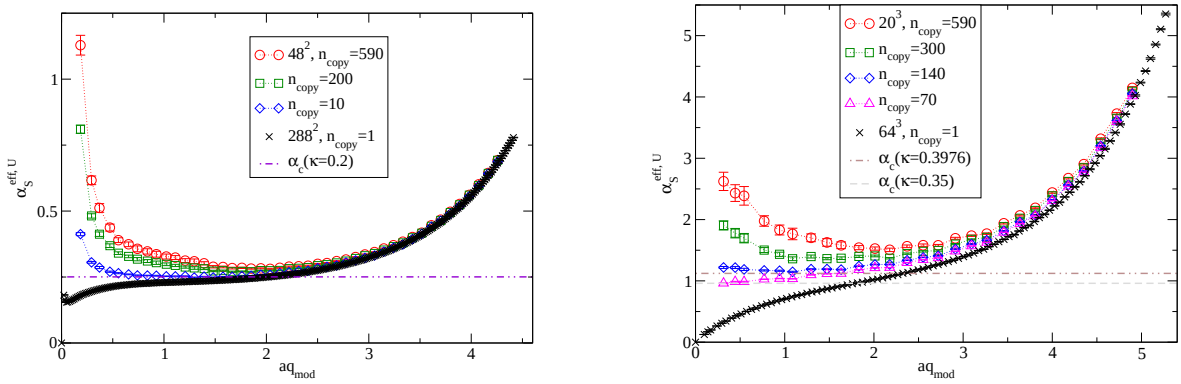

Figure 6.11: Modified definition of the effective running coupling, corresponding to its *upper* bound, in Landau max-B gauge with varying n_{copy} (see legend). Again, the prediction from functional continuum methods [54] is shown for comparison. *Left (a):* In two dimensions. *Right (b):* In three dimensions.

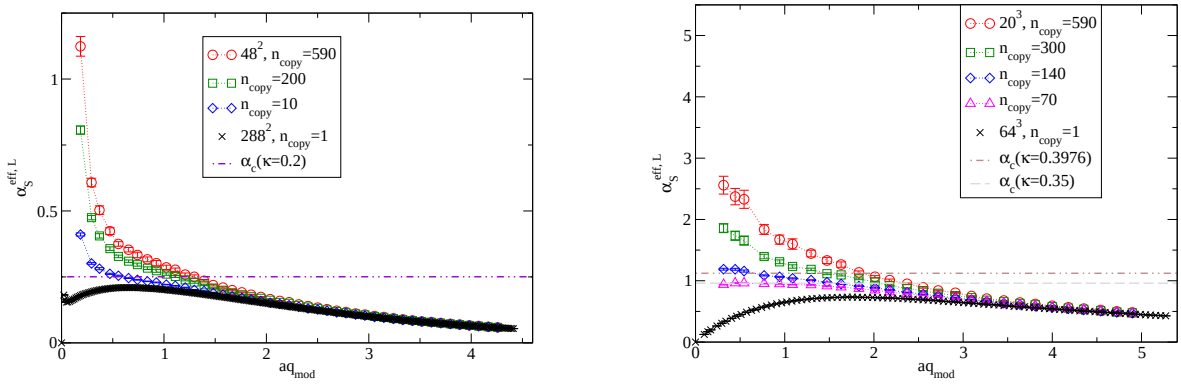

Figure 6.12: Modified definition of the effective running coupling, corresponding to its *lower* bound, in Landau max-B gauge with varying n_{copy} (see legend). *Left (a):* In two dimensions. *Right (b):* In three dimensions.

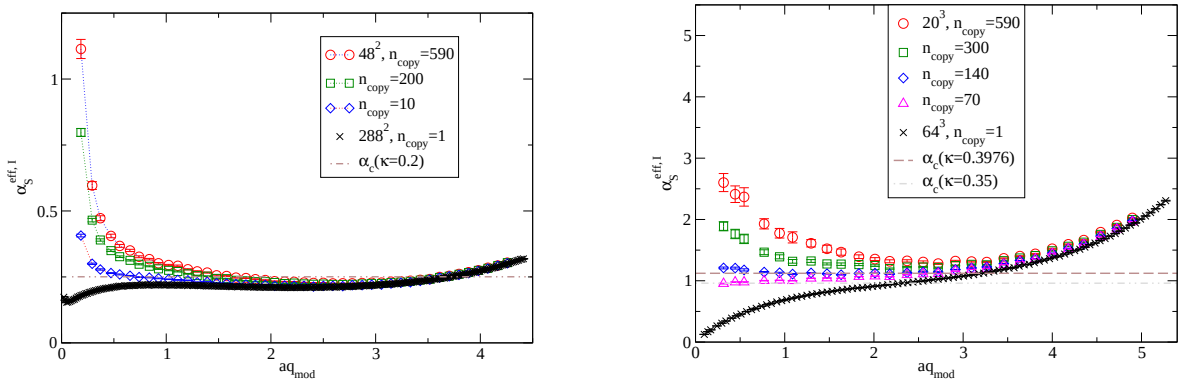

Figure 6.13: Modified definition of the effective running coupling, yielding intermediate values, in Landau max-B gauge with varying n_{copy} (see legend). *Left (a):* In two dimensions. *Right (b):* In three dimensions.

replacing the standard relation $q(k)$, eq. (2.87), by

$$(q_{\mathrm{mod}})_\mu = \frac{2}{a(\beta)} \frac{\pi k_\mu}{L_\mu}, \tag{6.2}$$

the difference to eq. (2.87) simply being the omission of the sin function via which q_μ depends on k_μ; instead, the modified dependence is linear.

This modified momentum may enter a modified definition of the effective running coupling, serving as an alternative to eq. (5.8), in different ways, depending on which powers of the momentum are replaced. We examine three possibilities.

One procedure that suggests itself is the straightforward replacement of q by q_{mod} in eq. (5.8). Since $q_{\mathrm{mod}} \geq q$, with the deviation $q_{\mathrm{mod}} - q$ growing toward larger momenta, this modified definition leads to a strong enhancement of the effective larger coupling at large momenta. Therefore, we denote this modified definition by '$\alpha_S^{\mathrm{eff,\,U}}$', with 'U' for 'upper bound'. I. e.,

$$\alpha_S^{\mathrm{eff,\,U}} = \frac{g^2}{4\pi} D_{\mathrm{gl}} D_{\mathrm{gh}}^2 (q_{\mathrm{mod}})^{2+d}. \tag{6.3}$$

In contrast, the effective running coupling becomes smaller than with the standard definition especially at large momenta if it is understood as the product of powers of dressing functions, not of propagators, multiplied by the power of momenta required to render it dimensionless, and only these latter momenta are replaced by the modified definition (6.2). I. e.,

$$\alpha_S^{\mathrm{eff,\,L}} = \frac{g^2}{4\pi} q^2 D_{\mathrm{gl}} (q^2 D_{\mathrm{gh}})^2 (q_{\mathrm{mod}})^{d-4}. \tag{6.4}$$

Here, 'L' abbreviates 'lower'. Finally, an 'intermediate' choice is also feasible, sc. to leave the power of the momenta that stem from the gluon dressing function unaffected and to replace only those related to the ghost dressing function. This yields

$$\alpha_S^{\mathrm{eff,\,I}} = \frac{g^2}{4\pi} q^2 D_{\mathrm{gl}} D_{\mathrm{gh}}^2 q_{\mathrm{mod}}^d. \tag{6.5}$$

We have applied each of these modified definitions of the effective running coupling to our data in both the two- and the three-dimensional case. The results are depicted in fig. 6.11 for $\alpha_S^{\mathrm{eff,\,U}}$, in fig. 6.12 for $\alpha_S^{\mathrm{eff,\,L}}$ and in fig. 6.13 for $\alpha_S^{\mathrm{eff,\,I}}$, always comparing $d = 2$ and $d = 3$.

We conclude from these results that whether the effective running coupling decreases at large aq or not is entirely within the uncertainty due to possible modifications of its definition. However, this does not affect the dramatic over-scaling that we have found at small lattice momenta. The discretization effects are generally larger at large aq, while the effect of Gribov copies in max-B gauge pertains mainly to the behavior at small aq.

6.3 Summary

We have studied the ghost and gluon propagators in two and three dimensions at $\beta = 0$ in Landau max-B gauge. The effect of the Gribov ambiguity turns out to be surprisingly large. This holds for the ghost propagator at small lattice momenta, and also for the lowest eigenvalue of the Faddeev–Popov operator. The effect carries over to the effective running coupling, which exhibits a dramatic 'over-scaling' at small and intermediate lattice

momenta. Despite rather extensive simulations, we have found no 'saturation' of the ghost propagator with an increasing number of gauge copies, in contrast to the gluon propagator, which proves to be much less sensitive to max-B gauge.

This behavior occurs both in two and three dimensions. This fact is notable since scaling was taken to be established in the former case and to be virtually ruled out in the latter case, based on lattice data. This constitutes some evidence against a qualitative difference between the two- and three-dimensional cases.

While over-scaling is ruled out in the continuum, these results are consistent with all members of the one-parameter family of infrared solutions found in the continuum (at finite coupling), i. e., with both a scaling behavior and a decoupling behavior. It is a significant statement that no type of solution can be excluded on the volumes used here. Gathering enough data to permit a simultaneous extrapolation to an infinite number of copies and to an infinitely large volume, if possible at all, would require yet another significant increase in the computational effort.

Moreover, we have shown that the decrease of the effective running coupling toward large lattice momenta in two and three dimensions, which is virtually unaffected by max-B gauge, is within the uncertainty due to discretization effects. But these effects do not influence the huge Gribov copy effect at small lattice momenta.

CHAPTER 7

FREE BOUNDARY CONDITIONS

Instead of explicitly changing the gauge fixing algorithm, like in ch. 4, we now alter the boundary conditions for the gauge field on the lattice (in short, the boundary conditions of the lattice). While the effect of boundary conditions generally disappear in the infinite volume limit, it is a priori possible that they induce a change in global properties of the gauge fixing, and by way of this in the infrared behavior of correlation functions, that survives this limit. We test this conjecture for the gluon propagator in various dimensions, both at $\beta = 0$ (sec. 7.2.1) and at $\beta > 0$ (7.2.2). We also study the influence of non-periodic gauge transformations on the gluon propagator in both cases (sec. 7.3).

7.1 Motivation and implementation

7.1.1 Introductory remarks

In our simulations presented so far, we have always employed periodic boundary conditions. This is the usual choice for pure Yang–Mills theory on the lattice, while dynamical fermions introduce an antiperiodicity in the temporal direction. However, it is worthwhile to try and employ a different type of boundary conditions in pure Yang–Mills theory, in particular with regard to the infrared gluon propagator. With periodic boundary conditions, lattice studies in three and four dimensions generally show an infrared non-vanishing gluon propagator at $q = 0$ when extrapolated to infinite volume [292, 266, 268, 267, 274, 275, 281, 293, 277, 278, 24], though not unanimously [285, 286]; see sec. 2.4 for an overview and more references. We have corroborated this with stochastic quantization and in the strong-coupling limit, as laid out in chapter 4 and 5, respectively. Dynamical fermions do not change the result in an essential way [269, 289].

The alternative approach involves a change of boundary conditions. It rests on an observation by Schaden and Zwanziger [366] (which has been noted, but not further pursued in [244]). The content of this observation is that free boundary conditions imply that the gluon propagator vanishes exactly at zero momentum. This is due to the relation

$$\frac{1}{V}\sum_x A^b_\mu(x) = 0. \tag{7.1}$$

Eq. (7.1) holds true for free boundary conditions, but not in the standard case of periodic boundary conditions. In the latter case, the number zero on the right hand side of eq. (7.1) is replaced by a constant, generically non-vanishing value. We explain this in sec. 7.1.2 below. The desired statement

$$D_{\mathrm{gl}}(q=0)=0 \tag{7.2}$$

follows immediately from the representation of this propagator as a Fourier transform of the spatial correlator of the gauge field, as spelled out in eqs. (2.88) and (2.89), which we repeat here for clarity,[1]

$$\begin{aligned} D_{\mathrm{gl}}(q(k)) &= \frac{1}{N_c^2-1}\frac{1}{d-1}\left\langle A_\mu^a(k)A_\mu^a(-k)\right\rangle \\ &= \frac{1}{N_c^2-1}\frac{1}{d-1}\frac{1}{V}\sum_{x,y}\left\langle A_\mu^a(x)A_\mu^a(y)\right\rangle \cos(k\cdot(x-y)), \end{aligned} \tag{7.3}$$

with $q(k)$ given by eq. (2.87) and the dot product by eq. (2.91).

Even though the expression 'free boundary conditions' may appear self-explanatory, we now state explicitly what it refers to. For simplicity, we take the lattice to be symmetric, with linear lattice extension $L_\mu = L$ for all directions μ. Free boundary conditions are obtained from periodic ones on an L^d lattice by setting the link variables $U_\mu(x^b)$ to zero whenever $x_\mu^b = L-1$, where μ is any positive direction, see fig. 7.1 for an illustration. Thus, the choice of free boundary conditions amounts to replacing a periodic lattice by a finite one, which comprises not $d\cdot L^d$ link variables like a periodic lattice does, but $d\cdot L^d - d\cdot L^{d-1} = d\cdot(L-1)\cdot L^{d-1}$ link variables.

7.1.2 A closer look

7.1.2.1 Some details concerning the proposition $D_{\mathrm{gl}}(0)=0$

Why does the important relation (7.1) hold? Intuitively, the fact that the number of sites per row of the lattice is larger by one than the number of links per row for free boundary conditions renders the Landau gauge condition more restrictive [366]. There is also a simple direct proof [366], which we briefly paraphrase here for completeness. For any direction ν ($0\le\nu\le d-1$), let the 'charge' Q_ν be defined by[2]

$$Q_\nu(x_\nu) := \sum_{\substack{x\\ x_\nu \text{ fixed}}} A_\nu(x). \tag{7.4}$$

The Landau gauge (or transversality) condition, eq. (2.11), which we repeat here,

$$\partial_\mu A_\mu(x)=0, \tag{7.5}$$

entails

$$\sum_{\substack{x\\ x_\nu \text{ fixed}}} \partial_\mu A_\mu(x)=0, \tag{7.6}$$

[1] Compared to eq. (2.89), we replace exp by cos, since the imaginary part of the exponential function, an odd function in $x=y$, vanishes after the Fourier transform in (2.89).

[2] These charges may also be used in order to define an improved criterion for the accuracy of gauge fixing, see app. B.2.2.

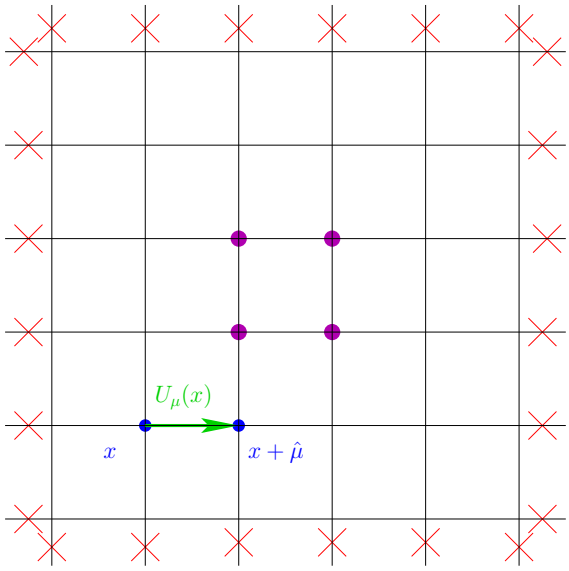

Figure 7.1: Illustration of a lattice with free boundary conditions (with $L^d = 6^2$ sites and $d \cdot (L-1) \cdot L^{d-1} = 60$ link variables). Red crosses symbolize links that are formally set to zero (these links are depicted in a split way, on both sides of the boundary of the lattice). Magenta dots denote the approximate centers of the lattice.

again for an arbitrary, but fixed ν. Hence, it follows for most charges – i. e., for all except those at a border of the finite lattice – that

$$Q_\nu(x_\nu) - Q_\nu(x_\nu - 1) = 0 \quad (0 \neq x_\nu \neq L_\nu - 1). \tag{7.7}$$

As a trivial consequence, the charges Q_ν are constant as a function of x_ν [124]. So far, this discussion applies both to free and to periodic boundary conditions. For free boundary conditions, but not for periodic ones, the charge $Q_\nu(x_\nu)$ vanishes if the coordinate x_ν takes its minimal or maximal value,

$$Q_\nu(0) = Q_\nu(L-1) = 0. \tag{7.8}$$

This immediately entails that all charges vanish,

$$Q_\nu(x_\nu) = \sum_{\substack{x \\ x_\nu \text{ fixed}}} A_\nu(x) = 0. \tag{7.9}$$

Eq. (7.9) can be summed over x_ν, yielding

$$\sum_x A_\nu(x) = 0. \tag{7.10}$$

The left hand side of (7.10) is proportional to $\tilde{A}_\nu(q = 0)$, which thus vanishes for any ν. Obviously, this implies that the gluon propagator, eq. (7.3), vanishes as well.

A vanishing gluon propagator at zero momentum is incompatible with the decoupling solution and constitutes some evidence for scaling. While it is clearly not a sufficient condition for the latter type of solution, it is a priori possible that free boundary conditions

could provide a way to obtain this solution on the lattice. While it might be argued that the effects of boundary conditions should be expected to disappear in the thermodynamic limit of infinite lattice volume, there is also room for the justified hope that a solution different from the usual lattice scenario could survive this limit due to a change in global properties of the gauge fixing. The potentially huge impact of changes in the gauge fixing procedure is demonstrated by our results in ch. 6.

Two steps would be required in order to establish such a different solution: first, to study the behavior of the gluon propagator at non-zero momenta, controlling the volume effect; and second, to examine the ghost propagator and to compare it with the gluon results. Of course, if the first step does not yield a significant change compared to standard lattice results, the prospects for the second step are rather dim. In a nutshell, this will be our main finding.

To our knowledge, we present here the first numerical investigation of the gluon propagator with free boundary conditions. We again study pure $SU(2)$ Yang–Mills theory in Landau gauge. Previously, another type of non-trivial boundary conditions, sc. twisted boundary conditions, was explored in lattice Landau gauge in [367]. In this case, no such statement as (7.2) can be made a priori. Still, like our explorations, this study was motivated by the prospect of possibly inducing a decisive change of the infrared gluon propagator. However, the outcome was that with twisted boundary conditions, the gluon propagator does not qualitatively alter its infrared behavior. Its values at small and intermediate momenta are somewhat smaller compared to periodic boundary conditions, but this difference decreases toward larger volumes [367].

7.1.2.2 Modified definition of the gluon propagator

Our analysis of free boundary conditions is complicated by a consideration which forces us to pursue significantly enlarged numerical efforts. This consideration is that the propagator calculation involves a discrete Fourier transform, which is not defined on a finite lattice due to the absence of periodic functions. Put differently, the standard definition of the gluon propagator, eq. (7.3), prescribes to calculate the correlator of the gluon field at points that are connected by the shortest path. If free boundary conditions are used, this path may intersect the boundary of the finite lattice. In order to avoid this, we employ the alternative definition of the gluon propagator[3]

$$D^f_{\mathrm{gl}}(q) = \frac{1}{2^d}\sum_C \frac{1}{N_c^2-1}\frac{1}{d-1}\sum_x \left\langle A^a_\mu(x)A^a_\mu(C)\right\rangle \cos\left(q\cdot(x-C)\right). \tag{7.11}$$

Here, C refers to any of the 2^d approximate centers of the finite lattice, i. e., all those points whose every coordinate is either $L_\mu/2$ or $L_\mu/2-1$, illustrated by the magenta dots in fig. 7.1. Still, a loss of statistics by a factor $V/2^d$ ensues. In practice, this means that instead of $\mathcal{O}(10^2)$ measurements for a clear result for the gluon propagator (like with the standard definition), $\mathcal{O}(10^5)$ independent configurations are required even on moderately sized lattices in order to avoid overly large statistical fluctuations. On huge lattices, the

[3]The upper 'f' is usually omitted in the following, as it would unnecessarily complicate the comparison with results from periodic boundary conditions and from non-periodic gauge transformations. Instead, the legends of the plots clarify which boundary conditions are used, which determines the gluon propagator definition that is used.

number of required configurations is even substantially higher. The largest lattices for which we have produced results with good statistics with free boundary conditions are 280^2, 60^3 and 32^4. In contrast, with periodic boundary conditions, we have been able to investigate lattices as large as 2560^2 (at finite coupling, not shown in this chapter, but in fig. 4.7) and 160^4. We now turn to the results for the gluon propagator on lattices with free boundary conditions, employing the modified definition (7.11).

7.2 Results

We have carried out simulations in different dimensions, both at finite coupling and in the strong-coupling limit. Apart from the alternative boundary conditions, standard methods are used for the generation of configurations and for fixing them to Landau gauge. To be specific, the generation of configurations is performed with a heat-bath algorithm (app. B.1.4) at finite coupling, and simply according to the Haar measure at $\beta = 0$ (app. B.1.4.2). Gauge fixing is done by stochastic overrelaxation with the overrelaxation parameter p adapted depending on the lattice size for fast convergence, see app. B.2.1.2.

The results at $\beta = 0$ and at finite coupling are now explored in turn.

7.2.1 Strong-coupling limit

Already chs. 5 and 6 are concerned with the strong-coupling limit. It is worth emphasizing again that while results obtained in this limit are open to some objections due to its not fully physical nature, this limit is useful here since a scaling behavior may a priori be expected at *all* lattice momenta in this case (see sec. 5.1.1), allowing for a comprehensive estimate of the deviation from this ideal behavior. Note, however, that strong-coupling studies with periodic boundary conditions have seen the appearance of a scale separating a 'scaling branch' at large lattice momenta from a 'decoupling branch' at small lattice momenta, for both the gluon and the ghost propagator [295, 221, 296]. The origin of this scale remains to be understood, see ch. 5.

Our extensive and numerically expensive investigations in various dimensions indicate a rather simple fact, sc. that there is a common infinite volume limit of the gluon propagator with free boundary conditions on the one hand and with periodic boundary conditions on the other hand. Therefore, investigating the (computationally demanding) ghost propagator in addition to the gluon appears not very promising, the more so as its implementation would first require an appropriate change of its definition.

Two dimensions. In two dimensions, where scaling would usually be expected also on the lattice (but see our results in ch. 6), a deviation from this behavior is visible only at small lattice momenta aq and appears to be a finite volume effect, see fig. 7.2. The data for periodic b.c. from ch. 5 are included in this fig. in order to facilitate a comparison. For periodic resp. free b.c., the gluon propagator at small aq is larger resp. smaller than predicted for the scaling solution.[4] At large and especially at intermediate aq, the locally obtained power-law exponent is close to the expected one, cp. sec. 5.2.2.1.

[4]The data with periodic b.c. are the same as in ch. 5, fig. 5.1.

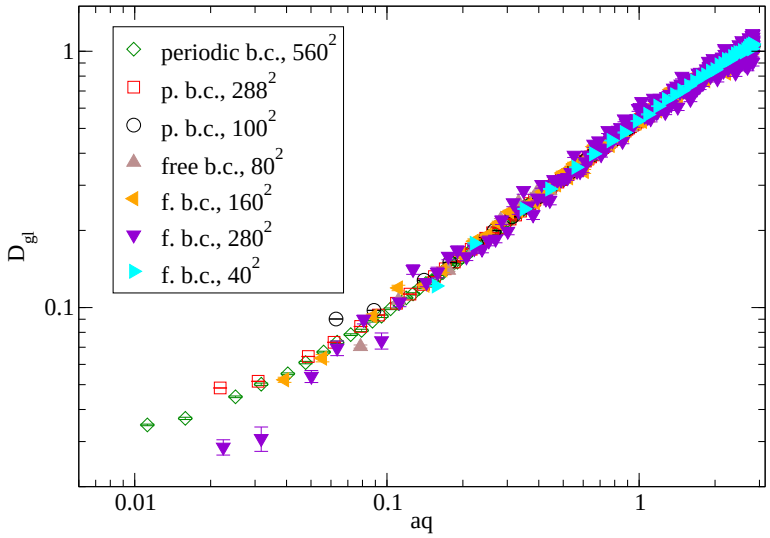

Figure 7.2: Gluon propagator in the strong-coupling limit in two dimensions. Free vs. periodic boundary conditions (see also ch. 5 for the data in the latter case). About 500,000 independent configurations for each of the larger lattices with free boundary conditions. Here and in the following, the 'center definition', eq. (7.11), has been used for the gluon propagator with free b. c.

Three dimensions. In three dimensions, where the decoupling branch with periodic b. c. survives in the infinite volume limit, see sec. 5.2.2.2, the data from free boundary conditions even slightly 'overshoot' the periodic b. c. data. While the free b. c. data show a scaling branch at large lattice momenta in agreement with the periodic b. c. data, a uniform scaling at all lattice momenta is ruled out by the data for free b. c., see fig. 7.3. We emphasize again that these statements always refer to the appropriately modified definition for the gluon propagator in the case of free b. c., the 'center definition' given in (7.11).

Four dimensions. The four-dimensional case resembles the three-dimensional case. As is apparent from fig. 7.4, with free b. c., only the gluon propagator at the lowest possible lattice momentum deviates significantly from the periodic b. c. case. Since the value of this momentum decreases with increasing lattice volume, the agreement between periodic and free b. c. data improves.

A note on the statistics. The approximate numbers of 'measurements' at $\beta = 0$ on each of the lattice sizes shown here are indicated in the following table. The numbers for periodic boundary conditions (with standard gauge transformations) are mostly given in the legends to fig. 5.1 ($d = 2$, ad fig. 7.2) and fig. 5.5 ($d = 3$, ad fig. 7.3). In $d = 4$ (fig. 7.4), we have used 778 independent configurations on 40^4.

V	40^2	80^2	160^2	280^2	20^3
nr. of config's	$4.0 \cdot 10^5$	$3.3 \cdot 10^5$	$5.8 \cdot 10^5$	$4.8 \cdot 10^5$	$3.6 \cdot 10^5$
	40^3	60^3	10^4	16^4	22^4
	$2.6 \cdot 10^6$	$1.0 \cdot 10^6$	$1.2 \cdot 10^5$	$2.5 \cdot 10^5$	$4.3 \cdot 10^5$

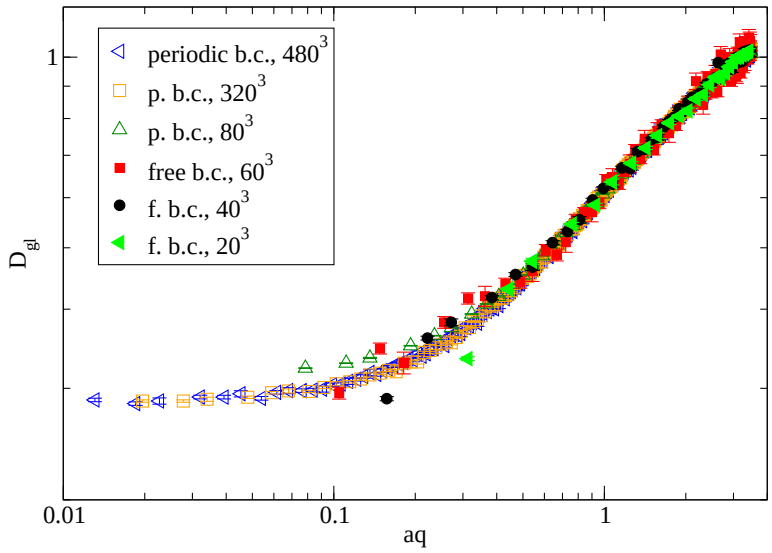

Figure 7.3: Gluon propagator in the strong-coupling limit in three dimensions. At small lattice momenta, the gluon propagator with periodic resp. free b. c. decreases resp. increases with the volume. Number of configurations for the free b. c. case: $N \approx 10^6$ for $V = 60^3$ and $N \approx 2.5 \cdot 10^6$ for $V = 40^3$.

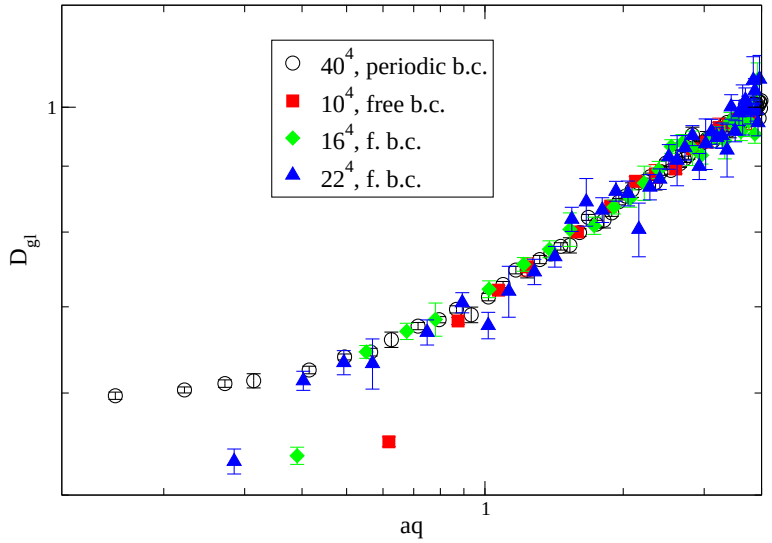

Figure 7.4: Gluon propagator in the strong-coupling limit in four dimensions. On the 22^4 lattice with free b. c., more than 400, 000 configurations.

7.2.2 Finite coupling

We have also carried out simulations with free boundary conditions at finite coupling, sc. at $\beta = 4.2$ in three dimensions and at $\beta = 2.2$ in four dimensions.

Three dimensions. The result in three dimensions for $V = 60^3$ mainly serves an illustrative purpose, as we have not performed a finite volume analysis here, see fig. 7.5. We have not done so for the following reason. In $d = 3$, the gluon propagator with periodic b. c. has a peak at $q \approx 350\,\mathrm{MeV}$, as found in [258] with a standard method and confirmed by us with stochastic gauge fixing, see sec. 4.3.1.2. Even though it clearly does not go to zero at vanishing momentum, this decrease toward the infrared makes it more difficult to see a difference to the free b. c. behavior. With free boundary conditions, 60^3 is the largest volume we have simulated in three dimensions, as the number of measurements required (here, we have used $1.76 \cdot 10^5$ ones) makes the simulations computationally expensive. A significant difference below the peak is visible, but only at a single non-vanishing momentum.

Four dimensions. In four dimensions, the difference is easier to detect, since the gluon propagator with periodic b. c. is approximately constant at the smallest momenta, i. e., it hardly decreases toward $q = 0$ within standard Landau gauge. A comparison of periodic and free b. c. data is presented in fig. 7.6. The periodic b. c. data in this figure have been produced with stochastic gauge fixing on a 40^4 lattice (already presented in ch. 4) and with standard gauge fixing on 160^4. As we have shown in ch. 4, stochastic gauge fixing makes no difference to standard methods as far as the propagators at accurate gauge fixing are concerned. The finite volume effect for free b. c. appears strong enough to be consistent with a common infinite volume limit of periodic and free b. c. This corresponding effect for periodic b. c. is weaker (see e. g. [273, 272, 285, 286, 122]), which is also visible from the data presented in fig. 7.6, comparing the 40^4 and 160^4 lattices.

A lattice with 160^4 points, as used here, corresponds at $\beta = 2.2$ to a linear lattice extension of approx. 34 fm. We have used $4^4 = 256$ computing cores for this parallel simulation. Accordingly, much larger lattices are currently hardly accessible even on rather large computing clusters. So, our current simulations should give a good idea of the volume effect. The free b. c. simulations, on the other hand, are all just parallel in a trivial sense (production runs are performed with different random number seeds in parallel, but the lattice is not distributed onto different processes). This is because the number of measurements required in order to obtain a clear result from the center definition of the gluon propagator, eq. (7.11), is enlarged by a factor $V/2^d$ compared to the standard definition. This renders this number so large that lattice volumes which require more than a single computing core are inaccessible for practical purposes.

A more quantitative analysis of the finite volume effect for free b. c. proves difficult, since there is only a small number of momentum values in the infrared where the result differs from the one with periodic b. c. Only on a lattice as large as 32^4, requiring approx. 10^6 meas., there are two momentum values at which the free and periodic b. c. results differ non-trivially.

Note on the statistics. The numbers N of 'measurements', i.e., uncorrelated configurations, at finite coupling on various volumes V with standard free b. c. are as follows.

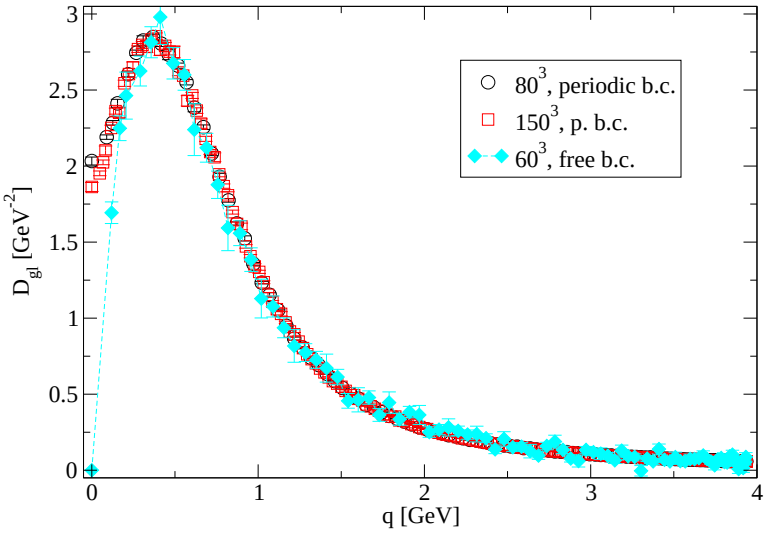

Figure 7.5: Gluon propagator in three dimensions with periodic vs. free b. c. at finite coupling, sc. $\beta = 4.2$. Periodic b. c. results in this case obtained with stochastic gauge fixing, see ch. 4. For free b. c., approx. 178,000 measurements. The line is drawn to guide the eye.

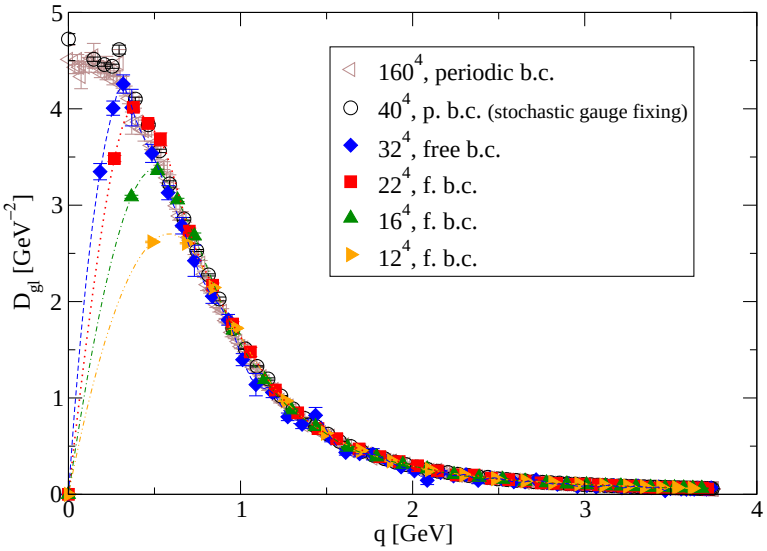

Figure 7.6: Gluon propagator in four dimensions with periodic vs. free b. c. at finite coupling, sc. $\beta = 2.2$. The lines are spline interpolations to guide the eye.

V	60^3	12^4	16^4	22^4	32^4
N	$1.8 \cdot 10^5$	$1.5 \cdot 10^5$	$1.3 \cdot 10^5$	$1.5 \cdot 10^5$	$0.96 \cdot 10^5$

The corresponding numbers for periodic b. c. are given in the following table.

V	80^3	150^3	40^4	160^4
N	1280	874	1145	144

All data with periodic b. c. at finite coupling used here, with the exception of those on the 160^4 lattice, have been produced by stochastic quantization (ch. 4), which yields at sufficiently small Δ^2 results indistinguishable from standard gauge fixing, as we have demonstrated in ch. 4.

7.3 Non-periodic gauge transformations

It is possible to change the configurations in a different way, which may at first seem to constitute a milder change, since some periodicity is conserved, but which might nevertheless exert a stronger effect on the infrared gluon propagator. The basic idea is to perform non-periodic gauge transformations of a periodic configuration. This has a similar effect on the gluon propagator at zero momentum as free boundary conditions, with the difference that $D_{\mathrm{gl}}(0) = 0$ is not an exact identity, but holds only in the infinite volume limit (if non-periodic gauge transformations are combined with periodic boundary conditions, sec. 7.3.1.2).

For simplicity, we again describe the implementation on symmetric lattices with $L_\mu = L$ for all directions μ. The generalization to asymmetric lattices is straightforward, but not needed here.

7.3.1 Implementation

We have implemented the basic idea of non-periodic gauge transformations in two different ways, which indeed yield quite different results, although these may well converge against the same value in the limit of infinite lattice volume. Roughly speaking, these gauge transformations can be combined either with free or with periodic boundary conditions. We explain the two alternatives in turn.

7.3.1.1 First possibility: Non-periodic gauge transformations combined with free boundary conditions

The first way to implement non-periodic gauge transformations on an L^d lattice proceeds as follows. A periodic configuration on a slightly smaller symmetric lattice is generated, sc. on one of volume $(L-1)^d$, with an appropriate algorithm for the dynamics. At finite coupling, we employ, as usual, the heat-bath algorithm (app. B.1.4) to this end. The corresponding numerical routine is rewritten in order to handle odd lattice extensions. At $\beta = 0$, the implementation is simpler, as all links are independent, see app. B.1.4.2.

Every configuration thus generated is subsequently embedded into an L^d lattice. Obviously, not all links of the L^d lattice are assigned values thereby. The links that are not

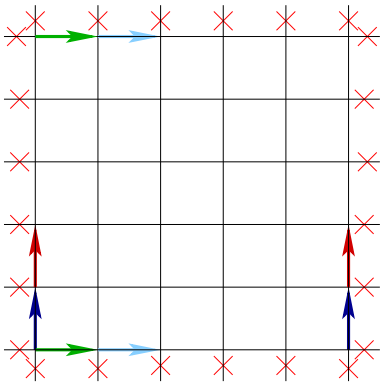

Figure 7.7: Illustration of a lattice with free boundary conditions and non-periodic gauge transformations. Red crosses again symbolize links that are formally set to zero (thus implementing free b. c.) and that are again depicted in a split way (like in fig. 7.1), links of the same color take the same value (for the method of non-periodic g. t.).

assigned values are those links emanating in positive directions from lattice sites having a coordinate that takes the maximal value (i. e., $L-1$ if counting starts at 0). There are two types of such links: (i) those perpendicular to that surface of the smaller hypercubic lattice to which the site from which they emanate belongs, and (ii) those that lie in that surface. Those of the first type (perpendicular), symbolized by red crosses in fig. 7.7, are formally set to zero in order to implement free boundary conditions. Doing so ensures that eq. (7.8) is satisfied. Those of the second type (inside the surface) are of the form $U_\mu(x)$ with $x_\nu = L-1$ for some $\nu \neq \mu$. They are assigned the same values as the links parallel to them with $x_\nu = 0$ and otherwise identical coordinates, see the colored arrows symbolizing links in fig. 7.7 for an illustration (only a few such identifications are made explicit in this figure). Now, crucially, gauge fixing is performed. The gauge transformations take place on a finite lattice. Hence, they are non-periodic. During gauge fixing, those (parallel) links of the free b. c. lattice that are initially chosen to be periodic remain periodic up to gauge transformations.

The configurations that can thus be obtained are a proper subset of all configurations with free boundary conditions. Therefore, in this sense, the new condition is more restrictive (even though, as remarked above, it may at first glance seem milder, since some specific kind of periodicity is conserved). As a corollary, the lattice is again non-periodic, and it is mandatory to use a modified definition of the gluon propagator, for which we choose eq. (7.11) as before. This again greatly enlarges the numerical effort compared to the case of periodic boundary conditions.

7.3.1.2 Second possibility: Non-periodic gauge transformations combined with periodic boundary conditions

There is another way of implementing non-periodic gauge transformations, which permits to employ the usual definition of the gluon propagator. It differs from the first way only with respect to the last step, sc. regarding the way the gluon propagator is calculated. The dynamics and the gauge fixing are identical. But the gluon propagator is calculated on the ensemble of configurations on the $(L-1)^d$ lattice. As this (smaller) lattice has periodic

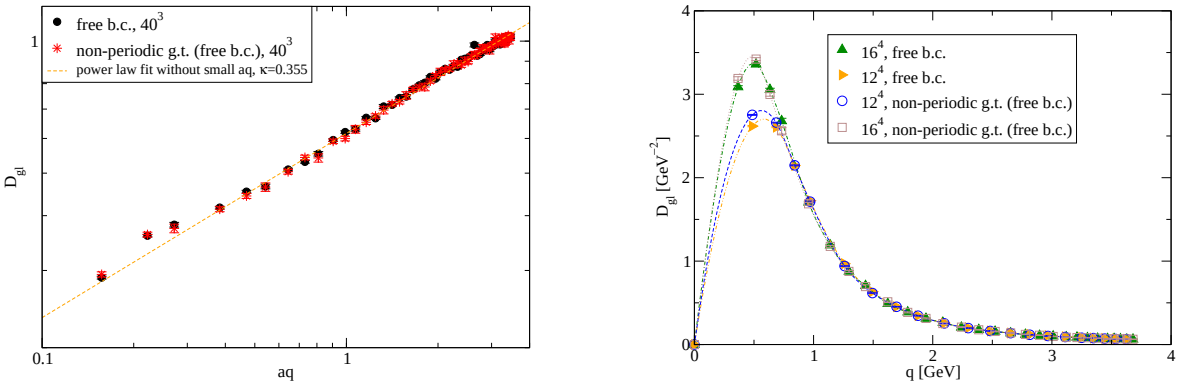

Figure 7.8: Comparison of 'standard' free b. c. with the method of non-periodic gauge transformations on free b. c. lattice. *Left (a):* At $\beta = 0$ in $d = 3$. $1.4 \cdot 10^6$ configurations for non-periodic g. t. on free b. c. lattice (vs. $2.6 \cdot 10^6$ for usual free b. c.). The fit is to the former data from the sixth non-vanishing momentum onwards. *Right (b):* At finite coupling, $\beta = 2.2$, in $d = 4$. Lines are spline interpolations.

boundary conditions, the usual definition of the gluon propagator, eq. (7.3), can be used. This allows to obtain results with satisfactory statistical accuracy on much larger lattice volumes. Larger lattices are indeed necessary in this case, as our results demonstrate, to which we now turn.

7.3.2 Results

7.3.2.1 Regarding the first possibility

When implementing non-periodic gauge transformations in combination with free boundary conditions, the gluon propagator at zero momentum is again bound to vanish exactly, as this is just a special case of free boundary conditions, see sec. 7.1.

Our results at $\beta = 0$ are shown in fig. 7.8a (for the three-dimensional case), and those at finite coupling in fig. 7.8b (in four dimensions). For comparison, we include results from 'standard' free boundary conditions in both cases. The differences between the results with and without non-periodic gauge transformations are small; at $\beta = 0$, they are insignificant. In particular, at $\beta = 0$, the same deviation from a uniform scaling behavior at small lattice momenta is visible as with 'standard' free boundary conditions (sec. 7.2.1).

We stress that again, a large number of measurements (essentially the same as for standard free b. c.) is required in order to verify the seemingly simple result that non-periodic gauge transformations induce no crucial change in this case. For example, from the first 130,000 configurations with non-periodic gauge transformations out of the 1.4 million ones included in the results of fig. 7.8a, a fit of the function $D_{\mathrm{gl}} = c \cdot (aq)^{4\kappa-1}$ to the data yields the value $\kappa = 0.354(2)$ with $\chi^2/\mathsf{ndf} \approx 0.97$. This could lead to the conclusion that a uniform scaling behavior at all lattice momenta is observed, which would be a very remarkable and novel result. However, this conclusion would be premature. With ten times as many measurements, χ^2/ndf for this fit increases to ≈ 1.96. The usual free boundary conditions ($2.6 \cdot 10^6$ measurements) yield $\chi^2/\mathsf{ndf} \approx 3.2$. Thus, this fit is in both cases unsatisfactory once sufficiently many configurations are employed.

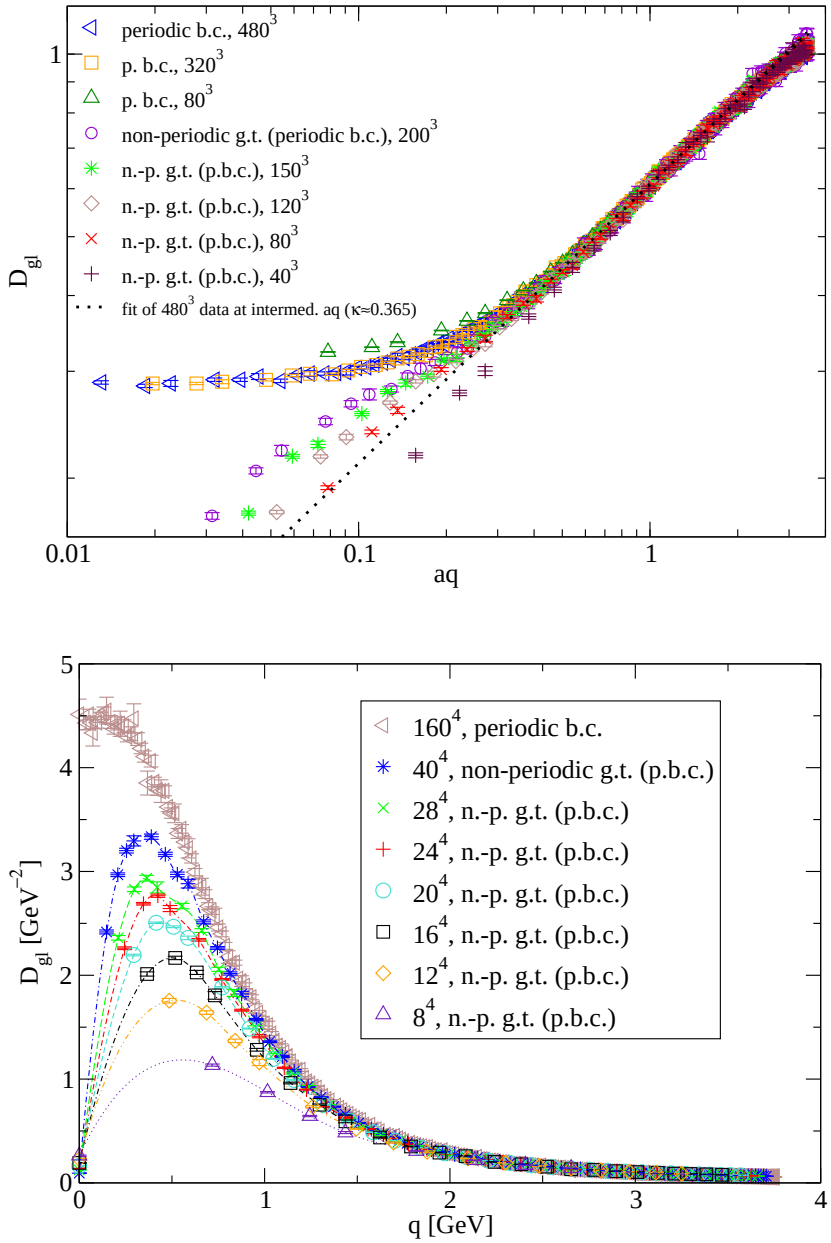

Figure 7.9: Non-periodic g. t. on periodic b. c. *Top (a):* At $\beta = 0$ in $d = 3$, contrasted with results from the standard procedure. The dotted line is a fit to standard results at intermediate aq. *Bottom (b):* At $\beta = 2.2$ in $d = 4$, contrasted with the largest lattice from the standard procedure. Lines are spline interpolations.

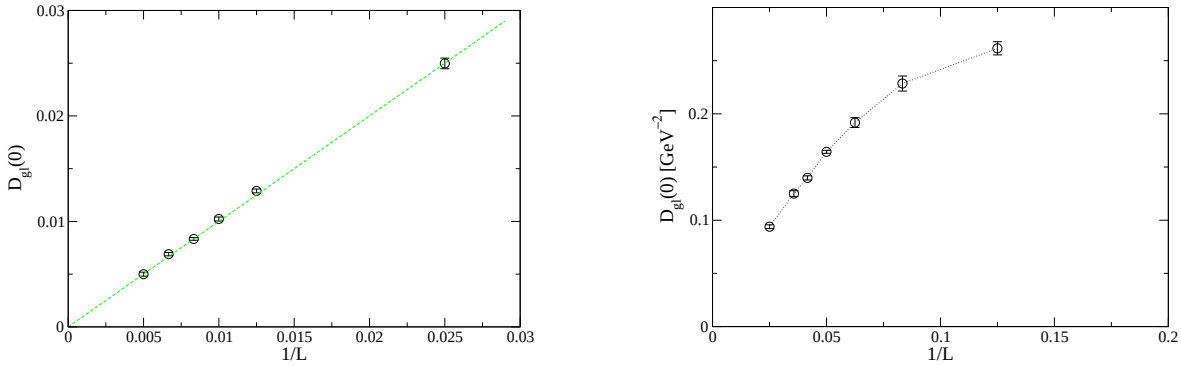

Figure 7.10: Finite volume behavior of the gluon propagator at vanishing momentum from non-periodic g. t. on periodic b. c. *Left (a):* At $\beta = 0$ in $d = 3$, data from fig. 7.9a. The green line represents the function $D_{\mathrm{gl}}(0) = 1/L$. *Right (b):* At $\beta = 2.2$ in $d = 4$, data from fig. 7.9b. Line is drawn to guide the eye.

7.3.2.2 Regarding the second possibility

The main results from non-periodic gauge transformations combined with periodic boundary conditions are shown in fig. 7.9, again both for the strong-coupling limit in three dimensions (fig. 7.9a) and for finite coupling in four dimensions (fig. 7.9b). In both cases, we compare the results directly with those obtained on lattices with periodic boundary conditions. It is apparent from fig. 7.9 that the gluon propagator at non-zero momenta increases with the lattice volume, like for free boundary conditions both with and without non-periodic gauge transformations. However, the volume effect is much weaker. Indeed, the result on an 80^3 lattice is not far from a uniform scaling behavior. But the $V \to \infty$ extrapolation is far from such a behavior, even though not much more can be said about the result of this extrapolation. The reason why the volume dependence is so weak here is not clear, and we will not indulge in speculations. It is a surprising fact.

As noted in sec. 7.3.1 above, we can employ in this case the standard definition of the gluon propagator. This allows us to obtain a clear picture from a few hundred configurations for each set of parameters. At $\beta = 0$ in three dimensions (fig. 7.9a), we have used more than 1000 measurements for most values of β (about 400 for 200^3). At $\beta = 2.2$ in four dimensions (fig. 7.9b), some numbers are: more than 2000 for 20^4 and about 500 for 40^4.

As this version of non-periodic gauge transformations comes without free boundary conditions, the gluon propagator at zero momentum does not anymore vanish exactly. However, it does vanish in the limit of infinite volume. This can be inferred from the data shown in fig. 7.10. The behavior at $\beta = 0$ in three dimensions (fig. 7.10a) is especially striking. Here, $D_{\mathrm{gl}}(0)$ as a function of L is well described by the function $1/L$ (the corresponding straight line in fig. 7.10a is not a fit).

Hence, the finite volume behavior of $D_{\mathrm{gl}}(0)$ and that of $D_{\mathrm{gl}}(aq > 0)$ are just the opposite of one another if non-periodic gauge transformations are combined with periodic boundary conditions. The former quantity decreases with growing volume, while the latter quantities increase. No convergence can be inferred from the data. The data on moderate and large volumes are already clearly above a uniform scaling branch, which is indicated by the broken line in fig. 7.9a. Hence, at non-zero aq, uniform scaling is again not obtained for large volumes. But it is an open question whether the same decoupling branch as with

the other methods develops in this case. In order to possibly clarify this, huge lattices will need to be used; however, we have drawn a line here.

7.4 Summary

We have considered and implemented a change of boundary conditions that makes the gluon propagator exactly vanish at zero momentum. Thus, it possesses by default an important property that is at odds with a decoupling-type behavior and in line with the scaling solution.

The definition of the gluon propagator needs to be modified due to the lack of periodicity of the lattice. This greatly enlarges the numerical effort. We have analyzed the finite volume behavior of the gluon propagator both with periodic and with free boundary conditions. We have done so in two, three and four dimensions and both at finite coupling and at $\beta = 0$. In three and four dimensions, we have found that the 'glimpse of scaling' which is enforced in the latter case does not carry over to non-zero momenta, given that sufficiently large lattice volumes are considered.

Non-periodic gauge transformations can be implemented in combination either with free or with periodic boundary conditions. The first choice yields essentially the same results as usual free boundary conditions. For the second choice, a uniform scaling behavior is again not visible on large volumes, and a decoupling branch might again be reached in the $V \to \infty$ limit, although the hypothetical approach to it is much slower. Interestingly, this finite volume behavior is at odds with a priori expectations, as the combination with periodic boundary conditions should be expected to lead instead to a faster approach to the usual solution. Hence, it might be speculated that this is a signature for a relevant change in properties of the gauge fixing procedure, brought about by non-periodic gauge transformations. Therefore, the second choice may deserve further investigation.

Apart from this surprising fact, the upshot is as follows. While it is a priori possible that the modification of boundary conditions might change global properties of the gauge fixing, we find a posteriori that this does not occur, at least not to a degree sufficient to change the infrared behavior of the gluon propagator at non-zero momenta in a qualitative manner.

This concludes our extensive studies of the infrared Yang–Mills propagators with regard to the confinement mechanism and the intricacies of gauge fixing (chs. 4, 5, 6 and the present one). We will provide a combined summary in ch. 10 (sec. 10.1.1).

While the next chapter still deals with infrared properties of the gluon propagator in Landau gauge, we shift our focus from the mechanism of confinement to the deconfinement phase transition at finite temperature. In that context, gauge fixing is still required, but it is less afflicted with the problems and subtleties studied in detail in the foregoing chapters.

CHAPTER 8

DECONFINEMENT TRANSITION AT NON-ZERO TEMPERATURE

After a number of investigations of pure $SU(2)$ Yang–Mills theory at zero temperature in the foregoing chapters, we now analyze the behavior of the gluon propagator at non-zero temperature in $2+1$ dimensions. Details on the motivation and implementation are provided in sec. 8.1. Sec. 8.2 is devoted to numerical results, in particular at temperatures around the deconfinement phase transition. These results give information about signals of this transition from the chromoelectric and chromomagnetic sectors of the theory, as encoded in the gluon propagator.

8.1 Introduction

8.1.1 Motivation

The present chapter is the first of two chapters which are concerned with aspects of the phase diagram of QCD, albeit indirectly so and in rather different ways. We explore non-zero density in the Thirring model in ch. 9, where we also make some general remarks on the phase diagram. The subject of the present chapter is the deconfinement transition of pure $SU(2)$ Yang–Mills theory in $2+1$ dimensions at vanishing chemical potential μ. Again, lattice gauge theory is studied in the quenched approximation. While full QCD as it is realized in nature – in four spatio-temporal dimensions, with gauge group $SU(3)$ and including dynamical fermions – exhibits a crossover at $\mu = 0$ [368], the quenched $SU(3)$ gauge theory in four dimensions undergoes a first-order transition [369]. With the gauge group $SU(2)$, which we study throughout this work, the transition is of second order both in three $(2+1)$ and four $(3+1)$ dimensions.

The four-dimensional case has been investigated of late in ref. [370] with a combination of lattice simulations and Dyson–Schwinger equations, and considering both the deconfinement transition and the chiral transition at which chiral symmetry is restored. As a side note, a recent new path to study the relation between confinement and chiral symmetry breaking revolves around dual observables, which have been proposed first on the

lattice [371] and have been explored both in lattice simulations, e. g. [372, 373, 374, 375], and with functional methods [376, 121, 120] (see [370] for further references). However, we focus exclusively on the deconfinement transition. For our purposes, an especially interesting finding of ref. [370] is that the deconfinement temperature in $3+1$ dimensions can be extracted from properties of the gluon propagator. We complement these studies in $2+1$ dimensions, where we are able to simulate the theory on a much finer grid along the temperature axis.

8.1.2 Non-zero temperature on the lattice

8.1.2.1 Implementation

In continuum field theory, treating the case of non-zero temperature entails that the time direction is compactified. Since any lattice in numerical simulations is of finite extent, the implementation of non-zero temperature in lattice gauge theory is straightforward. Namely, the temperature is the inverse temporal lattice extension. This extension is simply the product of the number L_t of lattice points in that direction and the lattice spacing a, which is here always taken not to depend on the direction. The lattice spacing is determined by the lattice coupling β (eq. (2.68)) and the number d of dimensions. Hence, the temperature is[1]

$$T = \frac{1}{L_t\, a(\beta)}. \tag{8.1}$$

In order to simulate the theory at non-zero temperature, $L_t \ll L_s$ is chosen. To this end, we have generalized our C++ code originally designed for the various results on symmetric lattices such that it also allows for asymmetric lattices of volume $L_s^{d-1} \times L_t$ with $L_s \neq L_t$. This contrasts with the studies of chs. 4 through 7, which pertain to pure Yang–Mills theory at vanishing temperature, implemented by choosing $L_s = L_t$. – Obviously, changing L_t permits only a very coarse tuning of the temperature. In practice, therefore, the lattice coupling β is adapted in fine steps in order to obtain many different temperatures, see sec. 8.2.1.2 for details.

A major aim of these investigations is to test whether gauge-invariant properties of the deconfinement transition of pure Yang–Mills theory can be extracted from gauge-dependent correlation functions, in particular, from the gluon propagator. This complements standard approaches which employ the Polyakov loop (also referred to as thermal Wilson line), a gauge-invariant quantity. We now very briefly review the definition and basic properties of the Polyakov loop. The calculation of its values in the course of our simulations is required order to filter for the positive Polyakov loop sector, which in turn is necessary for a correct determination of the gluon propagator (see sec. 8.1.2.4).

8.1.2.2 Polyakov loop

The Polyakov loop is a specific Wilson loop (see sec. 2.3.1.2), sc. one corresponding to a straight contour that winds in temporal direction around the compactified lattice. On the lattice, the Polyakov loop is given by the average trace of the product of link variables along

[1] An implicit dependence of $a(\beta)$ on d is understood.

such a contour,

$$\Phi = \frac{1}{V_s}\sum_{\vec{x}}\Phi(\vec{x}) = \frac{1}{V_s}\sum_{\vec{x}}\left[\frac{1}{N_c}\mathrm{tr}\,P(\vec{x})\right] \tag{8.2}$$

with the 'spatial volume' $V_s = L_s^{d-1}$ and the holonomy

$$P(\vec{x}) = \prod_{x_0=0}^{L_t-1} U_0(x_0,\vec{x}). \tag{8.3}$$

$P(\vec{x})$ is topologically nontrivial, as it cannot be continuously contracted to a point; in other words, it is null-homotopic. Evidently, Φ is a gauge-invariant quantity, as is the trace of any Wilson loop.

The Polyakov loop is related to the free energy of a single static quark, denoted by '$\hat{F}_Q$' in lattice units, by [377]

$$|\langle\Phi\rangle| \propto \exp\left(-\hat{F}_Q L_t\right). \tag{8.4}$$

If the Polyakov loop vanishes, the static quark possesses an infinitely large free energy, which implies that it is confined. Hence, the Polyakov loop serves as an order parameter for confinement, related to global center symmetry. But it does strictly so only in the quenched limit, where the quarks are infinitely heavy, $m_q \to \infty$. In this limit, the Polyakov loop vanishes exactly in the confined phase. From eq. (8.4), this is equivalent to the free energy of a static quark being infinite, entailing confinement. In practice, the expectation value of the absolute value of Φ is calculated, i. e., the quantity $\langle|\Phi|\rangle$, since $\langle\Phi\rangle = 0$ in finite volumes. In the infinite volume limit, this does not make a difference, $\langle|\Phi|\rangle = |\langle\Phi\rangle|$. – On the other hand, if the masses of dynamical quarks are finite, center symmetry is explicitly broken.

8.1.2.3 Deconfinement transition on the lattice

It is well known from lattice simulations that pure $SU(2)$ Yang–Mills theory in three dimensions at vanishing chemical potential, but non-zero temperature exhibits a second-order phase transition [378] in the universality class of the two-dimensional Ising model [379], as shown in ref. [380], in line with a conjecture by Svetitsky and Yaffe [381]. A second-order phase transition is characterized by a divergent correlation length close to the critical point. More specifically, the correlation length diverges like

$$\xi \propto \left(\frac{\beta}{\beta_c} - 1\right)^{-\nu} \tag{8.5}$$

with a critical exponent ν and a critical value β_c of the lattice coupling. The behavior of other quantities in the vicinity of the critical point defines further critical exponents. For example, the critical exponent β is defined[2] via the (absolute value of) the Polyakov loop (resp. via the magnetization of a ferromagnet), and γ via the corresponding susceptibility. Values of the critical exponents of the Ising model in two spatial dimensions are $\nu = 1$, $\beta = 1/8$, and $\gamma = 7/4$ [382]. We concentrate on the critical exponent ν, which we aim to extract from the electric screening mass, see the remarks around eq. (8.12) below.

[2]The use of the symbol 'β' here is unrelated to its other occurrences throughout this thesis (where it denotes the lattice coupling or the β-function).

8.1.2.4 Gluon propagator and its role

Our investigations are in part motivated by results recently obtained in $3+1$-dimensional pure Yang–Mills theory with the gauge groups $SU(2)$ and $SU(3)$ [370]. It has been found that the gluon propagator is sensitive to the deconfinement phase transition, but that this essentially does not hold for the ghost propagator, in line with results from functional methods [383]. For this reason, and also in view of the intricacies related to the dramatic gauge-copy dependence of the infrared ghost propagator (as shown in ch. 6), we focus here exclusively on the gluon propagator. Since its calculation is numerically much cheaper than an accurate ghost propagator calculation, it is feasible to study temperatures close to the phase transition in quite some detail.

Yang–Mills propagators at non-zero temperature have been investigated on the lattice e. g. in refs. [384, 385, 386, 387, 383, 388, 370], sometimes also for the unquenched case [389]. A review is provided e. g. in [390]. We choose standard Landau gauge, like most of these previous studies.[3] The gauge is fixed by a standard method, sc. stochastic overrelaxation, see app. B.2.1.2, like already in chs. 5, 6 and 7.

At non-zero temperature, the tensor structure of the gluon propagator is slightly more involved than at $T = 0$. It can be decomposed as

$$\left(D_{\mathrm{gl}}\right)^{ab}_{\mu\nu}(q) = D^{ab}_T(q_0,\vec{q})P^T_{\mu\nu}(q) + D^{ab}_L(q_0,\vec{q})P^L_{\mu\nu}(q). \tag{8.6}$$

Thus, the gluon propagator at non-zero temperature is characterized by two scalar functions, instead of just one at zero temperature, eq. (2.25). The respective terms multiplied by the scalar functions $D_{T/L}$ are transverse resp. longitudinal in the $(d-1)$-dimensional spatial subspace. (In the full d-dimensional space-time, both are transverse, due to the Landau gauge condition.) P^T and P^L are the transverse and longitudinal projectors, respectively. They read

$$P^T_{\mu\nu}(q) = \left(1-\delta_{\mu 0}\right)\left(1-\delta_{\nu 0}\right)\left(\delta_{\mu\nu} - \frac{q_\mu q_\nu}{\vec{q}^2}\right), \tag{8.7}$$

$$P^L_{\mu\nu}(q) = P_{\mu\nu}(q) - P^T_{\mu\nu}(q) \tag{8.8}$$

with the full transverse projector in d dimensions

$$P_{\mu\nu}(q) = \delta_{\mu\nu} - \frac{q_\mu q_\nu}{q^2}. \tag{8.9}$$

The scalar propagator functions are[4]

$$D_T(q(k)) = \frac{1}{(N_c^2-1)(d-2)}\left\langle A^a_\mu(k)A^a_\mu(-k) - \frac{q_0^2}{\vec{q}^2}A^a_0(k)A^a_0(-k)\right\rangle, \tag{8.10}$$

$$D_L(q(k)) = \frac{1}{N_c^2-1}\left(1+\frac{q_0^2}{\vec{q}^2}\right)\left\langle A^a_0(k)A^a_0(-k)\right\rangle. \tag{8.11}$$

[3] By 'standard Landau gauge', we refer to a first-copy approach with standard techniques (not with stochastic quantization like in ch. 4). It is also referred to as 'minimal Landau gauge', e. g. in [391, 297, 295]. This term tends to be ambiguous, however, as it was earlier used for 'best copy' approaches more than once, e. g. [294, 242, 392], even though this is not in line with the usage of the term in [19], where it may have been coined.

[4] See e.g. [383] for a few details on the derivation of these expressions. We use the Einstein summation convention, see app. A.1.1. The relation between momentum vectors k and the lattice momentum q is again given by eq. (2.87).

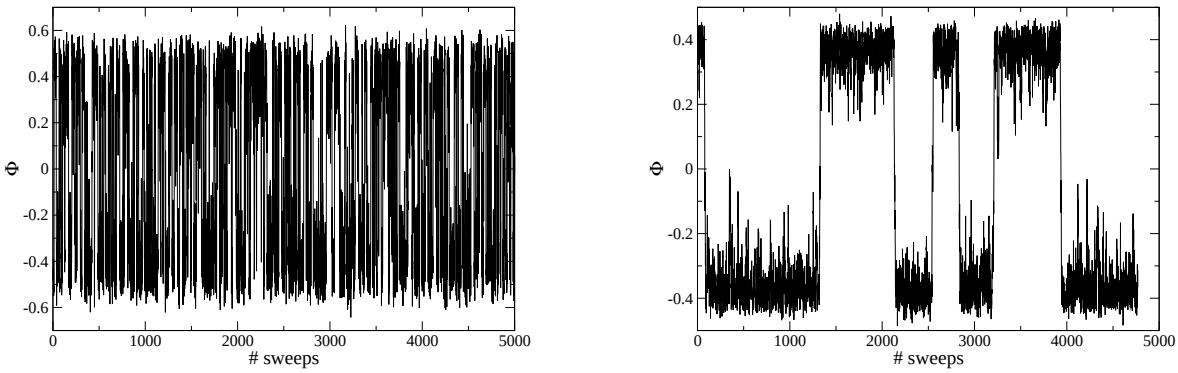

Figure 8.1: Monte Carlo history of the Polyakov loop in computer time (after thermalization) at $\beta = 6.65$, i. e., a little above the deconfinement transition temperature ($\beta_c \approx 6.5364$ for $L_t = 4$ [393]). *Left:* Results from a small lattice, sc. $16^2 \times 4$. Frequent tunneling between the two degenerate vacua. *Right:* Results from a larger lattice, sc. $64^2 \times 4$, where tunneling is much less frequent.

This holds at $q \neq 0$. At zero momentum, slightly different expressions for D_T and D_L follow. First, the terms proportional to $q_0^2/\vec{q}^2$ vanish. Second, the normalization of D_T is different: the factor $d-2$ in the denominator is to be replaced by $d-1$ at $q=0$.[5]

Another important remark is in order. Only configurations with positive real part of the Polyakov loop, eq. (8.2), must enter the propagator calculation in the high-temperature phase [384]. This is because the usual definition of the gluon fields in terms of the link variables is not reasonable otherwise. – For the gauge group $SU(2)$, the Polyakov loop is real, and there are just two sectors (vacua) between which the Polyakov loop 'tunnels' back and forth in the deconfined phase, see fig. 8.1 for examples. We need to impose a restriction to the positive sector, i. e., to evaluate the gluon propagator only from configurations with $\Phi[U] > 0$.

A quantity of specific relevance to our studies is the electric screening mass, related to the longitudinal gluon propagator at zero momentum via

$$m_L = D_L(0)^{-1/2}. \tag{8.12}$$

It has been demonstrated in [370] that the electric screening mass provides a clear signal of the deconfinement phase transition of $SU(2)$ and $SU(3)$ Yang–Mills theory in $3+1$ dimensions. For $SU(2)$, the behavior of m_L as a function of temperature is smoother near T_c than for $SU(3)$, possibly indicating the second-order nature of the $SU(2)$ transition in contrast to the first-order nature of its counterpart in $SU(3)$. – At least in $3+1$ dimensions, it is doubtful [370] whether the magnetic screening mass

$$m_T = D_T(0)^{-1/2} \tag{8.13}$$

is also sensitive to the transition.

We now turn to the results. In addition to the screening masses m_L and m_T, we also analyze the full momentum dependence of the transverse and longitudinal propagators. The main aim is to show that the deconfinement transition at non-zero temperature is

[5]The reason is analogous to the reason for the necessity to replace $d-1$ by d at $q=0$ in the normalization of the gluon propagator at vanishing temperature, see eq. (2.92).

encoded in the gluon propagator and can be determined from it, as an alternative to usual approaches employing gauge-invariant quantities like the susceptibility of the Polyakov loop. This pertains to the transition temperature and also to the critical exponent ν.

8.2 Numerical results

8.2.1 Preliminaries

8.2.1.1 Fine temperature grid

In order to achieve the aims stated above, a high resolution along the temperature axis is indispensable, especially in a region close to the critical temperature of the phase transition. For fixed L_t, the temperature is a monotonic function of β by virtue of eq. (8.1). Thus, we need values of m_L at many different values of β close to the phase transition. For each of these values of β, we calculate the full momentum dependence of the transverse and longitudinal part of the gluon propagator. In order to render the differences between nearby temperatures (couplings) significant, many independent configurations are needed. The typical numbers of independent configurations that we have produced in our simulations are listed in the following table. Note that these numbers pertain to each single value of β; they are not summed over the given intervals. These numbers indicate that the computational task is rather demanding. Most of the data for the electric screening mass are shown in fig. 8.3 as a function of the lattice coupling β, giving a sense of the accuracy of the results.

$V = L_s^2 \times L_t$	$\beta \in \ldots$	$\approx$ nr. of config's per value of β
$16^2 \times 4$	$]6.5, 6.6[$	$2.8 \cdot 10^6$
	$[6.4, 6.9]$	$2.2 \cdot 10^5$
32^4	$[4.5, 6.3]$	$1.4 \cdot 10^5$
	$]6.5, 6.6[$	$(0.3 - 1.3) \cdot 10^6$
	$[6.4, 6.9]$	$(3.8 - 4.3) \cdot 10^5$
	$[7.1, 8.3]$	$(0.7 - 1.3) \cdot 10^5$
$64^4 \times 4$	$[4.5, 6.3]$	$(2 - 3) \cdot 10^4$
	$]6.5, 6.6[$	$(0.8 - 1.8) \cdot 10^5$
	$[6.4, 6.9]$	$(0.8 - 1.7) \cdot 10^5$
	$[7.1, 8.3]$	$4 \cdot 10^4$
$128^2 \times 4$	$[4.5, 8.3]$	$(1.8 - 4.5) \cdot 10^4$
$128^2 \times 6$	$[9.1, 10.7]$	$(1.0 - 4.5) \cdot 10^4$
$256^2 \times 4$	$[6.0, 7.0]$	$(1.5 - 3.4) \cdot 10^3$

8.2.1.2 Setting the scale

It is sometimes desirable to obtain results for the propagators and the masses as a function not of the dimensionless lattice coupling β, but of the physical temperature scale T. Thus, some remarks about setting the physical scale at $T > 0$ are in order. See sec. 2.3.4 for

general remarks about setting such a scale in lattice simulations. This usually yields results in terms of powers of GeV.[6] However, it is also customary to express the temperature of the deconfinement phase transition in units of the string tension. This renders the explicit setting of a value of $\sqrt{\sigma}$ obsolete. In these units, the expected temperature of the deconfinement phase transition in pure Yang–Mills theory is in four $(3+1)$ dimensions $T_c/\sqrt{\sigma} \approx 0.69$ [260] resp. 0.71 [394], see also [261], and $T_c/\sqrt{\sigma} \approx 0.65$ for $SU(3)$ [394], see also [395].[7] Values in MeV can be obtained by using $\sqrt{\sigma} = 440\,\mathrm{MeV}$.

In $2+1$ dimensions, the deconfinement phase transition of $SU(2)$ Yang–Mills theory occurs at a much higher temperature in units of the string tension, sc. at $T_c \approx 1.12\sqrt{\sigma}$ [378], see also [396]. Recent results [397, 393] confirm the value predicted in [378] and allow for very precise estimates.

As noted above, a high resolution along the temperature axis is required. While we have also implemented the string tension calculation ourselves, sc. along the lines sketched in sec. 2.3.4, and have confirmed that our results agree well with values from the literature, there is an alternative to the large numerical effort of high-precision string tension determinations at various values of β. This is because existing data for the $SU(2)$ string tension in lattice units in $2+1$ dimensions from [256, 257, 258] can be fitted[8] by the simple interpolation formula

$$\sqrt{\sigma}a = \frac{b_1}{\beta} + \frac{b_2}{\beta^2}. \tag{8.14}$$

For the data at $L_t = 4$, we take the string tension up to and including $\beta = 7.5$ into account for the fit. This yields $b_1 = 1.2883(59)$ and $b_2 = 1.418(41)$ with $\chi^2/\mathsf{ndf} \approx 0.6$, indicating a good quality of the fit. For $L_t = 6$, we use the data for $\sqrt{\sigma}a$ from $\beta = 7.5$ onwards, which results in $b_1 = 1.3283(90)$ and $b_2 = 1.118(78)$, albeit with $\chi^2/\mathsf{ndf} \approx 2.9$, indicating an unsatisfactory fit. This induces a (controllable and not large) systematic error in the absolute scale used in this case.[9]

[6] The $T = 0$ string tension is also used to set the scale of the lattice spacing in physical units at $T > 0$, see e.g. [394] where this is explicitly stated.

[7] In [394], a successful fit for the dependence of T_c on the number N_c of colors in the range $2 \leq N_c \leq 8$ is presented.

[8] An analogous procedure has been used in [370]. – For transparency, we reproduce here the data to which we fit eq. (8.14):

β	3	3.47	3.75	4.2	4.5	5	6
$\sqrt{\sigma}a$	0.584(16)	0.4889(56)	0.4487(33)	0.387(3)	0.3527(30)	0.3129(20)	0.2529(33)
source	[256]	[256]	[256]	[258]	[256]	[256]	[256]

6.56	7.5	9	10	12	14.5
0.2297(10)	0.1970(2)	0.1622(4)	0.1437(2)	0.1179(5)	0.09713(2)
[256]	[257]	[256]	[257]	[256]	[256]

[9] Taking further terms in the expansion in $1/\beta$ in account is not helpful, due to the relatively small number of values of $\sqrt{\sigma}a$ at large β.

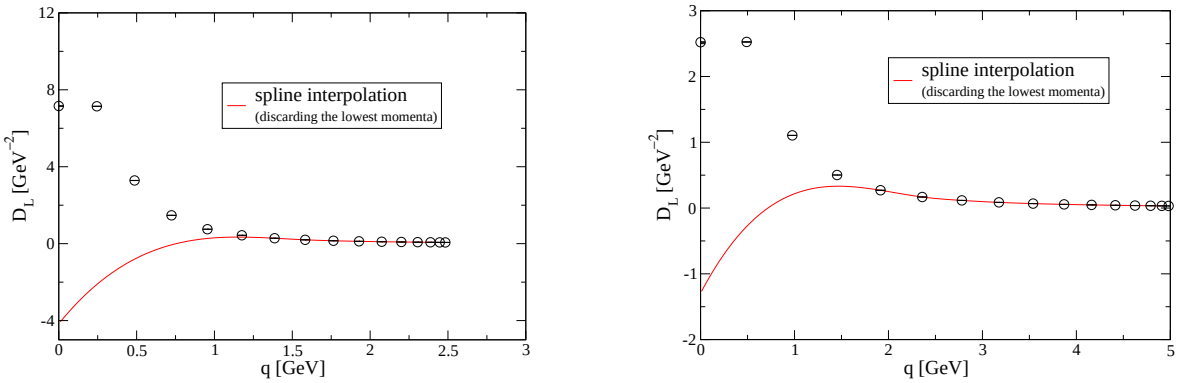

Figure 8.2: Longitudinal gluon propagator together with a spline interpolation (i. e., discarding the $L_s/8$ lowest momenta) on a $32^2 \times 4$ lattice. *Left:* At $\beta = 4.5$, corresponding to a relatively large lattice spacing $a \approx 0.16\,\text{fm}$. *Right:* At $\beta = 8.3$, thus at a smaller lattice spacing, $a \approx 0.079\,\text{fm}$.

8.2.1.3 Momenta and renormalization

We briefly comment on the selection of lattice momenta for the propagators at non-zero temperature. For the investigations presented in previous chapters, we have usually employed the cylinder cut, see sec. 2.3.3.3. But in the simulations at $T > 0$ discussed here, the momenta are aligned along an axis. In addition, we set $q_0 = 0$, i. e., we restrict the studies to the lowest Matsubara frequency (as also predominantly done in ref. [370]).

Multiplicative renormalization of the lattice data according to eq. (2.109) is performed at $\mu = 2.3\,\text{GeV}$. The renormalization constant now depends on the temperature, thus via eq. (8.1) on the lattice coupling β. Since β is varied in small steps near the phase transition in order to extract the critical physics, the demands on accuracy are especially high in this case. At the same time, the distance between adjacent on-axis lattice momenta is as large as $\approx 0.5\,\text{GeV}$ e. g. for a $16^2 \times 4$ lattice. Therefore, determining $D_{L/T}(\mu)$ by mere linear interpolation of the values of $D_{L/T}$ at the momenta just above and below μ is not precise enough for the present purpose. As an alternative, a spline interpolation with standard routines [398] is performed.[10] It is desirable to have a renormalization scale μ which is applicable over a wide range of couplings. I. e., on the one hand, μ should be below the largest accessible momentum q_{max} even at small β, where a is large and q_{max} therefore is small. (a and q_{max} are related since aq has a maximal value of 2 with on-axis momenta, cp. eq. (2.87).) On the other hand, it must not be too close to the non-perturbative regime, where the influence of temperature is large. The choice $\mu = 2.3\,\text{GeV}$ is reasonable for the present purpose. Some examples of spline interpolations are shown in fig. 8.2.

8.2.2 Results

8.2.2.1 Electric screening mass vs. β

We first concentrate on an important aspect of the longitudinal gluon propagator, sc. on the electric screening mass (8.12), which is directly related to $D_L(q = 0)$. We consider it

[10] The spline interpolation pertains mainly to the momenta at a perturbative scale. Thus, we have constructed it such that it does not take the lowest $L_s/8$ momenta into account.

initially as a function of the lattice coupling β, which is approximately, but of course not exactly, proportional to the temperature (see eq. (8.1) in combination with eq. (8.14)); the temperature dependence is analyzed explicitly in sec. 8.2.2.4. Results on different spatial lattice extensions are given in fig. 8.3. Prima facie, they roughly resemble previous results for the $3+1$-dimensional case [370]. But looking more closely at the vicinity of the phase transition, i. e., near $\beta_c = 6.5364(1)$ for $L_t = 4$, as determined to high precision in [393] (see [397, 380, 378] for earlier, consistent results), the behavior of $m_L(\beta)$ that we obtain for $SU(2)$ in $2+1$ dimensions is smoother than the one that results in $3+1$ dimensions according to ref. [370], even though both transitions are of second order.

Indeed, a different critical behavior is to be expected, since $SU(2)$ in $2+1$ resp. $3+1$ dimensions belongs to the universality class of the two- resp. three-dimensional Ising model (see also sec. 8.1.2.3). In order to examine the critical behavior in $2+1$ dimensions in a more quantitative manner, we perform a fit to the data for the electric screening mass with the function[11]

$$m_L = c + d \left| \frac{\beta}{\beta_c} - 1 \right|^{\nu} . \tag{8.15}$$

Here, d is understood to be multiplied with the sign of $\beta/\beta_c - 1$. – This fit proves to be rather successful for our data on lattices with spatial extensions $L_s = 16$ and $L_s = 32$. This pertains to the region $\beta \in [6.4, 6.9]$. Crucially, the value of the critical exponent ν thus obtained is very close to 1, which is the exact value in the universality class of the two-dimensional Ising model solved in [382]. For quantitative details, see fig. 8.4 and its caption. – In contrast, the three-dimensional Ising model, corresponding to $3+1$-dimensional $SU(2)$ Yang–Mills theory, shows a critical behavior with an exponent $\nu \approx 0.63$.[12] The computational power required in $3+1$ dimensions makes it difficult to reliably extract such an exponent.

On the lattices with a larger spatial volume, such a fit is considerably less successful. Even though we have already performed $\mathcal{O}(10^5)$ measurements for each value of β in the region around β_c on a $64^2 \times 4$ lattice, the fit still yields $\chi^2/\mathrm{ndf} \approx 5.4$.

Notably, the behavior of the electric screening mass near the phase transition is hardly sensitive to the change from a $128^2 \times 4$ lattice to a $256^2 \times 4$ lattices. Thus, we have not investigated even larger spatial volumes. It is not immediately evident why the screening mass does not tend to zero at the transition in the infinite volume limit.

8.2.2.2 Magnetic screening mass vs. β

With regard to the question of whether the magnetic screening mass, extracted from the transverse gluon propagator via eq. (8.13), conveys information about the deconfinement phase transition in the $3+1$-dimensional case, the results of ref. [370] were not fully conclusive. Our results for the $2+1$-dimensional case provide clear evidence that the magnetic screening mass is, at least for the volumes we have studied, rather insensitive to the deconfinement phase transition, see fig. 8.5. This is in contrast to its electric counterpart, sec.

[11] This fit is motivated by the expected behavior of the correlation length (an inverse mass), eq. (8.5). It is expected that the additive constant in eq. (8.15) significantly depends on the volume, and that $\nu = 1$.

[12] For the three-dimensional Ising model, an exact general solution is computationally intractable (as it is NP-complete) [399]. The given value of ν is a result of numerical studies, e. g. [400], and theoretical estimates; see the review [401] for a plethora of references.

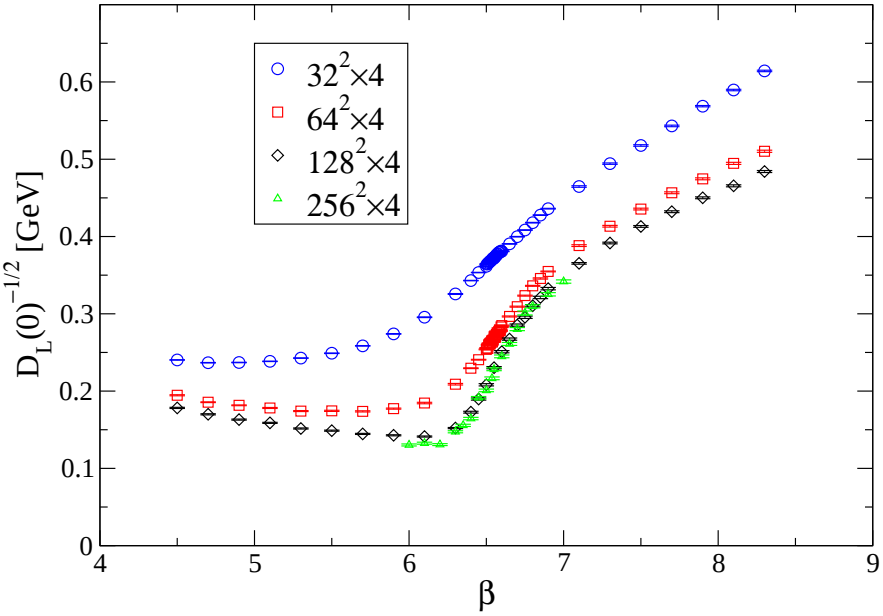

Figure 8.3: Electric screening mass vs. lattice coupling at $L_t = 4$ for four different spatial volumes.

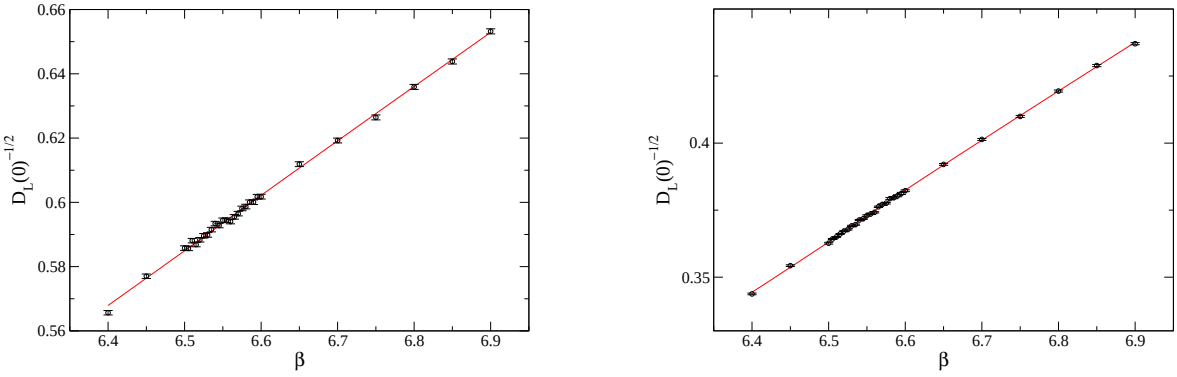

Figure 8.4: Fit of the function $c + d|\beta/\beta_c - 1|^\nu$ (see eq. (8.15)) to the data for the electric screening mass in the range $\beta \in [6.4, 6.9]$. We use $\beta_c = 6.5364$ [393] as an input. *Left (a):* $16^2 \times 4$ lattice (data not included in fig. 8.3). We obtain $c = 0.5912(2)$, $d = 1.08(5)$ and $\nu = 0.992(14)$ with $\chi^2/\mathrm{ndf} \approx 1.4$. *Right (b):* $32^2 \times 4$ lattice. We obtain $c = 0.3702(1)$, $d = 1.14(3)$ and $\nu = 0.977(6)$ with $\chi^2/\mathrm{ndf} \approx 1.7$.

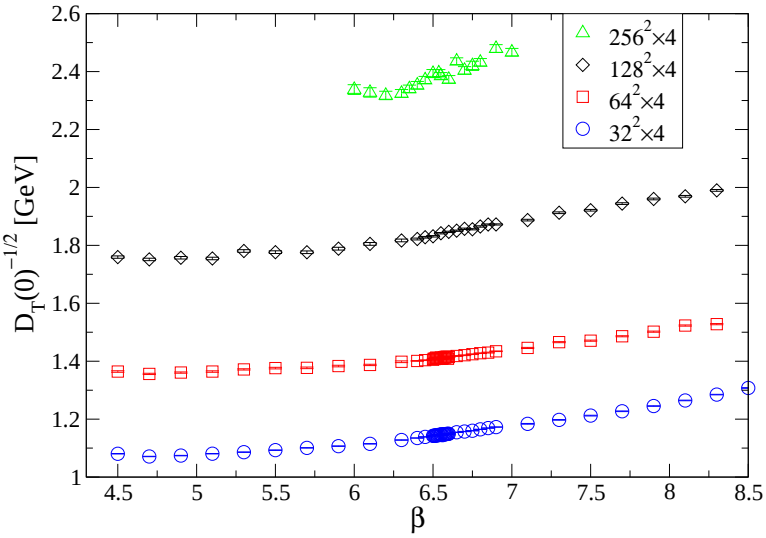

Figure 8.5: Magnetic screening mass vs. β for four different spatial lattice volumes.

8.2.2.1. This contrast becomes even clearer when considering the full momentum dependence of the longitudinal and the transverse gluon propagator, to which we now turn.

8.2.2.3 Full momentum dependence of the longitudinal and the transverse gluon propagator

Longitudinal propagator. Exemplary results for the full momentum dependence of the longitudinal gluon propagator at $L_s = 128$ (and again $L_t = 4$) are depicted in fig. 8.6.[13] The behavior at the largest momenta is not shown, since no difference between the results at different couplings (different temperatures) is visible in that region. The longitudinal gluon propagator at all momenta exhibits the same non-monotonic dependence on the lattice coupling (and thus on the temperature) that is evident already from the electric screening mass, calculated via eq. (8.12) from $D_L(q = 0)$.

Transverse propagator. The analogous plot for the transverse propagator is presented in fig. 8.7. In stark contrast to its longitudinal counterpart, the transverse propagator at all momenta depends monotonically on the coupling resp. the temperature. It shows a notable peak at non-zero momentum, from which it decreases toward the far infrared. This holds at all temperatures considered, although the peak becomes smaller at higher temperatures. In the four-dimensional case, such a peak is visible only above the deconfinement temperature [370].

Volume dependence. In fig. 8.8, we analyze the volume dependence of both the transverse and longitudinal part of the gluon propagator at a fixed lattice coupling, sc. $\beta = 6.5$,

[13] The attentive reader might notice that the relative errors of the longitudinal propagator at $q = 0$ are larger than those at $q \neq 0$ by a factor of around $\sqrt{3}$. This is caused by a slight inaccuracy in a single line of my C++ code, which did not average over the $N_c^2 - 1$ colors in eq. (8.11), leading to a loss of statistics by a factor of 3, causing a standard deviation larger by a factor of $\sqrt{3}$. The inaccuracy is restricted to this single case.

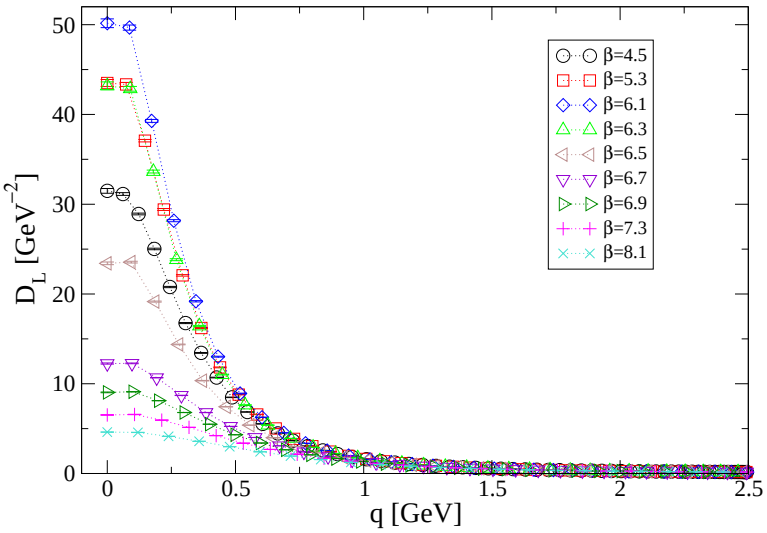

Figure 8.6: Longitudinal gluon propagator at various couplings ($\hat{=}$ various temperatures) on a $128^2 \times 4$ lattice. At large β, the momenta extend up to approx. 5 GeV (largest momenta not shown). Dotted lines are drawn to guide the eye. See fig. 8.9a for a depiction in a three-dimensional plot.

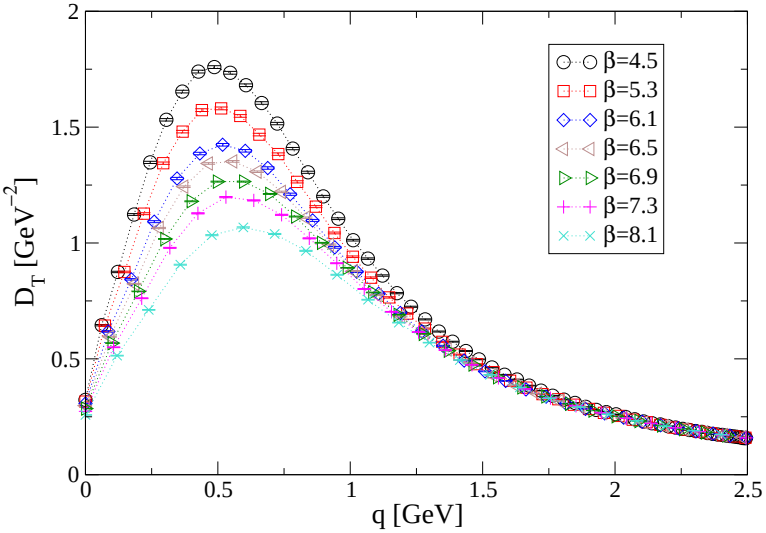

Figure 8.7: Transverse gluon propagator at various couplings (various temperatures) on a $128^2 \times 4$ lattice. (Largest momenta not shown.) See fig. 8.9b for a depiction in a three-dimensional plot.

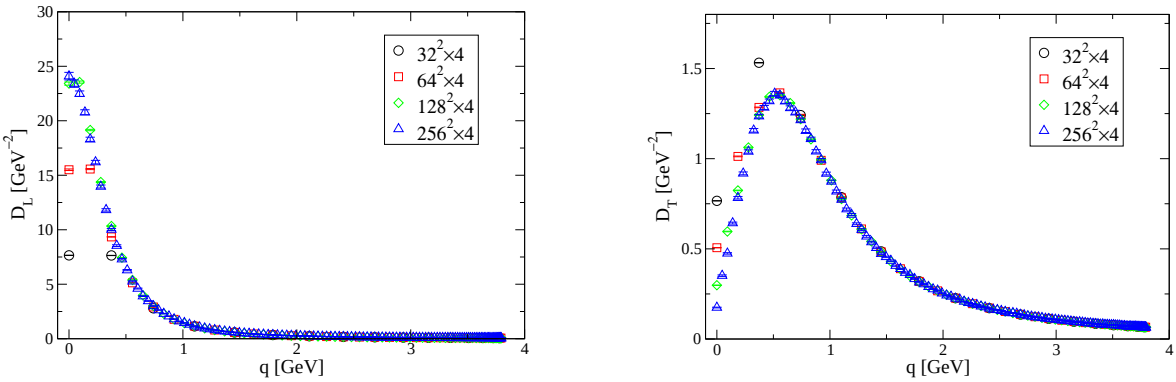

Figure 8.8: Longitudinal *(left, (a))* resp. transverse *(right, (b))* gluon propagator for various lattice sizes at $\beta = 6.5$.

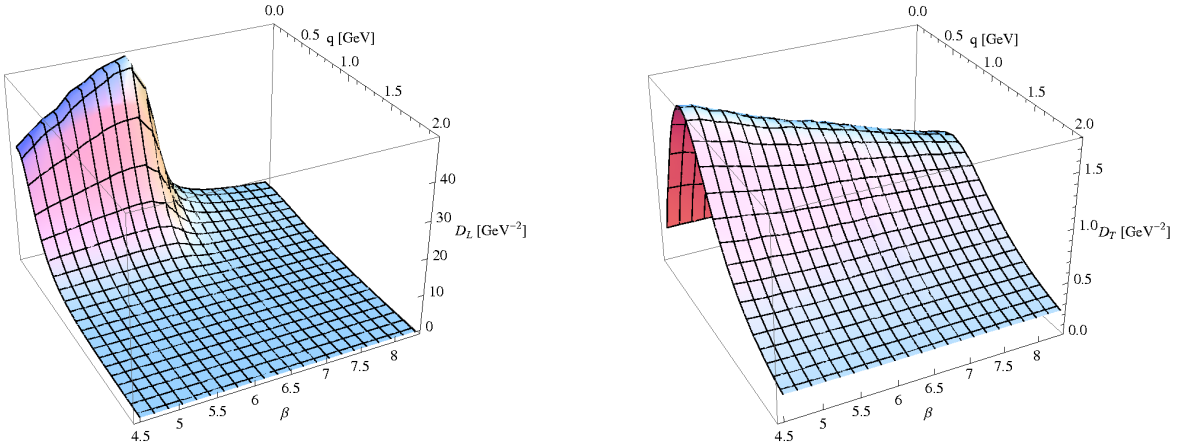

Figure 8.9: Longitudinal *(left, (a))* resp. transverse *(right, (b))* gluon propagator on a $128^2 \times 4$ lattice. The dependence on both the momentum and the lattice coupling is illustrated. See fig. 8.6 resp. fig. 8.7 for cross sections at constant values of β.

slightly below β_c. In both cases, only infrared momenta are significantly affected by the change in volume. For the longitudinal propagator, the finite volume effect when going from the spatial extension $L_s = 128$ to $L_s = 256$ is small, as already noted in sec. 8.2.2.1 above. This holds at all values of β that are investigated here, as is evident from the electric screening mass in fig. 8.10b.

Overview. An overview of the results for the momentum dependence of the longitudinal and transverse gluon propagator at different couplings is provided in the three-dimensional plots of fig. 8.9. These pictures of the combined dependence of $D_{L/T}$ on q and β clearly illustrate that only the chromoelectric sector shows a pronounced sensitivity to the deconfinement transition (fig. 8.9a), while in the chromomagnetic sector, the respective propagator behaves monotonically as a function of β at all momenta (fig. 8.9b). In addition, they illustrate that in particular the infrared part of the longitudinal gluon propagator is sensitive to the transition.

8.2.2.4 Transition temperature

We intend to test explicitly whether the deconfinement temperature is encoded in properties of the gluon propagator. Since our results in sec. 8.2.2.1 confirm that the chromoelectric sector is sensitive to the phase transition, we strive to calculate the susceptibility of the electric screening mass m_L in order to perform a more thorough and quantitative analysis. Before we do so, we again show the data for this mass, fig. 8.10a; however, now as a function not of β as in fig. 8.3, but of the temperature in units of the string tension, $T/\sqrt{\sigma}$. (This change of variables is discussed explicitly in sec. 8.2.1.2 above.) This allows us to include also data produced at $L_t = 6$ in the same plot. These are not part of fig. 8.3, since at larger L_t, larger β are required to cover the same temperature range, cp. eq. (8.1).

At $L_t = 6$, the phase transition is expected to take place at $\beta_c \approx 9.602$ [393]. From the remarks in sec. 8.2.1.2, it follows that this corresponds to $a = 0.067\,\text{fm}$.[14] In contrast, at $\beta_c(L_t = 4) \approx 6.5364$, the lattice spacing is $a = 0.103\,\text{fm}$ (from $\sqrt{\sigma}a \approx 0.2303$).

The behavior of m_L near the phase transition is smoother on a $128^2 \times 6$ lattice than it is on a $128^2 \times 4$ lattice. This is easily explained by the fact that the physical lattice extension is smaller. The linear spatial extension of a lattice with $L_s = 128$ at β_c amounts to 13.2 fm for $L_t = 4$, but only to 8.6 fm for $L_t = 6$. The latter value is closer to the physical extension of a $64^2 \times 4$ lattice at β_c, which is qualitatively in line with the data in fig. 8.10a.

Susceptibility of the electric screening mass. Finally, we discuss the susceptibility of the electric screening mass. This is calculated naïvely from the centered difference of the data for the electric screening mass in fig. 8.10a, following the procedure in [370]. The result is shown in fig. 8.10b. It exhibits a pronounced peak at the critical temperature T_c. On the smaller lattices, sc. $32^2 \times 4$ and $64^2 \times 4$, where we have chosen a very high resolution along the temperature axis, we omit some of the data points when calculating the susceptibility.[15] This avoids overly large fluctuations of the susceptibility and thus helps to enable a clear presentation. It does of course not affect our conclusions. – On the other

[14] This holds if the standard value $\sqrt{\sigma} = 440\,\text{MeV}$ is used. The value of $\sqrt{\sigma}a$ at $\beta = 9.6$ from our interpolation is 0.1505.

[15] Especially in the vicinity of β_c, we use only every fifth out of the multitude of values.

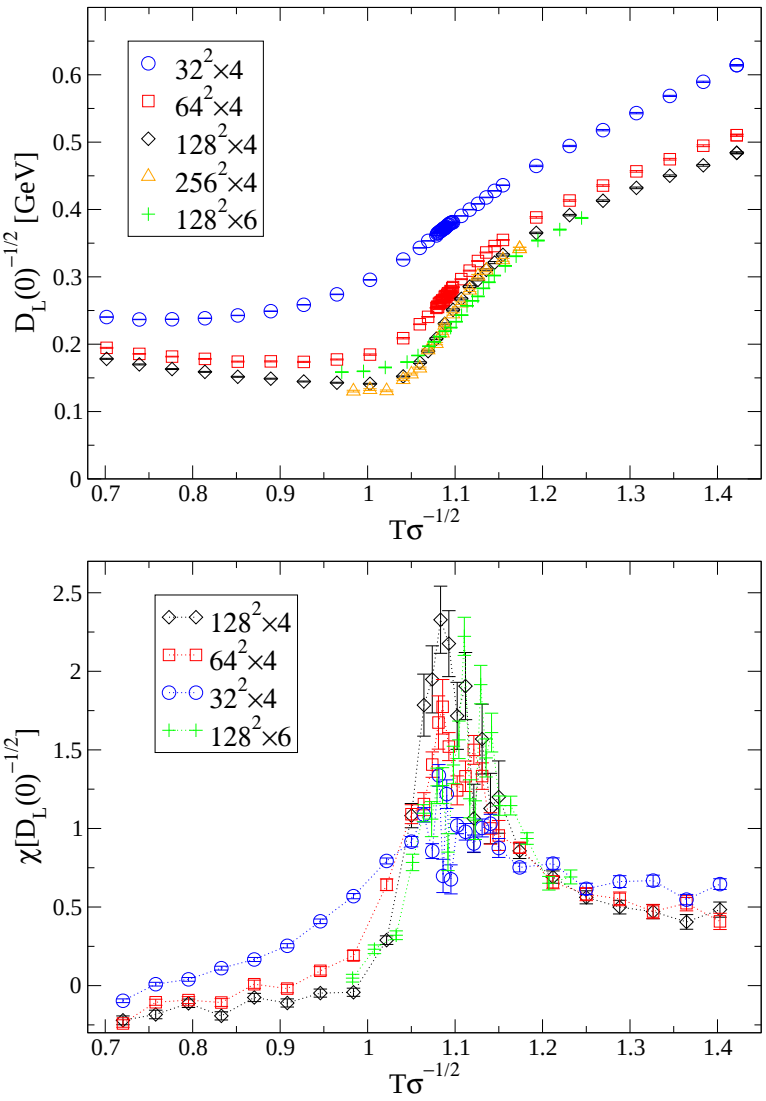

Figure 8.10: *Top (a):* Data like in fig. 8.3, but shown as a function of temperature (instead of β) and including data obtained at $L_t = 6$. *Bottom (b):* 'Susceptibility' calculated from the discretized derivative of the electric screening mass in fig. (a) (some data points of the screening mass now omitted for clarity).

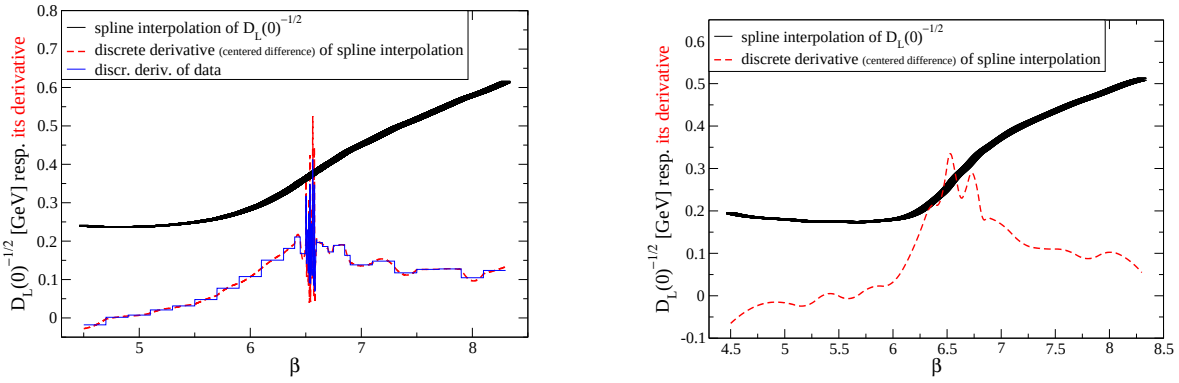

Figure 8.11: Spline interpolation of the data for the electric screening mass and derivative of the spline interpolation. This provides some evidence about the inflection point of the electric screening mass considered as a function of β. *Left:* On a $32^2 \times 4$ lattice (oscillations of the derivative around β_c simply stem from the high resolution). *Right:* On a $64^2 \times 4$ lattice.

hand, on the largest lattice, sc. $256^2 \times 4$, the statistics we have sampled (a few thousand measurements at each value of β) allows to see a peak in the susceptibility, but not to locate it with reasonable precision. Again for clarity, we do not show the susceptibility data on the largest lattice in fig. 8.10b (although, of course, we do show the corresponding data for the screening mass in fig. 8.10a).

From the data for the susceptibility on a $128^2 \times 4$-data, fig. 8.10b, we infer that the peak is located around $T_c \approx 1.08\sqrt{\sigma}$, with an naïve error estimate of at least ± 0.01 (this is roughly the distance along the temperature axis between adjacent data points). From the interpolation formula for the string tension that we employ, eq. (8.14), together with relation (8.1), we find $\beta_c \approx 6.52$,[16] with a naïve error estimate of at least ± 0.06. This is fully consistent with the value $\beta_c \approx 6.536$ found in [393], which, in turn, is close to the average of earlier values with larger error bars [397, 380, 378].[17]

As a side note, fig. 8.11 shows the outcome of calculating the discrete derivative from an interpolation of the data for the electric screening mass for $L_t = 4$ using cubic splines. This result is in line with the above statements, but less accurate.

For $L_t = 6$, we have done simulations on a $128^2 \times 6$ lattice. From the data which are also included in fig. 8.10b, we infer $T_c/\sqrt{\sigma} \approx 1.11$, which entails $\beta_c \approx 9.63$. The uncertainty of this value amounts to a few percent, as is apparent from the width of the corresponding peak in fig. 8.10b,[18] and is larger than on the $128^2 \times 4$ lattice. In any case, it agrees well with

[16] Eq. (8.14) immediately entails

$$\beta = \frac{c}{2\sqrt{\sigma}a} + \sqrt{\frac{c^2}{4\sigma a^2} + d}. \tag{8.16}$$

[17] A note regarding in particular the results at $L_t = 4$: While the critical coupling agrees well with the previous result of [393], the corresponding critical temperature has in [393] been found to be $T_c = 1.1225(23)$, consistent with the result of [397], instead of our values 1.11 at $L_t = 6$ resp. 1.08 at $L_t = 4$. But this seeming discrepancy can easily be accounted for. It merely rests on the fact that the way to fix a scale employed in [393] slightly differs from our way to do so. In addition, the difference to our result at $L_t = 6$ is well within the uncertainty of the latter estimate.

[18] In addition, the interpolation formula for $\sqrt{\sigma}a^2(\beta)$ introduces an additional error, see the remarks below eq. (8.14).

the value $\beta_c \approx 9.602$ found in the study [393] aimed at high precision. We stress again that our objective in determining the transition temperature is not to achieve an outstanding precision, but to see that it can be well determined from the gluon propagator, instead of from gauge-invariant quantities (like the Polyakov loop or the specific heat) as usual, see e. g. [397, 394] and reviews like [402], or by an analysis of the center vortex free energy like in [393]. The analysis of the electric screening mass and its susceptibility indeed confirms that the infrared gluon propagator gives information about the deconfinement transition of pure $SU(2)$ Yang–Mills theory in $2+1$ dimensions.

8.3 Summary

Our simulations show that infrared properties of the Landau gauge gluon propagator carry information about the deconfinement phase transition of pure $SU(2)$ Yang–Mills theory in $2+1$ dimensions. The electric screening mass exhibits a pronounced response to the second-order phase transition, while the chromomagnetic sector is insensitive to this transition. From the electric screening mass, we extract a critical temperature in good agreement with previous results obtained by other methods. The critical exponent ν is consistent with the expected universality class.

In addition, our results nicely fit into a more general picture if considered together with recent results in $3+1$ dimensions. In both cases, the information obtained from the longitudinal part of the infrared gluon propagator provides evidence about the correct critical behavior of pure Yang–Mills theory. This constitutes a nontrivial connection of gauge-dependent quantities to experimentally accessible facts.

CHAPTER 9

SIGN PROBLEM AND STOCHASTIC QUANTIZATION

In the present chapter, we discuss an application of stochastic quantization (chs. 3 and 4) outside of gauge theory. In contrast to chs. 3 and 4, it is complex stochastic quantization that is relevant here. We employ it since it is a promising approach to the 'sign problem'. This problem greatly complicates the numerical treatment of a lattice formulation for fermions at non-zero density. The fermionic model considered here is the three-dimensional Thirring model. After introducing the sign problem, the approach of complex Langevin evolution and the Thirring model, we describe and discuss a number of results for important observables and also for the phase factor of the fermion determinant.

9.1 Introduction

9.1.1 Non-zero density and the sign problem

9.1.1.1 QCD phase diagram

The phase diagram of QCD describes the dependence of the state of strongly interacting matter on the values of the temperature T and the chemical potential μ. It is a subject of major significance, as it comprises a variety of states of hadronic resp. quark matter occurring in vastly different contexts. This includes the early universe at high temperature T and low density ρ resp. chemical potential μ, neutron stars at high μ and low T and the quark–gluon plasma at high T and μ.

Heavy ion collisions allow to probe the QCD phase diagram experimentally, see e. g. the review [403], and to search for a (possible) critical point at which the first-order deconfinement phase transition at larger μ ceases to exist, turning into a crossover at small μ, as found in lattice studies [368]. Within lattice gauge theory, the phase diagram has been thoroughly explored along the temperature axis, where it is comparatively well understood, even though the debate about the temperature of the deconfinement crossover at $\mu = 0$ is not yet settled [404, 405].

In addition to the confinement–deconfinement transition, a transition between a chirally broken and a chirally symmetric phase takes place. The order parameter of this transition is the chiral condensate. These two crossovers at $\mu = 0$ occur at remarkably similar and possibly identical temperatures, as obtained again by lattice studies [406, 407, 408, 368], although the possibility of a slight difference remains open.

9.1.1.2 Sign problem

The simulation of QCD at non-zero baryon density with lattice gauge theory techniques poses an especially challenging numerical problem, see e. g. [409, 410, 219] for recent reviews and also ref. [411] which includes methods beyond lattice simulations. The quenched approximation, see sec. 2.3.1, is not sufficient in this case, since at $\mu \neq 0$, this theory is not the limit of QCD for a vanishing number of quark flavors, $N_f \to 0$ [412]. Hence, it is de facto indispensable to include dynamical fermions. This renders the path integral measure complex, since the fermion determinant is complex at $\mu \neq 0$ for the gauge group $SU(3)$ of the strong interactions (due to a non-Hermitian Dirac operator). The fermion determinant arises when the fermion fields in the partition function of unquenched lattice gauge theory (see also sec. 2.3),

$$Z = \int \mathcal{D}\psi \, \mathcal{D}\overline{\psi} \, \mathcal{D}U \, e^{-(S_G[U] + S_F[\psi, \overline{\psi}, U])}, \tag{9.1}$$

are integrated out. S_G is the gauge action and S_F the fermionic action; the latter involves the Dirac operator D, which is at $\mu = 0$ the sum of a lattice discretization of $\gamma_\mu \left(\partial_\mu + iA_\mu\right)$ and the bare quark mass m. The partition function can thus be written solely in terms of the link variables as

$$Z = \int \mathcal{D}U \, e^{-S_G[U]} \det M[U] = \int \mathcal{D}U \, e^{-S_{\text{eff}}[U]} \tag{9.2}$$

with the effective gauge action[1]

$$S_{\text{eff}} = S_G - \ln \det M = S_G \underbrace{- \operatorname{tr} \ln M}_{=S_F}, \tag{9.3}$$

composed of the proper gauge action S_G and the fermionic part S_F. For $S \in \mathbb{C}$, standard Monte Carlo methods based on importance sampling are not feasible, since a complex path integral measure does not permit a probability interpretation.

Possible solutions to, or ways around, the sign problem include

(i) reweighting approaches [413, 414, 415, 416],

(ii) Taylor expansion around vanishing chemical potential $\mu = 0$ [417, 418, 419, 420, 421] and

(iii) the use of an imaginary value of μ, see e. g. [422, 423, 424, 425], with subsequent analytical continuation toward real values.

Every one of these approaches suffers from specific problems, especially for $\mu/T \gtrsim 1$, see e. g. [426, 427] concerning reweighting and again the reviews [409, 410, 219, 411].

[1] The second identity in eq. (9.3) follows from the standard relation $\det \exp N = \exp \operatorname{tr} N$.

9.1.2 Complex stochastic quantization

An alternative to these 'standard' methods for simulating a theory with a sign problem at non-zero density is to employ a complex Langevin evolution, i. e., to take the complex action at face value and to insert it into a Langevin equation (see chs. 3 and 4), which thereby separates into a real and an imaginary part. The hope is that this leads to the correct distribution of configurations even for a complex action S. But unlike for real S, no proof of such a convergence exists. We further comment on this a few paragraphs below.

The idea dates back already a few decades [428, 429, 430, 431]. The hope mentioned above is not completely unfounded, as some encouraging results were soon obtained, see e. g. [432, 433]. However, the method turned out not to be unambiguously successful. 'Runaway trajectories' occurred in the simulations, e. g. [434], requiring a careful numerical treatment (e. g. an adaptive step size), but not invalidating the method. Still, there is a more severe obstacle. Namely, cases were found for which the evolution does converge, but against the wrong value, e. g. for $SU(2)$ and $SU(3)$ gauge theory with static charges included in the action [435], see also [436]; many more references may be found e. g. in [437]. See [438, 439] for further early studies of complex Langevin evolution.

Despite these doubts, complex Langevin dynamics has recently led to surprisingly good results at non-zero chemical potential for simple models [440, 441, 442, 443], like e. g. for the relativistic Bose gas. This has revived the hope that it may be a viable method to tackle the sign problem. See also [444] which includes both formal arguments and their testing with simple models, arriving at rather cautious conclusions. In addition, it has been shown that complex Langevin dynamics is able to solve the sign problem in the thermodynamic limit of one-dimensional QCD [445].

However, in another recent investigation, complex Langevin evolution has been shown to fail for the three-dimensional XY-model especially at small β, although the sign problem is mild in this case for this model [446]. The evolution converges against the wrong value, similarly to the negative result found in [435]. In fact, here it fails even at vanishing chemical potential. This has been interpreted as evidence that the reason for this failure may not be the sign problem itself [446]. Diagnostics of the failure are facilitated in this case by the fact that independent results with a different method, sc. a world-line formulation, exist.[2]

We study the Thirring model with complex Langevin evolution, see sec. 9.2. For this model, the situation is less fortunate insofar as no other results at $\mu > 0$ are available for comparison. Like QCD, it has a severe sign problem, which makes it an especially interesting challenge. At $\mu = 0$, we find very good agreement between the results of complex Langevin evolution and usual, reliable methods like Hybrid Monte Carlo or real Langevin evolution, see sec. 9.2.3.1.

Another application of Langevin evolution to theories with a complex action aims at studying non-equilibrium dynamics by virtue of simulations in real time, i. e., in Minkowski space-time instead of Euclidean one. This has been done both for scalar field theory and for non-Abelian gauge theory, sc. for pure $SU(N_c)$ Yang–Mills theory, see e. g. [447, 437]. Here, however, we focus on the application of complex Langevin evolution to non-zero density, which is potentially of great interest e. g. for studies concerning the phase diagram of QCD, as sketched in sec. 9.1.1.

It does not come as a surprise that the investigations of complex Langevin evolution,

[2] See the corresponding references in [446].

successful are they are in some cases, do not in general lead to fully satisfactory results. On the contrary, it should be expected from a theoretical point of view that special care is required when applying the Langevin equation to complex actions, as opposed to real ones. This is because only in the latter case it is proven that the Langevin evolution of observables eventually converges toward their correct value [298], see [301, 309] for reviews. For a complex action, the situation is much more problematic [432, 434, 448, 449, 450, 451, 452], see also [453] for a more extensive overview. On the other hand, studies of complex Langevin evolution may provide the opportunity to tackle what is undoubtedly one of the most important challenges in QCD nowadays. Hence, this is an endeavor that potentially offers very rewarding results, but that also comes with a considerable risk of failure.

9.2 Thirring model

9.2.1 Introduction

9.2.1.1 Generalities and continuum formulation

The Thirring model [454],[3] which we study in three dimensions, is a fermionic model that exhibits the sign problem described in sec. 9.1. We also investigate the related 'Silver Blaze' problem, see sec. 9.2.2.3. We focus on these two properties. There are other relevant applications of the Thirring model, for example to the description of high-T_c superconductors or of graphene (see [457] and references therein).

The Lagrangian of the Thirring model reads in a continuum formulation in Euclidean space-time[4]

$$\mathcal{L}_{\text{Thirring}} = \overline{\psi}_i \left(\not{\partial} + m + \mu\gamma_0\right) \psi_i + \frac{g^2}{2N_f} \left(\overline{\psi}_i \gamma_\nu \psi_i\right)^2 . \tag{9.4}$$

This is a theory describing relativistic fermions that interact via a contact term between vector currents. The parameters of $\mathcal{L}_{\text{Thirring}}$ comprise the bare fermion mass m, the chemical potential μ, the number of fermion flavors N_f and the squared coupling g^2. (We will frequently refer to the inverse coupling g^{-2} instead of g^2.) $\overline{\psi}$ and ψ are mutually independent four-component spinors, and the index i runs over the N_f flavors. Corresponding conventions concerning the γ-matrices are given explicitly in [458, 457]; as stated therein, it is advisable to work with a reducible representation of the Dirac algebra. In the chiral limit $m \to 0$, $\mathcal{L}_{\text{Thirring}}$ exhibits chiral symmetry under continuous $U(1)$ transformations.

A bosonic auxiliary field may be introduced in order to resolve the four-fermion interaction (see e. g. [459, 458]), yielding

$$\mathcal{L}_{\text{Thirring, aux}} = \overline{\psi}_i \left(\not{\partial} + i\not{A} + m + \mu\gamma_0\right) \psi_i + \frac{N_f}{2g^2} \left(A_\nu\right)^2 . \tag{9.5}$$

Several studies indicate that in the Thirring model, chiral symmetry is spontaneously broken at $\mu = 0$ below some critical number of flavors N_{f_c}, given that the interaction strength is

[3] Our work on the Thirring model was done in collaboration with Gert Aarts and Simon Hands. We acknowledge benefiting from unpublished notes by them. In particular, the formulation of the Thirring model which we give in the following is in parts based on [455] and also [456].

[4] See app. A.1.3 for the notation (Feynman slash and γ-matrices).

sufficiently large.[5] This has been predicted via Dyson–Schwinger equations [462, 463, 464] and confirmed by numerical simulations, see e. g. [465, 458]. The value of N_{f_c} has mostly been found to be larger than 4,[6] with recent results pointing toward $N_{f_c} \approx 6.6$ [466, 467], see [457] for further references. The precise value of N_{f_c} is not important for our purposes, as long as $N_{f_c} > 2$. Here, we choose $N_f = 2$, which corresponds to $N = 1$ in the lattice formulation given below. This choice ensures spontaneous breaking of chiral symmetry at $\mu = 0$.

9.2.1.2 Lattice formulation

On the lattice, the action of the Thirring model reads [465]

$$S = \sum_{x,y} \sum_{i=1}^{N} \overline{\chi}_i(x) M_{x,y} \chi_i(y) + \frac{N}{4g^2} \sum_{x,\nu} A_\nu^2(x). \tag{9.6}$$

The sum runs over x and y run over all lattice sites, of which there are $V = L_s^2 \times L_t$ ones, with the spatial resp. (Euclidean) temporal lattice xextension $L_{s/t}$. The action contains the fermion matrix

$$\begin{aligned} M(x,y) =& \frac{1}{2} \left[(1 + iA_0(x)) e^{\mu} \delta_{y,x+\hat{0}} - (1 - iA_0(y)) e^{-\mu} \delta_{y,x-\hat{0}} \right] + \\ &+ \frac{1}{2} \sum_{\nu=1}^{2} \eta_\nu(x) \left[(1 + iA_\nu(x)) \delta_{y,x+\hat{\nu}} - (1 - iA_\nu(y)) \delta_{y,x-\hat{\nu}} \right] \\ &+ m\delta_{x,y}. \end{aligned} \tag{9.7}$$

M is a complex $V \times V$ matrix.

This is a formulation in terms of N flavors of staggered fermions; $\overline{\chi}$ and χ are the staggered fermion fields. The number of continuum flavors is twice as large in three dimensions, $N_f = 2N$. The inclusion of the chemical potential follows the customary prescription by Hasenfratz and Karsch [468]. Again, $\hat{0}$ is the (Euclidean) temporal direction, $\hat{1}$ and $\hat{2}$ are the spatial directions.

The Kawamoto-Smit phases [469] entering M are given by

$$\eta_\nu(x) = (-1)^{\sum_{i=0}^{\nu-1} x_i}, \tag{9.8}$$

thus in particular, $\eta_0(x) = 1$ for any x.

The fermion matrix satisfies the relation

$$\det M(\mu) = [\det M(-\mu^*)]^* \tag{9.9}$$

and also

$$M_{x,x+\hat{\nu}}(\mu) = -M^*_{x+\hat{\nu},x}(-\mu^*). \tag{9.10}$$

Both eq. (9.9) and eq. (9.10) follow from the identity

$$\varepsilon(x) M_{x,y}(\mu) \varepsilon(y) = M^*_{y,x}(-\mu^*) \tag{9.11}$$

[5] The coupling separating a chirally broken from a chirally symmetric phase has been determined to be $g_c^{-2} = 1.92(2)$ at $N_f = 2$ [458] and $g_c^{-2} = 0.69(1)$ at $N_f = 4$ [460], see also [461].

[6] Even $N_{f_c} = \infty$ was claimed, see [463].

with $\varepsilon(x) := (-1)^{x_0+x_1+x_2}$. This resembles the relation

$$\gamma_5 D(\mu)\gamma_5 = D^\dagger(-\mu) \tag{9.12}$$

for the Dirac operator in QCD and related theories (see p. 159), which reduces at $\mu = 0$ to 'γ_5-hermiticity' of D, rendering the fermion determinant real. – Eq. (9.10) immediately implies that the complex matrix M is in general not Hermitian, except for $\mu = 0$.

An important property of the fermion matrix, without which its definition would be incomplete, is that antiperiodic boundary conditions in the temporal direction are to be taken into account. In practice, this means that a hopping term is multiplied by (-1) exactly if the shortest path between the sites it connects crosses the temporal boundary of the lattice.

9.2.1.3 Complex Langevin evolution

The action (9.20) is the starting point for a complex Langevin evolution, which is determined by the Langevin equation. We state this equation here initially in continuous Langevin time θ,

$$\frac{\partial}{\partial\theta} A_\nu(x,\theta) = -\frac{\delta S_{\text{eff}}[A]}{\delta A_\nu(x,\theta)} + \eta_\nu(x,\theta). \tag{9.13}$$

This is analogous to the applications of the Langevin eq. in chs. 3 and 4, e. g. eq. (4.1) for the gauge field of pure Yang–Mills theories. But S_{eff} takes fermions into account, cp. eq. (9.3). Again, θ must not be confused with the ordinary time, which is among the three spatio-temporal variables x. Compared to the equation that incorporates a gauge fixing term in Yang–Mills theories, eq. (4.2), and that we have implemented on the lattice (sec. 4.2.2), eq. (9.13) appears at first glance simpler – due to the absence of a gauge fixing term. However, the fact that the action takes complex values makes its treatment rather involved in a way that is very different from the intricacies of gauge fixing.

In eq. (9.13) and in the formulations of the Langevin eq. we give below, η does, of course, not denote a Kawamoto-Smit phase (9.8), but Gaussian white noise

$$\langle \eta_\nu(x,\theta) \rangle = 0, \tag{9.14}$$

$$\langle \eta_\nu(x,\theta)\eta_\mu(x',\theta') \rangle = 2\delta_{\nu\mu}\delta(x-x')\delta(\theta-\theta'), \tag{9.15}$$

just like in the version of the Langevin equation given in ch. 4. Since S_{eff} is complex, the auxiliary field $A_\nu(x)$ is accordingly complexified,

$$A_\nu(x) = A_\nu^{\text{R}}(x) + iA_\nu^{\text{I}}(x) \tag{9.16}$$

with $A_\nu^{R/I}(x) \in \mathbb{R}$. Eq. (9.13) can be discretized in a very straightforward manner, sc. by introducing a Langevin step size ε via $\theta = n \cdot \varepsilon$, with the Langevin time θ and the number of steps $n \in \mathbb{N}$. The discretized Langevin equation, separated into real and imaginary part, reads

$$A_\nu^{\text{R}}(x,n+1) = A_\nu^{\text{R}}(x,n) + \varepsilon\, K_\nu^R(x,n) + \sqrt{\varepsilon}\,\eta_\nu(x,n), \tag{9.17a}$$

$$A_\nu^{\text{I}}(x,n+1) = A_\nu^{\text{I}}(x,n) + \varepsilon\, K_\nu^I(x,n). \tag{9.17b}$$

The drift term is, just like in previous applications of the Langevin equation (chs. 3 and 4), the negative gradient of the action,

$$K_\nu^R(x,n) = -\mathrm{Re}\,\frac{\delta S_{\mathrm{eff}}[A_\nu]}{\delta A_\nu(x,n)}, \tag{9.18a}$$

$$K_\nu^I(x,n) = -\mathrm{Im}\,\frac{\delta S_{\mathrm{eff}}[A_\nu]}{\delta A_\nu(x,n)}, \tag{9.18b}$$

which is also useful for formulating the random walk dynamics, see sec. 9.2.1.4 below.

In order to explicitly evaluate the force term, it is helpful to note that the partition function can be written as

$$Z = \int \mathcal{D}A_\nu\, e^{-S_{\mathrm{eff}}[A]} \tag{9.19}$$

with the action

$$S_{\mathrm{eff}}[A] = \frac{N}{4g^2}\sum_{x,\nu} A_\nu^2(x) - \ln\det M[A]. \tag{9.20}$$

From this, we immediately obtain for the force term, eq. (9.18),

$$K_\nu(x,n) = -\frac{\delta S_{\mathrm{eff}}[A]}{\delta A_\nu(x,n)} = -\frac{N}{2g^2}A_\nu(x,n) + \mathrm{tr}\,M^{-1}[A]\frac{\delta M[A]}{\delta A_\nu(x,n)}. \tag{9.21}$$

From the explicit expression for the fermion matrix, eq. (9.7), we infer

$$K_\nu(x,n) = -\frac{N}{2g^2}A_\nu(x) + \frac{i}{2}\eta_\nu(x)\left[e^{\mu\delta_{\nu 0}}M^{-1}(x+\hat{v},x) + e^{-\mu\delta_{\nu 0}}M^{-1}(x,x+\hat{v})\right]. \tag{9.22}$$

Most of the numerical effort is caused by the inversion of the fermion matrix M. It does not depend on the bare fermion mass (unlike a usual Hybrid Monte Carlo algorithm, which invokes the conjugate gradient algorithm).

Note on imaginary noise. It is possible to introduce a noise term in the Langevin equation also for the imaginary component [470]. In this case, the noise terms read $\sqrt{\varepsilon}\,C_{R/I}\eta_{R/I}$ with

$$\langle\eta_R^2\rangle = \langle\eta_I^2\rangle = 2 \quad \text{and} \quad \langle\eta_R\eta_I\rangle = 0. \tag{9.23}$$

The condition

$$C_R - C_I = 1 \tag{9.24}$$

is required to hold. Despite a few experiments with non-vanishing imaginary noise, we always choose $C_I = 0$ for production runs.

9.2.1.4 Complex random walk

In addition to the complex Langevin equation, we have implemented a propagation by means of a complex random walk. Here, an imaginary component of the noise is required, in contrast to the Langevin approach. An individual updating step reads

$$A_\nu^{R/I}(x) \to A_\nu^{R/I}(x) \pm \Delta_{R/I}, \tag{9.25}$$

with the step sizes for the real resp. imaginary part of the auxiliary field A given by

$$\Delta_{R/I} = \eta\sqrt{2C_{R/I}}, \tag{9.26}$$

where $\eta \in \mathcal{O}(\sqrt{\varepsilon})$ is the generic step size of a random walk (see also secs. 3.2.2.2 and 4.2.2.1) and where again eq. (9.24) holds. The probability for an updating step (9.25) is given by

$$p_x^{\pm} = \frac{1}{2}\left(1 \pm \frac{\Delta_{R/I}}{2C_{R/I}} K_\nu^{R/I}(x)\right). \tag{9.27}$$

We have performed some random walk simulations for purposes of testing, but usually, we have employed the complex Langevin algorithm (9.17).

9.2.2 Preliminaries to numerical studies

At vanishing chemical potential $\mu = 0$, the Thirring model has previously been simulated on the lattice, e. g. with a Hybrid Monte Carlo (HMC) algorithm for even N_f, e. g. [465, 458, 460], otherwise with a Hybrid Molecular Dynamics algorithm [471]. We explore the phase diagram at vanishing temperature and $\mu > 0$, where standard algorithms are inapplicable (see sec. 9.1), with complex stochastic quantization. We state in advance that our results are not fully conclusive with respect to the question to which extent complex stochastic quantization is a successful approach to the Thirring model. There is some evidence justifying hope, but there are also severe signals for skepticism. We elaborate on this in the following.

9.2.2.1 Relevant quantities

The main observables we calculate are the chiral condensate

$$\langle\overline{\chi}\chi\rangle = \frac{1}{V}\left\langle \operatorname{tr} M^{-1}\right\rangle, \tag{9.28}$$

with a non-vanishing vacuum condensate signaling spontaneous breaking of chiral symmetry, and the density

$$\langle n\rangle = \frac{1}{V}\frac{\partial \ln Z}{\partial\mu} = \frac{1}{V}\left\langle \operatorname{tr} M^{-1}\frac{\partial M}{\partial\mu}\right\rangle. \tag{9.29}$$

The density is trivially zero at $\mu = 0$, and is non-zero at large μ where bound states form. Regarding the behavior at small μ in the limit $T \to 0$, see the remarks on the 'Silver Blaze' behavior in sec. 9.2.2.3.

As we work in lattice units, the quantities (9.28) and (9.29) are dimensionless. The expectation values, symbolized by $\langle\cdots\rangle$, are always taken as averages over uncorrelated configurations (see app. B.1.1). This serves as an approximation to the ideal expectation value

$$\langle B\rangle = \frac{\int \mathcal{D}A_\nu\, B[A] e^{-S_{\text{eff}}[A]}}{\int \mathcal{D}A_\nu\, e^{-S_{\text{eff}}[A]}} \tag{9.30}$$

of the respective observable B. Here, the configurations are generated employing the Langevin algorithm (9.17), with sufficient numbers of dummy sweeps between 'measurements', and of initial 'thermalization' sweeps before the first measurement.

In addition, we study the phase factor of the fermion determinant $\det M$

$$e^{i\phi} = \frac{\det M(\mu)}{|\det M(\mu)|} \tag{9.31}$$

resp.

$$e^{2i\phi} = \frac{\det M(\mu)}{\det M(-\mu)}, \tag{9.32}$$

which is a quantity relevant to the sign problem. The sign problem is severe if the average phase factor is very small, since this induces strong cancellations in the path integrals. Note that after complexification, the relation[7]

$$\det M(\mu) = [\det M(-\mu)]^* \tag{9.33}$$

holds only on average. Thus, the 'phase factor' does, in general, not lie on the unit circle in the complex plane if calculated from eq. (9.32). If defined according to eq. (9.31), its absolute value is of course 1. We present the corresponding numerical results in sec. 9.2.3.6.

9.2.2.2 Implementation

The implementation rests on the explicit formulation of the lattice Langevin equation, given in sec. 9.2.1.3. From the formulation of the force term (9.18), which enters into the discrete Langevin equation (9.17), it is evident that the inversion of the fermion matrix M is part of each updating sweep. Indeed, the bulk of the numerical effort is devoted to this inversion. It can be performed in a straightforward manner with standard numerical routines.[8] The time required for the inversion does not depend significantly on the bare fermion mass m.

[7] Eq. (9.33) must not be confused with eq. (9.9), where the *complex conjugate of* the chemical potential serves as the argument of the fermion matrix on the right hand side.

[8] We have done so with the Intel Math Kernel Library by previously computing the LU factorization (routine `zgetrf` followed by `zgetri`). – Alternatively, the inversion can be performed via singular value decomposition, e. g. with the Gnu Scientific Library [472]. This method decomposes a general real $m \times n$ matrix R as

$$R = U \cdot S \cdot V^T, \tag{9.34}$$

where U is an $m \times n$ column-orthogonal matrix, S is a diagonal $n \times n$ matrix, which can be represented by just a vector, and W is an $n \times n$ orthogonal matrix. The fact that the fermion matrix M is complex can easily be circumvented by computing the LU factorization of the real $2V \times 2V$ matrix (lattice volume $V = L_s^2 L_t$)

$$R \equiv \begin{pmatrix} \mathrm{Re}\, M & \mathrm{Im}\, M \\ -\mathrm{Im}\, M & \mathrm{Re}\, M \end{pmatrix} \tag{9.35}$$

with the result

$$R^{-1} \equiv \begin{pmatrix} \mathrm{Re}\, M^{-1} & \mathrm{Im}\, M^{-1} \\ -\mathrm{Im}\, M^{-1} & \mathrm{Re}\, M^{-1} \end{pmatrix}. \tag{9.36}$$

Then, $m = n = 2V$ in the singular value decomposition algorithm. Once the LU decomposition is at hand, the inversion is trivial,

$$R^{-1} = V \cdot S^{-1} \cdot U^T, \tag{9.37}$$

as is the transition from R^{-1} to M^{-1} by way of eq. (9.36).

9.2.2.3 'Silver Blaze' problem

In addition to the sign problem, there is another aspect of the Thirring model which we also investigate numerically, sc. the 'Silver Blaze' problem. This term was coined in ref. [473]. That a theory exhibits a 'Silver Blaze' behavior means that

(i) observables are independent of the chemical potential μ below an onset to a condensed phase, which occurs at a value μ_c, and that, in addition,

(ii) μ_c generically differs between the full and the phase-quenched theory.

(The second part of the criterion extends the original definition.)

The phase-quenched theory is obtained from the full theory by replacing the action S by its real part $\operatorname{Re} S$,

$$S \to \operatorname{Re} S \quad \text{and thus} \quad e^{-S} \to e^{-\operatorname{Re} S} = |e^{-S}|. \tag{9.38}$$

Since this theory has a real action, it does not have a sign problem. It is accessible with standard methods and with a real Langevin algorithm, which we usually use for simulating it. This can be done by simply setting the imaginary parts of the auxiliary field and of the drift term to zero. The Langevin equation for the Thirring model is introduced in eqs. (9.13) and (9.17) below.

Thus, the criterion for 'Silver Blaze' behavior is twofold. The first part alone can sometimes easier be tested numerically, as we will also see in the Thirring model (sec. 9.2.3.2), even though it strictly holds only in the limit $T \to 0$ ($\hat{=}\ L_t \gg L_s$). It entails that the density is zero up to some μ_c, and that the chiral condensate is constant in this region. We also investigate explicitly the second part of the criterion (sec. 9.2.3.4).

The 'Silver Blaze' property is nontrivial, since it is far from obvious how the dependence on μ cancels in observables while being explicitly present in the Boltzmann weight (functional integral) of the microscopic theory.

9.2.3 Results of numerical studies

Before presenting numerical results, in particular for the chiral condensate, the density and the phase factor, we state the parameters at which we have usually produced them. We work at the coupling $g^{-2} = 1.6$ with $N_f = 2$, unless mentioned otherwise. By virtue of this choice of parameters, the theory is at $\mu = 0$ in the phase of broken chiral symmetry, since the critical coupling at $N_f = 2$ is $g_c^{-2} = 1.92(2)$ at $N_f = 2$ [458]. The lattices have a volume $V = L_s^2 \times L_t$ in lattice units (number of lattice sites). The lattices we employ are mostly symmetric, i. e., $L_s = L_t$. We usually use the complex Langevin algorithm (as opposed to random walk) with a constant step size $\varepsilon = 0.005$. An adaptive step size proves to be not necessary, see sec. 9.2.3.1 for a brief discussion.

When referring to the expectation values of the chiral condensate or the density, we denote by '$\langle\overline{\chi}\chi\rangle$' and '$\langle n\rangle$' the real part of the respective quantity. This is a reasonable shorthand notation since the imaginary part of observables vanishes on average.

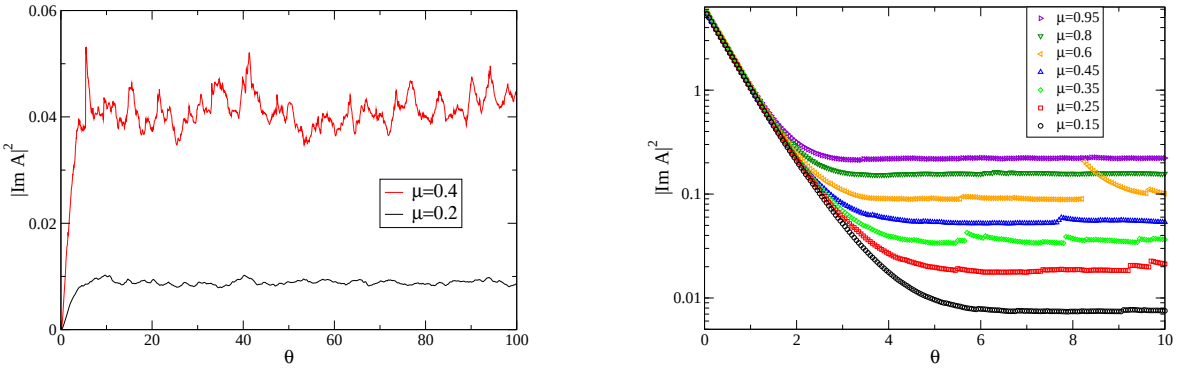

Figure 9.1: Imaginary part of the field A (averaged over the volume) vs. 'Langevin time' $\theta = n \cdot \varepsilon$, here with constant step size $\varepsilon = 0.005$. *Left (a):* 'Cold start', 6^3 lattice, mass $m = 0.2$. *Right (b):* 'Hot start', 12^3 lattice, $m = 0.03$.

9.2.3.1 Convergence and basic tests

(In order to ensure some clarity of arrangement in this chapter, each part of thre present sec. 9.2.3 is preceded by the numbers of the figures relevant to it. For the present one, the relevant figures are 9.1 and 9.2.)

We start with a basic observation that provides some initial confidence in the usefulness of complex Langevin evolution for the Thirring model. The content of this observation is that no 'runaway trajectories' occur, i. e., the imaginary part of the field remains bounded during the Langevin evolution also at non-vanishing chemical potential μ, as illustrated in fig. 9.1. This already holds without employing an adaptive step size method and without choosing a particularly small fixed step size; its typical value in our simulations is $\varepsilon = 0.005$. (For the data shown in fig. 9.1a, a cold start has been chosen for illustrative purposes, i. e., the starting configuration is the constant real configuration $\forall x, \mu : \; A_\mu(x) = 1$. Usually, we perform a 'hot' start, i. e., we start with a complex auxiliary field $A_\mu(x)$ that is randomly generated for each x and μ independently.)

At a smaller mass and with a 'hot' start, fig. 9.1b, we observe that the imaginary part of the auxiliary field decreases during 'thermalization' and then essentially fluctuates around a constant value. There are a few instances where $|\mathrm{Im}\, A|^2$ jumps to a larger value. But this does not result in runaway trajectories. Instead, $|\mathrm{Im}\, A|^2$ returns to an equilibrium value, although not in a single step.

In addition, there is a separate, but similar phenomenon. Fig. 9.2 demonstrates that some rather isolated large values of the observables ('spikes') occur during the Langevin evolution. We call them 'isolated' because they are uncorrelated with subsequently measured configurations, where $\overline{\chi}\chi$ and n again take normal values. We digress briefly to discuss these 'spikes' in a little more detail.

They are not an artifact of constant step size, as they also occur when a Langevin algorithm with an adaptive step size is employed. The version of the adaptive step size procedure that corresponds to the data shown in fig. 9.2 proceeds in the following simple way: In each Langevin updating sweep (number n), the maximum of the drift terms at all sites and directions is determined, and the step size ε is chosen proportional to the inverse

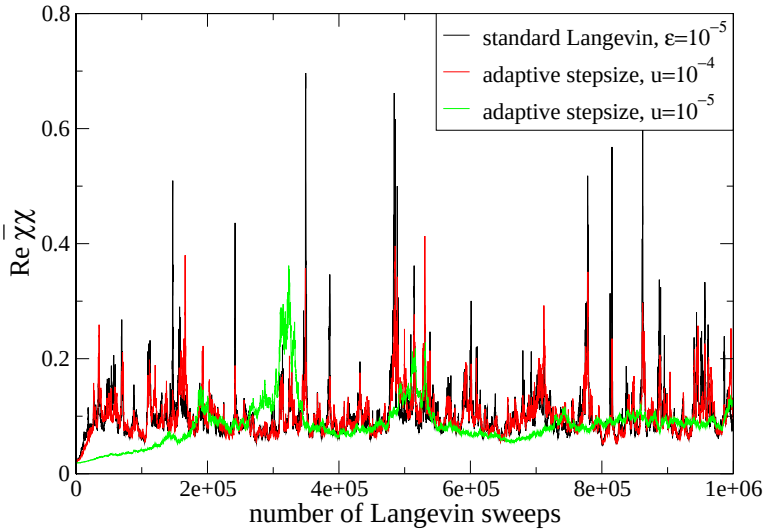

Figure 9.2: Langevin evolution of the (real part of the) chiral condensate at $m = 0.05$ on a 4^3 lattice, $g^{-2} = 2.8$, $\varepsilon = 5 \cdot 10^{-5}$, with constant and with adaptive step size (eq. (9.39)).

of this maximum, sc. as

$$\varepsilon(n) = \frac{u}{\max_{x,\mu} \left| K_\mu(x,n) \right|} \tag{9.39}$$

with a real parameter u. Fig. 9.2 shows that this does little to diminish the 'spikes', unless u is chosen so small that the autocorrelation time increases significantly and correspondingly more sweeps would be required. – Note, moreover, that these spikes are particularly large at small bare fermion masses m, since the inverse fermion matrix enters in the calculation of expectation values (which is especially evident for the chiral condensate, eq. (9.28)), and this inverse is proportional to the inverse fermion determinant. Their impact on expectation values is also discussed around fig. 9.20 in sec. 9.2.3.5 below. – This closes our brief digression.

The results presented above reassure us that it is indeed prima facie reasonable to calculate expectation values in the Thirring model with the complexified stochastic algorithm that we utilize. We consider expectation values mainly of the chiral condensate $\overline{\chi}\chi$, eq. (9.28), and the density n, eq. (9.29). Initial thermalization steps as well as typically $\mathcal{O}(100)$ dummy sweeps between any two 'measurements' are of course discarded.

These calculations of expectation values at different values of μ result in some clear findings, although they leave some other questions open. We first explore the clear findings.

An indispensable test of the algorithm is the comparison of its results with those of standard methods at $\mu = 0$. For example in [458], numerical values of the chiral condensate are given for different bare fermion masses and lattice volumes. They were produced with a standard algorithm (Hybrid Monte Carlo), which works well at $\mu = 0$, as opposed to non-zero μ. These results mostly agree within error bars with our results, which are included e. g. in fig. 9.20 below.

Another clear finding pertains to the 'Silver Blaze' problem, which is discussed in the following.

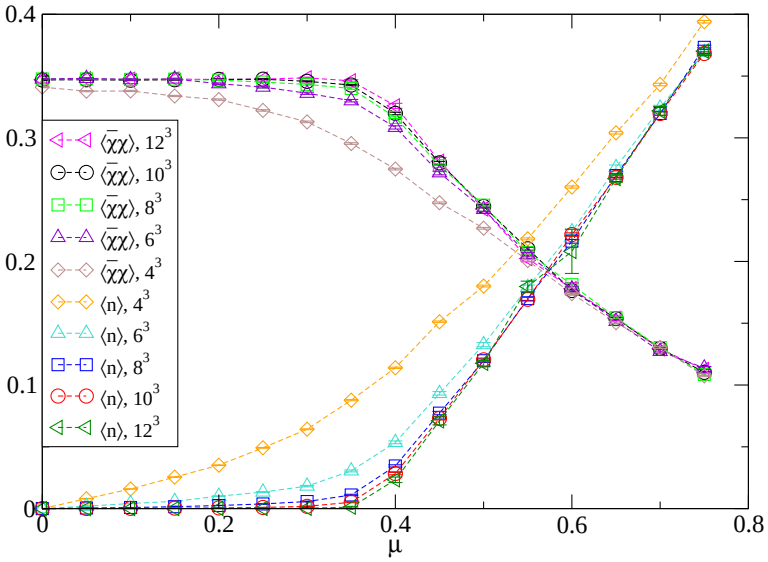

Figure 9.3: Finite volume effect for the density $\langle n \rangle$ and the chiral condensate $\langle \overline{\chi}\chi \rangle$ as a function of the chemical potential at a mass $m = 0.2$ with step size $\varepsilon = 0.005$. Lines are drawn to guide the eye.

9.2.3.2 'Silver Blaze', part one

(Relevant figures are 9.3 through 9.7.)

Our simulations at non-zero μ show that the first of the two criteria for a 'Silver Blaze' behavior, see sec. 9.2.1, is fulfilled. This criterion states that below some μ_c, observables like the density and the chiral condensate do not depend on μ. More precisely, $\langle n \rangle$ vanishes and $\langle \overline{\chi}\chi \rangle$ takes a constant non-vanishing value (at the chosen parameters). Only in the limits of infinite volume and vanishing temperature does this statement hold exactly.

The results on symmetric lattices already strongly suggest such a behavior, see fig. 9.3. The finite volume effect is notable, but no very huge lattices are required to identify signs of a 'Silver Blaze' behavior. The difference between the $V \to \infty$ extrapolations of $\langle n \rangle$ for small μ and for large μ is virtually evident to the naked eye from fig. 9.3. Blowups of the chiral condensate and the density, respectively, at small μ are shown in figs. 9.4 and 9.5. We perform a straightforward finite volume analysis for the density, shown in fig. 9.6. It reveals that the density indeed decreases exponentially with the linear lattice extension at small values of μ and does not do so at larger values of μ, corroborating the behavior already inferred from fig. 9.3.

Moreover, the 'Silver Blaze' behavior is even more pronounced when the temperature is further lowered by using asymmetric lattices, more specifically, by choosing the linear temporal lattice extension $L_t \propto 1/T$ (cp. eq. (8.1)) to be larger than the spatial one, see fig. 9.7. E. g., the density on a lattice with $L_s = 8$ and $L_t = 12$ resembles much more its counterpart from a 12^3 lattice than the one from a 8^3 lattice. Thus, the influence of the spatial extension is small compared to the thermal effect.

9.2.3.3 Difference between full and phase-quenched theory beyond the onset

(Relevant figures are 9.8 through 9.11.)

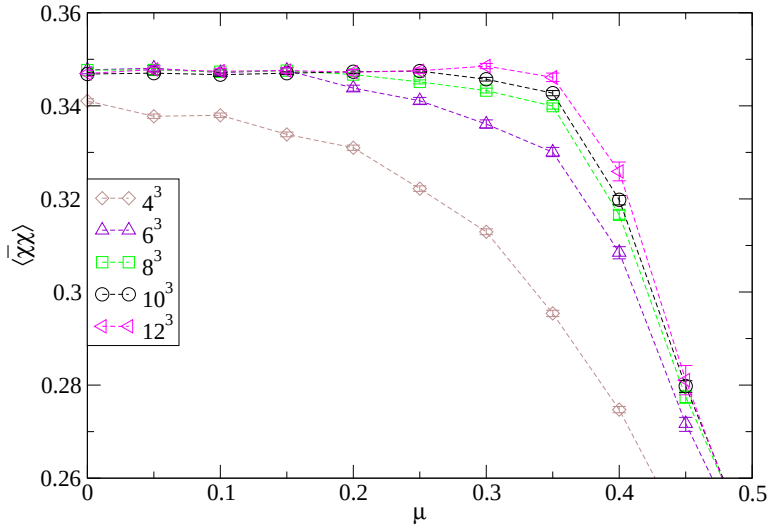

Figure 9.4: Blowup of the chiral condensate from fig. 9.3 (see caption to that fig. for parameters).

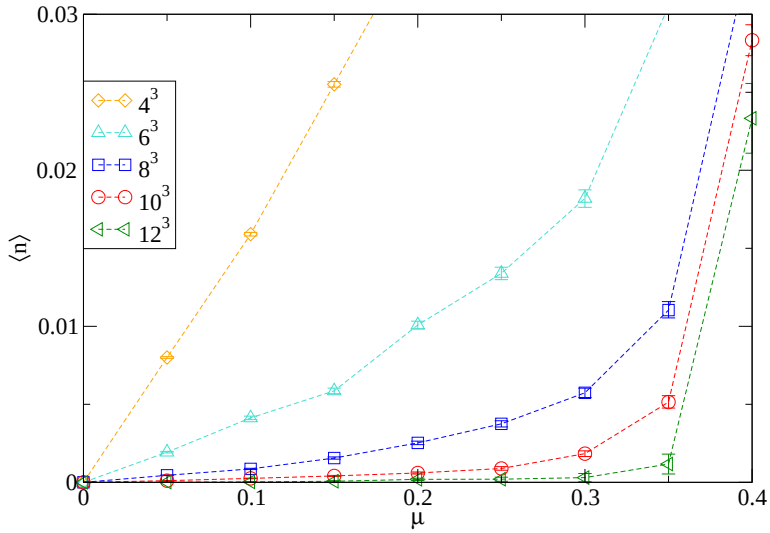

Figure 9.5: Blowup of the density from fig. 9.3.

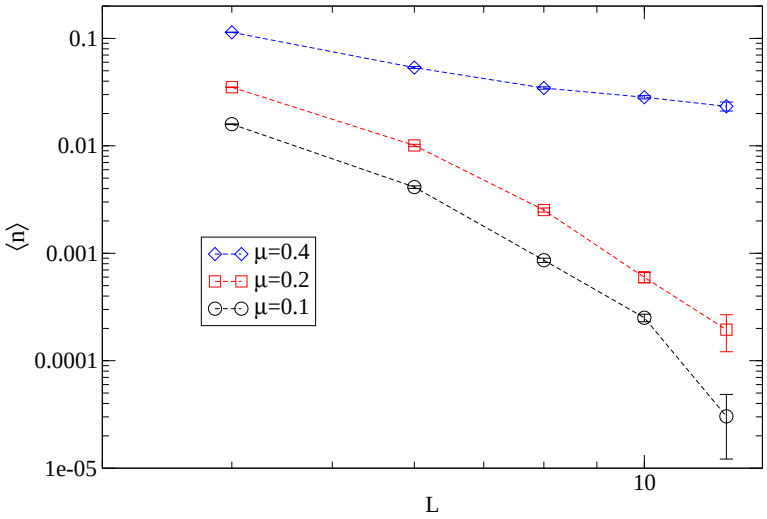

Figure 9.6: Finite volume behavior of the density below and above μ_c (a 'cross section' of the data from fig. 9.5). Only for $\mu < \mu_c$, the behavior is consistent with $\langle n \rangle = 0$ in the $V \to \infty$ limit.

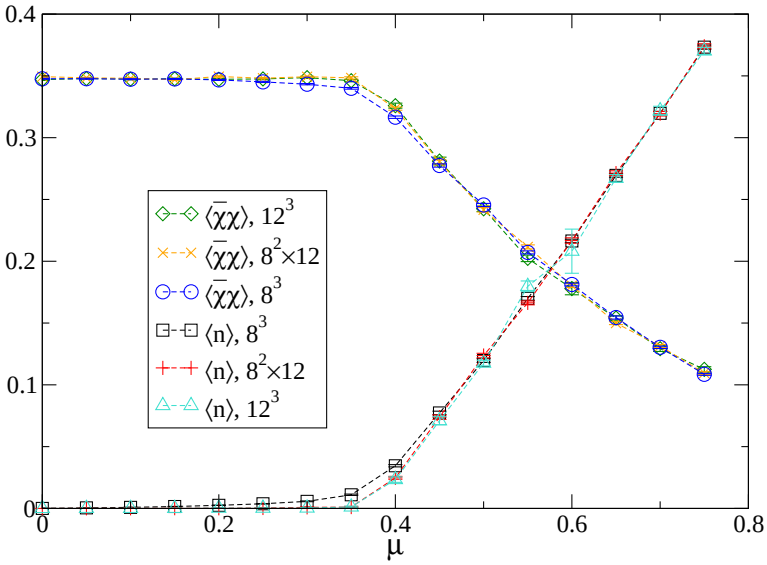

Figure 9.7: A plot similar to fig. 9.3, also at $m = 0.2$, but including an asymmetric lattice with $L_t > L_s$. This makes the 'Silver Blaze' behavior even more obvious.

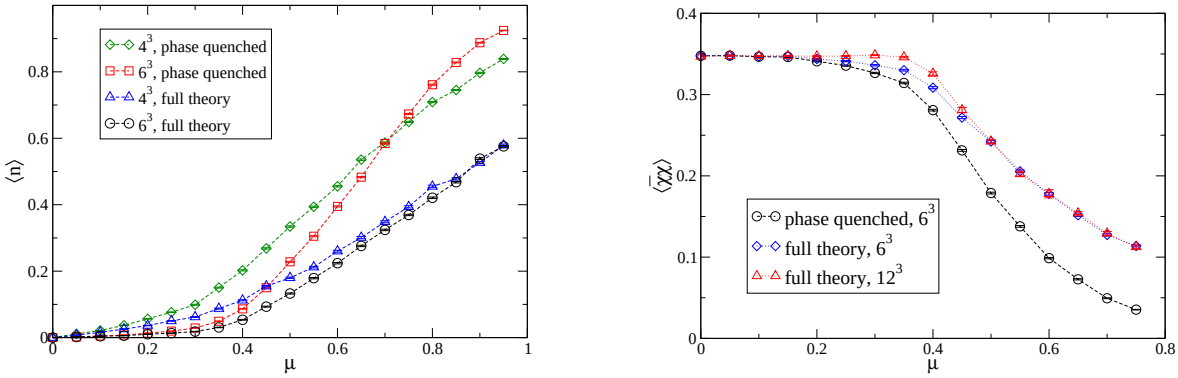

Figure 9.8: Comparison of the phase-quenched theory with the full theory at $m = 0.2$. Lines are drawn to guide the eye. *Left (a):* Density. *Right (b):* Chiral condensate.

So far, we have shown that the full theory, simulated with complex Langevin evolution, exhibits one of the 'Silver Blaze' properties. Another test of complex Langevin evolution is whether it is able to see a difference between the full theory and its phase-quenched counterpart (defined in sec. 9.2.2.3), which have a complex resp. real action. This can be understood in two different ways. The second 'Silver Blaze' criterion, as stated in sec. 9.2.2.3, is that a difference in the onset is observed. Before we examine this question, we analyze the similar, but distinct question of whether the Langevin simulation can distinguish between the full and the phase-quenched theory at large μ, i. e., beyond the onset.

From our results, the answer is affirmative. Namely, the values of $\langle n \rangle$ and $\langle \overline{\chi}\chi \rangle$ at large μ differ considerably and systematically between these two cases. This is shown in fig. 9.8 for a large mass, $m = 0.2$ (we will soon comment on why it is reasonable to call this mass 'large'). We have studied a number of much smaller masses; at all these masses, qualitatively the same statement holds, even though the difference between the observables in the full and in the phase-quenched theory tends to decrease toward smaller bare fermion masses. A direct comparison of the chiral condensate in the full and phase-quenched theory at $m = 0.05$ is shown in fig. 9.9. In fig. 9.10, the density in the full and in the phase-quenched theory is compared at $m \in \{0.01, 0.02, \ldots, 0.05\}$. (For results for the chiral condensate at the same five values of the mass, see fig. 9.20 below.) The density clearly differs between the full and the phase-quenched theory at large values of the chemical potential for all of these bare masses. (A blowup of fig. 9.10, focusing on the onset, is provided in fig. 9.15 below.)

As a side note, in order to assess whether a mass is large, we consider here the volume dependence of the average phase factor, eq. (9.32). The naïve expectation is that below μ_c, Re $\langle e^{2i\phi} \rangle$ decreases exponentially with the lattice volume and is thus smaller on larger lattices. For $m = 0.2$ in the phase-quenched theory, this expectation is violated, see fig. 9.11a. Possibly, this can be explained by the fact that the partition function is independent of μ (below μ_c) and that therefore the average phase factor approaches 1 for large volumes [455]. – At a small bare fermion mass $m = 0.01$, on the other hand, the volume dependence of the phase factor is qualitatively as expected, see fig. 9.11b. At $m = 0.05$, we find only a small volume dependence at small μ (not shown in a figure).

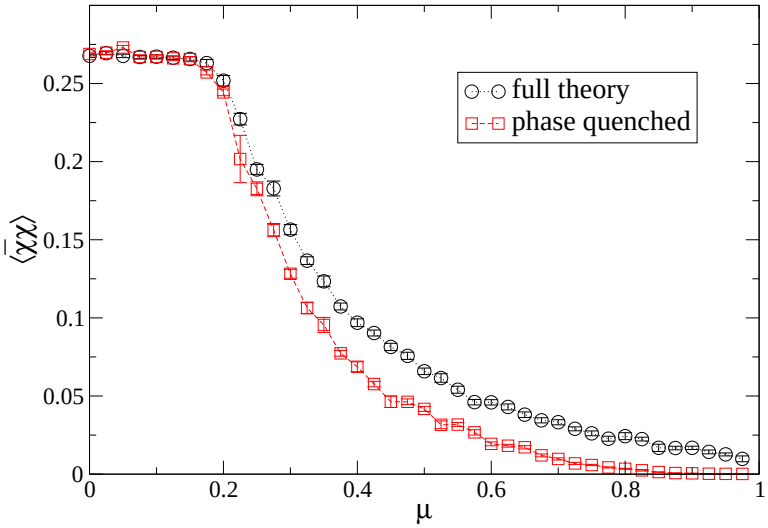

Figure 9.9: Chiral condensate vs. chemical potential at $m = 0.05$ on a 12^3 lattice. These data are also included in fig. 9.20.

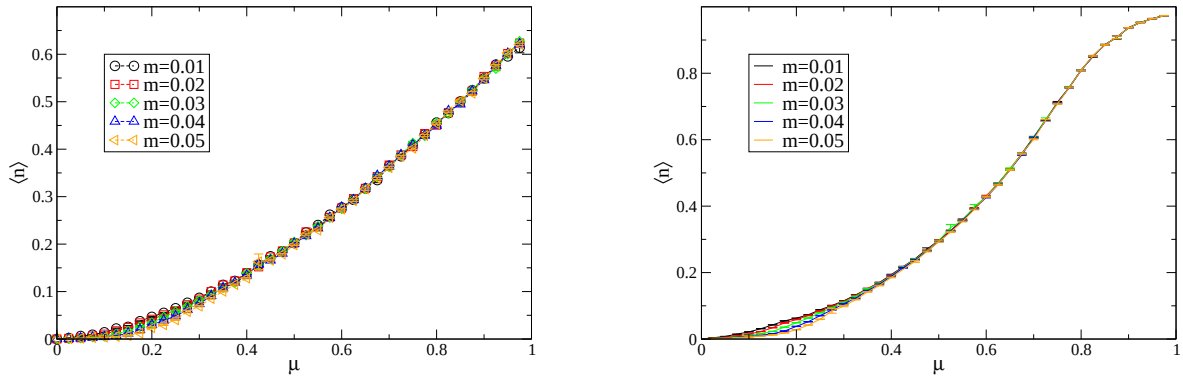

Figure 9.10: Density on an 8^3 lattice in the full theory *(left, (a))* and in the phase-quenched theory *(right, (b))*. A blowup of these data at small μ is provided in fig. 9.15 and allows to further analyze the dependence on the bare mass; in the present context of sec. 9.2.3.3, the focus is on the difference between the full and the phase-quenched theory at large μ.

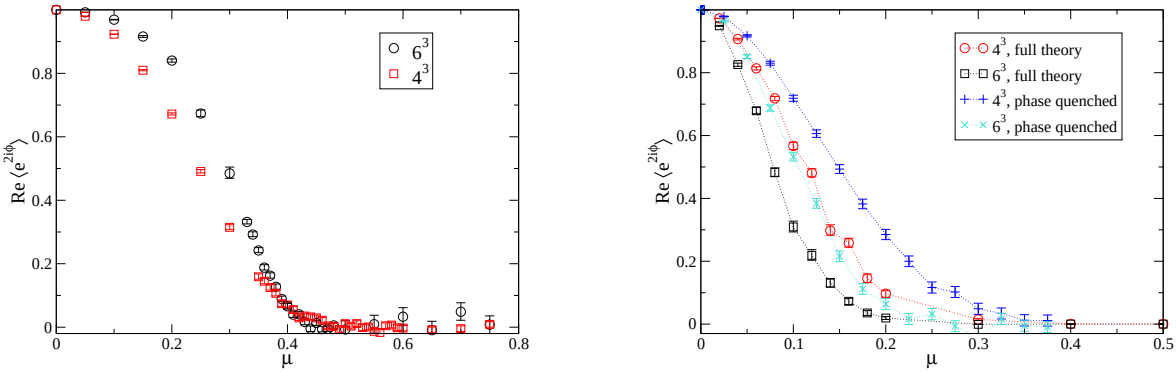

Figure 9.11: *Left (a)*: Real part of the phase factor, eq. (9.32), in the phase-quenched theory at $m = 0.2$. *Right (b):* The same quantity, but at the much smaller mass $m = 0.01$ and both for the phase-quenched and the full theory.

9.2.3.4 'Silver Blaze', part two: Difference between the full and phase-quenched theory at the onset

(Relevant figures are 9.12 through 9.18.)

While our results show that the first criterion for 'Silver Blaze' behavior is fulfilled (sec. 9.2.3.2), the second criterion defined in sec. 9.2.2.3 still needs to be tested in order to rule out that a 'fake onset' is seen by the complex Langevin evolution. It is not sufficient that the data above the onset differ between the full and the phase-quenched theory (sec. 9.2.3.3). In addition, different values μ_c of the onset are required.

Expectations. A priori, it is expected that the onset occurs at the fermion mass, $\mu = M_f$, in the full theory, and at half the pion mass, $\mu = M_\pi/2$, in the phase-quenched theory. The latter statement holds since the pion mass is composed of a fermion and a 'conjugate fermion'. In QCD, $M_f = m_B/3$ with the baryon mass m_B. M_f is the physical fermion mass, as opposed to the bare fermion mass m that enters as a parameter in the Lagrangian (9.4).

The pion mass M_π has been determined previously from $\mu = 0$ simulations at parameters similar to ours. Results of ref. [458] are $M_\pi = 0.20(1)$, $0.280(4)$ and $0.398(4)$ at the bare fermion masses 0.01, 0.02 and 0.05, respectively.

Some data for the (physical) fermion mass M_f at $g^{-2} = 1.6$ given in ref. [458] are $0.36(3)$ at $m = 0.01$, $0.330(40)$ at $m = 0.02$ and $0.480(40)$ at $m = 0.05$. The finite volume effects were found to be rather small in the chirally broken phase [458].

From these values of M_π and M_f, it can be inferred that at least at small bare fermion masses, one should expect the onsets in the full and in the phase-quenched theory to differ significantly; the latter one should occur at lower values of the chemical potential. We now turn to some numerical results, which we have obtained with complex stochastic quantization for the full theory, and with ordinary langevin evolution for the phase-quenched theory.

Results. A comparison of the density $\langle n \rangle$ in the full and the phase-quenched theory is shown in fig. 9.12a, and of the chiral condensate $\langle \overline{\chi}\chi \rangle$ in these two cases in fig. 9.12b, all for the rather large bare fermion mass $m = 0.2$. Fig. 9.13 shows the same comparison for

$m = 0.05$. Moreover, we have studied the theory at a mass as small as $m = 0.005$, see fig. 9.14 for results for the density.

For all three values of the mass used here, it is impossible to extract different onsets in the full resp. phase-quenched theory from these data. This does not fit the expectations we have articulated. In the following table, we summarize some expectations for the position of the onset μ_c, based on previous determinations of the fermion and pion masses, together with estimates read off from our results. Where no explicit errors are given,[9] the numbers are to be understood with an uncertainty of at least $10 - 20\%$.

m	$M_\pi/2$	M_f	μ_c (full and ph'q')	see fig. ...
0.01	0.10(1)	0.36(3)	$0.06 - 0.08$	9.15, 9.16
0.02	0.140(2)	0.33(4)	$0.08 - 0.12$	9.15, 9.16
0.03	0.199(2)		$0.1 - 0.15$	9.15, 9.16
0.05		0.48(4)	≈ 0.19	9.13
0.2			$0.36 - 0.38$	9.12

A more systematic analysis of the density at five masses from $m = 0.01$ to 0.05 is given in figs. 9.15 and 9.16 for values of μ close to the onset μ_c. (Fig. 9.15 is a blowup of fig. 9.10a, with the focus now on the dependence on the bare mass, not on the difference between the full and the phase-quenched theory.)

We conclude that the second criterion for 'Silver Blaze' behavior is not fulfilled. The algorithm is apparently unable to distinguish between the onsets in the full and in the phase-quenched theory.

Assuming that the bare fermion mass is sufficiently small, a possible explanation for this conclusion is a failure of complex Langevin evolution, which would be neither unprecedented nor entirely unexpected, see sec. 9.1.2. I. e., even though complex Langevin evolution does converge, it might converge toward the wrong value, like in [435] or the much more recent study [446]. Since convergence of observables toward their correct values under complex Langevin evolution is not proven for a complex action S, this explanation remains a genuine possibility even for a careful and correct implementation. (For a recent attempt at developing some criteria for cases in which this method can be considered reliable, see [444].)

Results in the chirally symmetric phase. We have also carried out a few simulations outside the phase where chiral symmetry is broken at $\mu = 0$, sc. at $g^{-2} = 2.5$ instead of 1.6 (note again that $g_c^{-2} = 1.92(2)$ [458]). The results are shown in fig. 9.17. There is a *quantitative* difference in the values of the observables between the full and the phase-quenched theory, which amounts to $\mathcal{O}(10\%)$ for the density (less for the chiral condensate). But there is no *qualitative* difference between the results of complex Langevin evolution for the full theory and the results for the phase-quenched theory, which does not suffer from a sign problem.

Results for a larger number of flavors. We also take a brief look at the Thirring model at a larger number of flavors of staggered fermions, sc. $N = 2$, which corresponds to $N_f = 4$

[9] Those errors that are given are from ref. [458].

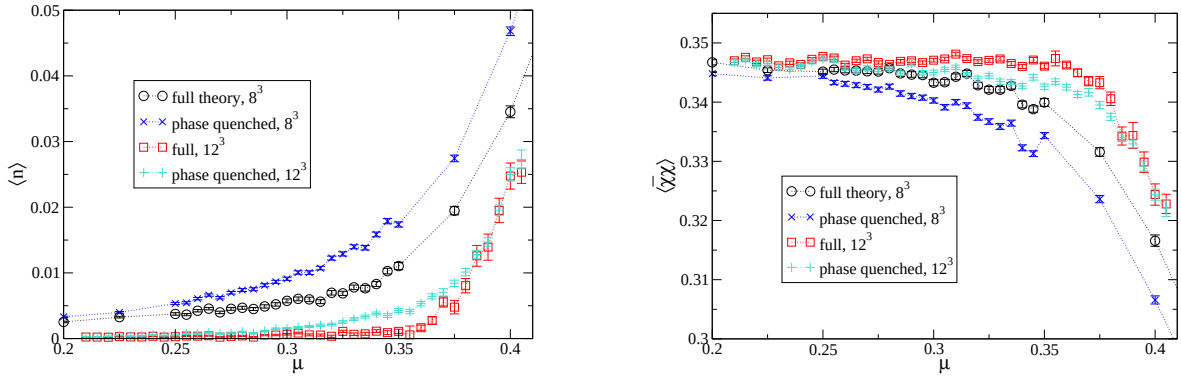

Figure 9.12: Density *(left, (a))* resp. chiral condensate *(right, (b))* vs. chemical potential for the full theory and for the phase-quenched theory, $m = 0.2$.

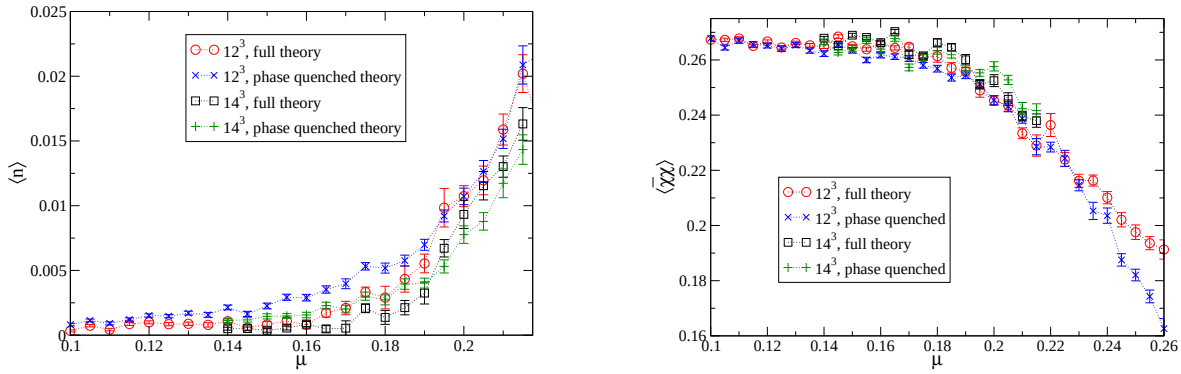

Figure 9.13: *Left (a):* Density vs. chemical potential, *right (b):* chiral condensate vs. chemical potential. In both cases, at $m = 0.05$ and close to the onset.

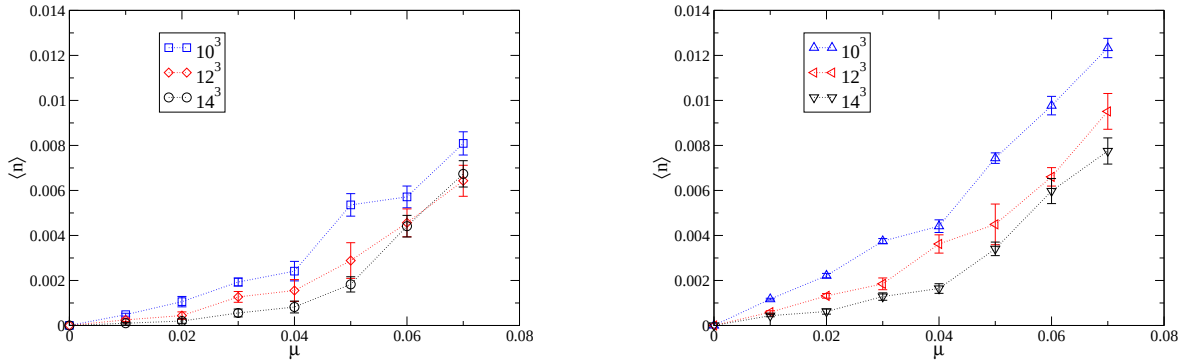

Figure 9.14: Density vs. chemical potential on different lattice sizes at $m = 0.005$. *Left (a):* Full theory. *Right (b):* phase-quenched theory.

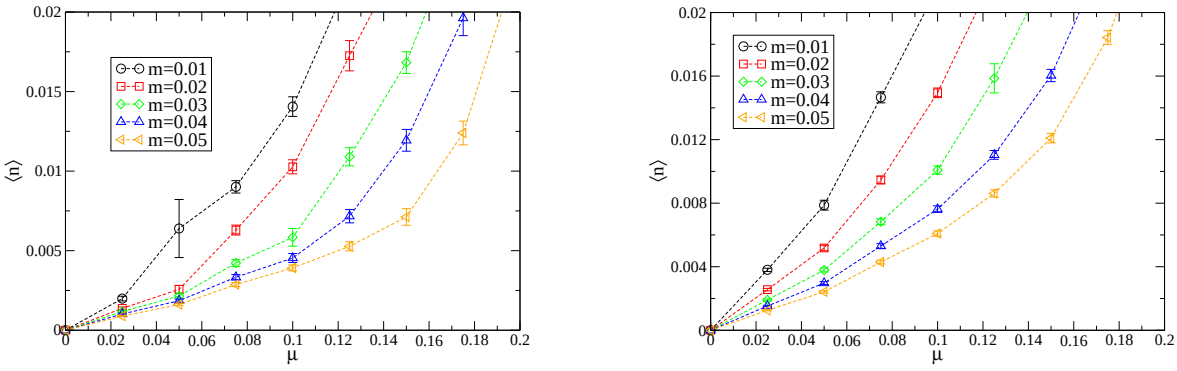

Figure 9.15: Density on a 8^3 lattice in the full theory *(left, (a))* and in the phase-quenched theory *(right, (b))* close to the onset (these are blowups of fig. 9.10).

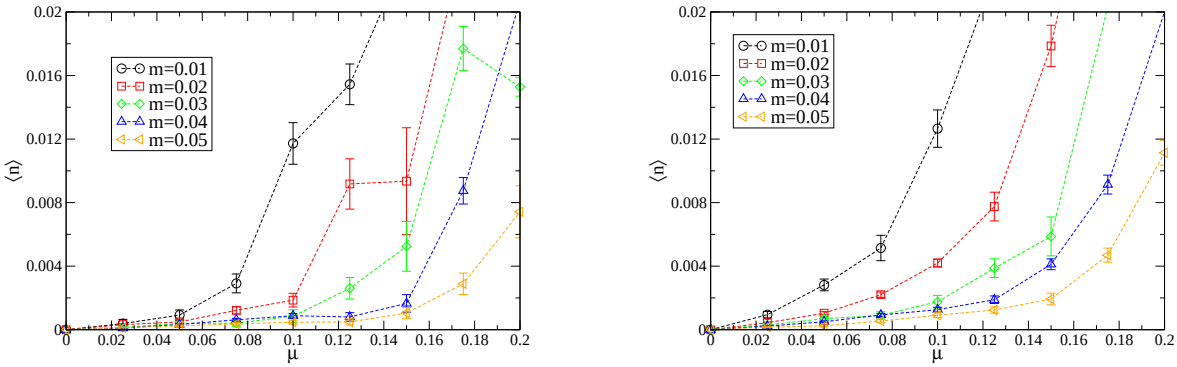

Figure 9.16: Like fig. 9.15, but on a 12^3 lattice. The comparison to fig. 9.15 shows that finite volume effects are strong.

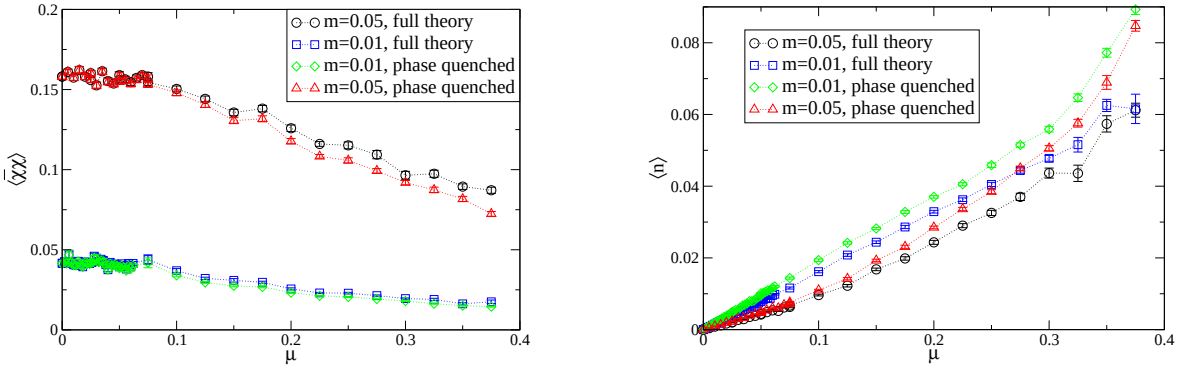

Figure 9.17: Results at $g^{-2} = 2.5 > g_c^{-2}$ on a 10^3 lattice. *Left (a):* Chiral condensate, *right (b):* density vs. chemical potential.

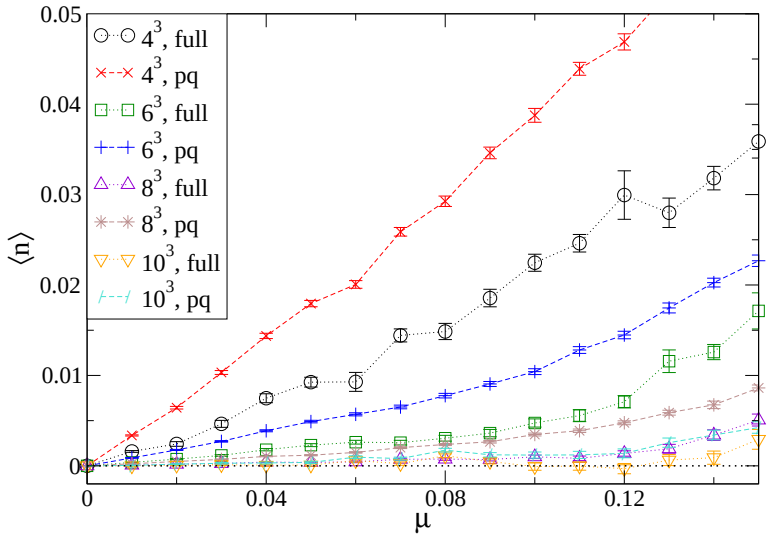

Figure 9.18: Larger number of flavors, sc. $N = 2$ ($\hat{=}\ N_f = 4$), with $1/g^2 = 0.6$ at $m = 0.05$. Comparison of the density in the full vs. phase-quenched theory for different lattice volumes.

in the continuum formulation. In order for the theory to be in the chirally broken phase at vanishing chemical potential, it is required to choose $1/g^2 < 1/g_c^2 = 0.69(1)$ [460] (here, $1/g^2 = 0.6$).

The finite volume behavior again does not appear to be relevantly different between the full and the phase-quenched theory in this case, see fig. 9.18, where the bare fermion mass is $m = 0.05$. The results for the phase-quenched theory on a volume $V = 10^3$ and for the full theory with $V = 8^3$ essentially agree within error bars.

9.2.3.5 Extrapolation to small bare masses and large volumes

(Relevant figures are 9.19 and 9.20.)

We now explicitly consider the dependence of the chiral condensate on the bare fermion mass. Data for such an analysis at vanishing chemical potential are depicted in fig. 9.19. Corresponding data at non-zero μ are included in fig. 9.20a for the full theory and in fig. 9.20b for the phase-quenched theory, respectively. An extrapolation is hardly feasible with certainty. But at least at $\mu = 0$, the data are consistent with a rather weak dependence of $\langle\overline{\chi}\chi\rangle$ on the bare fermion mass at zero chemical potential.

Fig. 9.20 demonstrates that the full and the phase-quenched theory essentially agree at $\mu = 0$, as they should, since in that case, the action is real and thus the phase zero (cp. (9.38)). On the other hand, the results for the full and the phase-quenched theory differ significantly at large values of the chemical potential, as illustrated by the same figure. Both is in line with general expectations, but it cannot conceal the fact that the position of the onset does not differ between the two theories, as discussed in sec. 9.2.3.4.

Another remark about the data shown in fig. 9.20 is in order. Among the various combinations of the parameters m and μ which we have studied, there are a few where for a single configuration (measurement), both $\mathrm{Re}\,\overline{\chi}\chi$ and $\mathrm{Re}\,n$ take anomalously large values, along with $\mathrm{Im}\,\overline{\chi}\chi$ and $\mathrm{Im}\,n$, which usually fluctuate around zero. To be precise, out of the

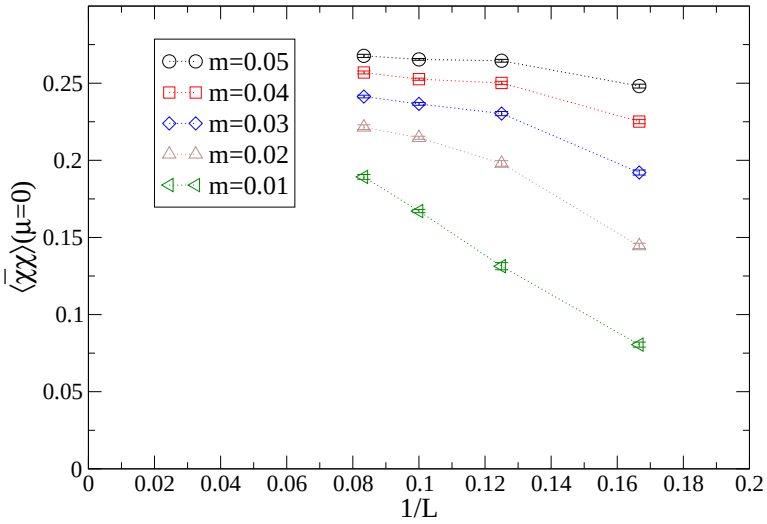

Figure 9.19: Data for a $V \to \infty$ extrapolation of $\langle\bar{\chi}\chi\rangle$ ($\mu = 0$).

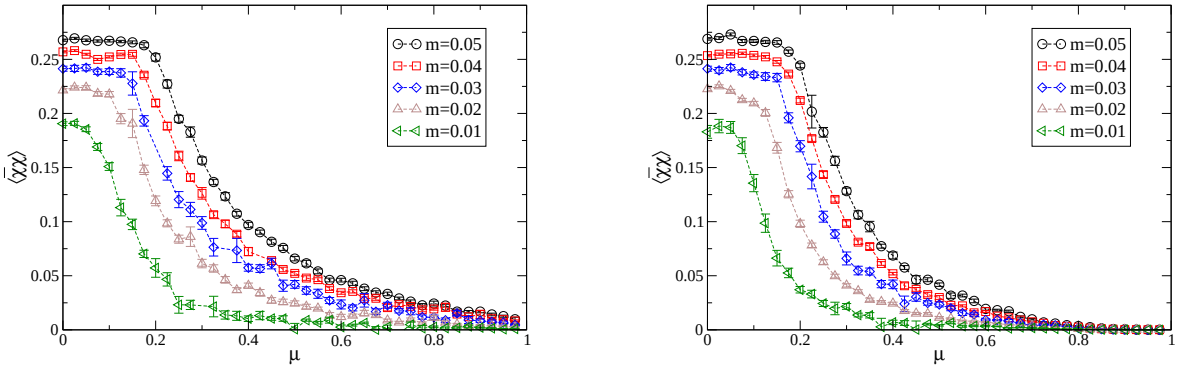

Figure 9.20: Chiral condensate vs. chemical potential on a 12^3 lattice. *Left (a):* Full theory. *Right (b):* phase-quenched theory.

$5 \cdot 40 = 200$ combinations of parameters (m, μ) studied in fig. 9.20, there are four where this occurs,[10] in each case for a single configuration, while between 50 and 400 (typically 200) independent configurations were generated for each pair (m, μ). Thus, these anomalies occur about once per 10^4 measurements. They may be related to the 'spikes' noted in sec. 9.2.3.1. They do not affect subsequent measurements, which is evidence that the number of dummy sweeps (here, 100) between measurements suffices to avoid correlations. For clarity, we have omitted the data points at the corresponding combinations of parameters in fig. 9.20.

(Some information about the dependence of the onset on the bare mass is also contained in figs. 9.15 and 9.16 for the density.)

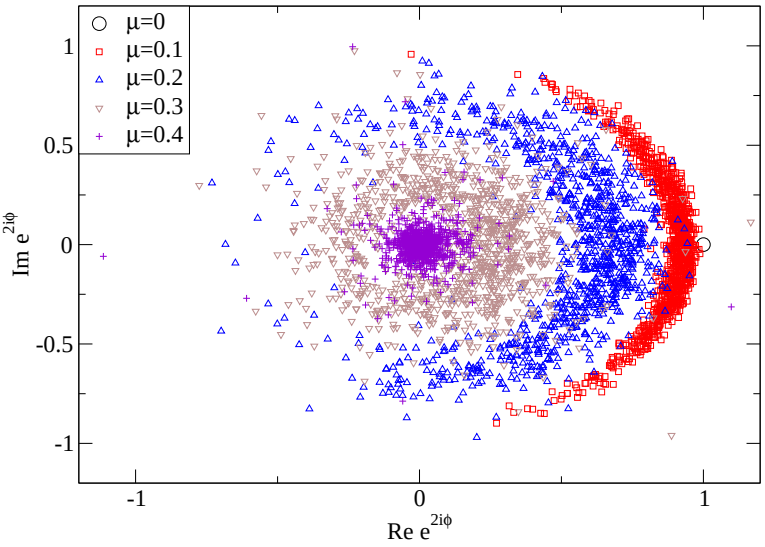

Figure 9.21: Scatter plot of the phase factor at $m = 0.2$ and different μ, employing the definition $e^{2i\phi} = \frac{\det M(\mu)}{\det M(-\mu)}$, eq. (9.32). Of course, $\mathrm{Re}\, e^{2i\phi} \equiv 1$ at $\mu = 0$.

9.2.3.6 Phase factor and eigenvalues

(Relevant figures are 9.21 through 9.23.)

On the positive side, we find evidence that the algorithm is able to sample configurations with all possible phases of the fermion determinant, see figs. 9.21 and 9.22. This property is necessary, although certainly not sufficient in order for the algorithm to tackle the sign problem. Correspondingly, the real part of the phase factor is very close to zero at large μ (as confirmed by the results for its expectation value at various μ, fig. 9.11). In figs. 9.21 and 9.22, two different definitions of the phase factor are used, as explained in sec. 9.2.2.1, eqs. (9.31) and (9.32). Only the definition used in fig. 9.22 entails that the absolute value of the phase factor equals 1.[11] In both cases (figs. 9.21 and 9.22), it is apparent that the phase factor, which trivially equals 1 at $\mu = 0$, gradually spreads out into the complex plane as μ is increased. At larger μ, it covers all angles. This illustrates that configurations with all phases of the fermion determinant are sampled. Thus, the complex Langevin algorithm satisfies a necessary condition for a correct simulation of the theory at non-zero μ. It is not a sufficient one, as is already apparent from the fact that our results presented above indicate that the complex Langevin evolution may not converge against the correct values for observables.

Similar information is conveyed by the scatter plots of the eigenvalues of the fermion matrix in fig. 9.23. Fig. 9.23a illustrates that the distribution is close to $\mathrm{Re}\,\lambda = m$ at small chemical potential μ and that it overlaps the origin at larger μ. The former behavior is expected, as the eigenvalues of the Dirac operator (p. 159) at $\mu = 0$ lie along a line parallel to the imaginary axis, with the offset given by the bare fermion mass. The latter behavior – overlapping the origin – indicates that the sign problem is indeed severe at the respective

[10] Sc. at the parameter pairs $m = 0.01$, $\mu = 0.3$; $m = 0.03$, $\mu = 0.2$ and 0.35; and $m = 0.04$, $\mu = 0.425$.

[11] The alternative definition does of course not represent a phase factor in the narrow sense, but it is still useful.

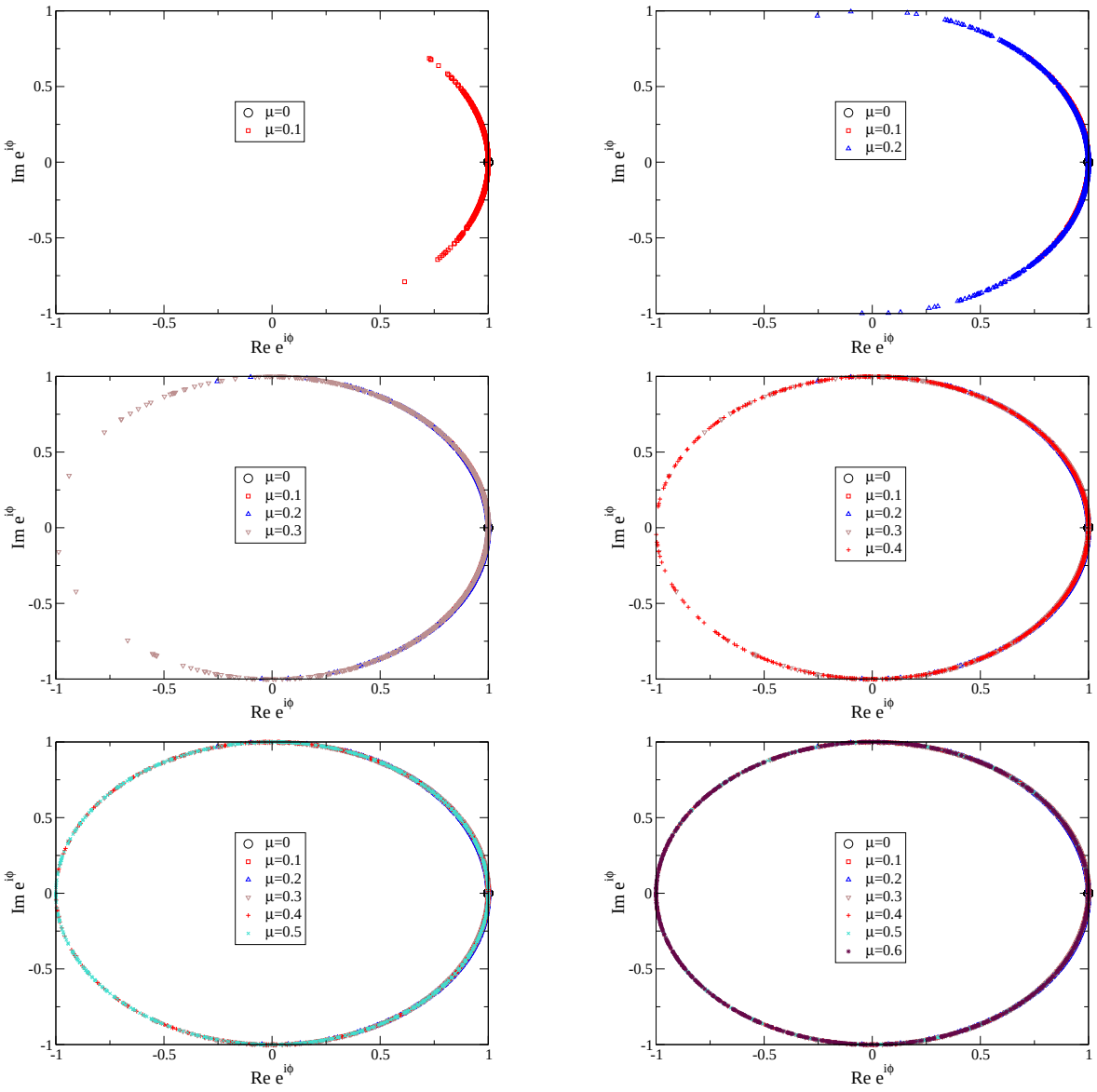

Figure 9.22: Scatter plot of the phase factor at different μ, employing the definition $e^{i\phi} = \frac{\det M(\mu)}{|\det M(\mu)|}$, eq. (9.31).

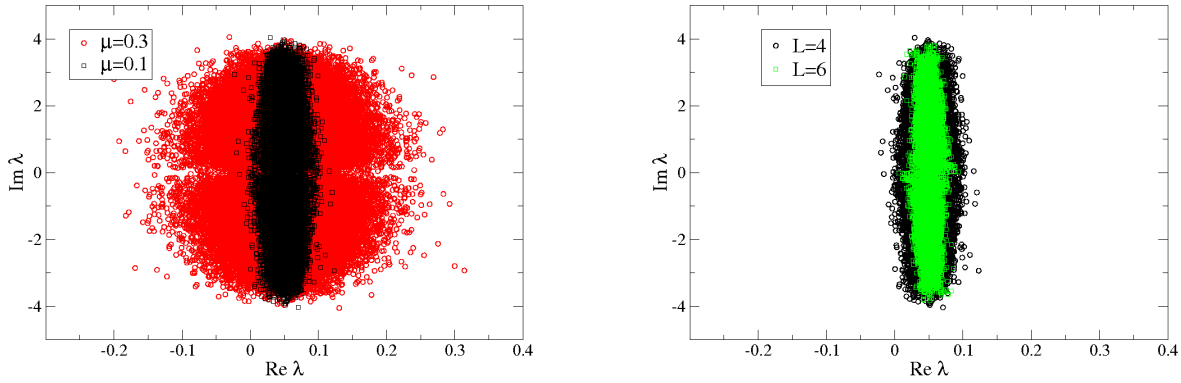

Figure 9.23: Distribution of the eigenvalues λ of the fermion matrix M in the complex plane, $m = 0.05$. *Left (a):* Linear lattice extension $L := L_s = L_t = 4$, two different μ. *Right (b):* for $\mu = 0.1$ at two different lattice sizes.

values of μ.

9.2.3.7 Comparison with heavy dense limit at large μ

(Relevant figures are 9.24 and 9.25.)

The results presented so far suggest that complex Langevin evolution fails near the onset to a phase of non-zero density, i. e., for intermediate μ. It remains to be clarified whether it works at large μ, where a clear difference between the results for the full and the phase-quenched theories does exist.

To this end, it is useful to compare the above results for the Thirring model with those in the model's heavy dense limit, where the chemical potential is taken to be large ('$\mu \to \infty$'). In this limit, which is discussed for QCD in [440] (see also references therein; motivated by the model studied in [474]), all spatial hopping terms are suppressed. The fermion matrix of the Thirring model in the heavy dense limit reads

$$M_{\mathrm{HD}}(x,y) = \frac{1}{2}[(1+iA_0(x))e^{\mu}\delta_{y,x+\hat{0}} - (1-iA_0(y))e^{-\mu}\delta_{y,x-\hat{0}} + m\delta_{x,y}]. \tag{9.40}$$

It is a $L_t \times L_t$-matrix. Again, the antiperiodic boundary conditions in temporal direction need to be taken into account.

One practical virtue of the heavy dense limit is that the force term, eq. (9.18), entering the Langevin equation (9.17) can be calculated analytically, as the fermion matrix can be inverted analytically for moderate L_t.[12] In the full theory, where the fermion matrix M is a $V \times V$ matrix, this is not feasible, and it is mandatory to resort to a numerical approach, as explained above (in particular in sec. 9.2.2.2).

We intend to compare the results for the chiral condensate in the full theory, figs. 9.9 and 9.8b, with the heavy dense limit. Fig. 9.24 indicates that the data in the heavy dense limit at large μ do not agree with the results of stochastic quantization in the full theory, although the difference decreases toward larger masses.

[12] We have used the computer algebra system `Mathematica` to this end.

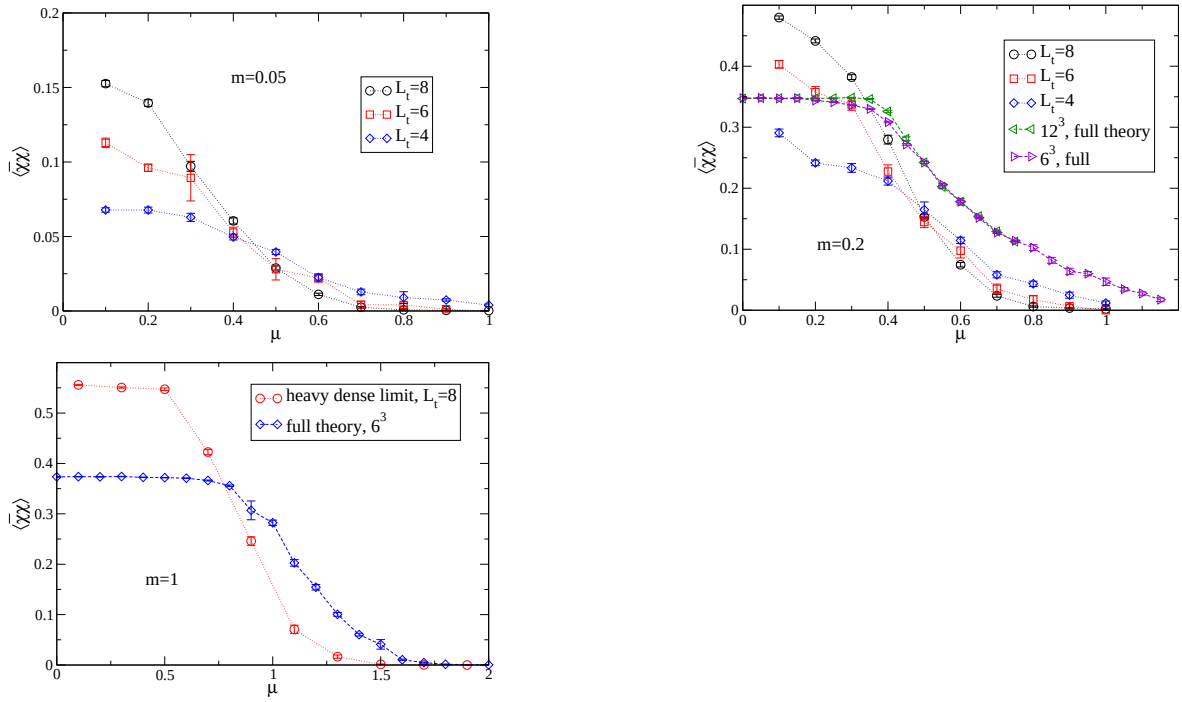

Figure 9.24: Chiral condensate vs. chemical potential in the heavy dense limit at different masses (indicated in the plots). At the two larger masses, data for the full theory included for comparison.

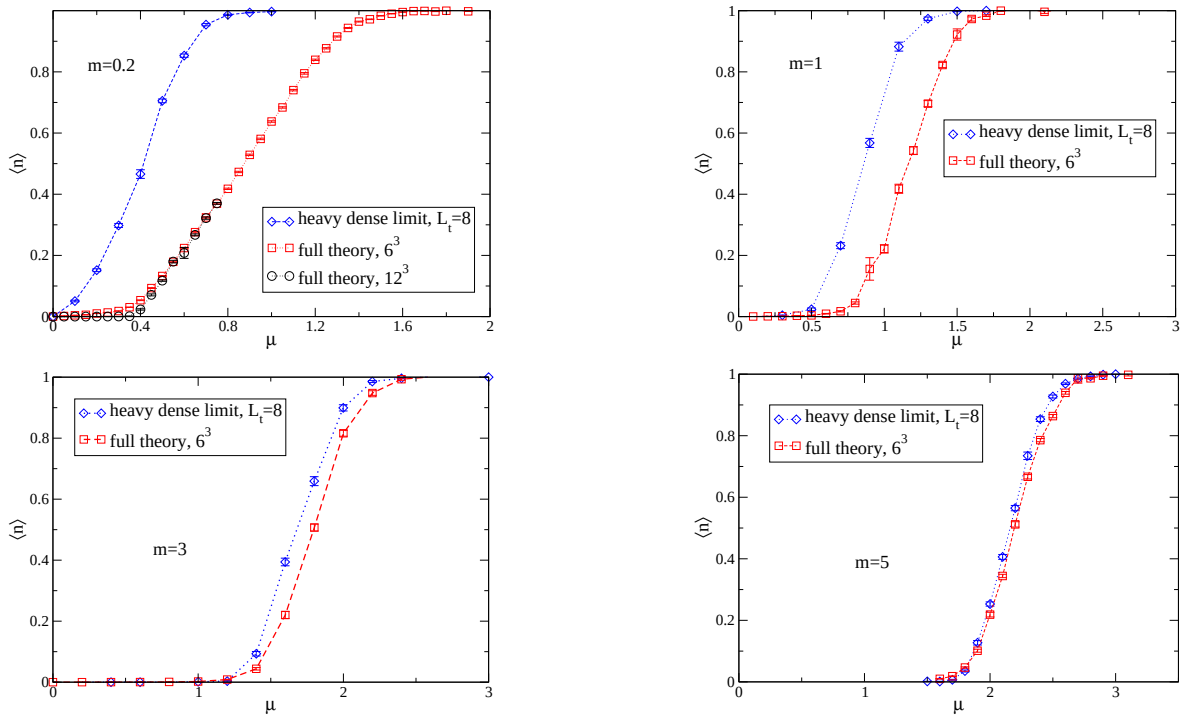

Figure 9.25: Density vs. chemical potential in the heavy dense limit and in the full theory at different masses (indicated in the plots).

Of course, one might doubt that the masses used here are large enough for the heavy dense limit to be a reasonable approximation. This objection is easily answered by extending the simulations to considerably larger masses. Fig. 9.25 shows the density at four different masses, up to $m = 5$. While the results for the heavy dense limit approach those of the full theory as m increases, the results for both cases never agree within errors before saturation sets in, i. e., unless $\langle n \rangle \approx 1$ (meaning that all lattice sites are occupied). A qualitative difference between the data in the heavy dense limit and in the full theory remains even at large μ.

Hence, the comparison with the heavy dense limit does not support the hope that complex Langevin equation is able to simulate the Thirring model at non-zero chemical potential correctly.

9.3 Summary

We have studied the Thirring model in three dimensions at non-zero chemical potential with complex Langevin evolution. The main observables we have calculated are the chiral condensate and the density. Despite the complex action, the algorithm converges without runaway trajectories, already with a constant step size. It is able to sample all phases of the fermion determinant. Moreover, the observables calculated with this algorithm exhibit 'Silver Blaze' behavior, as an extrapolation to zero temperature shows that they are independent of the chemical potential below an onset to a phase of non-zero density.

For a better understanding of the results, we have also performed simulations of the the phase-quenched theory in addition to the full theory. Within the uncertainties due to finite volume effects, no difference between the full and the phase-quenched theory can be discerned regarding the position of the onset. This is contrary to expectations. Beyond the onset, the values of the two observables differ significantly betweeen both theories. A comparison with the heavy dense limit does not confirm the validity of the results for the full theory at large chemical potential. Hence, there is reason to doubt that the results of complex Langevin evolution are correct in the presence of the sign problem in the Thirring model.

So far, during several, often mutually independent studies, both successful and unsuccessful applications of complex Langevin evolution were observed. An independent criterion for the prospects of this method is lacking. (See sec. 9.1.2 for references.) Our results constitute evidence that the Thirring model falls in the class of models for which this method converges against the wrong solution. This is a negative result and nevertheless an interesting and informative one.

CHAPTER 10

CONCLUSIONS

10.1 Summary

The results of the studies presented in the thesis at hand are not easily summed up, since they are concerned with a variety of questions and give detailed answers to each one.

Most of our studies deal with the infrared behavior of the gluon and ghost propagators of pure $SU(2)$ Yang–Mills theory in Landau gauge at zero temperature. They are motivated by a mismatch between previous lattice results and findings from functional continuum methods. Only the latter include a 'scaling solution' that is in line with the standard predictions of the Gribov–Zwanziger/Kugo–Ojima scenarios of confinement in Landau gauge. This is also the only solution that is consistent with an unbroken BRST symmetry, at least as long as no alternative BRST formulation has been spelled out. Our various approaches to this subject comprise alternative gauge fixing procedures, based on the idea that standard gauge fixing methods on the lattice may sample configuration space in a different way from continuum methods, thus bringing about a different infrared behavior of correlation functions. This could seem to affect the status of the aforesaid confinement scenarios, which makes it desirable to explore the possible range of gauge fixing methods.

After summarizing the results of these approaches (sec. 10.1.1), we turn to studies of the deconfinement phase transition at non-zero temperature, and of the sign problem that lattice simulations of QCD face at non-zero chemical potential. Both subjects are related to the phase diagram of QCD, and we have investigated them with methods that possess counterparts in our studies of the confinement mechanism. Namely, the gluon propagator has played a crucial role in our analysis of the deconfinement phase transition, and we have used stochastic quantization, one of the methods employed for gauge fixing, in a complex version in order to possibly circumvent the sign problem.

10.1.1 Infrared propagators and confinement scenarios

We divide our summary of the larger part of this thesis into four components, such that secs. 10.1.1.1 through 10.1.1.4 correspond to chapters 4 through 7, before a brief joint conclusion to this part is provided in sec. 10.1.1.5.

10.1.1.1 Stochastic gauge fixing

At finite coupling, we have initially utilized the method of stochastic quantization for gauge fixing.[1] As a preparation, this method and the interplay of different effects (gauge fixing, action and number of dimensions) have been illustrated by means of a toy model, where the results are well understood and in line with expectations. More importantly, we have applied stochastic quantization to the considerably more intricate case of Yang–Mills theory, in which informative 'a priori' statements about the distribution of gauge-fixed configurations are much more difficult to justify. We have calculated the Landau gauge gluon and ghost propagators with stochastic gauge fixing in two, three and four dimensions. The results of this procedure include quantitative evidence, like an extraction of infrared power-law exponents. They unanimously corroborate the standard lattice scenario. I. e., the infrared behavior of the propagators is compatible with the scaling solution in two dimensions, but it is closer to a decoupling behavior in three and four dimensions. The deviation from scaling is even larger in the four-dimensional case.

Far from being a mere reproduction of previous lattice results, this provides an interesting and nontrivial confirmation of them, the more so since stochastic gauge fixing exhibits properties different from standard gauge fixing methods. It induces a much more local evolution in configuration space, and it leads generically to different values of the lowest Faddeev–Popov eigenvalue, which elucidates the position of a configuration relative to the Gribov horizon. Hence, our results for the Yang–Mills propagators in Landau gauge with stochastic quantization suggest that the gauge fixing problem on the lattice may be more general than previously assumed.

10.1.1.2 Strong-coupling limit with standard gauge fixing

The strong-coupling limit of pure Yang–Mills theory allows to assess the infrared behavior of the propagators already at large lattice momenta. We have performed a thorough analysis of the Landau gauge ghost and gluon propagators in the two- and three-dimensional cases, initially in standard Landau gauge, motivated by previous results in four dimensions.

Both in two and in three dimensions, we find no uniform scaling behavior, but rather a 'scaling window', i. e., a region of lattice momenta in which the effective running coupling calculated from the propagators is not far from predictions by functional continuum methods. It shifts toward large lattice momenta as the number of dimensions increases. The statistical accuracy of our studies allows for conclusive statements concerning the local behavior not only of the gluon, but equally well of the ghost propagator. It is mainly the ghost propagator that is responsible for the violation of a uniform scaling behavior. The gluon propagator deviates rather mildly from a behavior that would allow for scaling.

The effective running coupling has an infrared fixed point at a non-zero value if the scaling solution is realized. In the strong-coupling limit, this translates to a constant behavior of the effective running coupling as a function of lattice momentum. The results indicate instead rather a concave behavior, with a maximal value not very far from continuum predictions. The position of the maximum shifts towards large lattice momenta as the number of dimensions increases.

[1] We dispense with references in this concluding chapter, as they have been extensively provided throughout the individual chapters summarized here.

In this regard, the results at non-zero lattice momenta point toward a more unified picture in all dimensions. On the other hand, the infinite volume extrapolation of the gluon propagator at zero momentum is in line with the standard lattice scenario, as the extrapolated value vanishes only in two dimensions. – We have also addressed a possible problem of the strong-coupling limit via an explicit analysis of discretization artifacts. The deviation from a uniform scaling behavior at large lattice momenta may be within the uncertainty due to these artifacts.

10.1.1.3 Effect of the Gribov ambiguity in the strong-coupling limit

In order to further assess the effect of gauge copies on the infrared behavior of correlation functions, we have explored a recently proposed non-perturbative completion of Landau gauge, sc. max-B gauge, in the strong-coupling limit. It is defined so as to maximize the ghost propagator at small lattice momenta on each gauge orbit. It can be related to the one-parameter family of solutions for the infrared propagators found in continuum studies.

Our results show that an enormous dependence of the ghost propagator at small lattice momenta on the chosen Gribov copy in Landau max-B gauge, while the gluon propagator exhibits only a mild variation as a function of the number of gauge copies taken into account. The effect of the Gribov ambiguity on the ghost propagator is both much stronger and opposite to that of some recent other 'best copy' studies that aim at a better approximation to the global maximum of the gauge fixing functional. Remarkably, the effect is so pronounced that no subset of infrared solutions for the propagators can be excluded, at least on the lattice volumes used in the present study. On these volumes, our results serve as a lower bound on possible Gribov copy effects. This lower bound is remarkably large. We even observe a very significant 'over-scaling' behavior of the effective running coupling at small and intermediate momenta, which is prohibited in the continuum.

This provides strong evidence that it is still an unresolved question whether the Gribov ambiguity affects the infrared behavior of the Yang–Mills propagators in a qualitative manner. More specifically, the possibility is left open that in the joint limit of infinitely many copies and infinite lattice volume, a scaling behavior might result. We emphasize that the data surely do not warrant the conclusion that it does result, but they do provide numerical evidence that it would be premature to rule it out as a valid solution on the lattice. Given the current state of the debate, this is a valuable finding.

10.1.1.4 Free boundary conditions

Besides altering the gauge fixing algorithm, going to the strong-coupling limit and studying a non-perturbative completion of Landau gauge, we have probed the infrared sector of pure gauge theory in yet another way. The choice of free boundary conditions of the lattice enforces an exactly vanishing gluon propagator at zero momentum, which is incompatible with the decoupling solution usually obtained from lattice simulations. The definition of the gluon propagator has to be modified due to the lack of periodicity, which greatly increases the computational cost.

Usually, the effect of boundary conditions can be expected to disappear in the infinite volume limit. However, as we consider gauge-dependent quantities, it is a priori possible that global changes in properties of the gauge fixing procedure might survive in this limit.

We have found that the behavior of the gluon propagator at non-zero momenta closely resembles its counterpart obtained with periodic boundary conditions, if the considerable finite volume effect is taken into account. We have performed such simulations both in the strong-coupling limit and at finite coupling.

Non-periodic gauge transformations yield a very similar result if combined with free boundary conditions. But if non-periodic gauge transformations are combined with periodic boundary conditions, the volume effect is considerably weaker, which is at odds with naïve expectations and indicates an interesting further line of research. – Both statements hold both for the strong-coupling limit in three dimensions and for the case of finite coupling in four dimensions. Still, the lattices we have simulated are clearly sufficiently large to rule out a uniform scaling behavior at least in the former case.

10.1.1.5 Upshot regarding infrared propagators and confinement scenarios

We now bring together our results concerning the relation between the infrared behavior of the ghost and gluon propagators and the mechanism of confinement in Landau gauge. The picture that emerges from our comprehensive simulations within different, predominantly nonstandard gauge fixing approaches is not a simple one. The standard lattice scenario in two, three and four dimensions proves resilient to quite different approaches that change either the explicit gauge fixing algorithm, like stochastic quantization, or possibly global properties of the gauge fixing procedure, like free boundary conditions or non-periodic gauge transformations. However, another method, Landau max-B gauge, does lead to a dramatic change of the ghost propagator and thereby of the effective running coupling at small lattice momenta. It would be desirable to ascertain this effect on very large lattice volumes. But as number of Gribov copies increases exponentially with the lattice volume, this poses a severe computational challenge, hardly second to the computationally intractable task of reaching the fundamental modular region.

Hence, despite different approaches and a high computational effort, our numerical studies do not reveal an explicit confirmation of the validity of the scaling solution on the lattice. The standard predictions of the Gribov–Zwanziger/Kugo–Ojima scenarios of confinement are not borne out by our results.

But on the other hand, we wish to emphasize that our investigations of a non-perturbative completion of Landau gauge do provide evidence of surprisingly strong Gribov copy effects, and that the possibility to observe a scaling behavior on the lattice remains open.

While further investigations are certainly possible (see sec. 10.2), we consider the detailed map that we have sketched of this very special area to be sufficiently accurate for many purposes.

10.1.2 Further results

In addition to our rather extensive studies of the relation between confinement scenarios and infrared propagators and of the intricacies of gauge fixing, we have explored two other subjects, both of them related to the phase diagram of QCD and to topics like the deconfinement phase transition. In both cases, aspects of the first, larger part of our studies resurface – in one case, the gluon propagator in Landau gauge, but now at non-zero temperature; in the other case, stochastic quantization, but now in a complexified version, applied to the sign problem at non-zero density.

10.1.2.1 Deconfinement phase transition at non-zero temperature

Infrared properties of the gluon propagator in Landau gauge carry information not only about the mechanism of confinement in that gauge, but also about the deconfinement phase transition, which is of course gauge-invariant. This has recently been demonstrated for $3+1$-dimensional pure Yang–Mills theory.

Thus motivated, we have investigated the gluon propagator of pure $SU(2)$ Yang–Mills theory at non-zero temperature in $2+1$ dimensions in standard Landau gauge, in particular with a very fine resolution around the critical temperature. We have found that the chromoelectric sector is sensitive to the deconfinement phase transition, in contrast to the chromomagnetic one. In particular, the electric screening mass shows a pronounced response to the second-order transition. This is in line with previous findings in $3+1$ dimensions. The dependence on temperature is smoother in $2+1$ dimensions, and we have obtained a critical exponent ν in line with the expected universality class. We have quantitatively determined the transition temperature, which concurs with results of standard methods.

10.1.2.2 Sign problem at non-zero chemical potential

The sign problem is a major challenge for lattice QCD at non-zero chemical potential. The ability to circumvent it would constitute crucial progress toward reliable calculations of the phase diagram of QCD from first principles. As the sign problem is based on the fermion determinant being complex, the method of stochastic quantization offers a potential way to deal with this problem. However, knowledge of the conditions under which this method converges against the correct solution is lacking, and the outcomes of previous studies in different models have sometimes, but not always indicated success.

Our efforts to circumvent the sign problem in a fermionic model, the three-dimensional Thirring model at non-zero chemical potential, with the help of complex Langevin evolution have yielded differentiated results. – On the one hand, the algorithm is able to sample configurations with all phases of the fermion determinant, it leads to convergence of observables (chiral condensate and density) without runaway solutions, and it also generates results at large chemical potential that clearly differ from the respective results in the phase-quenched theory. Notably, it shows 'Silver Blaze' behavior in the sense of an independence of observables on the chemical potential below an onset to a phase of non-zero density.

On the other hand, our best evidence is consistent with the statement that simulations of the Thirring model with complex stochastic quantization result in the same position of the onset to a phase of non-zero density as in the phase-quenched theory, contrary to expectations. In this regard, complex stochastic quantization presumably fails to correctly simulate the Thirring model. This negative result, however, is interesting and potentially valuable, as it conveys information about the care and effort that is required in order to eventually simulate QCD at non-zero density on the lattice in a reliable manner.

10.1.3 Most concise listing of the main results

Finally, we summarize the main numerical results of this work even more concisely in five short statements. First: The effect of the Gribov ambiguity on the infrared ghost propagator in Landau gauge is very strong on moderate lattice volumes in the strong-coupling limit

in two and three dimensions. No subset of infrared solutions can be excluded yet. Second: Stochastic quantization can serve as an alternative gauge fixing algorithm. It confirms the results from standard gauge fixing for the infrared gluon and ghost propagators of pure $SU(2)$ Yang–Mills theory in two, three and four dimensions. Third: Free boundary conditions force the gluon propagator to vanish at zero momentum, but do not qualitatively affect its behavior at non-zero momenta. Neither do non-periodic gauge transformations yield a uniform scaling behavior. Fourth: The gluon propagator carries quantitative information about the deconfinement transition of pure $SU(2)$ gauge theory in $2+1$ dimensions. Fifth: Complex stochastic quantization is an only partly successful approach to circumvent the sign problem in the three-dimensional Thirring model.

10.2 Outlook

We conclude this thesis by indicating some possible directions for future research.

We consider the issue of the application of stochastic gauge fixing to the infrared Yang–Mills propagators in Landau gauge as essentially settled by our results. We see no way to modify this procedure that has realistic prospects of affecting the infrared behavior.

Our other application of stochastic quantization, sc. complex Langevin evolution, is a promising, but so far not reliable approach to the sign problem of lattice QCD at non-zero chemical potential. It does not always converge against the correct solution. An independent criterion that allows to determine the cases of correct convergence from properties of the simulated model remains to be found.

The conclusions drawn from our studies of free boundary conditions with regard to the infrared gluon propagator are rather definite. But non-periodic gauge transformations deserve further attention, as it has not yet been clarified why the finite volume effect on the gluon propagator occurs so slowly for them.

Regarding the results for pure $SU(2)$ gauge theory in $2+1$ dimensions at non-zero temperature, a natural aim is to increase the statistical resolution also in $3+1$ dimensions. Thus it may be possible to obtain further quantitative evidence for the viability of elucidating the critical dynamics by means of the gluon propagator.

Based on the very strong impact of the Gribov ambiguity that we have found, it is natural to suggest further investigations along these lines, both in Landau max-B gauge and possibly also in other non-perturbative completions of Landau gauge. It is currently an open question what happens in the joint limit of infinitely many gauge copies and infinite lattice volume. As exponentially more copies exist on larger lattices, this poses a very formidable numerical challenge. To the extent that this can be met, we expect these further investigations to be valuable both at $\beta = 0$ and at finite coupling.

Another direction of research on these intriguing questions pertains to the status of global BRST symmetry, whose violation may have severe consequences for the possibility to construct a physical state space. A recent approach based on stereographic projection of the gauge field offers a possibility to include all Gribov copies, not only those from the first Gribov region. In light of this approach, efforts toward a numerical implementation of lattice BRST appear promising, though still very challenging in practice.

Our own contributions to several issues revolving around confinement in QCD end here.

APPENDIX A

NOTATION AND CONVENTIONS

A.1 Generalities

A.1.1 Indices

We generally adhere to the usual Einstein summation convention in order to simplify the notation, i. e., a sum is understood over indices occurring twice in an expression.

We work in Euclidean space, and we do not distinguish between upper and lower indices. Indices are usually counted from zero, unless explicitly mentioned otherwise, in compliance with C++ coding conventions. The space-time index 0 denotes the time direction, even though in Euclidean space-time, which we use here, $d-1$ is frequently chosen for this purpose elsewhere. (We use varying numbers of dimensions and consider it useful to have a common name of the time variable.)

A.1.2 Units

We choose a system of so-called natural units, also known as Planck units, as is customary in high energy physics. In these units, some crucial physical constants equal unity. These constants comprise, among others, the speed of light, the reduced Planck constant and Boltzmann's constant

$$c = \hbar = k_B = 1. \tag{A.1}$$

As an immediate consequence, an action is dimensionless. The dimension of any quantity can be given in powers of GeV, which is the unit of mass. Both space and time coordinates have the dimension of inverse mass ('mass dimension -1').

A.1.3 Dirac notation

For the formulation of QCD in sec. 2.1.1 and also when studying the fermionic Thirring model in ch. 9, we employ the 'Dirac slash' notation, which is simply the abbreviation

$$\not{B} := \gamma^\mu B_\mu \tag{A.2}$$

with the Dirac matrices γ^μ in Euclidean space defined via the anticommutator[1]

$$\{\gamma^\mu, \gamma^\nu\} = 2\delta^{\mu\nu}\mathbb{1}. \tag{A.3}$$

The matrix γ_5 is defined such that it anticommutes with all Dirac matrices,

$$\{\gamma_5, \gamma^\mu\} = 0, \tag{A.4}$$

and that it satisfies the equation $(\gamma_5)^2 = \mathbb{1}$.

A.2 Some group-theoretical notions

A.2.1 Haar measure

In the context of pure lattice gauge theory, whose dynamical variables are elements of the gauge group, the Haar measure of the gauge group is frequently invoked, in particular in the functional integrals that are to be evaluated numerically. A simple example for such an integral is provided by the partition function

$$Z = \int \mathcal{D}U \, \exp(-S[U]) = \int \prod_{x,\mu} \int_G dU_\mu(x) \, \exp(-S[U]). \tag{A.5}$$

The Haar measure is the measure of integration over a continuous compact group G. It is uniquely determined and has the following properties.[2] It is left- and right-invariant, i. e., for all $V \in G$,

$$\int \mathcal{D}U \, f(U) = \int \mathcal{D}U \, f(VU) = \int \mathcal{D}U \, f(UV). \tag{A.6}$$

It satisfies the normalization condition

$$\int \mathcal{D}U = 1. \tag{A.7}$$

In particular,

$$\int \mathcal{D}U \, f(U) = \int \mathcal{D}U \, f\left(U^{-1}\right). \tag{A.8}$$

A.2.2 Lie groups

The symmetry groups relevant for our purposes are usually compact Lie groups. Lie groups are differentiable manifolds with group structure. Their elements are determined by a set of continuous parameters on which the group operation depends in a smooth manner.

[1] For a Minkowski space, the Kronecker δ in eq. (A.3) is to be replaced by the metric $g_{\mu\nu}$.

[2] See standard textbooks like [216, 218, 219] for further details.

A.2.3 Generators

The structure constants f^{abc} of a Lie algebra are the numbers that characterize the commutators of the elements of this algebra, the generators, via

$$[T^a, T^b] = if^{abc}T^c. \tag{A.9}$$

The generators of the groups $SU(N_c)$ are normalized as

$$\operatorname{tr} T^a T^b = \frac{1}{2}\delta^{ab}. \tag{A.10}$$

In particular, the generators of $SU(2)$ are usually chosen to be proportional to the well-known Pauli matrices σ^a,

$$T^a = \frac{1}{2}\sigma^a. \tag{A.11}$$

For completeness, we reproduce here the Pauli matrices,

$$\sigma_1 = \begin{pmatrix} 0 & 1 \\ 1 & 0 \end{pmatrix}, \quad \sigma_2 = \begin{pmatrix} 0 & -i \\ i & 0 \end{pmatrix}, \quad \sigma_3 = \begin{pmatrix} 1 & 0 \\ 0 & -1 \end{pmatrix}. \tag{A.12}$$

They are both Hermitian and unitary,

$$\sigma_a = \sigma_a^\dagger = \sigma_a^{-1}, \tag{A.13}$$

and they satisfy the useful relation

$$\sigma_a\sigma_b = \delta_{ab}\mathbb{1} + i\varepsilon_{abc}\sigma_c \tag{A.14}$$

with the total antisymmetric Levi-Civita tensor ε_{abc} that neatly sums up the structure constants of $SU(2)$ (more precisely, of its Lie algebra $su(2)$).

A.2.4 Representations of groups

A representation of a group G is a homomorphism from the group space into the representation space,

$$G \ni g \mapsto \mathsf{D}(g) \tag{A.15}$$

with a linear operator $\mathsf{D}(g)$ that respects the group operation $\cdot$,

$$\mathsf{D}(g_1 \cdot g_2) = \mathsf{D}(g_1)\mathsf{D}(g_2). \tag{A.16}$$

Let R be a representation of G and $\overline{R}$ its complex conjugate representation. If there is a basis such that all matrices in the representation R are purely real, then R is a real representation and equivalent to $\overline{R}$. If R and $\overline{R}$ are unitarily equivalent, i. e., the generators are connected by unitary transformations, but at the same time no basis exists in which all matrices in the representation R are purely real, then R is a pseudoreal representation. If none of the above holds true, i. e., if R and $\overline{R}$ are unitarily inequivalent, then R is complex.

A.2.5 Center of a group

The center of a group is the subgroup of elements commuting with all elements of the group. The center of $SU(N)$ is $\mathbb{Z}_N$. Regarding confinement, the center is important in the context of center vortices, see sec. 2.2.3.1. Moreover, the Polyakov loop, see sec. 8.1.2, is related to center symmetry.

A.2.6 Parametrization of $SU(2)$

In order to enable an efficient numerical implementation and to reduce memory requirements, we utilize the Cayley–Klein parametrization of the link variables, a quaternionic parametrization already given in eq. (2.72),

$$U_\mu(x) = u^0_\mu(x) + iu^a_\mu(x)\sigma^a, \tag{A.17}$$

which allows to characterize any element of $SU(2)$ by four real numbers, which are mutually related by the normalization condition eq. (2.73). This parametrization allows to express any $SU(2)$ element in terms of the Pauli matrices (A.12).

APPENDIX B

ISSUES OF IMPLEMENTATION

B.1 Markov chain Monte Carlo

B.1.1 Expectation values on the lattice

Calculating the expectation value of any observable B in a Euclidean lattice gauge field theory amounts to the evaluation of the functional integral, eq. (2.56), which we repeat here,

$$\langle B \rangle = \frac{1}{Z} \int \mathcal{D}U \exp\left(-S[U]\right) B[U] \tag{B.1}$$

with the partition function Z, eq. (2.57), as already laid out in sec. 2.3. Usually, there is no need to evaluate Z explicitly, as some independent normalization of $\langle B \rangle$ is given (see e. g. sec. 2.3.4.2 concerning the propagators). For a numerical treatment, it is helpful to be aware of the form of the functional Haar measure (see also app. A.2.1),

$$\mathcal{D}U = \prod_{x,\mu} \int_G dU_\mu(x), \tag{B.2}$$

which is the measure of the discretized functional integral. G is the respective Lie group, in our case the gauge group, in the present work chosen to be $SU(2)$. Even on moderately sized lattices, such an integral is of very high dimensionality. Already for a $\mathbb{Z}_2$ gauge theory on a 10^4 lattice, i. e., a simple theory on a moderate volume, the possible spin configurations number $2^{4 \cdot 10^4}$, i. e., the number of dimensions of configuration space exceeds 10^{12000}.

Thus, a Monte Carlo integration suggests itself. The integral (B.1) is approximated by the average of its values at a much smaller number of mutually independent configurations. The Gibbs measure proportional to the Boltzmann factor $\exp(-S)$ requires an 'importance sampling', i. e., a sampling of configurations which occur with a probability proportional to $\exp(-S)$; to be precise (see e. g. [219]),

$$dP(U) = \frac{e^{-S[U]}\mathcal{D}U}{\int \mathcal{D}U e^{-S[U]}}. \tag{B.3}$$

To this end, a Markov chain of configurations obeying the distribution $\exp(-S_G[U])$ is numerically generated, see sec. B.1.2. From such configurations, the value of a quantity B can be calculated as

$$\langle B \rangle = \frac{1}{N} \sum_{i=1}^{N} B[U_i], \tag{B.4}$$

with a statistical standard error decreasing approximately proportional to $1/\sqrt{N}$ with the number of measurements,

$$\frac{\sigma_B}{\sqrt{N}} = \sqrt{\frac{1}{N-1} \left(\langle B^2 \rangle - \langle B \rangle^2 \right)}, \tag{B.5}$$

the expectation values here being understood in the sense of eq. (B.4), i. e., as approximate.

In actual lattice simulations, subsequent configurations are correlated, in contrast to an ideal Markov chain (app. B.1.2). Thus, a number of 'dummy configurations' between subsequent 'measurements' of quantities has to be discarded, so that typically $\mathcal{O}\left(10^1\right) - \mathcal{O}\left(10^2\right)$ configurations need to be generated for a single measurement. In addition, a (usually larger) number of initial configurations, obtained before the process is in equilibrium, is required for thermalization before the measurements start.

B.1.2 Stochastic processes and Markov chains

A stochastic process is a temporal sequence of random variables.[1] An important class of stochastic processes is the class of Markov processes. These are characterized by the condition that the probability for a certain state to occur depends only on the immediately preceding state, i. e., it is independent of any previous history.[2]

For the transition probability (conditional probability) between subsequent states of a Markov process, the Chapman-Kolmogorov equation holds. Formulated for a temporal evolution in space, it reads

$$p(x_3, t_3 | x_1, t_1) = \int dx_2 \, p(x_3, t_3 | x_2, t_2) p(x_2, t_2 | x_1, t_1). \tag{B.6}$$

From this, the Fokker–Planck equation (FPE) for the probability density can be derived, subject to certain requirements on the first two moments of the transition probability (they have to be linear in the temporal increment, see [307] for further details). The FPE is in turn equivalent to the Langevin equation. We have given a version of the FPE in eq. (3.7).

In our case, the stochastic variable evolving in the process is not simply a single real variable x, or some ordinary vector, but the entire spatio-temporal configuration of link variables $U_\mu(x) \in SU(2)$ for all sites x and directions $\mu \in \{0, \ldots, d-1\}$. Here, we denote an entire such configuration by "U". In order for the Markov process to be stationary, a balance equation for the transition between configurations U and U' has to hold,[3]

$$\sum_U p(U'|U) \varrho(U) = \sum_U p(U|U') \varrho(U'). \tag{B.7}$$

[1] An overview of stochastic processes is provided, e. g., in [307], which we sometimes follow.

[2] Relaxing the Markov condition, generalized Markov processes may be defined, where a state depends on the n preceding states, instead of only on the immediately preceding one. In the present thesis, we understand by 'Markov process' always 'Markov process of first order', i. e., the $n = 1$ case.

[3] See textbooks like [215, 219].

Here, ϱ is the probability for the system to be in the configuration U. A sufficient (not necessary) condition for eq. (B.7) to hold is the detailed balance condition,

$$p(U'|U)\varrho(U) = p(U|U')\varrho(U'). \tag{B.8}$$

B.1.3 Metropolis algorithm

The Metropolis algorithm [475], which we present here immediately for the specific case of lattice Yang–Mills theory, is a local updating procedure that helps to generate a Markov chain of configurations. Since the change is (in lattice calculations) a local one, we refer by "U" resp. "U'"in the following to an entire configuration, characterized by the link variable U (old) resp. U' (updated). Typically, for a link $U_\mu(x) \equiv U$, an updating element g of the gauge group G is determined randomly; g should be not too far from $\mathbb{1}$. The last condition is important to avoid an overly small acceptance probability. In practice, a parameter determining the distance of g from $\mathbb{1}$ may be dynamically tuned such that the ratio of accepted proposals is close to 0.5. The update of the link variable is determined as $U' = gU$.

Two probability functions are important here. First, the probability distribution $P_C(\cdot)$ for the proposal of a change. Second, the distribution $P_A(\cdot)$ for the acceptance of a proposed change. P_A is what we intend to calculate in the Metropolis algorithm. P_C is not fixed by the Metropolis algorithm, but its choice is important for practical purposes, like the efficiency of the algorithm, i. e., the number of iterations required to obtain fluctuations around the equilibrium. The acceptance probability in the Metropolis algorithm is given by

$$P_A(U' \leftarrow U) = \min\left(1, \exp\left(-\Delta S\right) \frac{P_C(U \leftarrow U')}{P_C(U' \leftarrow U)}\right), \tag{B.9}$$

where ΔS is the change of the Euclidean action induced by the update from U to U',

$$\Delta S = S[U'] - S[U]. \tag{B.10}$$

In particular, the update is always accepted if it causes the action to decrease.

The combined transition probability $P = P_A P_C$ satisfies the detailed balance condition (B.8).

B.1.4 Heat-bath algorithm

B.1.4.1 General algorithm

The heat-bath algorithm [39] is a special case of the Metropolis algorithm described in sec. B.1.3 above. It is special insofar as a specific value of the prior selection probability P_C is chosen. This algorithm is particularly suitable for $SU(2)$, where a simple formulation exists, but can also be applied to other gauge groups like $SU(N)$ or $Sp(N)$ via Cabibbo–Marinari updates [476].

The heat-bath algorithm sets the prior selection probability in the Metropolis acceptance prescription eq. (B.9) to

$$P_C(U \leftarrow U') \propto \exp(-S[U]). \tag{B.11}$$

By virtue of this choice, the local acceptance rate (B.9) is maximal, $P_A \equiv 1$.

The local contribution to the Wilson action (2.67), i. e., the part in which a single link variable $U_\mu(x) =: U$ enters, is composed of the product of this link with the sum of the $2(d-1)$ staples surrounding it. An illustration of a link variable $U_\mu(x)$ together with the staples entering the local contribution is provided in fig. B.1 for the three-dimensional case.

These staples are oriented such that the product of each of them with U yields a plaquette (this is just the opposite of the smearing algorithm useful for calculating the string tension, sec. 2.3.4). The sum of staples $B_\mu(x) =: B$ is defined as

$$B = \sum_{\substack{\nu=0 \\ \nu\neq\mu}}^{d-1} \Big(U_\nu(x+\hat{\mu})U_\mu^\dagger(x+\hat{\nu})U_\nu^\dagger(x) + \\ + U_\nu^\dagger(x+\hat{\mu}-\hat{\nu})U_\mu^\dagger(x-\hat{\nu})U_\nu(x-\hat{\nu})\Big). \tag{B.12}$$

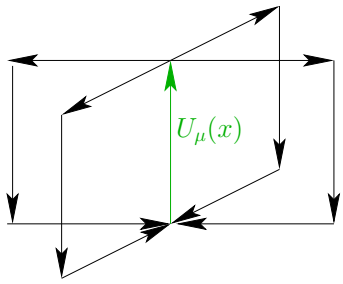

Figure B.1: Illustration of the local contribution to the heat-bath algorithm by the staples surrounding the link $U_\mu(x)$.

Their projection $\tilde{U}$ on an element of $SU(2)$ is trivially given by

$$\tilde{U} = \frac{1}{k}B \qquad (k := \sqrt{\det B}). \tag{B.13}$$

Invariance of the Haar measure (see app. A.2.1) warrants that the following relation holds:

$$dP(U) \propto dU \exp\left(\frac{\beta k}{2}\operatorname{tr} U\tilde{U}\right) = dV \exp\left(\frac{\beta k}{2}\operatorname{tr} V\right). \tag{B.14}$$

V can be written in the standard Cayley–Klein parametrization (A.17) as

$$V = v_0 + i\vec{v}\cdot\vec{\sigma} = \cos\left(\frac{\varphi}{2}\right) + i\sin\left(\frac{\varphi}{2}\right), \tag{B.15}$$

where $v_0^2 + \vec{v}^2 =: v^2 = 1$ and $\varphi \in [0, \pi[$. The parameters v_0 and $\vec{v}$ are determined randomly with a distribution according to the Haar measure of $SU(2)$,

$$\begin{aligned} dV &\propto \delta(v^2-1)d^4v \exp(\beta k v_0) \\ &\propto dv_0\, d\Omega_{\vec{v}} \sqrt{1-v_0^2}\exp(\beta k v_0). \end{aligned} \tag{B.16}$$

Thus, we have to determine $v_0 \in [-1, 1]$ according to the distribution $\exp(\beta k v_0)$, which can easily be done. To be explicit, v_0 is obtained as follows: The uniformly distributed auxiliary variable $z \in [0, 1]$ is randomly determined. Now it is useful to abbreviate

$$x := \exp(-2\beta k) + (1 - \exp(-2\beta k))z \in [e^{-2\beta k}, 1]. \tag{B.17}$$

The proposal

$$v_0 = 1 + \frac{\ln x}{\beta k} \tag{B.18}$$

is rejected with probability $\sqrt{1-v_0^2}$ and accepted otherwise.

Here and whenever random numbers (more exactly, pseudo-random numbers) are needed, we employ the standard high-quality random number generator `ranlux` [477]. The vector $\vec{v}$ then has the length $\sqrt{1-v_0^2}$, and its direction in the residual three-dimensional subspace is determined randomly via uniformly distributed random variables $\varphi \in [0, 2\pi[$, $\theta \in [0, \pi[$ representing the angles. From this, of course,

$$v_1 = \cos\varphi \sin\theta \sqrt{1-v_0^2}, \tag{B.19}$$

$$v_2 = \sin\varphi \sin\theta \sqrt{1-v_0^2}, \tag{B.20}$$

$$v_3 = \cos\theta \sqrt{1-v_0^2}. \tag{B.21}$$

After v_0 and $\vec{v}$ have thus been determined, the relation $U = V\tilde{U}^{-1}$ allows to finally calculate the link variable U.

B.1.4.2 Special case: Strong-coupling limit

In the strong-coupling limit, i. e., at $\beta = 0$, link configurations need to be generated according to the Haar measure. Thus, the Cayley–Klein parameters u_0, $\vec{u}$ of each link lie uniformly distributed on the hypersphere S^3 of unit radius. I. e., the variables u_1, u_2, u_3 need to be randomly distributed according to

$$d\Omega_{\vec{u}} \sin^2\left(\frac{\varphi}{2}\right), \tag{B.22}$$

while $u_0 \in [0, \sqrt{1-\vec{u}^2}]$ obeys a uniform distribution. The algorithm that produces this outcome is a simple special case of the heat-bath procedure presented above. Of course, the surrounding staples have no influence on a link update at $\beta = 0$, where all link variables are mutually independent.

B.1.5 Bootstrap error calculation

We briefly sketch a bootstrap error calculation [348] for a set of N data. It is helpful for derived quantities (as opposed to direct averages) if the variables do not obey a normal distribution. We use it especially for the calculation of the error bars of the local exponents in the strong-coupling limit in chs. 5 and 6.

The basic idea is to calculate the standard deviation of a set of data from an ensemble of resampled data sets. There are obviously N^N possible resamplings arising from sampling N data with replacement out of the original set. Of course, even for moderate values of N, the calculation of all resamplings is de facto impossible. Hence, n resamplings are used, with typically $n \in \mathcal{O}(1000)$ in this work. From the averages of the resampled data sets, a new set of n data is formed, from which the standard deviation is calculated.

B.2 Gauge fixing on the lattice

B.2.1 Methods

Here, we mainly explain stochastic overrelaxation and, as a preparation, the simpler 'Los Alamos' method. Much more extensive reviews of lattice gauge fixing with reference to

related methods may be found in [220, 347]. Among the common alternatives to the method we employ is Fourier acceleration [478].

A necessary condition for adequate Landau gauge fixing on the lattice is to bring the lattice version of the Lorenz gauge fixing condition (characterized by the quantity Δ^2, see eq. (2.85)) close to zero. I. e., a local maximum of the gauge fixing functional R, defined in eq. (2.80), is to be found. Stochastic overrelaxation is an iterative scheme that achieves this.

Stochastic overrelaxation is best understood by first considering a special case, the 'Los Alamos' method [479, 346].[4]

B.2.1.1 'Los Alamos' method

The Los Alamos method is a deterministic local algorithm. It is designed such that R strictly increases with each local step. Moreover, the local increase is maximal within the chosen scheme. To be specific, one complete over the lattice sweep consists of a gauge transformation, eq. (2.64), at each lattice site with the local gauge transformation matrix

$$\Omega(x) = \frac{1}{\sqrt{\det h(x)}} h^\dagger(x), \tag{B.23}$$

where

$$h(x) = \sum_{\mu=0}^{d-1} \left[U_\mu(x) + U_\mu^\dagger(x - \hat{\mu}) \right]. \tag{B.24}$$

For a simple illustration of the link variables thus entering into a gauge transformation matrix, see fig. 4.5.

B.2.1.2 Stochastic overrelaxation

Stochastic overrelaxation [346] can be considered as a generalization of the Los Alamos method. It is also local, but it is not deterministic. It has the benefit of a significantly improved efficiency compared to the Los Alamos method, see e. g. [347]. The stochastic overrelaxation procedure depends on an additional parameter $p \in [0, 1]$. The prescription is to perform a usual Los Alamos update only with probability $1 - p$ and a deliberately non-optimal local update with probability p. A non-optimal local update in the sense of this prescription is given by using the gauge transformation matrix $\Omega^2(x)$ instead of $\Omega(x)$ in a gauge transformation (2.64). On reasonably large lattices, the optimal value of the parameter p is typically not far from 1, e. g. around 0.97 on a 40^4 lattice.

The Los Alamos algorithm is the special case of stochastic overrelaxation for $p = 0$, i. e., the case where always Ω is chosen, never Ω^2.

Contrast to 'global maximization' methods. While stochastic overrelaxation is more efficient than the Los Alamos method in finding a local maximum of the gauge fixing functional R (2.80) and usually finds a higher maximum, it does not aim at finding the global maximum, which is a NP-hard problem, see sec. 2.3.2. Methods like simulated annealing are sometimes applied in order to come closer to the global maximum. See sec. 6.1.1 and also sec. 2.4 for references.

[4] The term 'Los Alamos method' was first used in [480].

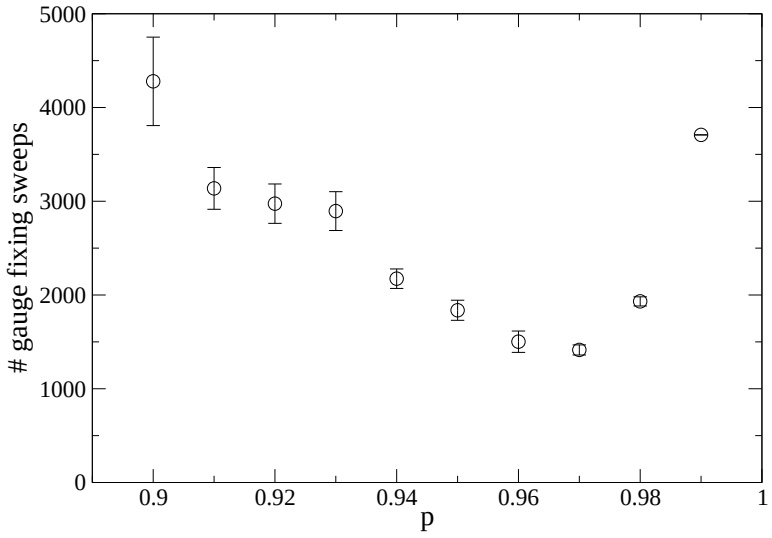

Figure B.2: Average convergence time of gauge fixing via stochastic overrelaxation vs. probability p of non-optimal updates. Here, the convergence criterion is $\Delta^2 < 10^{-20}$ on a 40^3 lattice with free boundary conditions at $\beta = 4.2$. Only rather large values of p are shown here.

Contrast to stochastic gauge fixing. We stress again that stochastic overrelaxation must not be confused with stochastic gauge fixing, in spite of a superficial similarity in name. The former is a standard gauge fixing method in the sense that it has frequently been used in gauge-fixed lattice simulations e. g. of the infrared propagators (an arbitrary example is ref. [282]), and that it does not strive to implement a local evolution in configuration space, in contrast to stochastic gauge fixing, see chs. 3 and 4.

B.2.2 Results from stochastic overrelaxation

Typically, if the overrelaxation parameter p is larger than some value which mainly depends on the geometry of the lattice, Δ^2 decreases at a fixed rate. At some smaller value, it tends to decrease sometimes faster, but often not monotonically; thus, the fluctuations of the convergence time between different configurations are much larger. This is also apparent from fig. B.2, where the number of configurations used to determine the average convergence time on a 40^3 lattice is held fixed at 50 for each value of p; hence, the error bars can be directly used to compare the variance of the convergence time among different p. There is a minimum around $p = 0.97$. The value of this minimum depends much more on the linear extension of the lattice than on its volume. E. g., $p = 0.97$ is typically also a reasonable value on a 40^4 lattice. See fig. B.3 for some exemplary data concerning the volume dependence of the optimal value of p – on larger lattices, the optimal p is close to 1, meaning that most of the updating steps are deliberately chosen such that they do not maximize the short-term increment of R.

The quantity we consider, Δ^2, is the average of $\Delta^2(x)$ over the space-time points (lattice sites) x. However, it is a priori possible that there are large spatio-temporal fluctuations in $\Delta^2(x)$, such that the maximum of $\Delta^2(x)$ is large while its average is small. This might pose a problem for accurate gauge fixing. We have performed gauge-fixing studies monitoring both of these quantities, the average Δ^2 and the maximum $\max_x \Delta^2(x)$. Our results

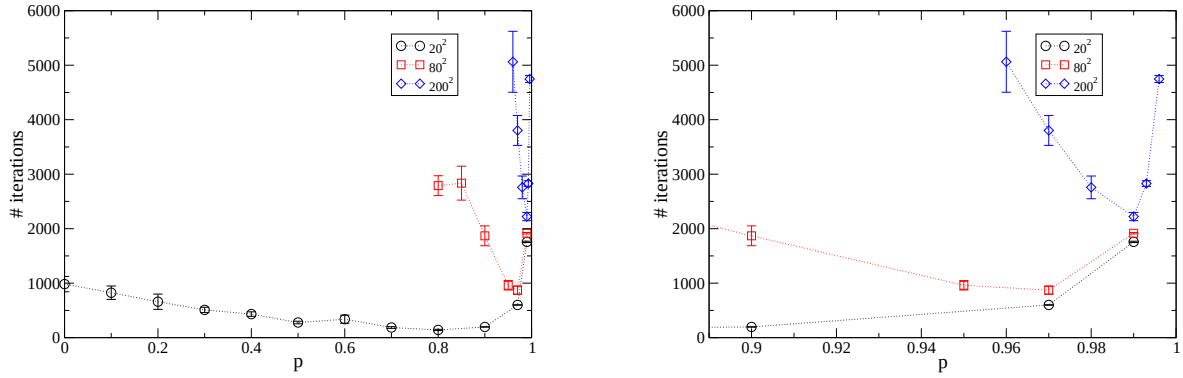

Figure B.3: Number of iterations until $\Delta^2 < 10^{-10}$ for different lattice sizes in two dimensions. Stochastic overrelaxation after random walk at $\beta = 10$. (p is the parameter of stochastic overrelaxation, see main text.) Right plot is a blowup of the left plot at large p.

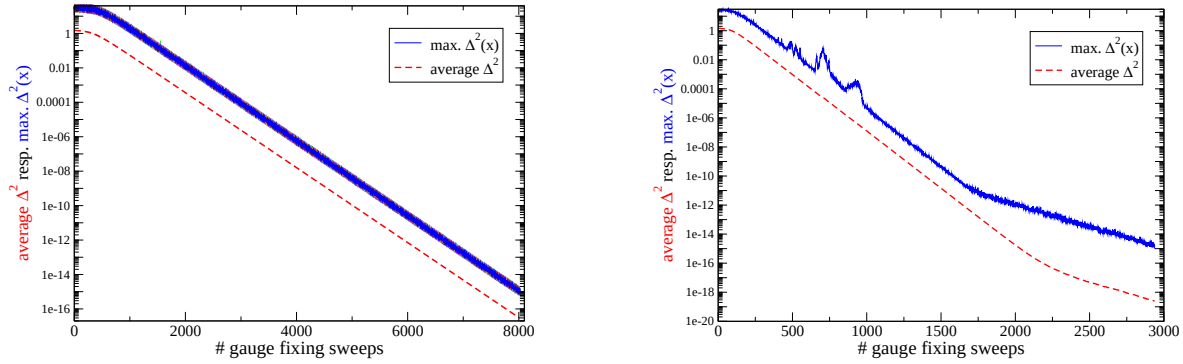

Figure B.4: Comparison of the convergence of the average value of $\Delta^2(x)$ with its spatio-temporal maximum, from simulations with periodic boundary conditions in the strong-coupling limit (see ch. 5). *Left (a):* 320^3 lattice, overrelaxation parameter $p = 0.995$. *Right (b):* 96^3 lattice, $p = 0.982$.

indicate that the spatio-temporal distribution induced during stochastic gauge fixing is sufficiently uniform to allow the use of the average Δ^2 instead of $\max_x \Delta^2(x)$ as the criterion for stopping a gauge fixing sweep; see fig. B.4.[5] In our parallel simulations on large lattices, though, we have been even more careful and usually used the maximum.

Moreover, one may pose the question whether $\Delta^2(x)$ is the most appropriate quantity to enter into the criterion for convergence of the gauge fixing algorithm. A more sensitive quantity has been proposed in ref. [347], i. e., one that converges more slowly during gauge fixing. It is in d dimensions defined as

$$e_6 := \frac{1}{d} \sum_{\nu=0}^{d-1} \frac{1}{3L_\nu} \sum_{j=1}^{3} \sum_{x_\nu=0}^{L_\nu-1} \frac{\left[Q_\nu(x_\nu) - \hat{Q}_\nu\right]_j^2}{\left[\hat{Q}_\nu\right]_j^2}, \tag{B.25}$$

where Q_ν are the charges familiar from our discussion of free boundary conditions, eq.

[5] Regarding fig. B.4a, note that the results of 30 runs virtually agree. This is due to the large value of p. The corresponding curves of $\max_x \Delta^2(x)$ have been superimposed. They do not differ visibly.

(7.4), and

$$\hat{Q}_\nu := \frac{1}{L_\nu} \sum_{x_\nu=0}^{L_\nu-1} Q_\nu(x_\nu), \tag{B.26}$$

where L_ν is the extension of the lattice in $\hat{\nu}$-direction, measured in lattice units.

A look at the results of [347] reveals that the convergence of e_6 is not any more problematic than that of Δ^2. This is corroborated by exemplary results of ours, see fig. B.5. They illustrate that it is not necessary for our purposes to track e_6 in addition to Δ^2 as a measure of the precision of gauge fixing.

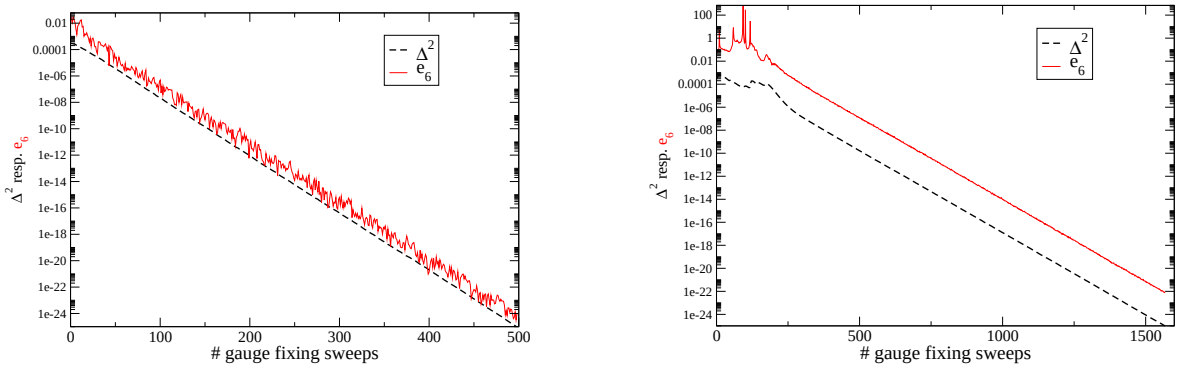

Figure B.5: Comparison of the behavior of the quantities e_6 as defined in eq. (B.25) and Δ^2, eq. (2.85), during gauge fixing. The algorithm here is random walk including gauge fixing, amended by stochastic overrelaxation, at $\beta = 4.2$. *Left (a):* 10^3 lattice. *Right (b):* 40^3 lattice.

B.3 Ghost propagator calculation

We now spell out the calculation of the ghost propagator and the difference between the two methods (point source vs. plane-wave source) in more detail. While $\mathbb{M}$ is a singular matrix in Landau gauge, a restriction to non-zero momenta k automatically induces a restriction to a subspace $\mathcal{A}_1$ orthogonal to the zero modes, as noted e. g. in [173]. The basic task is then to solve the equation

$$\mathbb{M} v_b = s_b \tag{B.27}$$

with a source term $s_b \in \mathbb{R}^{(N_c^2-1)V}$ for the gauge group $SU(N_c)$, thus $s_b \in \mathbb{R}^{3V}$ for the gauge group $SU(2)$ employed here. Two choices of s_b are discussed below (app. B.3.1).

A common method for solving this linear system (B.27) of $3V$ equations, i. e., for calculating the inverse of $\mathbb{M}$ (restricted to $\mathcal{A}_1$), is the conjugate gradient method, see app. B.3.2. In addition to the source term s_b, an initial guess v_0 serves as input to this algorithm. The source term may or may not depend on the momenta. We now discuss two different choices, the plane-wave source method [242] and the point source method [247, 248], already mentioned in sec. 2.3.3.2. We have used both of them for some of the simulations, but preferably the former one; see chs. 4, 5 and 6.

B.3.1 Choice of source term

B.3.1.1 Plane-wave source method

The plane-wave source method is a very accurate, but numerically rather expensive method for calculating the ghost propagator. As our results in chs. 4, 5 and 6 confirm, the increase in computer time compared to the point source method pays off. The gain in statistical accuracy is so large that the number of 'measurements' required for a result with a satisfactorily low level of statistical fluctuations is lower by several orders of magnitude, while the number of inversions for each single propagator calculation is determined by the number of lattice momentum vectors, which is typically of order $\mathcal{O}(10^2) - \mathcal{O}(10^3)$. (To be precise, the number of momenta surviving the cylinder cut on a symmetric lattice of linear extension L is $c(L/2) - c + 1$ with $c = 15$, 7 and 4 in 4, 3 and 2 dimensions, respectively.)

This method proceeds by choosing the source term $s_b \in \mathbb{R}^{3V}$ on which $\mathbb{M}$ is inverted, eq. (B.27), as a vector of plane waves,

$$s_b^{ax}(k) = \delta^{ab} e^{ik\cdot x}. \tag{B.28}$$

Note that k is a momentum vector, not the norm of one. The inner product between this vector and a spatial vector x is defined in eq. (2.91). In eq. (B.28), $a,\ b \in \{1, 2, \ldots, N_c^2 - 1\}$, while x is a spatial index that runs over all $V = L_s^{d-1} \cdot L_t$ lattice sites. Altogether, for $SU(2)$, $s \in \mathbb{R}^{3V}$. Hence, s is generically a high-dimensional vector. Inserting the choice (B.28) in eq. (B.27) leads to two systems of $3V$ real equations,[6]

$$\left(\mathbb{M} a_a(k)\right)^{bx} = \delta^{ab} \cos(k \cdot x), \tag{B.29}$$

$$\left(\mathbb{M} b_a(k)\right)^{bx} = \delta^{ab} \sin(k \cdot x). \tag{B.30}$$

The inverse ghost propagator in momentum space is readily obtained from the solution $v_b^{ax}(k) = a_b^{ax}(k) + i b_b^{ax}(k)$ to this linear equation via

$$\left(\mathbb{M}^{-1}\right)^{ab}(k) = \frac{1}{V} \sum_x e^{-ik\cdot x} v_b^{ax}(k). \tag{B.31}$$

B.3.1.2 Point source method

Here, the source term in eq. (B.27) is chosen as

$$\tilde{s}_b^{ax} = \delta^{ab} \left(\delta(x, 0) - \frac{1}{V} \right). \tag{B.32}$$

Note that $\tilde{s}$ does not depend on the momentum vector k, in contrast to the plane-wave source (B.28). Exploiting the relation

$$\delta(x, y) = \frac{1}{V} + \frac{1}{V} \sum_{k \neq 0} e^{-ik(x-y)}, \tag{B.33}$$

[6] We partially follow the presentation given in [173].

the source may be written as (following ref. [248])

$$\begin{aligned}\tilde{s}_b^{ax} &= \delta^{ab}\left(\frac{1}{V} + \frac{1}{V}\sum_{k\neq 0} e^{-ik\cdot x} - \frac{1}{V}\right) \\ &= \delta^{ab}\frac{1}{V}\sum_{k\neq 0} e^{-ik\cdot x}.\end{aligned} \tag{B.34}$$

Due to

$$G^{ab}(k) = \sum_x e^{-ik\cdot x}\langle \mathbb{M}^{-1} S_0^a\rangle + \delta(k)\sum_x G(x), \tag{B.35}$$

the ghost propagator at non-zero momenta can be calculated as

$$G^{ab}(k) = \sum_x \cos(k\cdot x)\mathbb{M}^{-1}\tilde{s}_b^{ax}, \tag{B.36}$$

where

$$\mathbb{M}^{-1}\tilde{s}_b \equiv \left(\mathbb{M}^{-1}\right)^{ax}\tilde{s}_b^{ax}$$

is the output of the conjugate gradient algorithm with a plane-wave source as the input.

Compared to the plane-wave source method, the point source method has the advantage that the number of necessary inversions is independent of the number of momenta. However, it suffers from the serious drawback that statistical fluctuations are greatly enhanced, especially those at large momenta. Hence, the former method is to be preferred, given that the accessible computing power permits it.

B.3.2 Conjugate gradient algorithm

The basic idea of the conjugate gradient algorithm is as follows. A system of equations of the form

$$Av = b, \tag{B.37}$$

with $v,\ b \in \mathbb{R}^n$, $A \in \mathbb{R}^{n\times n}$, may be solved by minimizing the function

$$F(v) := \frac{1}{2}\langle v, Av\rangle - \langle b, v\rangle. \tag{B.38}$$

A procedure with steps along 'conjugate gradients' is more conducive to this goal (i. e., converges faster) than a simple steepest descent procedure following the gradient of $F(v)$, see the simple sketch in fig. B.6 for the $n = 2$ case.

The conjugate gradient algorithm can be found in many textbooks, such as ref. [481]. Still, we briefly present it here, also in order to introduce some notation. The aim is to solve the system of equations (B.27), which is the specialization of (B.37) to the ghost propagator calculation, with $A = \mathbb{M}$ and v identified as the source term discussed in app. B.3.1.

Starting from some arbitrary vector $v^{(0)}$, the difference between the left hand side and the right hand side of eq. (B.27) is calculated,[7]

$$p^{(0)} = r^{(0)} = s - \mathbb{M}v^{(0)}. \tag{B.39}$$

[7] We now write $s := s_b$ for simplicity.

Obviously, the algorithm aims at minimizing the norm of F during subsequent iterations, which proceed as follows. For $k = 0, 1, \ldots$,

$$\begin{aligned} \alpha_k &= \frac{\left\langle r^{(k)}, r^{(k)} \right\rangle}{\left\langle p^{(k)}, \mathbb{M} p^{(k)} \right\rangle} \\ v^{(k+1)} &= v^{(k)} + \alpha_k p^{(k)} \\ r^{(k+1)} &= r^{(k)} - \alpha_k \mathbb{M} p^{(k)} \\ \beta_k &= \frac{\left\langle r^{(k+1)}, r^{(k+1)} \right\rangle}{\left\langle r^{(k)}, r^{(k)} \right\rangle} \\ p^{(k+1)} &= r^{(k+1)} + \beta_k p^{(k)}. \end{aligned} \tag{B.40}$$

The scalar product is simply defined as

$$\langle x, y \rangle = \sum_{i=0}^{3V-1} x_i y_i. \tag{B.41}$$

One may also write $\langle x, x \rangle = \|x\|_2^2$. – The measure of convergence of this algorithm is the relative residuum

$$\frac{\left\langle r^{(k)}, r^{(k)} \right\rangle}{\langle s, s \rangle}. \tag{B.42}$$

Once the relative residuum is below a small number ε, the algorithm has converged. We have compared different values of ε for the ghost propagator calculation and have found that typically, a value $\varepsilon = 10^{-8}$ is safely sufficient, in the sense that no further change in the propagator occurs is ε is lowered even more.

Examples of the evolution of the relative residuum during the numerical application of the conjugate gradient algorithm are shown in fig. B.7. They also illustrate that without a sufficient gauge fixing, i. e., if Δ^2 is not small enough, the algorithm may take much longer to converge. This can be explained in a very straightforward way by the fact that the algorithm is designed for positive-definite matrices. The discretized Faddeev–Popov operator has this property only if the Landau gauge fixing condition (2.11) resp., in the lattice formulation, (2.82) is satisfied.

B.3.3 Connection of matrix inversion to eigenvalue calculation

When calculating the eigenvalues of the FPO on lattices that are not tiny, it is useful to circumvent the exact calculation of the entire spectrum. An example of such a case is fig. 4.23 in ch. 4. In this case, the connection of the conjugate gradient algorithm to the Lanczos algorithm can be used [343]. To this end, two additional quantities are calculated at each iteration of the conjugate gradient algorithm, stated in eq. (B.40). These are, for $k \geq 1$,

$$\tilde{\alpha}_k = \frac{1}{\alpha_{k-1}} + \frac{\beta_{k-2}}{\alpha_{k-2}}, \tag{B.43a}$$

$$\eta_{k+1} = \frac{\sqrt{\beta_{k-1}}}{\alpha_{k-1}}. \tag{B.43b}$$

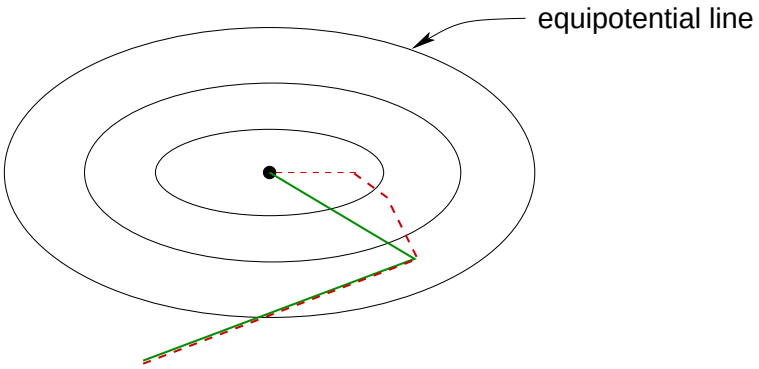

Figure B.6: Simple illustration of the conjugate gradient method for $n = 2$. The points in the plane symbolize (v_1, v_2). Broken red line: gradient, solid green line: conjugate gradient. The potential defining the equipotential lines is the function (B.38).

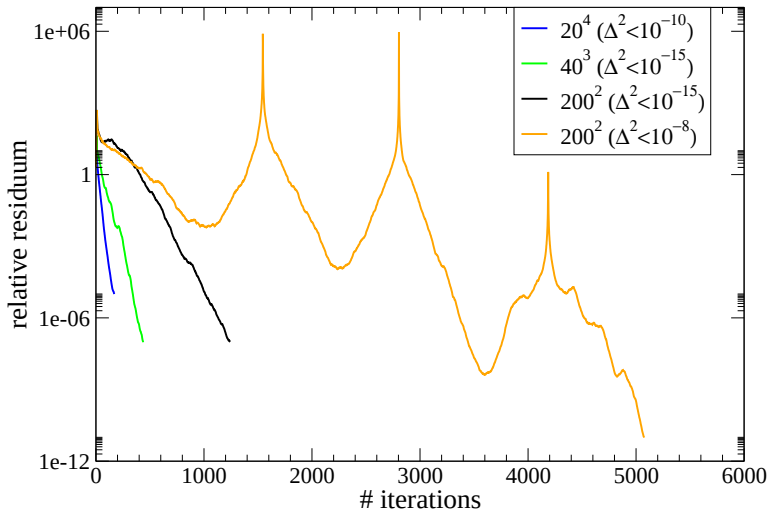

Figure B.7: Convergence of the conjugate gradient algorithm, measured by the evolution of the relative residuum (B.42), for different gauge fixing accuracies (Δ^2, eq. (2.85)).

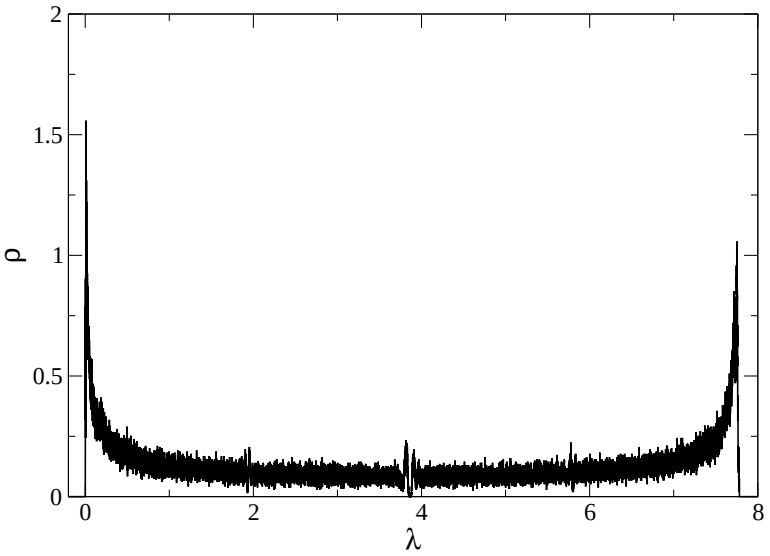

Figure B.8: Approximate spectrum from Lanczos, 24 lattice at $\beta = 10$ with random walk amended by stochastic overrelaxation, $\Delta^2 < 10^{-15}$. Underpopulation of the middle of the spectrum is visible.

For this purpose, the conventions $\beta_{-1} = 0$ and $\alpha_{-1} = 1$ apply. From $\tilde{\alpha}_i$ and η_i, a tridiagonal matrix is constructed,

$$T_k = \begin{pmatrix} \tilde{\alpha}_1 & \eta_2 & 0 & \dots & 0 & 0 \\ \eta_2 & \tilde{\alpha}_2 & \eta_3 & \dots & 0 & 0 \\ 0 & \eta_3 & \tilde{\alpha}_3 & \dots & 0 & 0 \\ 0 & 0 & \dots & \dots & \dots & 0 \\ 0 & \dots & \dots & \dots & \dots & \eta_k \\ 0 & \dots & \dots & 0 & \eta_k & \tilde{\alpha}_k \end{pmatrix}. \tag{B.44}$$

This is a $n_{\mathrm{cg}} \times n_{\mathrm{cg}}$ matrix, with n_{cg} the number of iterations until the conjugate gradient algorithm inverting $\mathbb{M}$ has converged to sufficient accuracy, see app. B.3.2. Typically, $n_{\mathrm{cg}} \in \mathcal{O}(1000)$ (see also fig. B.7). Evidently, the matrix T is much smaller than $\mathbb{M}$. The eigenvalues of T are approximations of a subset of the eigenvalues of $\mathbb{M}$. The fact that T is tridiagonal facilitates the eigenvalue calculation, which we perform with the QR algorithm, following standard textbooks like [482].

It is known that the Lanczos algorithm leads to an underpopulation of the middle of the spectrum, as is apparent e. g. from fig. B.8. These data were obtained after stochastic gauge fixing and qualitatively resemble data obtained after standard gauge fixing, see e. g. [115].

B.4 Parallelization procedure

B.4.1 Parallelization of dynamics and gauge fixing

In order to perform simulations on large lattices, I have written a parallel version of the serial code for simulating pure $SU(2)$ gauge theory that had been previously written by myself. The parallel C++ code is based on the 'Message Passing Interface' MPI, a library

of routines for passing messages between processes. This parallel code allows to simulate comparatively huge lattices, like e. g. a 160^4 lattice with a volume of $V = (34\,\mathrm{fm})^4$, see fig. 7.6, which has rarely been accomplished before.

The approach pursued here, including most of the notation, closely follows the QCDMPI implementation [483], but we have implemented it independently along the lines of the given reference and have also augmented it by gauge fixing. The algorithms we employ in the course of this work, sc. 'heat-bath', 'Langevin' and 'random walk', share the property that the update of any link variable $U_\mu(x)$ is entirely determined by the adjacent staples

$$S_\mu(x) := U_\nu(x)U_\mu(x+\hat{\nu})U_\nu^\dagger(x+\hat{\mu}) \quad (\nu \neq \mu) \tag{B.45}$$

in a local manner. See fig. B.1 above for an illustration of such staples in three dimensions. – In a further step, we have also parallelized the gauge fixing procedure, which does not involve staples, see app. B.4.1.2. Standard gauge fixing is more readily parallelized than stochastic gauge fixing, since in the former case, dynamical sweeps and gauge-fixing sweeps over all lattice points are clearly separated, while they are intertwined in the latter case (cp. sec. 4.2).

B.4.1.1 Dynamics

We parallelize the code by slicing the hypercubic lattice with L^d lattice sites into several sublattices. For simplicity, we restrict the parallelization here to symmetric lattices, i. e., such ones where the linear extension in $\hat{\mu}$-direction is independent of μ, $L_\mu = L$ for any $\mu \in \{0, \ldots, d-1\}$. The basic partition of the lattice is straightforward: We divide it into $\prod_{\mu=0}^{d-1} M_\mu$ sublattices of equal size and shape. That is, M_μ is the number of different processes onto which the sites in $\hat{\mu}$-direction are distributed. It may depend on μ, in contrast to our stipulation for L_μ. Figuratively speaking, each spatial sublattice contains a full hypercuboid of mutually neighboring sites. The numbers stored in the memory of a single computing core are the link variables on the links pointing in positive directions $\mu \in \{0, \ldots, d-1\}$ from these sites, and some additional ones required for communication.

In addition, we introduce a checkerboard decomposition of the lattice and thereby of each sublattice. By updating links of each direction and of each 'checkerboard parity' (even or odd) separately, we ensure that no link from a staple around $U_\mu(x)$ is updated simultaneously with $U_\mu(x)$. This is crucial in order for the simultaneous updates to be mutually independent, which justifies performing them in parallel. Note that the set of even resp. the set of odd sites is *not* the set of sites with even resp. odd addresses, where the address of a site is defined e. g. in $d = 3$ as

$$x_2 + x_1 L_1 + x_0 L_1 L_2. \tag{B.46}$$

Instead, the set of even resp. odd sites is the set of sites x for which the sum of coordinates,

$$\sum_{\mu=0}^{d-1} x_\mu, \tag{B.47}$$

is even resp. odd. The number of sites in each sublattice of fixed 'checkerboard parity' is

$$V_{\mathrm{local}} = \frac{1}{2} \prod_{\mu=0}^{d-1} m_\mu, \tag{B.48}$$

where

$$m_\mu := L_\mu / M_\mu \tag{B.49}$$

is the number of sites in $\hat{\mu}$-direction covered by a single process.

Some arrays are introduced which store the address of the neighboring site of any site in any direction. Here, the addresses are defined in terms of the number of a site in a 'sublattice of fixed checkerboard parity'. Note that these arrays take values not only in $\{0, 1, \ldots, V_{\mathrm{local}} - 1\}$, but also in $\{V_{\mathrm{local}}, V_{\mathrm{local}} + 1, \ldots, V_{\mathrm{local}} + V_{\mathrm{local}}/m_\mu - 1\}$. This is necessary in order to take the case into account that the neighbor of this lattice site is located in a different spatial sublattice (its parity is different by default, as the neighbor of an even site is odd and vice versa).

We emphasize again that mutually dependent link variables must not be updated simultaneously. For the purpose of the heat-bath algorithm, links that are part of the same plaquette contour are mutually dependent, since in this case, one of the links belongs to a staple around the other (and vice versa). Hence, the parallel update takes place for a fixed 'parity' (even/odd) and direction in all parallel processes at once. This entails that each process has to wait for each other one to finish this partial sweep, and that links that emanate from sites of different parity or that point in different directions are not updated simultaneously.

The parallel implementation of the calculation of staples will not be presented in detail here, since it is of mainly technical interest and can essentially be found in ref. [483]. We merely emphasize two aspects. First, some communication between processes that store and update the link variables in spatial sublattices which share a border is indispensable. This necessitates an appropriate sending-receiving schedule. In order to avoid the mutual sending and receiving ending in a deadlock, 'even' processes send first and receive afterwards, 'odd' ones do it vice versa. Again, 'even' and 'odd' refers here to the sum of coordinates (now in 'processor space'), not to the addresses.[8] Second, for the staples pointing in a negative direction $-\hat{v}$, communication requirements can be greatly reduced by calculating them starting from the site $i - \hat{v}$ instead of i and shifting the resulting staples in the positive $\hat{v}$-direction afterwards.

B.4.1.2 Gauge fixing

In order to work out a parallel implementation of gauge fixing by stochastic overrelaxation (see app. B.2.1.2), we have to consider that the gauge transformation $\Omega(x)$ at a lattice site x is determined by the 'hedgehog' of links around this site, see eq. (B.23) and (B.24), and, in turn, changes exactly these links (an illustration is provided in fig. 4.5). For communicating these links between processes where necessary, we can essentially employ the same routines as for the communication of the staples, given that some additional auxiliary arrays containing neighboring lattice sites are introduced.

[8] Let us single out a process. We refer to it as the p_μ-th one in the $\hat{\mu}$-direction, where

$$p_\mu \in \{0, 1, \ldots, M_\mu - 1\}.$$

If

$$\sum_{\mu=0}^{d-1} p_\mu$$

is an even number, the process is called 'even', otherwise 'odd'.

Random numbers play an indispensable role for any Monte Carlo simulation and any simulation by means of stochastic processes. Obviously, they need to be mutually independent. In serial simulations, this is easily accomplished, since standard random number generators produce sufficiently long independent sequences even for the demanding purposes of lattice gauge theory – e. g. the generator `ranlux` [477], which we employ, guarantees a period greater than 10^{165}. Of course, during parallelization of the code it has to be ensured the random numbers are independent also across parallel processes. Since in case of the generator `ranlux`, the random number sequences for different seeds do not overlap, the required and desired independence is achieved by simply choosing different seeds for different parallel processes.

B.4.2 Parallelized conjugate gradient algorithm

In order to calculate the ghost propagator on large lattices, we have also parallelized the conjugate gradient algorithm. This method inverts the lattice Faddeev–Popov operator $\mathbb{M}$, as laid out in app. B.3.2. We have parallelized the conjugate gradient method along the lines described in [481], to which we refer the reader for any details. It suffices to say that the (symmetric and positive-definite) matrix $\mathbb{M} \in \mathbb{R}^{3V\times 3V}$ is distributed by rows across processes. This distribution, i. e., the function assigning a process to each row of $\mathbb{M}$, is not unique. We have implemented two different distributions. The first one distributes $\mathbb{M}$ on the processes in a 'blockwise' fashion, i. e., the matrix is sliced into blocks of $3 \cdot 2 \cdot V_{\text{local}}$ consecutive rows each.[9] The first block goes to process 0, the second one to process 1, etc. The second implementation uses that distribution of the link variables onto the processes which is also used for updating the configurations. It is much faster than the first one, so we prefer it.[10]

For the ghost propagator, a parallel calculation can be helpful even in cases where the memory of a single computing core would be sufficient for the entire calculation. This is due to the fact that a single calculation with the plane-wave source method (app. B.3.1.1) takes a long time, combined with the strict upper limits on job execution times on many computing clusters. We have used the parallel ghost propagator code e. g. for the results on 64^3 and 288^2 lattices in chs. 5 and 6, and also for the results in app. C.3.

[9] For a general number of colors N_c, the factor of 3 is replaced by $N_c^2 - 1$. Hence, this factor depends on the number of color degrees of freedom. The factor of 2 is due to the fact that V_{local} counts the number of sites on a process with a given parity, cp. (B.48).

[10] A closer analysis provides evidence that this is due to frequent calls to the function `MPI_Allgather` in the other approach.

APPENDIX C

MISCELLANEOUS RESULTS

C.1 Discretization effects

C.1.1 Different lattice gauge fields and gauge conditions

The lattice formulation of continuum quantities is not unique at non-vanishing lattice spacing a, see also sec. 2.3.1. Rather, it is affected by discretization effects. Here, we are concerned with the corresponding freedom to explore other valid definitions in particular of two quantities on the lattice, sc. of the gauge field definition $A[U]$ and of the gauge fixing functional $R[U]$ (see sec. 2.3.2.1). The gauge fixing functional defines the lattice gauge fixing condition $F[U] = 0$, which is satisfied if and only if the gauge fixing functional is stationary under gauge transformations.

We assign an additional upper index (D) to R, F and A, as well as to the Faddeev–Popov operator M. This index runs over the different definitions, which are explicitly presented below. For much of the following, it is useful to parametrize a gauge transformation $\Omega(x)$ as

$$\Omega(x) = \exp\left(i\tau T^a \omega^a\right), \tag{C.1}$$

where $\tau \in \mathbb{R}$ and $\omega^a \in \mathbb{R}$ are parameters and T^a are the generators of the gauge group. Here, we specialize to $SU(2)$.

The gauge fixing functional, the gauge condition and the Faddeev–Popov operator are related via eq. (2.96), which we repeat here,[1]

$$\frac{\partial^2}{\partial\tau^2} R^{(D)}\bigg|_{\tau=0} = \frac{\partial}{\partial\tau} \sum_x F^{(D)}\bigg|_{\tau=0} = -\sum_{x,y,a,b} \omega_x^c \mathbb{M}^{(D)}{}^{a,b}_{x,y} \omega_y^b, \tag{C.2}$$

This expresses that the gauge condition $F^{(D)}$ is the variation of $R^{(D)}$, and the Faddeev–Popov operator is the negative Hessian (i. e., the negative second variation) of $R^{(D)}$. We define the gauge field $A_\mu^{(D)}(x)$ such that its discrete derivative equals the gauge condition,

$$F^{(D)} = \partial_\mu A_\mu^{(D)}(x) = 0. \tag{C.3}$$

[1] This way to define the Faddeev–Popov operator for a given gauge condition, following [17], is not unique, see e. g. the remark in [236].

The gauge field definition $A^{(D)}$ and the gauge fixing functional $R^{(D)}$ are related insofar as the 'natural' choice of $A^{(D)}$ for a given $R^{(D)}$ is the one from can be read off from writing the variation of $R^{(D)}$ with respect to the gauge parameter in the form (C.3).

We now explicitly present the alternative definitions we have implemented and tested. We frequently omit constant prefactors for simplicity, as our studies of these discretization effects are performed at finite coupling, where we always renormalize the propagators, usually at $\mu = 2.5\,\mathrm{GeV}$ (see sec. 2.3.4.2). This renders any prior prefactors irrelevant.[2]

0. Standard gauge condition.

$$R^{(0)} \propto \sum_{x,\mu} \mathrm{tr}\, U_\mu(x) \propto \sum_{x,\mu} u^0_\mu(x) \tag{C.4}$$

$$A^{(0)\,a}_{\mu}(x) \propto u^a_\mu(x) \tag{C.5}$$

1. Stereographic projection of the link variables [235, 237].

$$R^{(1)} \propto -\sum_{x,\mu} \ln\left(\frac{1}{2} + \frac{1}{4}\mathrm{tr}\, U_\mu(x)\right) \tag{C.6}$$

$$A^{(1)}{}_\mu(x) \propto \left(\tilde{U}_\mu(x) - \tilde{U}^\dagger_\mu(x)\right) \text{ with } \tilde{U}_\mu(x) := \frac{2U_\mu(x)}{1 + \frac{1}{2}\mathrm{tr}\, U_\mu(x)} \tag{C.7}$$

2. Lattice gluon fields based on the adjoint representation [147].[3]

$$R^{(2)} \propto \sum_{x,\mu} \mathrm{tr}\, U^2_\mu(x) \tag{C.8}$$

$$A^{(2)\,a}_{\mu}(x) \propto u^0_\mu(x) u^a_\mu(x) \tag{C.9}$$

3. The gauge functional may be chosen to include two-link terms, like [484, 485][4]

$$R^{(3)} \propto \sum_{x,\mu} \mathrm{tr}\, U_\mu(x) U_\mu(x+\hat{\mu}) \tag{C.10}$$

$$\begin{aligned} A^{(3)\,a}_{\mu}(x) \propto &- u^0_\mu(x) u^a_\mu(x+\hat{\mu}) - u^a_\mu(x) u^0_\mu(x+\hat{\mu}) - u^0_\mu(x-\hat{\mu}) u^a_\mu(x) - \\ &- u^a_\mu(x-\hat{\mu}) u^0_\mu(x) + \varepsilon^{abc}\left[u^b_\mu(x) u^c_\mu(x+\hat{\mu}) + u^b_\mu(x-\hat{\mu}) u^c_\mu(x)\right] \end{aligned} \tag{C.11}$$

4. A definition used in [486], see also [487, 488],

$$R^{(4)} \propto \sum_{x,\mu} \mathrm{tr}\, \left(\tilde{A}_\mu(x)\right)^2 \tag{C.12}$$

with $\tilde{A}_\mu(x)$ defined via $U_\mu(x) = \exp(ia\tilde{A}_\mu(x))$. Thus, we refer to this definition in shorthand notation as '$A = \ln U$'. Since

$$u^0_\mu(x)\mathbb{1} + i\sigma\cdot\vec{u}_\mu(x) = \exp\left(\frac{i}{2}\vec{\theta}\cdot\vec{\sigma}\right) \quad\Leftrightarrow\quad \vec{\theta} = \frac{2\vec{u}_\mu(x)}{|\vec{u}_\mu(x)|}\arccos u^0_\mu(x), \tag{C.13}$$

[2] The Einstein summation convention is in effect, see app. A.1.1.

[3] In eq. (C.9), no sum over μ is performed.

[4] In ref. [485], a linear combination of one- and two-link functionals is used to remove $\mathcal{O}(a^2)$ errors between the lattice gauge fixing functional and the corresponding continuum condition.

eq. (C.12) can be rewritten as

$$R^{(4)} \propto \sum_{x,\mu} \left(\arccos(u^0_\mu(x)) \right)^2, \tag{C.14}$$

from which it can in turn be derived that the gauge condition $F^{(4)} = 0$ amounts to

$$\frac{\partial}{\partial \tau} R^{(4)}[\Omega_\tau] \Big|_{\tau=0} = \sum_{x,\mu} \left[{A^{(4)}}^a_\mu(x) - {A^{(4)}}^a_\mu(x - \hat{\mu}) \right] \omega^a_x = 0, \tag{C.15}$$

given that we define

$${A^{(4)}}^a_\mu(x) \propto \frac{u^a_\mu(x) \arccos u^0_\mu(x)}{|\vec{u}_\mu(x)|}. \tag{C.16}$$

This definition is equivalent to the one explicitly given in [489], with $\arccos\left(u^0_\mu(x)\right)$ rewritten as $\arctan\left(\left|\vec{u}_\mu(x)\right| / u^0_\mu(x)\right)$.

The following table serves as a brief overview of the various discretizations of the gauge fixing functional and gauge field definitions that we study here.

D	gauge fixing functional $R^{(D)} \propto \sum_{x,\mu} \ldots$	gauge field definition ${A^{(D)}}^a_\mu(x) \propto \ldots$
0	$\mathrm{tr}\, U_\mu(x) \propto u^0_\mu(x)$	$u^a_\mu(x)$
1	$\ln\left(\frac{1}{2} + \frac{1}{4}\mathrm{tr}\, U_\mu(x)\right)$	$2u^a_\mu(x) / \left[1 + u^0_\mu(x)\right]$
2	$\mathrm{tr}\, U^2_\mu(x)$	$u^0_\mu(x) u^a_\mu(x)$
3	$\mathrm{tr}\, U_\mu(x) U_\mu(x + \hat{\mu})$	(eq. (C.11))
4	$(\arccos u^0_\mu(x))^2$	$\left[u^a_\mu(x) \arccos u^0_\mu(x)\right] / \left|\vec{u}_\mu(x)\right|$

The lengthiest part of the discussion of these different discretizations is the presentation of the explicit form of the respective Faddeev–Popov operator derived from the various gauge fixing conditions, following the idea of ref. [17], eq. (C.16). $\mathbb{M}^{(0)}$ and $\mathbb{M}^{(1)}$ have previously been given explicitly, the former one (also for more general cases than $SU(2)$) e. g. in refs. [245, 173, 246], the latter one in ref. [235]. We find

0.

$$\begin{aligned}
\frac{\partial^2}{\partial\tau^2}R^{(0)}\Big|_{\tau=0} &\propto \sum_{x,\mu}\mathrm{tr}\left[\left(i\sigma^a(\omega^a_x-\omega^a_{x+\hat\mu})\right)\left(i\sigma^b\omega^b_x U_\mu(x)-i\omega^b_{x+\hat\mu}U_\mu(x)\sigma^b\right)\right]\\
&=-2\sum_{x,\mu}\left(\omega^a_x-\omega^a_{x+\hat\mu}\right)\left(\delta^{ab}u^0_\mu(x)(\omega^b_x-\omega^b_{x+\hat\mu})-\varepsilon^{abc}u^c_\mu(x)(\omega^b_x+\omega^b_{x+\hat\mu})\right)\\
&\propto\sum_{x,\mu}\Big[\omega^a_x\omega^b_x\Big(-\delta^{ab}u^0_\mu(x)+\varepsilon^{abc}u^c_\mu(x)\Big)+\\
&\qquad+\omega^a_x\omega^b_{x+\hat\mu}\Big(\delta^{ab}u^0_\mu(x)+\varepsilon^{abc}u^c_\mu(x)\Big)+\\
&\qquad+\omega^a_{x+\hat\mu}\omega^b_x\Big(\delta^{ab}u^0_\mu(x)-\varepsilon^{abc}u^c_\mu(x)\Big)+\\
&\qquad+\omega^a_{x+\hat\mu}\omega^b_{x+\hat\mu}\Big(-\delta^{ab}u^0_\mu(x)-\varepsilon^{abc}u^c_\mu(x)\Big)\Big]\\
&=\sum_{x,y,\mu}\omega^a_x\Big[\Big(-\delta^{ab}(u^0_\mu(x)+u^0_\mu(x-\hat\mu))-\\
&\qquad-\varepsilon^{abc}\underbrace{(u^c_\mu(x-\hat\mu)-u^c_\mu(x))}_{=0\text{ after }\sum_\mu\text{ (Landau gauge)}}\Big)\delta(x-y)+\\
&\qquad+\Big(\delta^{ab}u^0_\mu(x)+\varepsilon^{abc}u^c_\mu(x)\Big)\delta(x+\hat\mu-y)+\\
&\qquad+\Big(\delta^{ab}u^0_\mu(x-\hat\mu)-\varepsilon^{abc}u^c_\mu(x-\hat\mu)\Big)\delta(x-\hat\mu-y)\Big]\omega^b_y\\
&=-\sum_{x,y}\omega^a_x\mathbb{M}^{(0)}{}^{a,b}_{x,y}\omega^b_y.
\end{aligned}\tag{C.17}$$

Eq. (2.97) is a trivial reformulation of this result.

This means that the elements of the standard lattice Faddeev–Popov operator $\mathbb{M}^{(0)}$, which we often simply refer to as $\mathbb{M}$, read explicitly

- for $y=x$: $\quad\delta^{ab}(u^0_\mu(y)+u^0_\mu(y-\hat\mu))$,
- for $y=x+\hat\mu$: $-\delta^{ab}u^0_\mu(y-\hat\mu)-\varepsilon^{abc}u^c_\mu(y-\hat\mu)$,
- for $y=x-\hat\mu$: $-\delta^{ab}u^0_\mu(y)+\varepsilon^{abc}u^c_\mu(y)$,
- zero otherwise.

For practical purposes, like the conjugate gradient algorithm (see app. B.3.2), it is sometimes useful to implement in the numerical code directly an expression for the product of the lattice Faddeev–Popov operator with a vector $v\in\mathbb{R}^{3V}$, which can be trivially obtained from the explicit representation of $\mathbb{M}$ above.

1. As a first step (with the generators $T^a=\sigma^a/2$ of $SU(2)$),

$$\frac{\partial R^{(1)}}{\partial\tau}=\sum_{x,\mu}\frac{\frac{1}{4}\mathrm{tr}\left\{iT^a\omega^a_x e^{i\tau T^a\omega^a_x}U_\mu(x)e^{-i\tau T^a\omega^a_{x+\hat\mu}}-e^{i\tau T^a}U_\mu(x)iT^a\omega^a_{x+\hat\mu}e^{-iT^a\omega^a_{x+\hat\mu}}\right\}}{\frac{1}{2}+\frac{1}{4}\mathrm{tr}\left[e^{i\tau T^a\omega^a_x}U_\mu(x)e^{-i\tau T^a\omega^a_{x+\hat\mu}}\right]}.\tag{C.18}$$

In order to obtain the Faddeev–Popov operator, we need to differentiate one more time with respect to τ and evaluate the resulting expression at $\tau = 0$. The expression on the right hand side of (C.18) consists of two summands, which we now discuss in turn.

The first summand of (C.18) closely resembles $\omega^a_x \mathbb{M}^{(0)}{}^{a,b}_{x,y} \omega^b_y$, the sole exception being that the individual summands inside $\sum_{a,b,x,y,\mu}$ are multiplied by the factor

$$\frac{\left[\frac{1}{2} + \frac{1}{4}\mathrm{tr}\, U_\mu(x)\right]}{\left[\frac{1}{2} + \frac{1}{4}\mathrm{tr}\, U_\mu(x)\right]^2} = \frac{2}{1 + u^0_\mu(x)}.$$

Thus, this part of $\mathbb{M}^{(1)}$ has the form of the standard FPO $\mathbb{M}^{(0)}$, but with the standard Cayley–Klein parameters $u^i_\mu(x)$ ($i \in \{0,1,2,3\}$) replaced by terms proportional to their stereographic projection[5]

$$\tilde{u}^i_\mu(x) = \frac{u^i_\mu(x)}{1 + u^0_\mu(x)} \quad (i \in \{0,1,2,3\}). \tag{C.19}$$

The second summand in (C.18) amounts to

$$\begin{aligned}
&\sum_{x,\mu} \frac{-\left(\frac{1}{4}\mathrm{tr}\left[iT^a(\omega^a_x - \omega^a_{x+\hat{\mu}})U_\mu(x)\right]\right)\left(\frac{1}{4}\mathrm{tr}\left[iT^b(\omega^b_x - \omega^b_{x+\hat{\mu}})U_\mu(x)\right]\right)}{(\frac{1}{2} + \frac{1}{4}\mathrm{tr}\, U_\mu(x))^2} \propto \\
\propto &\sum_{x,\mu} \frac{-\left(\omega^a_x u^a_\mu(x) - \omega^a_{x+\hat{\mu}} u^a_\mu(x)\right)\left(\omega^b_x u^b_\mu(x) - \omega^b_{x+\hat{\mu}} u^b_\mu(x)\right)}{(1 + u^0_\mu(x))^2} \\
= &\sum_{x,y,\mu} -\omega^a_x \Big\{ \left[\tilde{u}^a_\mu(x)\tilde{u}^b_\mu(x) + \tilde{u}^a_\mu(x-\hat{\mu})\tilde{u}^b_\mu(x-\hat{\mu})\right]\delta(x-y) - \\
&- \tilde{u}^a_\mu(x-\hat{\mu})\tilde{u}^b_\mu(x-\hat{\mu})\delta(y-x+\hat{\mu}) - \tilde{u}^a_\mu(x)\tilde{u}^b_\mu(x)\delta(y-x-\hat{\mu})\Big\}\omega^b_y.
\end{aligned} \tag{C.20}$$

Summing up, we obtain

$$\begin{aligned}
\mathbb{M}^{(1)}{}^{a,b}_{x,y} =& 2\mathbb{M}^{(0)}{}^{a,b}_{x,y}[\tilde{u}] + \\
&+ 2\sum_\mu \Big\{ \left[\tilde{u}^a_\mu(x)\tilde{u}^b_\mu(x) + \tilde{u}^a_\mu(x-\hat{\mu})\tilde{u}^b_\mu(x-\hat{\mu})\right]\delta(x-y) \\
&\qquad + \tilde{u}^a_\mu(x-\hat{\mu})\tilde{u}^b_\mu(x-\hat{\mu})\delta(y-x+\hat{\mu}) + \tilde{u}^a_\mu(x)\tilde{u}^b_\mu(x)\delta(y-x-\hat{\mu})\Big\} \\
= 2\sum_\mu \Big[&\Big\{\delta^{ab}\left(\tilde{u}^0_\mu(x) + \tilde{u}^0_\mu(x-\hat{\mu})\right) + \tilde{u}^a_\mu(x)\tilde{u}^b_\mu(x) + \tilde{u}^a_\mu(x-\hat{\mu})\tilde{u}^b_\mu(x-\hat{\mu})\Big\}\delta(x-y) - \\
&- \Big\{\delta^{ab}\tilde{u}^0_\mu(x) + \varepsilon^{abc}\tilde{u}^c_\mu(x) + \tilde{u}^a_\mu(x)\tilde{u}^b_\mu(x)\Big\}\delta(x+\hat{\mu}-y) - \\
&- \Big\{\delta^{ab}\tilde{u}^0_\mu(x-\hat{\mu}) - \varepsilon^{abc}\tilde{u}^c_\mu(x-\hat{\mu}) + \tilde{u}^a_\mu(x-\hat{\mu})\tilde{u}^b_\mu(x-\hat{\mu})\Big\}\delta(x-\hat{\mu}-y)\Big].
\end{aligned} \tag{C.21}$$

[5] When some 'u-terms' in the numerator are shifted (typically by $\pm\mu$) in order to obtain the structure $\omega^a_x \ldots \omega^b_x$ (before inserting the δ functions $\delta(x-y)$ etc.), the corresponding $u^0_\mu(x)$ in the denominator is shifted as well. Hence, the substitution (stereographic projection) is straightforward.

Thus, we essentially confirm the result stated in [235], although we arrive at a different sign of the terms proportional to the Levi-Civita tensor ε^{abc}.

2. The Faddeev–Popov operator $\mathbb{M}^{(2)}$ is derived as follows:

$$\frac{\partial}{\partial\tau}R^{(2)} \propto \sum_{x,\mu} 2\mathrm{tr}\,\left[i\sigma^a\left(U^{\Omega}_{\mu}(x)\right)^2(\omega^a_x - \omega^a_{x+\hat{\mu}})\right] \tag{C.22}$$

$$\begin{aligned}\frac{\partial^2}{\partial\tau^2}R^{(2)}\bigg|_{\tau=0} \propto \sum_{x,\mu} 2\mathrm{tr}\,\Big[i^2\sigma^a(\omega^a_x - \omega^a_{x+\hat{\mu}})\Big\{&\sigma^b U^2_\mu(x)\omega^b_x - U_\mu(x)\sigma^b U_\mu(x)\omega^b_{x+\hat{\mu}} + \\ &+ U_\mu(x)\sigma^b U_\mu(x)\omega^b_x - U^2_\mu\sigma^b\omega^b_{x+\hat{\mu}}\Big\}\Big] \\ = \sum_{x,\mu} -2\mathrm{tr}\,\Big[(\omega^a_x - \omega^a_{x+\hat{\mu}})\Big\{&\omega^b_x(\sigma^a\sigma^b U^2_\mu(x) + \sigma^a U_\mu(x)\sigma^b U_\mu(x)) - \\ &- \omega^b_{x+\hat{\mu}}(\sigma^b\sigma^a U^2_\mu(x) + \sigma^a U_\mu(x)\sigma^b U_\mu(x))\Big\}\Big].\end{aligned} \tag{C.23}$$

We arrive at[6]

$$\begin{aligned}\frac{\partial^2}{\partial\tau^2}R^{(2)}\bigg|_{\tau=0} \propto \sum_{x,\mu,y} -8\omega^a_x\Big[&(f^-_{ab\mu}(x) + f^+_{ab\mu}(x-\hat{\mu}))\delta(x-y) - \\ &- f^-_{ab\mu}(x-\hat{\mu})\delta(x-\hat{\mu}-y) - f^+_{ab\mu}(x)\delta(x+\hat{\mu}-y)\Big]\omega^b_y,\end{aligned} \tag{C.28}$$

where we have used the abbreviation

$$f^{\pm}_{ab\mu}(x) := \delta^{ab}u^0_\mu(x)u^0_\mu(x) - u^a_\mu(x)u^b_\mu(x) \pm \varepsilon^{abc}u^0_\mu(x)u^c_\mu(x). \tag{C.29}$$

[6] Exploiting

$$\mathrm{tr}\,(\sigma^{a/b}\sigma^{b/a}U^2_\mu(x)) = 2\delta^{ab}(u^0_\mu(x)u^0_\mu(x) - u^c_\mu(x)u^c_\mu(x)) - 4\varepsilon^{abc}u^0_\mu(x)u^c_\mu(x) \tag{C.24}$$

and

$$\mathrm{tr}\,(\sigma^a U_\mu(x)\sigma^b U_\mu(x)) = 2\delta^{ab}(u^0_\mu(x)u^0_\mu(x) + u^c_\mu(x)u^c_\mu(x)) - 4u^a_\mu(x)u^b_\mu(x) = 2\delta^{ab} - 4u^a_\mu(x)u^b_\mu(x), \tag{C.25}$$

we obtain

$$\begin{aligned}\mathrm{tr}\,(\sigma^a\sigma^b U^2_\mu(x) + \sigma^a U_\mu(x)\sigma_b U_\mu(x)) =& 2\delta^{ab}(u^0_\mu(x)u^0_\mu(x) - u^c_\mu(x)u^c_\mu(x)) - 4\varepsilon^{abc}u^0_\mu(x)u^c_\mu(x) + 2\delta^{ab} - 4u^a_\mu(x)u^b_\mu(x) \\ =& 4(\delta^{ab}u^0_\mu(x)u^0_\mu(x) - u^a_\mu(x)u^b_\mu(x) - \varepsilon^{abc}u^0_\mu(x)u^c_\mu(x)) \\ \propto& f^-_{ab\mu}(x)\end{aligned} \tag{C.26}$$

and

$$\begin{aligned}\mathrm{tr}\,(-\sigma^b\sigma^a U^2_\mu(x) - \sigma^a U_\mu(x)\sigma^b U_\mu(x)) =& -2\delta^{ab}(u^0_\mu(x)u^0_\mu(x) - u^c_\mu(x)u^c_\mu(x)) - 4\varepsilon^{abc}u^0_\mu(x)u^c_\mu(x) - 2\delta^{ab} + \\ &+ 4u^a_\mu(x)u^b_\mu(x) \\ =& -4(\delta^{ab}u^0_\mu(x)u^0_\mu(x) + u^a_\mu(x)u^b_\mu(x) - \varepsilon^{abc}u^0_\mu(x)u^c_\mu(x)) \\ \propto& -f^+_{ab\mu}(x).\end{aligned} \tag{C.27}$$

This may be slightly simplified by exploiting the gauge condition (which eliminates the ε-terms in the $\delta(x-y)$-term), such that

$$\begin{aligned}\mathbb{M}^{(2)}{}^{a,b}_{x,y} \propto \left[g_{ab\mu}(x) + g_{ab\mu}(x-\hat{\mu})\right]\delta(x-y) - \\ - f^{-}_{ab\mu}(x-\hat{\mu})\delta(x-\hat{\mu}-y) - f^{+}_{ab\mu}(x)\delta(x+\hat{\mu}-y),\end{aligned} \tag{C.30}$$

where

$$g_{ab\mu}(x) := \delta^{ab}u^0_\mu(x)u^0_\mu(x) - u^a_\mu(x)u^b_\mu(x). \tag{C.31}$$

Thus (with a summation also over y understood),

$$\mathbb{M}^{(2)}{}^{a,b}_{x,y}c^b(y) = \left[g_{ab\mu}(x) + g_{ab\mu}(x-\hat{\mu})\right]c^b(x) - f^{-}_{ab\mu}(x-\hat{\mu})c^b(x-\hat{\mu}) - f^{+}_{ab\mu}(x)c^b(x+\hat{\mu}). \tag{C.32}$$

3. From $R^{(3)}$, we obtain the gauge fixing condition

$$\begin{aligned}\frac{\partial}{\partial\tau}R^{(3)}\Big|_{\tau=0} = \sum_{\mu,x}\Big[&- u^0_\mu(x)u^a_\mu(x+\hat{\mu}) - u^a_\mu(x)u^0_\mu(x+\hat{\mu}) + \\ &+ u^0_\mu(x-2\hat{\mu})u^a_\mu(x-\hat{\mu}) + u^a_\mu(x-2\hat{\mu})u^0_\mu(x-\hat{\mu}) + \\ &+ \varepsilon^{abc}\left(u^b_\mu(x)u^c_\mu(x+\hat{\mu}) - u^b_\mu(x-2\hat{\mu})u^c_\mu(x-\hat{\mu})\right)\Big]\omega^a(x)\end{aligned} \tag{C.33}$$

and the Faddeev–Popov operator, defined as usual via

$$\frac{\partial^2}{\partial\tau^2}R^{(3)}\Big|_{\tau=0} = -\sum_{x,y,\mu,a,b}\omega^a(x)\mathbb{M}^{(3)}{}^{a,b}_{x,y}\omega^b(y), \tag{C.34}$$

as

$$\begin{aligned}\mathbb{M}^{(3)}{}^{a,b}_{x,y} = \sum_\mu\Big(\Big\{&\delta^{ab}\Big[u^0_\mu(y)u^0_\mu(y+\hat{\mu}) - u^c_\mu(y)u^c_\mu(y+\hat{\mu}) + \\ &+ u^0_\mu(y-2\hat{\mu})u^0_\mu(y-\hat{\mu}) - u^c_\mu(y-2\hat{\mu})u^c_\mu(u-\hat{\mu})\Big] \\ &+ u^a_\mu(y)u^b_\mu(y+\hat{\mu}) - u^b_\mu(y)u^a_\mu(y+\hat{\mu}) - u^a_\mu(y-2\hat{\mu})u^b_\mu(y-\hat{\mu}) + \\ &+ u^b_\mu(y-2\hat{\mu})u^a_\mu(y-\hat{\mu}) - \\ &- \varepsilon^{abc}\Big[u^c_\mu(y)u^0_\mu(y+\hat{\mu}) + u^0_\mu(y)u^c_\mu(y+\hat{\mu}) - \\ &- u^c_\mu(y-2\hat{\mu})u^0_\mu(y-\hat{\mu}) - u^0_\mu(y-2\hat{\mu})u^c_\mu(y-\hat{\mu})\Big]\Big\}\delta(x-y) + \\ &+ \Big\{\delta^{ab}\Big[-u^0_\mu(y-2\hat{\mu})u^0_\mu(y-\hat{\mu}) + u^c_\mu(y-2\hat{\mu})u^c_\mu(y-\hat{\mu})\Big] + \\ &+ u^a_\mu(y-2\hat{\mu})u^b_\mu(y-\hat{\mu}) - u^b_\mu(y-2\hat{\mu})u^a_\mu(y-\hat{\mu}) - \\ &- \varepsilon^{abc}\Big[u^c_\mu(y-2\hat{\mu})u^0_\mu(y-\hat{\mu}) + u^0_\mu(y-2\hat{\mu})u^c_\mu(y-\hat{\mu})\Big]\Big\}\delta(x+2\hat{\mu}-y) + \\ &+ \Big\{\delta^{ab}\Big[-u^0_\mu(y)u^0_\mu(y+\hat{\mu}) + u^c_\mu(y)u^c_\mu(y+\hat{\mu})\Big] - \\ &- u^a_\mu(y)u^b_\mu(y+\hat{\mu}) + u^b_\mu(y)u^a_\mu(y+\hat{\mu}) + \\ &+ \varepsilon^{abc}\Big[u^c_\mu(y)u^0_\mu(y+\hat{\mu}) + u^0_\mu(y)u^c_\mu(y+\hat{\mu})\Big]\Big\}\delta(x-2\hat{\mu}-y)\Big).\end{aligned} \tag{C.35}$$

4. The derivation of the Faddeev–Popov operator $\mathbb{M}^{(4)}$ runs along the following lines. We start from the gauge condition

$$\frac{\partial}{\partial\tau}R^{(4)}[\Omega_\tau]\bigg|_{\tau=0} = \sum_{x,\mu}\left[A^{(4)}{}^a_\mu(x) - A^{(4)}{}^a_\mu(x-\hat{\mu})\right]\omega^a_x = 0, \tag{C.36}$$

with $A^{(4)}$ defined in eq. (C.16). As a first step,

$$\begin{aligned}\frac{\partial}{\partial\tau}R^{(4)}[\Omega_\tau] \propto \sum_{x,\mu} 2\arccos\left(\frac{1}{2}\mathrm{tr}\,U^\Omega_\mu(x)\right)\frac{-1}{\sqrt{1-\left(\frac{1}{2}\mathrm{tr}\,U^\Omega_\mu(x)\right)^2}}\cdot\ldots \\ \ldots\cdot\frac{1}{2}\mathrm{tr}\,\left(iT^a(\omega^a_x - \omega^a_{x+\hat{\mu}})U^\Omega_\mu(x)\right).\end{aligned} \tag{C.37}$$

Thus,

$$\begin{aligned}\frac{\partial}{\partial\tau}R^{(4)}[\Omega_\tau]\bigg|_{\tau=0} \propto \sum_{x,\mu}\Bigg[\left\{\frac{2}{1-(u^0_\mu(x))^2} + 2\arccos(u^0_\mu(x))\frac{-2u^0_\mu(x)}{2\left(1-(u^0_\mu(x))^2\right)^{3/2}}\right\}\cdot\ldots \\ \ldots\cdot\left(\frac{1}{2}\mathrm{tr}\,(iT^a(\omega^a_x-\omega^a_{x+\hat{\mu}})U_\mu(x))\right)^2 - \\ -\frac{2\arccos(u^0_\mu(x))}{\sqrt{1-(u^0_\mu(x))^2}}\cdot\ldots \\ \ldots\cdot\frac{1}{2}\mathrm{tr}\,\left\{iT^a(\omega^a_x-\omega^a_{x+\hat{\mu}})(iT^bU_\mu(x) - iU_\mu(x)T^b\omega^b_{x+\hat{\mu}})\right\}\Bigg].\end{aligned} \tag{C.38}$$

As an intermediate step, we arrive at[7]

$$\begin{aligned}\frac{\partial}{\partial\tau}R^{(4)}[\Omega_\tau]\bigg|_{\tau=0} &\propto \sum_{x,\mu}\Bigg[\left\{\frac{1}{1-(u^0_\mu(x))^2} - \frac{u^0_\mu(x)\arccos(u^0_\mu(x))}{(1-(u^0_\mu(x))^2)^{3/2}}\right\}\left((\omega^a_x-\omega^a_{x+\hat{\mu}})u^a_\mu(x)\right)^2 \\ &\quad - \frac{\arccos(u^0_\mu(x))}{\sqrt{1-(u^0_\mu(x))^2}}\frac{1}{2}\mathrm{tr}\left\{U_\mu(x)\Big[-T^aT^b\omega^a_x\omega^b_x + T^aT^b\omega^a_{x+\hat{\mu}}\omega^b_x + \right. \\ &\quad \left. + T^bT^a\omega^a_x\omega^b_{x+\hat{\mu}} - T^bT^a\omega^a_{x+\hat{\mu}}\omega^b_{x+\hat{\mu}}\Big]\right\}\Bigg] \\ &\propto \sum_{x,\mu,y}\Bigg[\omega^a_x\Bigg(\left\{\frac{1}{1-(u^0_\mu(x))^2} - \frac{u^0_\mu(x)\arccos(u^0_\mu(x))}{(1-(u^0_\mu(x))^2)^{3/2}}\right\}\Big\{\Big[u^a_\mu(x)u^b_\mu(x) + \end{aligned}$$

[7] This equation is unnumbered for technical reasons. – We use relations like

$$\mathrm{tr}\,(i\sigma^aU_\mu(x)) = -2u^a_\mu(x)$$

and

$$\mathrm{tr}\,(\sigma^a\sigma^bU_\mu(x)) = 2(\delta^{ab}u^0_\mu(x) - \varepsilon^{abc}u^c_\mu(x)).$$

$$
\begin{aligned}
&+ u^a_\mu(x-\hat{\mu})u^b_\mu(x-\hat{\mu})\Big]\delta(x-y) \\
&- u^a_\mu(x)u^b_\mu(x)\delta(x+\hat{\mu}-y) - u^a_\mu(x-\hat{\mu})u^b_\mu(x-\hat{\mu})\delta(x-\hat{\mu}-y)\Big\} \\
&- \frac{\arccos(u^0_\mu(x))}{\sqrt{1-(u^0_\mu(x))^2}}\Big\{ -\delta^{ab}(u^0_\mu(x)+u^0_\mu(x-\hat{\mu}))\delta(x-y)+ \\
&+ (\delta^{ab}u^0_\mu(x)+\varepsilon^{abc}u^c_\mu(x))\delta(x+\hat{\mu}-y) \\
&+ (\delta^{ab}u^0_\mu(x)-\varepsilon^{abc}u^c_\mu(x-\hat{\mu}))\delta(x-\hat{\mu}-y)\Big\}\Bigg)\omega^b_y\Bigg].
\end{aligned}
$$

After further simplification, we obtain

$$
\begin{aligned}
\mathbb{M}^{(4)\,ab}_{xy} = \sum_\mu \Bigg\{ &\delta(x-y)\left[f^{ab}_\mu(x)+f^{ab}_\mu(x-\hat{\mu})+\delta^{ab}\left\{\tilde{u}^0_\mu(x)+\tilde{u}^0_\mu(x-\hat{\mu})\right\}\right] \\
&+\delta(x+\hat{\mu}-y)\left[-f^{ab}_\mu(x)-\delta^{ab}\tilde{u}^0_\mu(x)-\varepsilon^{abc}\tilde{u}^c_\mu(x)\right] \\
&+\delta(x-\hat{\mu}-y)\Big[-f^{ab}_\mu(x-\hat{\mu})-\delta^{ab}\tilde{u}^0_\mu(x-\hat{\mu})+\varepsilon^{abc}\tilde{u}^c_\mu(x-\hat{\mu})\Big]\Bigg\},
\end{aligned}
\tag{C.39}
$$

where we have defined the abbreviations

$$
f^{ab}_\mu(x) := 2\left(1-(u^0_\mu(x))^2\right)^{-3/2}\left[\sqrt{1-(u^0_\mu(x))^2}-u^0_\mu(x)\arccos(u^0_\mu(x))\right]u^a_\mu(x)u^b_\mu(x) \tag{C.40}
$$

and

$$
\tilde{u}^i_\mu(x) := \frac{2\arccos(u^0_\mu(x))}{\sqrt{1-(u^0_\mu(x))^2}}u^i_\mu(x) \quad (i\in\{0,1,2,3\}). \tag{C.41}
$$

C.1.2 Implementation of gauge fixing

We intend to maximize (or more precisely, extremize) different gauge fixing functionals $R^{(D)}$. This necessitates a change of the gauge transformations which minimize $\left(\Delta^{(D)}\right)^2$. They depend on the gauge condition $R^{(D)}$, not directly on the definition of the lattice gauge field.

In contrast, the lattice Langevin equation for the dynamics, eq. (4.5), remains unchanged, as it is formulated directly in terms of the link variables $U_\mu(x)$, which are elements of the gauge group. Hence, it is independent of the definition of the lattice gauge field, let alone of the gauge fixing functional.

We adapt a simple 'steepest descent' method for fine tuning of the gauge fixing, following [486]. With the gauge condition (C.3), we choose the gauge transformation matrices

$$
\Omega(x) = \exp(i\omega(x)), \tag{C.42}
$$

where

$$
\omega^a(x) = -b\phi^a(x) \tag{C.43}
$$

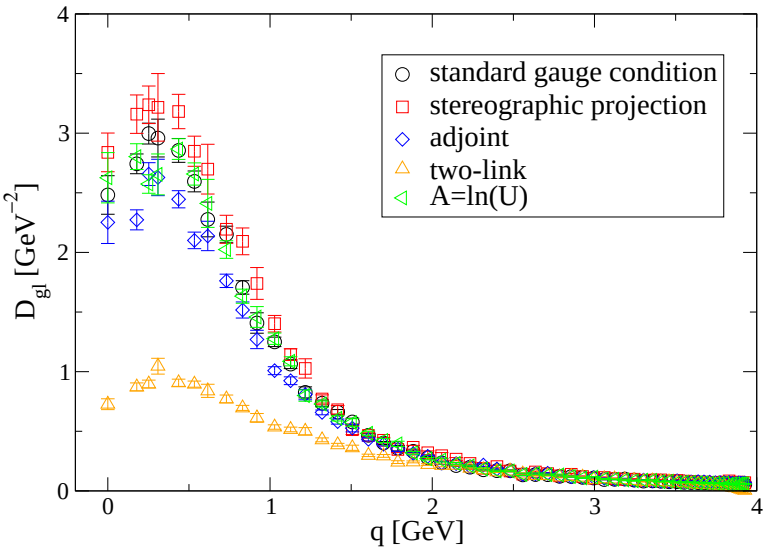

Figure C.1: Gluon propagator on a 40^3 lattice at $\beta = 2.2$ after stochastic gauge fixing for various discretizations of the gauge condition and accordingly of the gauge field.

with a positive real parameter b, whose value should be adjusted for fast convergence. (Typically, we have used values between 0.1 and 0.3.) In addition, a non-vanishing stochastic overrelaxation parameter p can be used (see sec. B.2.1.2).

C.1.3 Results

We have carried out calculations of the discretization dependence of the ghost and gluon propagator after stochastic gauge fixing only on a moderately sized three-dimensional lattice ($V = 40^3$ at $\beta = 4.2$). The results are shown in fig. C.1 for the gluon and in fig. C.2 for the ghost.[8]

For the gluon propagator D_{gl}, the results agree for all gauge field definitions except for the 'two-link' definition, eq. (C.11), see fig. C.1. We have no immediate explanation for this significant discrepancy. Note, however, that this discretization effect, even if taken at face value, would not indicate an approach to $D_{\mathrm{gl}}(0) = 0$, and thus a departure from a decoupling behavior. This is because the ratio of $D_{\mathrm{gl}}(0)$ to the maximum of $D_{\mathrm{gl}}(q)$ is not much smaller than for the other gauge conditions.

Regarding the ghost dressing function $q^2 D_{\mathrm{gh}}$ (fig. C.2), there is again one out of five gauge conditions which yields a deviating result, but this time, it is the 'adjoint' one. Again, this does not indicate a scaling behavior. On the contrary, the ghost propagator is even much less enhanced in the infrared than with the other gauge conditions, including the standard one. An immediate explanation is not at hand.

[8] We have calculated the ghost dressing functions in fig. C.2 only at small momenta (partially due to the fact that these data were produced in an early stage of the work for this thesis, when less computational resources were available). Since we do not calculate the ghost propagator at ultraviolet momenta in this case, we do not perform the usual multiplicative renormalization procedure, but simply set the dressing function at the largest momentum that is considered to the same value for all gauge conditions shown in fig. C.2.

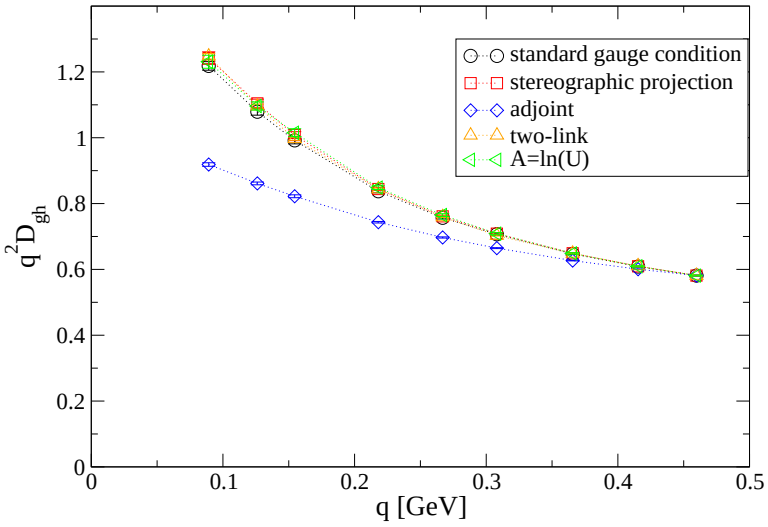

Figure C.2: Ghost dressing function on a 40^3 lattice at $\beta = 2.2$ after stochastic gauge fixing for various discretizations of the gauge condition and accordingly of the Faddeev–Popov operator.

C.2 On the Faddeev–Popov spectrum at imperfect gauge fixing

The standard lattice discretization of the Faddeev–Popov operator presupposes that the gauge fixing condition is fulfilled. This fact is evident from the derivation given in app. C.1, in particular eq. (C.17) for the standard FPO; we have briefly mentioned it already in ch. 4 (p. 80). This is reason to also take a look at that version of the FPO in which the terms that vanish only if the gauge fixing condition is satisfied are included. They are clearly indicated in eq. (C.17). Except for this addition, this is the usual FPO, i. e., derived from the usual discretization of the gauge field.

Some results for the spectrum of this modified operator from small two-dimensional lattices are shown in fig. C.3. They have been obtained both with stochastic gauge fixing and with standard gauge fixing, the latter again understood as stochastic overrelaxation at different overrelaxation parameters p (see app. B.2.1.2). Compared to fig. 4.19, obtained with the standard FPO, the spectra shown in fig. C.3 are much less sharp and less distinct from one another. The number of configurations with $\lambda_0 < 0$, i. e., outside the Gribov region, is larger than with the standard FPO. This puts the qualitative results obtained with the latter (see sec. 4.3.2) into perspective, but it does not invalidate them.

C.3 Propagators at weak coupling

We document a few results for propagators at weak coupling in three dimensions, sc. at $\beta = 12$. (These were produced in the context of a small project that was soon discontinued.) While this value of β is outside the scaling region and may lead to systematic errors, this choice also provides some insight into the dependence of the behavior of the propagators on the physical lattice size via the lattice spacing, which is notably small at such large values of β, sc. $a \approx 0.054\,\mathrm{fm}$ at $\beta = 12$.[9] This small lattice spacing contrasts with $a \approx 0.173\,\mathrm{fm}$

[9] This follows from $\sqrt{\sigma}a = 0.1197(8)$ [256] together with $\sqrt{\sigma} = 440\,\mathrm{MeV}$.

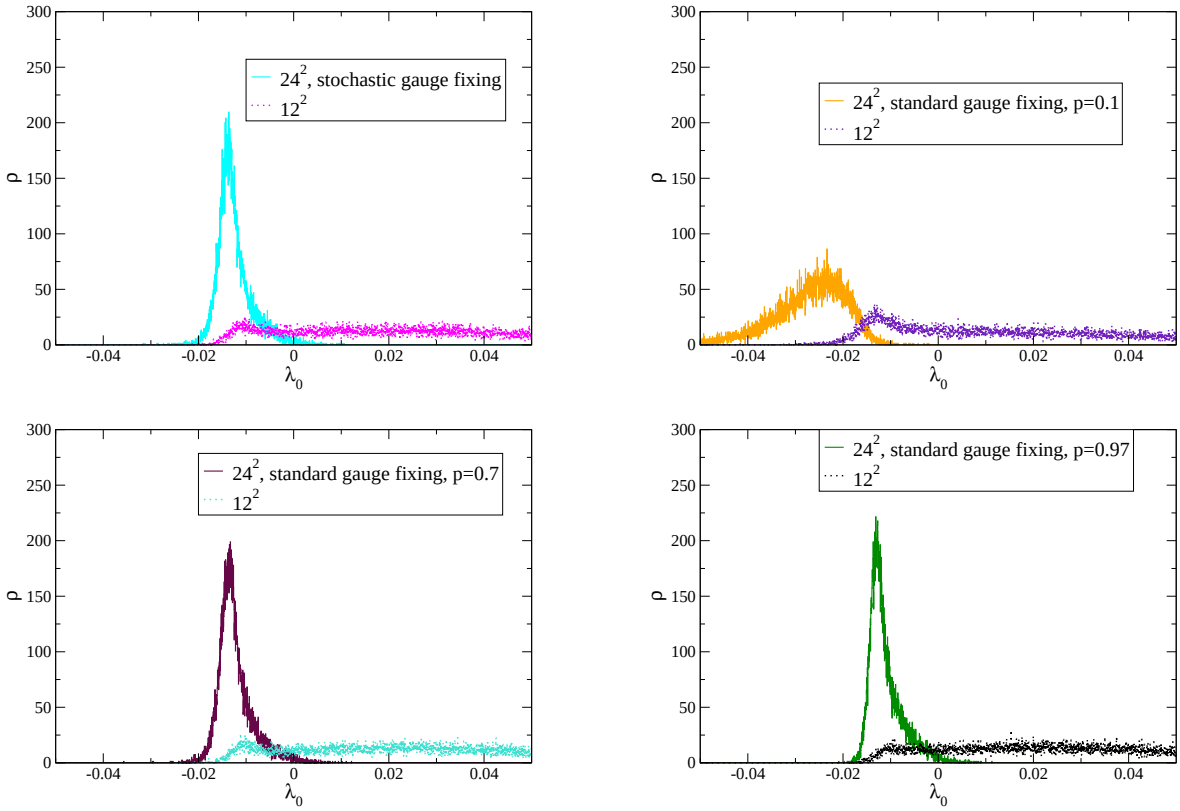

Figure C.3: Histogram of the smallest eigenvalue of a modified Faddeev–Popov operator more suitable for imperfect gauge fixing (in the sense of $\Delta^2 > 0$), obtained with stochastic quantization. This FPO is modified such that it includes also the terms that vanish if the gauge fixing condition is fulfilled.

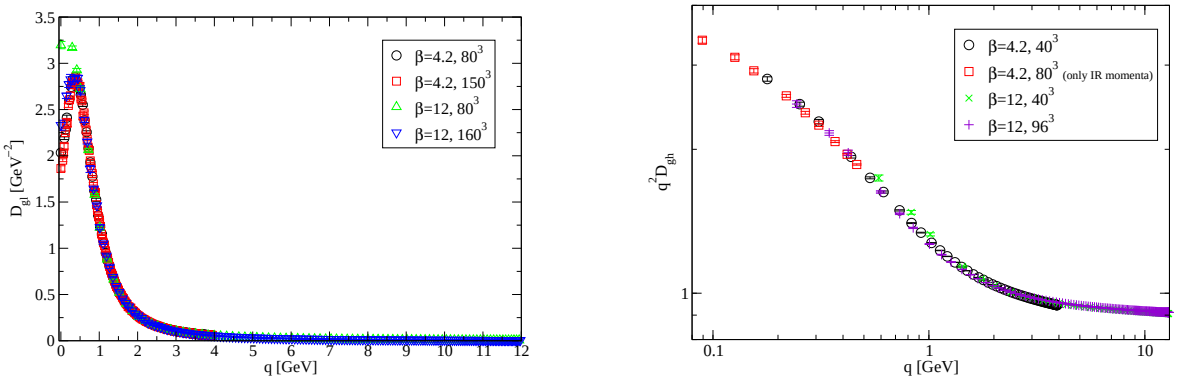

Figure C.4: Propagators at weak coupling ($\beta = 12$) compared to a usual value of the coupling ($\beta = 4.2$) with standard gauge fixing. *Left (a):* Gluon propagator. *Right (b):* Ghost dressing function.

at $\beta = 4.2$, which we usually employ in three dimensions unless we work in the strong-coupling limit.

Results are shown in fig. C.4. The gluon propagator (fig. C.4a) is clearly influenced by the small physical lattice size at $\beta = 12$. On the 80^3 lattice (with a volume of $(4.3\,\mathrm{fm})^3$), it does not even possess a peak a non-zero momenta, in contrast to the $\beta = 4.2$ case, where the 80^3 lattice has a physical volume of $(13.8\,\mathrm{fm})^3$. Concerning the ghost data (fig. C.4b), there is a small, but not completely insignificant deviation between data from different lattice sizes, surprisingly also at intermediate and large momenta. Possibly, the relatively small lattice sizes in physical units contribute to this effect.

LIST OF FIGURES

BIBLIOGRAPHY

[1] O. W. Greenberg, "Spin and Unitary Spin Independence in a Paraquark Model of Baryons and Mesons," *Phys. Rev. Lett.* **13** (1964) 598–602.

[2] M. Y. Han and Y. Nambu, "Three-triplet model with double SU(3) symmetry," *Phys. Rev.* **139** (1965) B1006–B1010.

[3] W. A. Bardeen, H. Fritzsch, and M. Gell-Mann, "Light-cone current algebra, pi0 decay, and e+ e- annihilation," in *Scale and conformal symmetry in hadron physics: proceedings*, R. Gatto, ed. New York: Wiley, 1973. `arXiv:hep-ph/0211388`.

[4] M. Gell-Mann, "A Schematic Model of Baryons and Mesons," *Phys. Lett.* **8** (1964) 214–215.

[5] E. D. Bloom *et al.*, "High-Energy Inelastic e p Scattering at 6-Degrees and 10-Degrees," *Phys. Rev. Lett.* **23** (1969) 930–934.

[6] M. Breidenbach *et al.*, "Observed Behavior of Highly Inelastic electron-Proton Scattering," *Phys. Rev. Lett.* **23** (1969) 935–939.

[7] D. J. Gross and F. Wilczek, "Asymptotically Free Gauge Theories. 1," *Phys. Rev.* **D8** (1973) 3633–3652.

[8] H. D. Politzer, "Reliable perturbative results for the strong interactions?," *Phys. Rev. Lett.* **30** (1973) 1346–1349.

[9] S. R. Coleman and D. J. Gross, "Price of asymptotic freedom," *Phys. Rev. Lett.* **31** (1973) 851–854.

[10] A. Zee, "Study of the renormalization group for small coupling constants," *Phys. Rev.* **D7** (1973) 3630–3636.

[11] G. 't Hooft, "Renormalization of Massless Yang-Mills Fields," *Nucl. Phys.* **B33** (1971) 173–199.

[12] G. 't Hooft, "Renormalizable Lagrangians for massive Yang-Mills fields," *Nucl. Phys.* **B35** (1971) 167–188.

[13] G. 't Hooft and M. J. G. Veltman, "Regularization and Renormalization of Gauge Fields," *Nucl. Phys.* **B44** (1972) 189–213.

[14] H. Fritzsch, M. Gell-Mann, and H. Leutwyler, "Advantages of the Color Octet Gluon Picture," *Phys. Lett.* **B47** (1973) 365–368.

[15] S. Weinberg, "Nonabelian Gauge Theories of the Strong Interactions," *Phys. Rev. Lett.* **31** (1973) 494–497.

[16] V. N. Gribov, "Quantization of non-Abelian gauge theories," *Nucl. Phys.* **B139** (1978) 1.

[17] D. Zwanziger, "Fundamental modular region, Boltzmann factor and area law in lattice gauge theory," *Nucl. Phys.* **B412** (1994) 657–730.

[18] D. Zwanziger, "Renormalizability of the critical limit of lattice gauge theory by BRS invariance," *Nucl. Phys.* **B399** (1993) 477–513.

[19] D. Zwanziger, "Vanishing of zero momentum lattice gluon propagator and color confinement," *Nucl. Phys.* **B364** (1991) 127–161.

[20] D. Zwanziger, "Non-perturbative Faddeev-Popov formula and infrared limit of QCD," *Phys. Rev.* **D69** (2004) 016002, `arXiv:hep-ph/0303028`.

[21] T. Kugo and I. Ojima, "Local Covariant Operator Formalism of Nonabelian Gauge Theories and Quark Confinement Problem," *Prog. Theor. Phys. Suppl.* **66** (1979) 1.

[22] T. Kugo, "The universal renormalization factors Z(1) / Z(3) and color confinement condition in non-Abelian gauge theory," in *Proceedings of International Symposium on BRS Symmetry on the Occasion of its 20th Anniversary*, M. Abe, N. Nakanishi, and I. Ojima, eds., vol. 17 of *Frontiers science series*. Tokyo: Univ. Acad. Pr., 1996. `arXiv:hep-th/9511033`.

[23] I. M. Singer, "Some Remarks on the Gribov Ambiguity," *Commun. Math. Phys.* **60** (1978) 7–12.

[24] J. M. Pawlowski, D. Spielmann, and I.-O. Stamatescu, "Lattice Landau gauge with stochastic quantisation," *Nucl. Phys.* **B830** (2010) 291–314, `arXiv:0911.4921 [hep-lat]`.

[25] A. Maas, J. M. Pawlowski, D. Spielmann, A. Sternbeck, and L. von Smekal, "Strong-coupling study of the Gribov ambiguity in lattice Landau gauge," *Eur. Phys. J.* **C68** (2010) 183–195, `arXiv:0912.4203 [hep-lat]`.

[26] M. E. Peskin and D. V. Schroeder, *An Introduction to quantum field theory*. Reading, USA: Addison-Wesley, 1995.

[27] L. H. Ryder, *Quantum field theory*. Cambridge, UK: University Press, second ed., 1996.

[28] R. Alkofer and L. von Smekal, "The infrared behavior of QCD Green's functions: Confinement, dynamical symmetry breaking, and hadrons as relativistic bound states," *Phys. Rept.* **353** (2001) 281, arXiv:hep-ph/0007355.

[29] C.-N. Yang and R. L. Mills, "Conservation of isotopic spin and isotopic gauge invariance," *Phys. Rev.* **96** (1954) 191–195.

[30] C. Becchi, A. Rouet, and R. Stora, "Renormalization of the Abelian Higgs-Kibble Model," *Commun. Math. Phys.* **42** (1975) 127–162.

[31] C. Becchi, A. Rouet, and R. Stora, "Renormalization of Gauge Theories," *Annals Phys.* **98** (1976) 287–321.

[32] I. V. Tyutin, "Gauge Invariance in Field Theory and Statistical Physics in Operator Formalism," arXiv:0812.0580 [hep-th]. Orig.: preprint of P.N. Lebedev Physical Institute, No. 39, 1975.

[33] M. Z. Iofa and I. V. Tyutin, "Gauge Invariance of Spontaneously Broken Nonabelian Theories in the Bogolyubov-Parasiuk-HEPP-Zimmerman Method," *Teor. Mat. Fiz.* **27** (1976) 38–47.

[34] L. D. Faddeev and V. N. Popov, "Feynman diagrams for the Yang-Mills field," *Phys. Lett.* **B25** (1967) 29–30.

[35] W. Pauli, "The Connection Between Spin and Statistics," *Phys. Rev.* **58** (1940) 716–722.

[36] J. Greensite, "The confinement problem in lattice gauge theory," *Prog. Part. Nucl. Phys.* **51** (2003) 1, arXiv:hep-lat/0301023.

[37] T. Regge, "Introduction to complex orbital momenta," *Nuovo Cim.* **14** (1959) 951.

[38] D. Spielmann, "Untersuchungen zum Confinement in der Sp(2)-Gittereichtheorie," 2006. Diploma thesis, University of Tübingen.

[39] M. Creutz, "Monte Carlo Study of Quantized SU(2) Gauge Theory," *Phys. Rev.* **D21** (1980) 2308–2315.

[40] G. S. Bali, "QCD forces and heavy quark bound states," *Phys. Rept.* **343** (2001) 1–136, arXiv:hep-ph/0001312.

[41] S. Necco and R. Sommer, "The N(f) = 0 heavy quark potential from short to intermediate distances," *Nucl. Phys.* **B622** (2002) 328–346, arXiv:hep-lat/0108008.

[42] K. Osterwalder and E. Seiler, "Gauge Field Theories on the Lattice," *Ann. Phys.* **110** (1978) 440.

[43] E. Seiler, "Gauge Theories as a Problem of Constructive Quantum Field Theory and Statistical Mechanics," *Lect. Notes Phys.* **159** (1982) 1–192.

[44] **STAR** Collaboration, J. Adams *et al.*, "Experimental and theoretical challenges in the search for the quark gluon plasma: The STAR collaboration's critical assessment of the evidence from RHIC collisions," *Nucl. Phys.* **A757** (2005) 102–183, arXiv:nucl-ex/0501009.

[45] **PHENIX** Collaboration, K. Adcox *et al.*, "Formation of dense partonic matter in relativistic nucleus nucleus collisions at RHIC: Experimental evaluation by the PHENIX collaboration," *Nucl. Phys.* **A757** (2005) 184–283, arXiv:nucl-ex/0410003.

[46] **BRAHMS** Collaboration, I. Arsene *et al.*, "Quark Gluon Plasma an Color Glass Condensate at RHIC? The perspective from the BRAHMS experiment," *Nucl. Phys.* **A757** (2005) 1–27, arXiv:nucl-ex/0410020.

[47] B. B. Back *et al.*, "The PHOBOS perspective on discoveries at RHIC," *Nucl. Phys.* **A757** (2005) 28–101, arXiv:nucl-ex/0410022.

[48] L. von Smekal and R. Alkofer, "What the infrared behavior of QCD Green functions can tell us about confinement in the covariant gauge," in *Quark confinement and the hadron spectrum IV: proceedings*, W. Lucha and K. M. Maung, eds. Singapore: World Scientific, 2001. arXiv:hep-ph/0009219.

[49] R. Alkofer, "QCD Green Functions and their Application to Hadron Physics," *Braz. J. Phys.* **37** (2007) 144–164, arXiv:hep-ph/0611090.

[50] E. M. Ilgenfritz, "Confinement encoded in Landau gauge gluon and ghost propagators," arXiv:0709.0200 [hep-ph].

[51] L. von Smekal, R. Alkofer, and A. Hauck, "The infrared behavior of gluon and ghost propagators in Landau gauge QCD," *Phys. Rev. Lett.* **79** (1997) 3591–3594, arXiv:hep-ph/9705242.

[52] L. von Smekal, A. Hauck, and R. Alkofer, "A solution to coupled Dyson-Schwinger equations for gluons and ghosts in Landau gauge," *Ann. Phys.* **267** (1998) 1, arXiv:hep-ph/9707327.

[53] P. Watson and R. Alkofer, "Verifying the Kugo-Ojima confinement criterion in Landau gauge QCD," *Phys. Rev. Lett.* **86** (2001) 5239, arXiv:hep-ph/0102332.

[54] C. Lerche and L. von Smekal, "On the infrared exponent for gluon and ghost propagation in Landau gauge QCD," *Phys. Rev.* **D65** (2002) 125006, arXiv:hep-ph/0202194.

[55] C. S. Fischer, R. Alkofer, and H. Reinhardt, "The elusiveness of infrared critical exponents in Landau gauge Yang-Mills theories," *Phys. Rev.* **D65** (2002) 094008, arXiv:hep-ph/0202195.

[56] C. S. Fischer and R. Alkofer, "Infrared exponents and running coupling of SU(N) Yang- Mills theories," *Phys. Lett.* **B536** (2002) 177–184, arXiv:hep-ph/0202202.

[57] R. Alkofer, C. S. Fischer, and F. J. Llanes-Estrada, "Vertex functions and infrared fixed point in Landau gauge SU(N) Yang-Mills theory," *Phys. Lett.* **B611** (2005) 279–288, arXiv:hep-th/0412330.

[58] W. Schleifenbaum, A. Maas, J. Wambach, and R. Alkofer, "Infrared behaviour of the ghost gluon vertex in Landau gauge Yang-Mills theory," *Phys. Rev.* **D72** (2005) 014017, arXiv:hep-ph/0411052.

[59] W. Schleifenbaum, M. Leder, and H. Reinhardt, "Infrared analysis of propagators and vertices of Yang-Mills theory in Landau and Coulomb gauge," *Phys. Rev.* **D73** (2006) 125019, arXiv:hep-th/0605115.

[60] P. Boucaud *et al.*, "Is the QCD ghost dressing function finite at zero momentum?," *JHEP* **06** (2006) 001, arXiv:hep-ph/0604056.

[61] A. C. Aguilar and J. Papavassiliou, "Infrared finite ghost propagator in the Feynman gauge," *Phys. Rev.* **D77** (2008) 125022, arXiv:0712.0780 [hep-ph].

[62] D. Binosi and J. Papavassiliou, "Gauge-invariant truncation scheme for the Schwinger-Dyson equations of QCD," *Phys. Rev.* **D77** (2008) 061702, arXiv:0712.2707 [hep-ph].

[63] R. Alkofer, M. Q. Huber, and K. Schwenzer, "Infrared singularities in Landau gauge Yang-Mills theory," *Phys. Rev.* **D81** (2010) 105010, arXiv:0801.2762 [hep-th].

[64] A. C. Aguilar, D. Binosi, and J. Papavassiliou, "Gluon and ghost propagators in the Landau gauge: Deriving lattice results from Schwinger-Dyson equations," *Phys. Rev.* **D78** (2008) 025010, arXiv:0802.1870 [hep-ph].

[65] P. Boucaud *et al.*, "IR finiteness of the ghost dressing function from numerical resolution of the ghost SD equation," *JHEP* **06** (2008) 012, arXiv:0801.2721 [hep-ph].

[66] P. Boucaud *et al.*, "On the IR behaviour of the Landau-gauge ghost propagator," *JHEP* **06** (2008) 099, arXiv:0803.2161 [hep-ph].

[67] D. Zwanziger, "Some exact infrared properties of gluon and ghost propagators and long-range force in QCD," arXiv:0904.2380 [hep-th].

[68] M. Q. Huber, R. Alkofer, and S. P. Sorella, "Infrared analysis of Dyson-Schwinger equations taking into account the Gribov horizon in Landau gauge," *Phys. Rev.* **D81** (2010) 065003, arXiv:0910.5604 [hep-th].

[69] M. Q. Huber, *On gauge fixing aspects of the infrared behavior of Yang- Mills Green functions*. PhD thesis, University of Graz, 2010. arXiv:1005.1775 [hep-th].

[70] A. C. Aguilar, D. Binosi, and J. Papavassiliou, "Nonperturbative gluon and ghost propagators for d=3 Yang-Mills," *Phys. Rev.* **D81** (2010) 125025, arXiv:1004.2011 [hep-ph].

[71] P. Boucaud *et al.*, "The low-momentum ghost dressing function and the gluon mass," *Phys. Rev.* **D82** (2010) 054007, arXiv:1004.4135 [hep-ph].

[72] C. S. Fischer, "Infrared properties of QCD from Dyson-Schwinger equations," *J. Phys.* **G32** (2006) R253–R291, arXiv:hep-ph/0605173.

[73] J. M. Pawlowski, D. F. Litim, S. Nedelko, and L. von Smekal, "Infrared behaviour and fixed points in Landau gauge QCD," *Phys. Rev. Lett.* **93** (2004) 152002, arXiv:hep-th/0312324.

[74] C. S. Fischer and H. Gies, "Renormalization flow of Yang-Mills propagators," *JHEP* **10** (2004) 048, arXiv:hep-ph/0408089.

[75] J. Kato, "Infrared non-perturbative propagators of gluon and ghost via exact renormalization group," arXiv:hep-th/0401068.

[76] J. M. Pawlowski, D. F. Litim, S. Nedelko, and L. von Smekal, "Signatures of confinement in Landau gauge QCD," *AIP Conf. Proc.* **756** (2005) 278–280, arXiv:hep-th/0412326.

[77] C. S. Fischer, A. Maas, and J. M. Pawlowski, "On the infrared behavior of Landau gauge Yang-Mills theory," *Annals Phys.* **324** (2009) 2408–2437, arXiv:0810.1987 [hep-ph].

[78] D. F. Litim and J. M. Pawlowski, "On gauge invariant Wilsonian flows," in *The Exact Renormalization Group: Proceedings*, A. Krasnitz, Y. A. Kubyshin, R. Potting, and P. Sa, eds. Singapore: World Scientific, 1998. arXiv:hep-th/9901063.

[79] J. M. Pawlowski, "Aspects of the functional renormalisation group," *Annals Phys.* **322** (2007) 2831–2915, arXiv:hep-th/0512261.

[80] H. Gies, "Introduction to the functional RG and applications to gauge theories," arXiv:hep-ph/0611146.

[81] Y. Igarashi, K. Itoh, and H. Sonoda, "Realization of symmetry in the ERG approach to quantum field theory," *Prog. Theor. Phys. Suppl.* **181** (2010) 1–166, arXiv:0909.0327 [hep-th].

[82] C. S. Fischer and J. M. Pawlowski, "Uniqueness of infrared asymptotics in Landau gauge Yang-Mills theory," *Phys. Rev.* **D75** (2007) 025012, arXiv:hep-th/0609009.

[83] C. S. Fischer and J. M. Pawlowski, "Uniqueness of infrared asymptotics in Landau gauge Yang-Mills theory II," *Phys. Rev.* **D80** (2009) 025023, arXiv:0903.2193 [hep-th].

[84] D. Zwanziger, "Non-perturbative Landau gauge and infrared critical exponents in QCD," *Phys. Rev.* **D65** (2002) 094039, arXiv:hep-th/0109224.

[85] D. Zwanziger, "Time-independent stochastic quantization, DS equations, and infrared critical exponents in QCD," *Phys. Rev.* **D67** (2003) 105001, arXiv:hep-th/0206053.

[86] M. Q. Huber, R. Alkofer, C. S. Fischer, and K. Schwenzer, "The infrared behavior of Landau gauge Yang-Mills theory in d=2, 3 and 4 dimensions," *Phys. Lett.* **B659** (2008) 434–440, arXiv:0705.3809 [hep-ph].

[87] M. Leder, J. M. Pawlowski, H. Reinhardt, and A. Weber, "Hamiltonian Flow in Coulomb Gauge Yang-Mills Theory," arXiv:1006.5710 [hep-th].

[88] M. Q. Huber, K. Schwenzer, and R. Alkofer, "On the infrared scaling solution of SU(N) Yang-Mills theories in the maximally Abelian gauge," *Eur. Phys. J.* **C68** (2010) 581–600, arXiv:0904.1873 [hep-th].

[89] D. Dudal, S. P. Sorella, N. Vandersickel, and H. Verschelde, "New features of the gluon and ghost propagator in the infrared region from the Gribov-Zwanziger approach," *Phys. Rev.* **D77** (2008) 071501, arXiv:0711.4496 [hep-th].

[90] D. Dudal, J. A. Gracey, S. P. Sorella, N. Vandersickel, and H. Verschelde, "A refinement of the Gribov-Zwanziger approach in the Landau gauge: infrared propagators in harmony with the lattice results," *Phys. Rev.* **D78** (2008) 065047, arXiv:0806.4348 [hep-th].

[91] S. P. Sorella, "Gribov horizon and BRST symmetry: a few remarks," *Phys. Rev.* **D80** (2009) 025013, arXiv:0905.1010 [hep-th].

[92] D. Dudal, N. Vandersickel, H. Verschelde, and S. P. Sorella, "Aspects of the Gribov-Zwanziger framework," *PoS* **QCD-TNT09** (2009) 012, arXiv:0911.0082 [hep-th].

[93] D. Dudal, O. Oliveira, and N. Vandersickel, "Indirect lattice evidence for the Refined Gribov-Zwanziger formalism and the gluon condensate $\langle A^2 \rangle$ in the Landau gauge," *Phys. Rev.* **D81** (2010) 074505, arXiv:1002.2374 [hep-lat].

[94] A. C. Aguilar and A. A. Natale, "A dynamical gluon mass solution in a coupled system of the Schwinger-Dyson equations," *JHEP* **08** (2004) 057, arXiv:hep-ph/0408254.

[95] A. C. Aguilar, D. Binosi, and J. Papavassiliou, "Infrared finite effective charge of QCD," *PoS* **LC2008** (2008) 050, arXiv:0810.2333 [hep-ph].

[96] D. Binosi and J. Papavassiliou, "Pinch Technique: Theory and Applications," *Phys. Rept.* **479** (2009) 1–152, arXiv:0909.2536 [hep-ph].

[97] A. C. Aguilar, D. Binosi, J. Papavassiliou, and J. Rodriguez-Quintero, "Non-perturbative comparison of QCD effective charges," *Phys. Rev.* **D80** (2009) 085018, arXiv:0906.2633 [hep-ph].

[98] J. M. Cornwall, "Dynamical Mass Generation in Continuum QCD," *Phys. Rev.* **D26** (1982) 1453.

[99] C. S. Fischer, A. Maas, and J. M. Pawlowski, "Aspects of confinement from QCD correlation functions," *PoS* **CONFINEMENT8** (2008) 043, arXiv:0812.2745 [hep-ph].

[100] K.-I. Kondo, "Kugo-Ojima color confinement criterion and Gribov- Zwanziger horizon condition," *Phys. Lett.* **B678** (2009) 322–330, arXiv:0904.4897 [hep-th].

[101] K.-I. Kondo, "Infrared behavior of the ghost propagator in the Landau gauge Yang-Mills theory," *Prog. Theor. Phys.* **122** (2010) 1455–1475, arXiv:0907.3249 [hep-th].

[102] K.-I. Kondo, "Decoupling and scaling solutions in Yang-Mills theory with the Gribov horizon," arXiv:0909.4866 [hep-th].

[103] K.-I. Kondo, "Gribov-Zwanziger horizon condition, ghost and gluon propagators and Kugo-Ojima confinement criterion," *PoS* **QCD-TNT09** (2009) 021, arXiv:0911.2880 [hep-th].

[104] A. Maas, "Constructing non-perturbative gauges using correlation functions," *Phys. Lett.* **B689** (2010) 107–111, arXiv:0907.5185 [hep-lat].

[105] M. Tissier and N. Wschebor, "Infrared propagators of Yang-Mills theory from perturbation theory," arXiv:1004.1607 [hep-ph].

[106] J. Rodriguez-Quintero, "On the massive gluon propagator, the PT-BFM scheme and the low-momentum behaviour of decoupling and scaling DSE solutions," arXiv:1005.4598 [hep-ph].

[107] L. von Smekal, "Landau Gauge QCD: Functional Methods versus Lattice Simulations," arXiv:0812.0654 [hep-th].

[108] D. Atkinson and J. C. R. Bloch, "Running coupling in non-perturbative QCD. I: Bare vertices and y-max approximation," *Phys. Rev.* **D58** (1998) 094036, arXiv:hep-ph/9712459.

[109] D. Atkinson and J. C. R. Bloch, "QCD in the infrared with exact angular integrations," *Mod. Phys. Lett.* **A13** (1998) 1055–1062, arXiv:hep-ph/9802239.

[110] J. C. Taylor, "Ward Identities and Charge Renormalization of the Yang- Mills Field," *Nucl. Phys.* **B33** (1971) 436–444.

[111] W. J. Marciano and H. Pagels, "Quantum Chromodynamics: A Review," *Phys. Rept.* **36** (1978) 137.

[112] A. Cucchieri, T. Mendes, and A. Mihara, "Numerical study of the ghost-gluon vertex in Landau gauge," *JHEP* **12** (2004) 012, arXiv:hep-lat/0408034.

[113] J. C. R. Bloch, A. Cucchieri, K. Langfeld, and T. Mendes, "Propagators and running coupling from SU(2) lattice gauge theory," *Nucl. Phys.* **B687** (2004) 76–100, arXiv:hep-lat/0312036.

[114] E. M. Ilgenfritz, M. Müller-Preussker, A. Sternbeck, and A. Schiller, "Gauge-variant propagators and the running coupling from lattice QCD," arXiv:hep-lat/0601027.

[115] A. Cucchieri, A. Maas, and T. Mendes, "Exploratory study of three-point Green's functions in Landau-gauge Yang-Mills theory," *Phys. Rev.* **D74** (2006) 014503, arXiv:hep-lat/0605011.

[116] A. Maas, "Two- and three-point Green's functions in two-dimensional Landau-gauge Yang-Mills theory," *Phys. Rev.* **D75** (2007) 116004, arXiv:0704.0722 [hep-lat].

[117] R. Alkofer, C. S. Fischer, M. Q. Huber, and K. Schwenzer, "Lower dimensional Yang-Mills theory as a laboratory to study the infrared regime," *POS* **LAT2007** (2007) 329, arXiv:0710.1054 [hep-ph].

[118] A. Eichhorn, H. Gies, and J. M. Pawlowski, "Gluon condensation and scaling exponents for the propagators in Yang-Mills theory," arXiv:1010.2153 [hep-ph].

[119] J. Braun, H. Gies, and J. M. Pawlowski, "Quark Confinement from Color Confinement," *Phys. Lett.* **B684** (2010) 262–267, arXiv:0708.2413 [hep-th].

[120] J. Braun, L. M. Haas, F. Marhauser, and J. M. Pawlowski, "On the relation of quark confinement and chiral symmetry breaking," arXiv:0908.0008 [hep-ph].

[121] C. S. Fischer and J. A. Mueller, "Chiral and deconfinement transition from Dyson-Schwinger equations," *Phys. Rev.* **D80** (2009) 074029, arXiv:0908.0007 [hep-ph].

[122] V. G. Bornyakov, V. K. Mitrjushkin, and M. Müller-Preussker, "SU(2) lattice gluon propagator: continuum limit, finite- volume effects and infrared mass scale m_{IR}," *Phys. Rev.* **D81** (2010) 054503, arXiv:0912.4475 [hep-lat].

[123] M. Blank, A. Krassnigg, and A. Maas, "Aspects of gauge-(in)dependence in Bethe-Salpeter-equation studies of mesons," arXiv:1007.3901 [hep-ph].

[124] J. E. Mandula and M. Ogilvie, "The Gluon Is Massive: A Lattice Calculation of the Gluon Propagator in the Landau Gauge," *Phys. Lett.* **B185** (1987) 127–132.

[125] G. Parisi and R. Petronzio, "On Low-Energy Tests of QCD," *Phys. Lett.* **B94** (1980) 51.

[126] J. H. Field, "A phenomenological analysis of gluon mass effects in inclusive radiative decays of the J/psi and Upsilon," *Phys. Rev.* **D66** (2002) 013013, arXiv:hep-ph/0101158.

[127] A. A. Natale, "QCD phenomenology with infrared finite SDE solutions," *PoS* **QCD-TNT09** (2009) 031, arXiv:0910.5689 [hep-ph].

[128] A. C. Aguilar and J. Papavassiliou, "Gluon mass generation without seagull divergences," *Phys. Rev.* **D81** (2010) 034003, arXiv:0910.4142 [hep-ph].

[129] A. Cucchieri and T. Mendes, "Propagators, running coupling and condensates in lattice QCD," *Braz. J. Phys.* **37** (2007) 484–493, hep-ph/0605224.

[130] O. Oliveira and P. Bicudo, "Running Gluon Mass from Landau Gauge Lattice QCD Propagator," arXiv:1002.4151 [hep-lat].

[131] J. Greensite, "Center vortices, and other scenarios of quark confinement," *Eur. Phys. J. ST* **140** (2007) 1–52.

[132] R. Alkofer and J. Greensite, "Quark Confinement: The Hard Problem of Hadron Physics," *J. Phys.* **G34** (2007) S3, arXiv:hep-ph/0610365.

[133] C. Feuchter and H. Reinhardt, "Quark and gluon confinement in Coulomb gauge," arXiv:hep-th/0402106.

[134] J. Greensite, S. Olejnik, and D. Zwanziger, "Center vortices and the Gribov horizon," *JHEP* **05** (2005) 070, arXiv:hep-lat/0407032.

[135] K. Langfeld and L. Moyaerts, "Propagators in Coulomb gauge from SU(2) lattice gauge theory," *Phys. Rev.* **D70** (2004) 074507, arXiv:hep-lat/0406024.

[136] A. Cucchieri, "Lattice Results in Coulomb Gauge," *AIP Conf. Proc.* **892** (2007) 22–28, arXiv:hep-lat/0612004.

[137] M. Quandt, G. Burgio, S. Chimchinda, and H. Reinhardt, "Coulomb gauge Green functions and Gribov copies in SU(2) lattice gauge theory," *PoS* **LAT2007** (2007) 325, arXiv:0710.0549 [hep-lat].

[138] A. Voigt, E. M. Ilgenfritz, M. Müller-Preussker, and A. Sternbeck, "The effective Coulomb potential in SU(3) lattice Yang- Mills theory," *Phys. Rev.* **D78** (2008) 014501, arXiv:0803.2307 [hep-lat].

[139] G. 't Hooft, "On the Phase Transition Towards Permanent Quark Confinement," *Nucl. Phys.* **B138** (1978) 1.

[140] G. 't Hooft, "A Property of Electric and Magnetic Flux in Nonabelian Gauge Theories," *Nucl. Phys.* **B153** (1979) 141.

[141] G. Mack, "Predictions of a theory of quark confinement," *Phys. Rev. Lett.* **45** (1980) 1378.

[142] H. B. Nielsen and P. Olesen, "A Quantum Liquid Model for the QCD Vacuum: Gauge and Rotational Invariance of Domained and Quantized Homogeneous Color Fields," *Nucl. Phys.* **B160** (1979) 380.

[143] J. Ambjorn and P. Olesen, "On the Formation of a Random Color Magnetic Quantum Liquid in QCD," *Nucl. Phys.* **B170** (1980) 60.

[144] J. Ambjorn and P. Olesen, "A Color Magnetic Vortex Condensate in QCD," *Nucl. Phys.* **B170** (1980) 265.

[145] L. Del Debbio, M. Faber, J. Giedt, J. Greensite, and S. Olejnik, "Detection of center vortices in the lattice Yang-Mills vacuum," *Phys. Rev.* **D58** (1998) 094501, arXiv:hep-lat/9801027.

[146] P. de Forcrand and M. D'Elia, "On the relevance of center vortices to QCD," *Phys. Rev. Lett.* **82** (1999) 4582–4585, arXiv:hep-lat/9901020.

[147] K. Langfeld, H. Reinhardt, and J. Gattnar, "Gluon propagators and quark confinement," *Nucl. Phys.* **B621** (2002) 131–156, arXiv:hep-ph/0107141.

[148] K. Langfeld, "Vortex induced confinement and the Kugo-Ojima confinement criterion," in *Confinement, topology, and other non-perturbative aspects of QCD: proceedings*, J. Greensite and S. Olejnik, eds. Dordrecht: Kluwer, 2002. arXiv:hep-lat/0204025.

[149] K. Langfeld, H. Reinhardt, and O. Tennert, "Confinement and scaling of the vortex vacuum of SU(2) lattice gauge theory," *Phys. Lett.* **B419** (1998) 317–321, arXiv:hep-lat/9710068.

[150] K. Langfeld, "Vortex structures in pure SU(3) lattice gauge theory," *Phys. Rev.* **D69** (2004) 014503, arXiv:hep-lat/0307030.

[151] L. Del Debbio, M. Faber, J. Greensite, and S. Olejnik, "Center dominance and Z(2) vortices in SU(2) lattice gauge theory," *Phys. Rev.* **D55** (1997) 2298–2306, arXiv:hep-lat/9610005.

[152] K. Langfeld, O. Tennert, M. Engelhardt, and H. Reinhardt, "Center vortices of Yang-Mills theory at finite temperatures," *Phys. Lett.* **B452** (1999) 301, arXiv:hep-lat/9805002.

[153] M. Engelhardt, K. Langfeld, H. Reinhardt, and O. Tennert, "Deconfinement in SU(2) Yang-Mills theory as a center vortex percolation transition," *Phys. Rev.* **D61** (2000) 054504, arXiv:hep-lat/9904004.

[154] J. Gattnar, K. Langfeld, A. Schäfke, and H. Reinhardt, "Center-vortex dominance after dimensional reduction of SU(2) lattice gauge theory," *Phys. Lett.* **B489** (2000) 251–258, arXiv:hep-lat/0005016.

[155] V. G. Bornyakov, D. A. Komarov, and M. I. Polikarpov, "P-vortices and drama of Gribov copies," *Phys. Lett.* **B497** (2001) 151–158, arXiv:hep-lat/0009035.

[156] K. Holland, M. Pepe, and U. J. Wiese, "The deconfinement phase transition of Sp(2) and Sp(3) Yang-Mills theories in 2+1 and 3+1 dimensions," *Nucl. Phys.* **B694** (2004) 35–58, arXiv:hep-lat/0312022.

[157] M. Pepe and U. J. Wiese, "Exceptional Deconfinement in G(2) Gauge Theory," *Nucl. Phys.* **B768** (2007) 21–37, arXiv:hep-lat/0610076.

[158] S. Mandelstam, "Vortices and Quark Confinement in Nonabelian Gauge Theories," *Phys. Rept.* **23** (1976) 245–249.

[159] Y. Nambu, "Strings, monopoles, and gauge fields," *Phys. Rev.* **D10** (1974) 4262.

[160] G. 't Hooft, "Gauge theories with unified weak, electromagnetic, and strong interactions," in *Palermo 1975, Proceedings, High energy physics, vol. 2*. Bologna: Ed. Compositori, 1975. Repr. in: 't Hooft, G. (ed.): Under the spell of the gauge principle. Singapore: World Scientific, 1994.

[161] G. 't Hooft, "Topology of the Gauge Condition and New Confinement Phases in Nonabelian Gauge Theories," *Nucl. Phys.* **B190** (1981) 455.

[162] E.-M. Ilgenfritz, S. Thurner, H. Markum, and M. Müller-Preussker, "Monopole characteristics in various Abelian gauges," *Phys. Rev.* **D61** (2000) 054501, arXiv:hep-lat/9904010.

[163] J. D. Stack, W. W. Tucker, and R. J. Wensley, "The maximal abelian gauge, monopoles, and vortices in SU(3) lattice gauge theory," *Nucl. Phys.* **B639** (2002) 203–222.

[164] J. Greensite, S. Olejnik, and D. Zwanziger, "Coulomb energy, remnant symmetry, and the phases of non-Abelian gauge theories," *Phys. Rev.* **D69** (2004) 074506, arXiv:hep-lat/0401003.

[165] S. Weinberg, *The quantum theory of fields. Vol. 2: Modern applications*. Cambridge, UK: University Press, 1996.

[166] M. Srednicki, *Quantum field theory*. Cambridge, UK: University Press, 2007.

[167] N. Nakanishi and I. Ojima, "Covariant operator formalism of gauge theories and quantum gravity," *World Sci. Lect. Notes Phys.* **27** (1990) 1–434.

[168] S. N. Gupta, "Theory of longitudinal photons in quantum electrodynamics," *Proc. Phys. Soc.* **A63** (1950) 681–691.

[169] K. Bleuler, "A New method of treatment of the longitudinal and scalar photons," *Helv. Phys. Acta* **23** (1950) 567–586.

[170] S. Furui and H. Nakajima, "Infrared features of the Landau gauge QCD," *Phys. Rev.* **D69** (2004) 074505, arXiv:hep-lat/0305010.

[171] S. Furui and H. Nakajima, "Infrared features of KS fermion and Wilson fermion in Lattice Landau Gauge QCD," *Few Body Syst.* **40** (2006) 101–128, arXiv:hep-lat/0503029.

[172] S. Furui and H. Nakajima, "Correlation of the ghost and the quark in the lattice Landau gauge QCD," *Braz. J. Phys.* **37** (2007) 186–192, arXiv:hep-lat/0609024.

[173] A. Sternbeck, *The infrared behavior of lattice QCD Green's functions*. PhD thesis, Humboldt University of Berlin, 2006. arXiv:hep-lat/0609016.

[174] D. Zwanziger, "Nonperturbative modification of the Faddeev-Popov formula and banishment of the naive vacuum," *Nucl. Phys.* **B209** (1982) 336.

[175] M. A. L. Capri, A. J. Gomez, M. S. Guimaraes, V. E. R. Lemes, and S. P. Sorella, "Study of the properties of the Gribov region in SU(N) Euclidean Yang-Mills theories in the maximal Abelian gauge," *J. Phys.* **A43** (2010) 245402, arXiv:1002.1659 [hep-th].

[176] G. Dell'Antonio and D. Zwanziger, "Every gauge orbit passes inside the Gribov horizon," *Commun. Math. Phys.* **138** (1991) 291.

[177] M. A. Semenov-Tian-Shansky and V. A. Franke, "A variational principle for the Lorentz condition and restriction of the domain of path integration in non-Abelian gauge theories," *J. Sov. Math.* **34** (1986) 1999. (Orig.: Zap. Nauch. Sem. Leningrad. Otdeleniya Mat. Inst. im. V. A. Steklov AN SSSR **120**:159, 1982).

[178] G. Dell'Antonio and D. Zwanziger, "All gauge orbits and some Gribov copies encompassed by the Gribov horizon," in *Proceedings of the NATO advanced workshop on probabilistic methods in quantum field theory and quantum gravity, Cargèse*, P. Damgaard, H. Hüffel, and A. Rosenblum, eds. New York: Plenum, 1989.

[179] P. van Baal, "More (thoughts on) Gribov copies," *Nucl. Phys.* **B369** (1992) 259–275.

[180] G. Esposito, D. N. Pelliccia, and F. Zaccaria, "Gribov problem for gauge theories: A pedagogical introduction," *Int. J. Geom. Meth. Mod. Phys.* **1** (2004) 423–441, arXiv:hep-th/0404240.

[181] P. van Baal, "Gribov ambiguities and the fundamental domain," in *Confinement, duality, and nonperturbative aspects of QCD: proceedings*, P. van Baal, ed. New York, N.Y.: Plenum Press, 1998. arXiv:hep-th/9711070.

[182] P. van Baal and B. van den Heuvel, "Zooming in on the SU(2) fundamental domain," *Nucl. Phys.* **B417** (1994) 215–237, arXiv:hep-lat/9310005.

[183] P. van Baal, "Global issues in gauge fixing," in *Nonperturbative approaches to quantum chromodynamics: proceedings*, D. Diakonov, ed. 1995. arXiv:hep-th/9511119.

[184] J. A. Gracey, "One loop gluon form factor and freezing of alpha(s) in the Gribov-Zwanziger QCD Lagrangian," *JHEP* **05** (2006) 052, arXiv:hep-ph/0605077.

[185] D. Zwanziger, "Goldstone bosons and fermions in QCD," *Phys. Rev.* **D81** (2010) 125027, arXiv:1003.1080 [hep-ph].

[186] D. Zwanziger, "Local and renormalizable action from the Gribov horizon," *Nucl. Phys.* **B323** (1989) 513–544.

[187] D. Dudal, R. F. Sobreiro, S. P. Sorella, and H. Verschelde, "The Gribov parameter and the dimension two gluon condensate in Euclidean Yang-Mills theories in the Landau gauge," *Phys. Rev.* **D72** (2005) 014016, arXiv:hep-th/0502183.

[188] D. Dudal, S. P. Sorella, and N. Vandersickel, "More on the renormalization of the horizon function of the Gribov-Zwanziger action and the Kugo-Ojima Green function(s)," *Eur. Phys. J.* **C68** (2010) 283–298, arXiv:1001.3103 [hep-th].

[189] D. Dudal, J. A. Gracey, S. P. Sorella, N. Vandersickel, and H. Verschelde, "The Landau gauge gluon and ghost propagator in the refined Gribov-Zwanziger framework in 3 dimensions," *Phys. Rev.* **D78** (2008) 125012, arXiv:0808.0893 [hep-th].

[190] D. Dudal, S. P. Sorella, N. Vandersickel, and H. Verschelde, "The effects of Gribov copies in 2D gauge theories," *Phys. Lett.* **B680** (2009) 377–383, arXiv:0808.3379 [hep-th].

[191] S. P. Sorella, "Pathways to Confinement," arXiv:1006.4500 [hep-th].

[192] J. A. Gracey, "Alternative refined Gribov-Zwanziger Lagrangian," arXiv:1009.3889 [hep-th].

[193] K.-I. Kondo, "The nilpotent 'BRST' symmetry for the Gribov-Zwanziger theory," arXiv:0905.1899 [hep-th].

[194] L. Baulieu *et al.*, "Gribov horizon and i-particles: about a toy model and the construction of physical operators," *Phys. Rev.* **D82** (2010) 025021, arXiv:0912.5153 [hep-th].

[195] S. P. Sorella *et al.*, "Gribov horizon and BRST symmetry: a pathway to confinement," arXiv:1003.0086 [hep-th].

[196] D. Dudal, S. P. Sorella, N. Vandersickel, and H. Verschelde, "Gribov no-pole condition, Zwanziger horizon function, Kugo-Ojima confinement criterion, boundary conditions, BRST breaking and all that," *Phys. Rev.* **D79** (2009) 121701, arXiv:0904.0641 [hep-th].

[197] S. Mandelstam, "Approximation Scheme for QCD," *Phys. Rev.* **D20** (1979) 3223.

[198] D. Atkinson, J. K. Drohm, P. W. Johnson, and K. Stam, "Nonperturbative confinement in quantum chromodynamics. 1. Study of an approximate equation of Mandelstam," *J. Math. Phys.* **22** (1981) 2704.

[199] D. Atkinson, P. W. Johnson, and K. Stam, "Nonperturbative confinement in quantum chromodynamics. 2. Mandelstam's gluon propagator," *J. Math. Phys.* **23** (1982) 1917.

[200] N. Brown and M. R. Pennington, "Studies of Confinement: How the Gluon Propagates," *Phys. Rev.* **D39** (1989) 2723.

[201] A. Hauck, L. von Smekal, and R. Alkofer, "Solving the gluon Dyson-Schwinger equation in the Mandelstam approximation," *Comput. Phys. Commun.* **112** (1998) 149, arXiv:hep-ph/9604430.

[202] G. B. West, "Confinement, the Wilson loop and the gluon propagator," *Phys. Lett.* **B115** (1982) 468.

[203] J. Braun, A. Eichhorn, H. Gies, and J. M. Pawlowski, "On the Nature of the Phase Transition in SU(N), Sp(2) and E(7) Yang-Mills theory," arXiv:1007.2619 [hep-ph].

[204] A. Sternbeck, E. M. Ilgenfritz, M. Müller-Preussker, A. Schiller, and I. L. Bogolubsky, "Lattice study of the infrared behavior of QCD Green's functions in Landau gauge," *PoS* **LAT2006** (2006) 076, arXiv:hep-lat/0610053.

[205] P. O. Bowman *et al.*, "Scaling behavior and positivity violation of the gluon propagator in full QCD," *Phys. Rev.* **D76** (2007) 094505, arXiv:hep-lat/0703022.

[206] A. Cucchieri, T. Mendes, and A. R. Taurines, "Positivity violation for the lattice Landau gluon propagator," *Phys. Rev.* **D71** (2005) 051902, arXiv:hep-lat/0406020.

[207] **UKQCD** Collaboration, D. B. Leinweber, J. I. Skullerud, A. G. Williams, and C. Parrinello, "Gluon propagator in the infrared region," *Phys. Rev.* **D58** (1998) 031501, arXiv:hep-lat/9803015.

[208] F. D. R. Bonnet, P. O. Bowman, D. B. Leinweber, and A. G. Williams, "Infrared behavior of the gluon propagator on a large volume lattice," *Phys. Rev.* **D62** (2000) 051501, arXiv:hep-lat/0002020.

[209] P. Marenzoni, G. Martinelli, and N. Stella, "The Gluon propagator on a large volume, at beta = 6.0," *Nucl. Phys.* **B455** (1995) 339–356, arXiv:hep-lat/9410011.

[210] A. Nakamura, H. Aiso, M. Fukuda, T. Iwamiya, T. Nakamura, and M. Yoshida, "Gluon propagators and confinement," in *Confinement 95: proceedings*, H. Toki, Y. Mizuno, H. Suganuma, T. Suzuki, and O. Miyamura, eds. River Edge, N.J.: World Scientific, 1995. arXiv:hep-lat/9506024.

[211] C. W. Bernard, C. Parrinello, and A. Soni, "The Gluon propagator in momentum space," *Nucl. Phys. Proc. Suppl.* **30** (1993) 535–538, arXiv:hep-lat/9211020.

[212] P. Marenzoni, G. Martinelli, N. Stella, and M. Testa, "High statistics study of the gluon propagator in the Landau gauge at beta = 6.0," *Phys. Lett.* **B318** (1993) 511–516.

[213] R. Alkofer, W. Detmold, C. S. Fischer, and P. Maris, "Analytic properties of the Landau gauge gluon and quark propagators," *Phys. Rev.* **D70** (2004) 014014, arXiv:hep-ph/0309077.

[214] K. G. Wilson, "Confinement of quarks," *Phys. Rev.* **D10** (1974) 2445–2459.

[215] M. Creutz, *Quarks, gluons and lattices*. Cambridge, UK: University Press, 1983.

[216] I. Montvay and G. Münster, *Quantum fields on a lattice*. Cambridge, UK: University Press, 1994.

[217] J. Smit, "Introduction to quantum fields on a lattice: A robust mate," *Cambridge Lect. Notes Phys.* **15** (2002) 1–271.

[218] H. J. Rothe, "Lattice gauge theories: An Introduction," *World Sci. Lect. Notes Phys.* **74** (2005) 1–605.

[219] C. Gattringer and C. B. Lang, "Quantum chromodynamics on the lattice," *Lect. Notes Phys.* **788** (2010) 1–211.

[220] L. Giusti, M. L. Paciello, C. Parrinello, S. Petrarca, and B. Taglienti, "Problems on lattice gauge fixing," *Int. J. Mod. Phys.* **A16** (2001) 3487–3534, arXiv:hep-lat/0104012.

[221] A. Sternbeck and L. von Smekal, "Infrared exponents and the strong-coupling limit in lattice Landau gauge," *Eur. Phys. J.* **C68** (2010) 487–503, arXiv:0811.4300 [hep-lat].

[222] F. J. Wegner, "Duality in Generalized Ising Models and Phase Transitions without Local Order Parameters," *J. Math. Phys.* **12** (1971) 2259–2272.

[223] R. Sommer, "A New way to set the energy scale in lattice gauge theories and its applications to the static force and alpha-s in SU(2) Yang-Mills theory," *Nucl. Phys.* **B411** (1994) 839–854, arXiv:hep-lat/9310022.

[224] C. G. Callan, Jr., "Broken scale invariance in scalar field theory," *Phys. Rev.* **D2** (1970) 1541–1547.

[225] K. Symanzik, "Small distance behavior in field theory and power counting," *Commun. Math. Phys.* **18** (1970) 227–246.

[226] S. Bethke, "The 2009 World Average of $\alpha_s(M_Z)$," *Eur. Phys. J.* **C64** (2009) 689–703, arXiv:0908.1135 [hep-ph].

[227] S. R. Coleman and E. J. Weinberg, "Radiative Corrections as the Origin of Spontaneous Symmetry Breaking," *Phys. Rev.* **D7** (1973) 1888–1910.

[228] K. G. Wilson, "Monte Carlo calculations for the lattice gauge theory," *NATO Adv. Study Inst. Ser. B Phys.* **59** (1980) 363–402.

[229] E. Marinari, C. Parrinello, and R. Ricci, "Evidence for the existence of Gribov copies in Landau gauge lattice QCD," *Nucl. Phys.* **B362** (1991) 487–497.

[230] F. Barahona, "On the computational complexity of Ising spin glass models," *J. Phys.* **A15** (1982) .

[231] D. Mehta, A. Sternbeck, L. von Smekal, and A. G. Williams, "Lattice Landau Gauge and Algebraic Geometry," *PoS* **QCD-TNT09** (2009) :025, arXiv:0912.0450 [hep-lat].

[232] P. Hirschfeld, "Strong evidence that Gribov copying does not affect gauge theory functional integral," *Nucl. Phys.* **B157** (1979) 37.

[233] H. Neuberger, "Nonperturbative BRS invariance," *Phys. Lett.* **B175** (1986) 69.

[234] H. Neuberger, "Nonperturbative BRS invariance and the Gribov problem," *Phys. Lett.* **B183** (1987) 337.

[235] L. von Smekal, D. Mehta, A. Sternbeck, and A. G. Williams, "Modified Lattice Landau Gauge," *PoS* **LAT2007** (2007) 382, arXiv:0710.2410 [hep-lat].

[236] L. von Smekal, M. Ghiotti, and A. G. Williams, "Decontracted double BRST on the lattice," *Phys. Rev.* **D78** (2008) 085016, arXiv:0807.0480 [hep-th].

[237] L. von Smekal, A. Jorkowski, D. Mehta, and A. Sternbeck, "Lattice Landau gauge via Stereographic Projection," *PoS* **CONFINEMENT8** (2008) 048, arXiv:0812.2992 [hep-th].

[238] M. Testa, "Lattice gauge fixing, Gribov copies and BRST symmetry," *Phys. Lett.* **B429** (1998) 349–353, arXiv:hep-lat/9803025.

[239] M. Schaden, "Equivariant gauge fixing of SU(2) lattice gauge theory," *Phys. Rev.* **D59** (1999) 014508, arXiv:hep-lat/9805020.

[240] **UKQCD** Collaboration, D. B. Leinweber, J. I. Skullerud, A. G. Williams, and C. Parrinello, "Asymptotic scaling and infrared behavior of the gluon propagator," *Phys. Rev.* **D60** (1999) 094507, arXiv:hep-lat/9811027.

[241] F. de Soto and C. Roiesnel, "On the reduction of hypercubic lattice artifacts," *JHEP* **09** (2007) 007, arXiv:0705.3523 [hep-lat].

[242] A. Cucchieri, "Gribov copies in the minimal Landau gauge: The influence on gluon and ghost propagators," *Nucl. Phys.* **B508** (1997) 353–370, hep-lat/9705005.

[243] L. Lorenz, "On the identity of the vibrations of light with electrical currents," *Phil. Mag.* **34** (1867) 287.

[244] A. Cucchieri, "Infrared behavior of the gluon propagator in lattice Landau gauge: The three-dimensional case," *Phys. Rev.* **D60** (1999) 034508, arXiv:hep-lat/9902023.

[245] J. Gattnar, *Aspects of confinement in lattice gauge field theory*. PhD thesis, University of Tübingen, 2005.

[246] D. Zwanziger, "Vanishing color magnetization in lattice Landau and Coulomb gauges," *Phys. Lett.* **B257** (1991) 168–172.

[247] H. Suman and K. Schilling, "First Lattice Study of Ghost Propagators in SU(2) and SU(3) Gauge Theories," *Phys. Lett.* **B373** (1996) 314–318, arXiv:hep-lat/9512003.

[248] P. Boucaud *et al.*, "Asymptotic behavior of the ghost propagator in SU3 lattice gauge theory," *Phys. Rev.* **D72** (2005) 114503, arXiv:hep-lat/0506031.

[249] **TXL** Collaboration, G. S. Bali *et al.*, "Glueballs and string breaking from full QCD," *Nucl. Phys. Proc. Suppl.* **63** (1998) 209–211, arXiv:hep-lat/9710012.

[250] E. Seiler, "Upper bound on the color-confining potential," *Phys. Rev.* **D18** (1978) 482.

[251] C. Bachas, "Convexity of the quarkonium potential," *Phys. Rev.* **D33** (1986) 2723.

[252] **APE** Collaboration, M. Albanese *et al.*, "Glueball Masses and String Tension in Lattice QCD," *Phys. Lett.* **B192** (1987) 163–169.

[253] R. Balian, J. M. Drouffe, and C. Itzykson, "Gauge Fields on a Lattice. 1. General Outlook," *Phys. Rev.* **D10** (1974) 3376.

[254] H. G. Dosch and V. F. Müller, "Lattice gauge theory in two space-time dimensions," *Fortschr. Phys.* **27** (1979) 547.

[255] G. Mack, "Confinement of static quarks in two-dimensional lattice gauge theories," *Commun. Math. Phys.* **65** (1979) 91.

[256] M. J. Teper, "SU(N) gauge theories in 2+1 dimensions," *Phys. Rev.* **D59** (1999) 014512, arXiv:hep-lat/9804008.

[257] P. Majumdar, "The string spectrum from large Wilson loops," *Nucl. Phys.* **B664** (2003) 213–232, arXiv:hep-lat/0211038.

[258] A. Cucchieri, T. Mendes, and A. R. Taurines, "SU(2) Landau gluon propagator on a 140^3 lattice," *Phys. Rev.* **D67** (2003) 091502, arXiv:hep-lat/0302022.

[259] M. Caselle, M. Pepe, and A. Rago, "Static quark potential and effective string corrections in the (2+1)-d SU(2) Yang-Mills theory," *JHEP* **10** (2004) 005, arXiv:hep-lat/0406008.

[260] J. Fingberg, U. M. Heller, and F. Karsch, "Scaling and asymptotic scaling in the SU(2) gauge theory," *Nucl. Phys.* **B392** (1993) 493–517, arXiv:hep-lat/9208012.

[261] J. Engels, J. Fingberg, and M. Weber, "Finite size scaling analysis of SU(2) lattice gauge theory in (3+1) dimensions," *Nucl. Phys.* **B332** (1990) 737.

[262] E. Marinari, M. L. Paciello, and B. Taglienti, "The String tension in gauge theories," *Int. J. Mod. Phys.* **A10** (1995) 4265–4310, arXiv:hep-lat/9503027.

[263] G. Burgio, M. Quandt, and H. Reinhardt, "BRST symmetry vs. Horizon condition in Yang-Mills theories," *Phys. Rev.* **D81** (2010) 074502, arXiv:0911.5101 [hep-lat].

[264] C. W. Bernard, C. Parrinello, and A. Soni, "A Lattice study of the gluon propagator in momentum space," *Phys. Rev.* **D49** (1994) 1585–1593, arXiv:hep-lat/9307001.

[265] A. Cucchieri, "Infrared behavior of the gluon propagator in lattice Landau gauge," *Phys. Lett.* **B422** (1998) 233–237, arXiv:hep-lat/9709015.

[266] P. J. Silva and O. Oliveira, "Gribov copies, lattice QCD and the gluon propagator," *Nucl. Phys.* **B690** (2004) 177–198, arXiv:hep-lat/0403026.

[267] A. Sternbeck, E. M. Ilgenfritz, M. Müller-Preussker, and A. Schiller, "Towards the infrared limit in SU(3) Landau gauge lattice gluodynamics," *Phys. Rev.* **D72** (2005) 014507, arXiv:hep-lat/0506007.

[268] I. L. Bogolubsky, G. Burgio, M. Müller-Preussker, and V. K. Mitrjushkin, "Landau gauge ghost and gluon propagators in SU(2) lattice gauge theory: Gribov ambiguity revisited," *Phys. Rev.* **D74** (2006) 034503, arXiv:hep-lat/0511056.

[269] E. M. Ilgenfritz, M. Müller-Preussker, A. Sternbeck, A. Schiller, and I. L. Bogolubsky, "Landau gauge gluon and ghost propagators from lattice QCD," *Braz. J. Phys.* **37** (2007) 193, arXiv:hep-lat/0609043.

[270] P. Boucaud *et al.*, "Short comment about the lattice gluon propagator at vanishing momentum," arXiv:hep-lat/0602006.

[271] A. Cucchieri, T. Mendes, O. Oliveira, and P. J. Silva, "SU(2) meets SU(3) in lattice-Landau-gauge gluon and ghost propagators," *PoS* **LAT2007** (2007) 322, arXiv:0710.0344 [hep-lat].

[272] A. Cucchieri and T. Mendes, "What's up with IR gluon and ghost propagators in Landau gauge? A puzzling answer from huge lattices," *PoS* **LAT2007** (2007) 297, arXiv:0710.0412 [hep-lat].

[273] I. L. Bogolubsky, E. M. Ilgenfritz, M. Müller-Preussker, and A. Sternbeck, "The Landau gauge gluon and ghost propagators in 4D SU(3) gluodynamics in large lattice volumes," *PoS* **LAT2007** (2007) 290, arXiv:0710.1968 [hep-lat].

[274] I. L. Bogolubsky *et al.*, "Improved Landau gauge fixing and the suppression of finite-volume effects of the lattice gluon propagator," *Phys. Rev.* **D77** (2008) 014504, arXiv:0707.3611 [hep-lat].

[275] A. Cucchieri and T. Mendes, "Constraints on the IR behavior of the gluon propagator in Yang-Mills theories," *Phys. Rev. Lett.* **100** (2008) 241601, arXiv:0712.3517 [hep-lat].

[276] I. L. Bogolubsky *et al.*, "Lattice results on gluon and ghost propagators in Landau gauge," arXiv:0804.1250 [hep-lat].

[277] V. G. Bornyakov, V. K. Mitrjushkin, and M. Müller-Preussker, "Infrared behavior and Gribov ambiguity in SU(2) lattice gauge theory," *Phys. Rev.* **D79** (2009) 074504, arXiv:0812.2761 [hep-lat].

[278] I. L. Bogolubsky, E. M. Ilgenfritz, M. Müller-Preussker, and A. Sternbeck, "Lattice gluodynamics computation of Landau gauge Green's functions in the deep infrared," *Phys. Lett.* **B676** (2009) 69–73, arXiv:0901.0736 [hep-lat].

[279] I. L. Bogolubsky, E. M. Ilgenfritz, M. Müller-Preussker, and A. Sternbeck, "The Landau gauge gluon propagator in 4D SU(2) lattice gauge theory revisited: Gribov copies and scaling properties," *PoS* **LATTICE2009** (2009) 237, arXiv:0912.2249 [hep-lat].

[280] A. Cucchieri and T. Mendes, "Numerical test of the Gribov-Zwanziger scenario in Landau gauge," *PoS* **QCD-TNT09** (2009) 026, arXiv:1001.2584 [hep-lat].

[281] A. Sternbeck, L. von Smekal, D. B. Leinweber, and A. G. Williams, "Comparing SU(2) to SU(3) gluodynamics on large lattices," *PoS* **LAT2007** (2007) 340, arXiv:0710.1982 [hep-lat].

[282] A. Cucchieri, T. Mendes, O. Oliveira, and P. J. Silva, "Just how different are SU(2) and SU(3) Landau-gauge propagators in the IR regime?," *Phys. Rev.* **D76** (2007) 114507, arXiv:0705.3367 [hep-lat].

[283] O. Oliveira, P. J. Silva, E. M. Ilgenfritz, and A. Sternbeck, "The gluon propagator from large asymmetric lattices," *PoS* **LAT2007** (2007) 323, arXiv:0710.1424 [hep-lat].

[284] O. Oliveira and P. J. Silva, "Infrared gluon and ghost propagators exponents from lattice QCD," *Eur. Phys. J.* **C62** (2009) 525–534, arXiv:0705.0964 [hep-lat].

[285] O. Oliveira and P. J. Silva, "The lattice infrared Landau gauge gluon propagator: the infinite volume limit," arXiv:0910.2897 [hep-lat].

[286] O. Oliveira and P. J. Silva, "The lattice infrared Landau gauge gluon propagator: from finite volume to the infinite volume," *PoS* **QCD-TNT09** (2009) 033, arXiv:0911.1643 [hep-lat].

[287] C. S. Fischer, B. Grüter, and R. Alkofer, "Solving coupled Dyson-Schwinger equations on a compact manifold," *Ann. Phys.* **321** (2006) 1918–1938, arXiv:hep-ph/0506053.

[288] C. S. Fischer, A. Maas, J. M. Pawlowski, and L. von Smekal, "Large volume behaviour of Yang-Mills propagators," *Annals Phys.* **322** (2007) 2916–2944, arXiv:hep-ph/0701050.

[289] P. O. Bowman, U. M. Heller, D. B. Leinweber, M. B. Parappilly, and A. G. Williams, "Unquenched gluon propagator in Landau gauge," *Phys. Rev.* **D70** (2004) 034509, arXiv:hep-lat/0402032.

[290] S. Furui and H. Nakajima, "The running coupling in lattice Landau gauge with unquenched Wilson fermion and KS fermion," *PoS* **LAT2005** (2006) 291, arXiv:hep-lat/0509035.

[291] G. 't Hooft, "A Two-Dimensional Model for Mesons," *Nucl. Phys.* **B75** (1974) 461.

[292] T. D. Bakeev, E.-M. Ilgenfritz, V. K. Mitrjushkin, and M. Müller-Preussker, "On practical problems to compute the ghost propagator in SU(2) lattice gauge theory," *Phys. Rev.* **D69** (2004) 074507, arXiv:hep-lat/0311041.

[293] A. Cucchieri and T. Mendes, "Constraints on the IR behavior of the ghost propagator in Yang-Mills theories," *Phys. Rev.* **D78** (2008) 094503, arXiv:0804.2371 [hep-lat].

[294] A. Cucchieri, "Numerical study of the fundamental modular region in the minimal Landau gauge," *Nucl. Phys.* **B521** (1998) 365–379, arXiv:hep-lat/9711024.

[295] A. Sternbeck and L. von Smekal, "The strong-coupling limit of minimal lattice Landau gauge," *PoS* **LATTICE2008** (2008) 267, arXiv:0810.3765 [hep-lat].

[296] A. Sternbeck and L. von Smekal, "The strong-coupling limit of lattice Landau gauge," *PoS* **CONFINEMENT8** (2008) 049, arXiv:0812.3268 [hep-lat].

[297] A. Maas, "More on Gribov copies and propagators in Landau-gauge Yang-Mills theory," *Phys. Rev.* **D79** (2009) 014505, arXiv:0808.3047 [hep-lat].

[298] G. Parisi and Y.-s. Wu, "Perturbation Theory Without Gauge Fixing," *Sci. Sin.* **24** (1981) 483.

[299] G. Parisi, "Correlation functions and computer simulations," *Nucl. Phys.* **B180** (1981) 378.

[300] E. Nelson, "Derivation of the Schrödinger equation from Newtonian mechanics," *Phys. Rev.* **150** (1966) 1079–1085.

[301] P. H. Damgaard and H. Hüffel, "Stochastic Quantization," *Phys. Rept.* **152** (1987) 227.

[302] P. H. Damgaard and H. Hüffel, eds., *Stochastic quantization*. Singapore: World Scientific, 1998.

[303] M. Namiki *et al.*, "Stochastic quantization," *Lect. Notes Phys.* **M9** (1992) 1–217.

[304] R. Brown, "A brief account of microscopical observations made in the months of June, July and August, 1827, on the particles contained in the pollen of plants; and on the general existence of active molecules in organic and inorganic bodies," *Phil. Mag.* **4** (1828) 161–173. Available online at `http://sciweb.nybg.org/science2/pdfs/dws/Brownian.pdf` (as of June 28th, 2010).

[305] A. Einstein, "Über die von der molekularkinetischen Theorie der Wärme geforderte Bewegung von in ruhenden Flüssigkeiten suspendierten Teilchen," *Ann. d. Physik* **17** (1905) 549.

[306] M. Smoluchowski, "Zur kinetischen Theorie der Brownschen Molekularbewegung und der Suspensionen," *Ann. d. Physik* **21** (1906) 756–780.

[307] J. Honerkamp, *Stochastic dynamical systems*. New York, Weinheim etc.: VCH, 1994. Transl. by Katja Lindenberg.

[308] N. G. v. Kampen, *Stochastic processes in physics and chemistry*. Amsterdam etc.: North-Holland Publishing Company, 1981.

[309] E. Seiler, "Stochastic quantization and gauge fixing in gauge theories," in *Stochastic methods and computer techniques in quantum dynamics: proceedings of 23rd Internationale Universitätswochen für Kernphysik, Schladming, Austria*, H. Mitter and L. Pittner, eds., vol. 26 of *Acta Physica Austriaca, Supp.* Vienna, Austria: Springer, 1984.

[310] K. Langfeld, "The Gribov problem and its solution from a toy model point of view," `arXiv:hep-lat/0301007`.

[311] I. O. Stamatescu, U. Wolff, and D. Zwanziger, "Simulation of Euclidean quantum field theories by a random walk process," *Nucl. Phys.* **B225** (1983) 377.

[312] E. Seiler, I. O. Stamatescu, and D. Zwanziger, "Numerical evidence for a barrier at the Gribov horizon," *Nucl. Phys.* **B239** (1984) 201.

[313] E. Seiler, I. O. Stamatescu, and D. Zwanziger, "Monte Carlo simulation of noncompact QCD with stochastic gauge fixing," *Nucl. Phys.* **B239** (1984) 177.

[314] D. Zwanziger, "Covariant Quantization of Gauge Fields Without Gribov Ambiguity," *Nucl. Phys.* **B192** (1981) 259.

[315] P. Rossi, C. T. H. Davies, and G. P. Lepage, "A comparison of a variety of matrix inversion algorithms for Wilson fermions on the lattice," *Nucl. Phys.* **B297** (1988) 287.

[316] A. Nakamura and M. Mizutani, "Numerical study of gauge fixing ambiguity," *Vistas Astron.* **37** (1993) 305.

[317] M. Mizutani and A. Nakamura, "Stochastic gauge fixing for compact lattice gauge theories," *Nucl. Phys. Proc. Suppl.* **34** (1994) 253–255.

[318] H. Aiso *et al.*, "Towards understanding of confinement of gluons," *Nucl. Phys. Proc. Suppl.* **53** (1997) 570–573.

[319] A. Nakamura, I. Pushkina, T. Saito, and S. Sakai, "Screening of hot gluon," *Phys. Lett.* **B549** (2002) 133–138, arXiv:hep-lat/0208075.

[320] A. Nakamura, T. Saito, and S. Sakai, "Lattice calculation of gluon screening masses," *Phys. Rev.* **D69** (2004) 014506, arXiv:hep-lat/0311024.

[321] Y. Nakagawa, A. Nakamura, T. Saito, and H. Toki, "Infrared gluons in the stochastic quantization approach," *PoS* **LATTICE2008** (2008) 266.

[322] A. Nakamura, I. Pushkina, T. Saito, and S. Sakai, "Screening mass and SU(3) gluon propagator at finite temperature," *Nucl. Phys. Proc. Suppl.* **119** (2003) 493–495.

[323] F. Shoji, T. Suzuki, H. Kodama, and A. Nakamura, "A new gauge fixing method for Abelian projection," *Phys. Lett.* **B476** (2000) 199–204, arXiv:hep-lat/9910042.

[324] F. Di Renzo, E. Onofri, G. Marchesini, and P. Marenzoni, "Four loop result in SU(3) lattice gauge theory by a stochastic method: Lattice correction to the condensate," *Nucl. Phys.* **B426** (1994) 675–685, arXiv:hep-lat/9405019.

[325] G. Burgio *et al.*, "Developments and new applications of numerical stochastic perturbation theory," *Nucl. Phys. Proc. Suppl.* **63** (1998) 808–810, arXiv:hep-lat/9709106.

[326] F. Di Renzo and L. Scorzato, "Numerical stochastic perturbation theory for full QCD," *JHEP* **10** (2004) 073, arXiv:hep-lat/0410010.

[327] E.-M. Ilgenfritz, H. Perlt, and A. Schiller, "The lattice gluon propagator in stochastic perturbation theory," *PoS* **LATTICE2007** (2006) 251, arXiv:0710.0560 [hep-lat].

[328] F. Di Renzo, L. Scorzato, and C. Torrero, "High loop renormalization constants by NSPT: a status report," *PoS* **LAT2007** (2007) 240, arXiv:0710.0552 [hep-lat].

[329] F. Di Renzo, E.-M. Ilgenfritz, H. Perlt, A. Schiller, and C. Torrero, "The Landau gauge lattice ghost propagator in stochastic perturbation theory," *PoS* **LATTICE2008** (2008) 217, arXiv:0809.4950 [hep-lat].

[330] F. Di Renzo, E. M. Ilgenfritz, H. Perlt, A. Schiller, and C. Torrero, "Two-point functions of quenched lattice QCD in Numerical Stochastic Perturbation Theory. (I) The ghost propagator in Landau gauge," *Nucl. Phys.* **B831** (2010) 262–284, arXiv:0912.4152 [hep-lat].

[331] F. Di Renzo, E. M. Ilgenfritz, H. Perlt, A. Schiller, and C. Torrero, "Two-point functions of quenched lattice QCD in Numerical Stochastic Perturbation Theory. (II) The gluon propagator in Landau gauge," *Nucl. Phys.* **B842** (2011) 122–139, arXiv:1008.2617 [hep-lat].

[332] L. Baulieu and D. Zwanziger, "Equivalence of Stochastic Quantization and the Faddeev-Popov Ansatz," *Nucl. Phys.* **B193** (1981) 163.

[333] H. Hüffel and G. Kelnhofer, "Nonperturbative stochastic quantization of the helix model," *Annals Phys.* **266** (1998) 417–453, arXiv:hep-th/9705009.

[334] H. Hüffel and G. Kelnhofer, "Generalized stochastic gauge fixing," *Phys. Lett.* **B408** (1997) 241–244, arXiv:hep-th/9702135.

[335] H. Hüffel and G. Kelnhofer, "Generalized stochastic quantization of Yang-Mills theory," *Annals Phys.* **270** (1998) 231–245, arXiv:hep-th/9804133.

[336] G. G. Batrouni *et al.*, "Langevin Simulations of Lattice Field Theories," *Phys. Rev.* **D32** (1985) 2736.

[337] A. S. Kronfeld, "Dynamics of Langevin simulations," *Prog. Theor. Phys. Suppl.* **111** (1993) 293–312, arXiv:hep-lat/9205008.

[338] H. Koibuchi, "Langevin simulation of interquark potential in SU(2) lattice gauge theory," *J. Phys.* **G13** (1987) 1463.

[339] A. Guha and S. C. Lee, "Stochastic quantization for numerical simulation," *Phys. Lett.* **B134** (1984) 216.

[340] A. Sternbeck, E. M. Ilgenfritz, M. Müller-Preussker, and A. Schiller, "Landau gauge ghost and gluon propagators and the Faddeev- Popov operator spectrum," *Nucl. Phys. Proc. Suppl.* **153** (2006) 185–190, arXiv:hep-lat/0511053.

[341] A. Sternbeck, E. M. Ilgenfritz, and M. Müller-Preussker, "Spectral properties of the Landau gauge Faddeev-Popov operator in lattice gluodynamics," *Phys. Rev.* **D73** (2006) 014502, arXiv:hep-lat/0510109.

[342] Y. Nakagawa, A. Nakamura, T. Saito, and H. Toki, "Spectral sum for the color-Coulomb potential in SU(3) Coulomb gauge lattice Yang-Mills theory," *Phys. Rev.* **D81** (2010) 054509, arXiv:1003.4792 [hep-lat].

[343] G. Meurant and Z. Strakoš, "The Lanczos and conjugate gradient algorithm in finite precision arithmetic," *Acta Numerica* **15** (2006) 471.

[344] P. de Forcrand and M. Fromm, "Nuclear Physics from lattice QCD at strong coupling," *Phys. Rev. Lett.* **104** (2010) 112005, arXiv:0907.1915 [hep-lat].

[345] A. Cucchieri and T. Mendes, "Landau-gauge propagators in Yang-Mills theories at beta = 0: massive solution versus conformal scaling," *Phys. Rev.* **D81** (2010) 016005, arXiv:0904.4033 [hep-lat].

[346] P. de Forcrand and R. Gupta, "Multigrid techniques for quark propagator," *Nucl. Phys. Proc. Suppl.* **9** (1989) 516.

[347] A. Cucchieri and T. Mendes, "Critical Slowing-Down in $SU(2)$ Landau Gauge-Fixing Algorithms," *Nucl. Phys.* **B471** (1996) 263–292, hep-lat/9511020.

[348] B. Efron and R. J. Tibshirani, *An introduction to the bootstrap*. New York etc.: Chapman & Hall, 1993.

[349] A. Sternbeck *et al.*, "Running alpha(s) from Landau-gauge gluon and ghost correlations," *PoS* **LAT2007** (2007) 256, arXiv:0710.2965 [hep-lat].

[350] P. Boucaud *et al.*, "Ghost-gluon running coupling, power corrections and the determination of $\Lambda_{\overline{\rm MS}}$," *Phys. Rev.* **D79** (2009) 014508, arXiv:0811.2059 [hep-ph].

[351] A. Sternbeck *et al.*, "QCD Lambda parameter from Landau-gauge gluon and ghost correlations," *PoS* **LAT2009** (2009) 210, arXiv:1003.1585 [hep-lat].

[352] A. Nakamura and R. Sinclair, "Fermion propagators in U(1) lattice gauge theory," *Phys. Lett.* **B243** (1990) 396–402.

[353] P. de Forcrand, J. E. Hetrick, A. Nakamura, and M. Plewnia, "Gauge fixing on the lattice," *Nucl. Phys. Proc. Suppl.* **20** (1991) 194–198.

[354] M. L. Paciello, C. Parrinello, S. Petrarca, B. Taglienti, and A. Vladikas, "Gribov copies and smeared correlation functions in lattice QCD," *Phys. Lett.* **B289** (1992) 405–410, arXiv:hep-lat/9208010.

[355] P. Marenzoni and P. Rossi, "Gribov copies in lattice QCD," *Phys. Lett.* **B311** (1993) 219–222, arXiv:hep-lat/9306010.

[356] M. L. Paciello, S. Petrarca, B. Taglienti, and A. Vladikas, "Gribov noise of the lattice axial current renormalization constant," *Phys. Lett.* **B341** (1994) 187–194, arXiv:hep-lat/9409012.

[357] S. Furui and H. Nakajima, "Infrared features of lattice Landau gauge QCD and the Gribov copy problem," *AIP Conf. Proc.* **717** (2004) 685–689, arXiv:hep-lat/0309166.

[358] H. Nakajima and S. Furui, "Infrared features of the lattice Landau gauge QCD," *Nucl. Phys. Proc. Suppl.* **129** (2004) 730–732, arXiv:hep-lat/0309165.

[359] S. Kirkpatrick, C. D. Gelatt, and M. P. Vecchi, "Optimization by Simulated Annealing," *Science* **220** (1983) 671–680.

[360] V. Černý, "Thermodynamical approach to the traveling salesman problem: An efficient simulation algorithm," *J. Optimiz. Theory App.* **45** (1985) 41–51.

[361] A. Nakamura and M. Plewnia, "Gauge fixing ambiguity and photon propagators in compact U(1) lattice gauge theory," *Phys. Lett.* **B255** (1991) 274–278.

[362] V. G. Bornyakov, V. K. Mitrjushkin, M. Müller-Preussker, and F. Pahl, "Dirac sheets and gauge fixing in U(1) lattice gauge theory," *Phys. Lett.* **B317** (1993) 596–603, arXiv:hep-lat/9307010.

[363] V. K. Mitrjushkin, "Classical solutions in lattice gauge theories," *Phys. Lett.* **B389** (1996) 713–719, arXiv:hep-lat/9607069.

[364] C. Parrinello and G. Jona-Lasinio, "A Modified Faddeev-Popov formula and the Gribov ambiguity," *Phys. Lett.* **B251** (1990) 175–180.

[365] D. Zwanziger, "Quantization of gauge fields, classical gauge invariance and gluon confinement," *Nucl. Phys.* **B345** (1990) 461–471.

[366] M. Schaden and D. Zwanziger, "Horizon condition holds pointwise on finite lattice with free boundary conditions," in *Proceedings of the Workshop on Quantum Infrared Physics: The American University of Paris 6-10 June 1994*, H. M. Fried and B. Muller, eds. River Edge, N.J.: World Scientific, 1995. arXiv:hep-th/9410019.

[367] T. Tok, K. Langfeld, H. Reinhardt, and L. von Smekal, "The gluon propagator in lattice Landau gauge with twisted boundary conditions," *PoS* **LAT2005** (2006) 334, arXiv:hep-lat/0509134.

[368] Y. Aoki, G. Endrodi, Z. Fodor, S. D. Katz, and K. K. Szabo, "The order of the quantum chromodynamics transition predicted by the standard model of particle physics," *Nature* **443** (2006) 675–678, arXiv:hep-lat/0611014.

[369] L. G. Yaffe and B. Svetitsky, "First Order Phase Transition in the SU(3) Gauge Theory at Finite Temperature," *Phys. Rev.* **D26** (1982) 963.

[370] C. S. Fischer, A. Maas, and J. A. Müller, "Chiral and deconfinement transition from correlation functions: SU(2) vs. SU(3)," *Eur. Phys. J.* **C68** (2010) 165–181, arXiv:1003.1960 [hep-ph].

[371] C. Gattringer, "Linking confinement to spectral properties of the Dirac operator," *Phys. Rev. Lett.* **97** (2006) 032003, arXiv:hep-lat/0605018.

[372] F. Bruckmann, C. Gattringer, and C. Hagen, "Complete spectra of the Dirac operator and their relation to confinement," *Phys. Lett.* **B647** (2007) 56–61, arXiv:hep-lat/0612020.

[373] F. Synatschke, A. Wipf, and C. Wozar, "Spectral sums of the Dirac-Wilson operator and their relation to the Polyakov loop," *Phys. Rev.* **D75** (2007) 114003, arXiv:hep-lat/0703018.

[374] E. Bilgici, F. Bruckmann, C. Gattringer, and C. Hagen, "Dual quark condensate and dressed Polyakov loops," *Phys. Rev.* **D77** (2008) 094007, arXiv:0801.4051 [hep-lat].

[375] F. Synatschke, A. Wipf, and K. Langfeld, "Relation between chiral symmetry breaking and confinement in YM-theories," *Phys. Rev.* **D77** (2008) 114018, arXiv:0803.0271 [hep-lat].

[376] C. S. Fischer, "Deconfinement phase transition and the quark condensate," *Phys. Rev. Lett.* **103** (2009) 052003, arXiv:0904.2700 [hep-ph].

[377] L. D. McLerran and B. Svetitsky, "Quark Liberation at High Temperature: A Monte Carlo Study of SU(2) Gauge Theory," *Phys. Rev.* **D24** (1981) 450.

[378] M. Teper, "The finite temperature phase transition of SU(2) gauge fields in (2+1)-dimensions," *Phys. Lett.* **B313** (1993) 417–424.

[379] E. Ising, "Beitrag zur Theorie des Ferromagnetismus," *Z. Phys.* **31** (1925) 253–258.

[380] J. Engels *et al.*, "A study of finite temperature gauge theory in (2+1) dimensions," *Nucl. Phys. Proc. Suppl.* **53** (1997) 420–422, arXiv:hep-lat/9608099.

[381] B. Svetitsky and L. G. Yaffe, "Critical Behavior at Finite Temperature Confinement Transitions," *Nucl. Phys.* **B210** (1982) 423.

[382] L. Onsager, "Crystal statistics. I. A two-dimensional model with an order-disorder transition," *Phys. Rev.* **D65** (1944) 117–149.

[383] A. Cucchieri, A. Maas, and T. Mendes, "Infrared properties of propagators in Landau-gauge pure Yang-Mills theory at finite temperature," *Phys. Rev.* **D75** (2007) 076003, arXiv:hep-lat/0702022.

[384] F. Karsch and J. Rank, "Landau gauge fixing and finite temperature gluon propagator in SU(2) lattice gauge theory," *Nucl. Phys. Proc. Suppl.* **42** (1995) 508–510.

[385] U. M. Heller, F. Karsch, and J. Rank, "The Gluon propagator at high temperature," *Phys. Lett.* **B355** (1995) 511–517, arXiv:hep-lat/9505016.

[386] A. Cucchieri, F. Karsch, and P. Petreczky, "Magnetic screening in hot non-Abelian gauge theory," *Phys. Lett.* **B497** (2001) 80–84, arXiv:hep-lat/0004027.

[387] A. Cucchieri, F. Karsch, and P. Petreczky, "Propagators and Dimensional Reduction of Hot SU(2) Gauge Theory," *Phys. Rev.* **D64** (2001) 036001, arXiv:hep-lat/0103009.

[388] A. Maas, "Describing gluons at zero and finite temperature," *Chin. J. Phys.* **34** (2010) 1328–1330, arXiv:0911.0348 [hep-lat].

[389] S. Furui and H. Nakajima, "Infrared features of unquenched finite temperature lattice Landau gauge QCD," *Phys. Rev.* **D76** (2007) 054509, arXiv:hep-lat/0612009.

[390] A. Maas, "Gluons at finite temperature in Landau gauge Yang-Mills theory," *Mod. Phys. Lett.* **A20** (2005) 1797–1811, arXiv:hep-ph/0506066.

[391] A. Maas, A. Cucchieri, and T. Mendes, "On the infrared behavior of Green's functions in Yang-Mills theory," *Braz. J. Phys.* **37N1B** (2007) 219–225, arXiv:hep-lat/0610006.

[392] A. Yamaguchi and H. Nakajima, "Landau gauge fixing supported by genetic algorithm," *Nucl. Phys. Proc. Suppl.* **83** (2000) 840–842, arXiv:hep-lat/9909064.

[393] S. Edwards and L. von Smekal, "SU(2) lattice gauge theory in 2+1 dimensions: critical couplings from twisted boundary conditions and universality," *Phys. Lett.* **B681** (2009) 484–490, arXiv:0908.4030 [hep-lat].

[394] B. Lucini, M. Teper, and U. Wenger, "The high temperature phase transition in SU(N) gauge theories," *JHEP* **01** (2004) 061, arXiv:hep-lat/0307017.

[395] G. Boyd *et al.*, "Thermodynamics of SU(3) Lattice Gauge Theory," *Nucl. Phys.* **B469** (1996) 419–444, arXiv:hep-lat/9602007.

[396] M. Teper, "Some physical properties of SU(2) gauge theories in three- dimensions," *Nucl. Phys. Proc. Suppl.* **30** (1993) 529–532.

[397] J. Liddle and M. Teper, "The deconfining phase transition in D=2+1 SU(N) gauge theories," arXiv:0803.2128 [hep-lat].

[398] W. H. Press, S. A. Teukolsky, W. T. Vetterling, and B. P. Flannery, *Numerical Recipes in C++: The Art of Scientific Computing*. Cambridge, UK: University Press, second ed., 2002.

[399] S. Istrail, "Statistical mechanics, three-dimensionality and NP-completeness. I. Universality of intractability for the partition function of the Ising model across non-planar surfaces (extended abstract)," in *Proceedings of the Thirty-Second Annual ACM Symposium on Theory of Computing*.

[400] K. Binder, "Finite size scaling analysis of Ising model block distribution functions," *Z. Phys.* **B43** (1981) 119–140.

[401] A. Pelissetto and E. Vicari, "Critical phenomena and renormalization-group theory," *Phys. Rept.* **368** (2002) 549–727, arXiv:cond-mat/0012164.

[402] H. Meyer-Ortmanns, "Phase transitions in quantum chromodynamics," *Rev. Mod. Phys.* **68** (1996) 473–598, arXiv:hep-lat/9608098.

[403] P. Braun-Munzinger and J. Wambach, "Colloquium: Phase diagram of strongly interacting matter," *Rev. Mod. Phys.* **81** (2009) 1031–1050.

[404] M. Cheng *et al.*, "The transition temperature in QCD," *Phys. Rev.* **D74** (2006) 054507, arXiv:hep-lat/0608013.

[405] Y. Aoki, Z. Fodor, S. D. Katz, and K. K. Szabo, "The QCD transition temperature: Results with physical masses in the continuum limit," *Phys. Lett.* **B643** (2006) 46–54, arXiv:hep-lat/0609068.

[406] M. Cheng *et al.*, "Equation of State for physical quark masses," *Phys. Rev.* **D81** (2010) 054504, arXiv:0911.2215 [hep-lat].

[407] M. Cheng *et al.*, "The finite temperature QCD using 2+1 flavors of domain wall fermions at $N_t = 8$," *Phys. Rev.* **D81** (2010) 054510, arXiv:0911.3450 [hep-lat].

[408] Y. Aoki *et al.*, "The QCD transition temperature: results with physical masses in the continuum limit II," *JHEP* **06** (2009) 088, arXiv:0903.4155 [hep-lat].

[409] C. Schmidt, "Lattice QCD at finite density," *PoS* **LAT2006** (2006) 021, arXiv:hep-lat/0610116.

[410] P. de Forcrand, "Simulating QCD at finite density," *PoS* **LAT2009** (2009) 010, arXiv:1005.0539 [hep-lat].

[411] K. Fukushima and T. Hatsuda, "The phase diagram of dense QCD," arXiv:1005.4814 [hep-ph].

[412] M. A. Stephanov, "Random matrix model of QCD at finite density and the nature of the quenched limit," *Phys. Rev. Lett.* **76** (1996) 4472–4475, arXiv:hep-lat/9604003.

[413] A. M. Ferrenberg and R. H. Swendsen, "Optimized Monte Carlo analysis," *Phys. Rev. Lett.* **63** (1989) 1195–1198.

[414] I. M. Barbour, S. E. Morrison, E. G. Klepfish, J. B. Kogut, and M.-P. Lombardo, "Results on finite density QCD," *Nucl. Phys. Proc. Suppl.* **60A** (1998) 220–234, arXiv:hep-lat/9705042.

[415] Z. Fodor and S. D. Katz, "Lattice determination of the critical point of QCD at finite T and mu," *JHEP* **03** (2002) 014, arXiv:hep-lat/0106002.

[416] Z. Fodor and S. D. Katz, "Critical point of QCD at finite T and mu, lattice results for physical quark masses," *JHEP* **04** (2004) 050, arXiv:hep-lat/0402006.

[417] C. R. Allton *et al.*, "The QCD thermal phase transition in the presence of a small chemical potential," *Phys. Rev.* **D66** (2002) 074507, arXiv:hep-lat/0204010.

[418] S. Ejiri *et al.*, "Study of QCD thermodynamics at finite density by Taylor expansion," *Prog. Theor. Phys. Suppl.* **153** (2004) 118–126, arXiv:hep-lat/0312006.

[419] R. V. Gavai and S. Gupta, "The critical end point of QCD," *Phys. Rev.* **D71** (2005) 114014, arXiv:hep-lat/0412035.

[420] C. R. Allton *et al.*, "Thermodynamics of two flavor QCD to sixth order in quark chemical potential," *Phys. Rev.* **D71** (2005) 054508, arXiv:hep-lat/0501030.

[421] R. V. Gavai and S. Gupta, "QCD at finite chemical potential with six time slices," *Phys. Rev.* **D78** (2008) 114503, arXiv:0806.2233 [hep-lat].

[422] P. de Forcrand and O. Philipsen, "The QCD phase diagram for small densities from imaginary chemical potential," *Nucl. Phys.* **B642** (2002) 290–306, arXiv:hep-lat/0205016.

[423] P. de Forcrand and O. Philipsen, "The QCD Phase Diagram for Three Degenerate Flavors and Small Baryon Density," *Nucl. Phys.* **B673** (2003) 170–186, arXiv:hep-lat/0307020.

[424] M. D'Elia and F. Sanfilippo, "Thermodynamics of two flavor QCD from imaginary chemical potentials," *Phys. Rev.* **D80** (2009) 014502, arXiv:0904.1400 [hep-lat].

[425] T. Takaishi, P. de Forcrand, and A. Nakamura, "Equation of State at Finite Density from Imaginary Chemical Potential," arXiv:1002.0890 [hep-lat].

[426] S. Ejiri, "Lee-Yang zero analysis for the study of QCD phase structure," *Phys. Rev.* **D73** (2006) 054502, arXiv:hep-lat/0506023.

[427] K. Splittorff, "Lattice simulations of QCD with mu(B) not = 0 versus phase quenched QCD," arXiv:hep-lat/0505001.

[428] G. Parisi, "On complex probabilities," *Phys. Lett.* **B131** (1983) 393–395.

[429] J. R. Klauder, "Stochastic quantization," in *Recent developments in high energy physics: proceedings of 22nd Internationale Universitätswochen für Kernphysik, Schladming, Austria*, H. Mitter and C. B. Lang, eds., vol. 25 of *Acta Physica Austriaca Supp.* 1983.

[430] J. R. Klauder, "Coherent state Langevin equations for canonical quantum systems with applications to the quantized Hall effect," *Phys. Rev.* **A29** (1984) 2036–2047.

[431] J. R. Klauder, "A Langevin approach to fermion and quantum spin correlation functions," *J. Phys.* **A16** (1983) L317.

[432] J. R. Klauder and W. P. Petersen, "Spectrum of certain non-self-adjoint operators and solutions of langevin equations with complex drift," *J. Stat. Phys.* **39** (1985) 53.

[433] F. Karsch and H. W. Wyld, "Complex Langevin simulation of the SU(3) spin model with nonzero chemical potential," *Phys. Rev. Lett.* **55** (1985) 2242.

[434] J. Ambjorn and S. K. Yang, "Numerical problems in applying the Langevin equation to complex effective actions," *Phys. Lett.* **B165** (1985) 140.

[435] J. Ambjorn, M. Flensburg, and C. Peterson, "The complex Langevin equation and Monte Carlo simulations of actions with static charges," *Nucl. Phys.* **B275** (1986) 375.

[436] H. W. Hamber and H.-c. Ren, "Complex probabilities and the Langevin equation," *Phys. Lett.* **B159** (1985) 330.

[437] J. Berges, S. Borsanyi, D. Sexty, and I. O. Stamatescu, "Lattice simulations of real-time quantum fields," *Phys. Rev.* **D75** (2007) 045007, arXiv:hep-lat/0609058.

[438] J. Flower, S. W. Otto, and S. Callahan, "Complex Langevin equations and lattice gauge theory," *Phys. Rev.* **D34** (1986) 598.

[439] E.-M. Ilgenfritz, "Complex Langevin simulation of chiral symmetry restoration at finite baryonic density," *Phys. Lett.* **B181** (1986) 327.

[440] G. Aarts and I.-O. Stamatescu, "Stochastic quantization at finite chemical potential," *JHEP* **09** (2008) 018, arXiv:0807.1597 [hep-lat].

[441] G. Aarts and I.-O. Stamatescu, "Stochastic quantization at nonzero chemical potential," *PoS* **LATTICE2008** (2008) 176, arXiv:0809.5227 [hep-lat].

[442] G. Aarts, "Can stochastic quantization evade the sign problem? – the relativistic Bose gas at finite chemical potential," *Phys. Rev. Lett.* **102** (2009) 131601, arXiv:0810.2089 [hep-lat].

[443] G. Aarts, F. A. James, E. Seiler, and I.-O. Stamatescu, "Adaptive stepsize and instabilities in complex Langevin dynamics," *Phys. Lett.* **B687** (2010) 154–159, arXiv:0912.0617 [hep-lat].

[444] G. Aarts, E. Seiler, and I.-O. Stamatescu, "The Complex Langevin method: When can it be trusted?," *Phys. Rev.* **D81** (2010) 054508, arXiv:0912.3360 [hep-lat].

[445] G. Aarts and K. Splittorff, "Degenerate distributions in complex Langevin dynamics: one-dimensional QCD at finite chemical potential," *JHEP* **08** (2010) 017, arXiv:1006.0332 [hep-lat].

[446] G. Aarts and F. A. James, "On the convergence of complex Langevin dynamics: the three-dimensional XY model at finite chemical potential," *JHEP* **08** (2010) 020, arXiv:1005.3468 [hep-lat].

[447] J. Berges and I. O. Stamatescu, "Simulating nonequilibrium quantum fields with stochastic quantization techniques," *Phys. Rev. Lett.* **95** (2005) 202003, arXiv:hep-lat/0508030.

[448] T. Matsui and A. Nakamura, "Parisi-Klauder algorithm for complex actions in stochastic quantization," *Phys. Lett.* **B194** (1987) 262–266.

[449] K. Okano, L. Schulke, and B. Zheng, "Kernel controlled complex Langevin simulation: Field dependent kernel," *Phys. Lett.* **B258** (1991) 421–426.

[450] L. L. Salcedo, "Spurious solutions of the complex Langevin equation," *Phys. Lett.* **B305** (1993) 125–130.

[451] K. Fujimura, K. Okano, L. Schulke, K. Yamagishi, and B. Zheng, "On the segregation phenomenon in complex Langevin simulation," *Nucl. Phys.* **B424** (1994) 675–689, arXiv:hep-th/9311174.

[452] H. Gausterer, "On the correct convergence of complex Langevin simulations for polynomial actions," *J. Phys.* **A27** (1994) 1325–1330, arXiv:hep-lat/9312003.

[453] K. Okano, L. Schulke, and B. Zheng, "Complex Langevin simulation," *Prog. Theor. Phys. Suppl.* **111** (1993) 313–347.

[454] W. E. Thirring, "A soluble relativistic field theory," *Annals Phys.* **3** (1958) 91–112.

[455] G. Aarts. Priv. comm., 2009.

[456] S. Hands. Priv. comm., 2009.

[457] H. Gies and L. Janssen, "UV fixed-point structure of the three-dimensional Thirring model," *Phys. Rev.* **D82** (2010) 085018, arXiv:1006.3747 [hep-th].

[458] **UKQCD** Collaboration, L. Del Debbio, S. J. Hands, and J. C. Mehegan, "Three-dimensional Thirring model for small N(f)," *Nucl. Phys.* **B502** (1997) 269–308, arXiv:hep-lat/9701016.

[459] S. Hands, "O (1/N(f)) corrections to the Thirring model in 2 < d < 4," *Phys. Rev.* **D51** (1995) 5816–5826, arXiv:hep-th/9411016.

[460] L. Del Debbio and S. J. Hands, "The three dimensional Thirring model for N(f) = 4 and N(f) = 6," *Nucl. Phys.* **B552** (1999) 339–362, arXiv:hep-lat/9902014.

[461] **UKQCD** Collaboration, L. Del Debbio, "Chiral symmetry breaking in the 3-d Thirring model for small N(f)," arXiv:hep-lat/9709034.

[462] M. Gomes, R. S. Mendes, R. F. Ribeiro, and A. J. da Silva, "Gauge structure, anomalies and mass generation in a three- dimensional Thirring model," *Phys. Rev.* **D43** (1991) 3516–3523.

[463] D. K. Hong and S. H. Park, "Large N analysis of (2+1)-dimensional Thirring model," *Phys. Rev.* **D49** (1994) 5507–5511, arXiv:hep-th/9307186.

[464] T. Itoh, Y. Kim, M. Sugiura, and K. Yamawaki, "Thirring model as a gauge theory," *Prog. Theor. Phys.* **93** (1995) 417–440, arXiv:hep-th/9411201.

[465] L. Del Debbio and S. Hands, "Monte Carlo Simulation of the Three Dimensional Thirring Model," *Phys. Lett.* **B373** (1996) 171–177, arXiv:hep-lat/9512013.

[466] S. Christofi, S. Hands, and C. Strouthos, "Critical flavor number in the three dimensional Thirring model," *Phys. Rev.* **D75** (2007) 101701, arXiv:hep-lat/0701016.

[467] S. Christofi, S. Hands, and C. Strouthos, "Phase diagram of the three dimensional Thirring model: A Monte Carlo study," *PoS* **LAT2006** (2006) 217, arXiv:hep-lat/0703016.

[468] P. Hasenfratz and F. Karsch, "Chemical Potential on the Lattice," *Phys. Lett.* **B125** (1983) 308.

[469] N. Kawamoto and J. Smit, "Effective Lagrangian and Dynamical Symmetry Breaking in Strongly Coupled Lattice QCD," *Nucl. Phys.* **B192** (1981) 100.

[470] I.-O. Stamatescu. Priv. comm., 2009.

[471] S. Hands and B. Lucini, "The phase diagram of the three dimensional Thirring model," *Phys. Lett.* **B461** (1999) 263–269, arXiv:hep-lat/9906008.

[472] M. Galassi, J. Davies, J. Theiler, B. Gough, G. Jungman, P. Alken, M. Booth, and F. Rossi, "GNU Scientific Library Reference Manual." Available online at http://www.gnu.org/software/gsl/manual/html_node/, 2010.

[473] T. D. Cohen, "Functional integrals for QCD at nonzero chemical potential and zero density," *Phys. Rev. Lett.* **91** (2003) 222001, arXiv:hep-ph/0307089.

[474] R. De Pietri, A. Feo, E. Seiler, and I.-O. Stamatescu, "A Model for QCD at High Density and Large Quark Mass," *Phys. Rev.* **D76** (2007) 114501, arXiv:0705.3420 [hep-lat].

[475] N. Metropolis, A. W. Rosenbluth, M. N. Rosenbluth, A. H. Teller, and E. Teller, "Equation of state calculations by fast computing machines," *J. Chem. Phys.* **21** (1953) 1087–1092.

[476] N. Cabibbo and E. Marinari, "A New Method for Updating SU(N) Matrices in Computer Simulations of Gauge Theories," *Phys. Lett.* **B119** (1982) 387–390.

[477] M. Lüscher, "A Portable high quality random number generator for lattice field theory simulations," *Comput. Phys. Commun.* **79** (1994) 100–110, arXiv:hep-lat/9309020.

[478] C. T. H. Davies *et al.*, "Fourier acceleration in lattice gauge theories. 1. Landau gauge fixing," *Phys. Rev.* **D37** (1988) 1581.

[479] R. Gupta *et al.*, "The hadron spectrum on a $18^3 \times 42$ lattice," *Phys. Rev.* **D36** (1987) 2813.

[480] H. Suman and K. Schilling, "A comparative study of gauge fixing procedures on the connection machines CM2 and CM5," *Parallel Computing* **20** (1994) 975.

[481] G. E. Karniadakis and R. M. Kirby, *Parallel Scientific Computing in C++ and MPI*. Cambridge, UK: University Press, 2003.

[482] H. R. Schwarz and N. Köckler, *Numerische Mathematik*. Wiesbaden: Vieweg + Teubner, seventh ed., 2009.

[483] S. Hioki, "Construction of staples in lattice gauge theory on a parallel computer," *Nucl. Phys. Proc. Suppl.* **42** (1995) 870–872, arXiv:hep-lat/9411031.

[484] F. D. R. Bonnet, P. O. Bowman, D. B. Leinweber, A. G. Williams, and D. G. Richards, "Discretisation errors in Landau gauge on the lattice," *Austral. J. Phys.* **52** (1999) 939–948, arXiv:hep-lat/9905006.

[485] F. D. R. Bonnet, P. O. Bowman, D. B. Leinweber, D. G. Richards, and A. G. Williams, "Improved Landau gauge fixing and discretisation errors," *Nucl. Phys. Proc. Suppl.* **83** (2000) 905–907, arXiv:hep-lat/9909110.

[486] I. L. Bogolubsky and V. K. Mitrjushkin, "Gluon propagators and the choice of the gauge field in SU(2) theory on the lattice," arXiv:hep-lat/0204006.

[487] H. Nakajima, S. Furui, and A. Yamaguchi, "Numerical study of the Kugo-Ojima criterion and the Gribov problem in the Landau gauge," in *ICHEP 2000: Proceedings*, C. S. Lim and T. Yamanaka, eds. Singapore: World Scientific, 2001. arXiv:hep-lat/0007001.

[488] S. Furui and H. Nakajima, "The new definition of lattice gauge fields and the Landau gauge," *Nucl. Phys. Proc. Suppl.* **73** (1999) 865–867, arXiv:hep-lat/9809080.

[489] K. Amemiya and H. Suganuma, "Effective mass generation of off-diagonal gluons as the origin of infrared Abelian dominance in the maximally Abelian gauge in QCD," *Phys. Rev.* **D60** (1999) 114509, arXiv:hep-lat/9811035.

ACKNOWLEDGMENTS – DANK

I would like to acknowledge the support of several people during my scientific work and also in my personal life. I will do so mostly in German and partly in English.

Ich möchte an erster Stelle meinem Doktorvater Herrn Prof. Dr. Jan M. Pawlowski für seine sehr kompetente und engagierte Betreuung danken. Er hat den Fortgang meiner Arbeit in vielerlei Hinsicht gefördert und hat durch seine zahlreichen wertvollen Ideen, sein tiefschürfendes Interesse und seine stete Bereitschaft zu aufschlussreichen physikalischen Diskussionen wesentlich zu ihrem Erfolg beigetragen.

Herrn Prof. Dr. Michael G. Schmidt danke ich für sein Interesse an meiner Arbeit und für die freundliche Übernahme des Zweitgutachtens.

Ich möchte Herrn Prof. Dr. Karlheinz Meier und Herrn PD Dr. Klaus Reygers für ihre freundliche Bereitschaft danken, im Prüfungskomitee mitzuwirken.

Herrn Prof. Dr. Ion-Olimpiu Stamatescu danke ich für seinen Beitrag dazu, diese Arbeit zu initiieren, und besonders dafür, dass er mit seiner Expertise gerade hinsichtlich stochastischer Quantisierung in zahlreichen Gesprächen wichtige Anstöße und Ideen für sie gegeben hat.

Zu anderen Themen dieser Arbeit gelang eine fruchtbare Zusammenarbeit mit Dr. Axel Maas, Dr. André Sternbeck und Dr. habil. Lorenz von Smekal. Ich möchte ihnen für ihre vielen guten, teils zentralen Ideen und Hinweise danken, von denen ich erheblich profitieren konnte.

I would like to thank Dr. Gert Aarts, Prof. Simon Hands and Dr. Denes Sexty for their helpful remarks and a number of useful discussions during our collaboration on the Thirring model.

Konstruktiven und netten Austausch über so manche verwickelte Frage zur QCD hatte ich während der letzten drei Jahre auch mit Astrid Eichhorn, Leonard Fister und Lisa Marie Haas. Den beiden Letztgenannten möchte ich außerdem für einige hilfreiche Bemerkungen zur vorliegenden Arbeit danken.

Ein großer Teil der Arbeit bestand in umfangreichen Computersimulationen, die ich anfangs auf dem Cluster des Instituts für Theoretische Physik durchgeführt habe und später meist auf dem bwGRiD, das größere parallele Rechnungen ermöglicht hat. Ich danke den Administrationsteams. Eine besondere Hervorhebung verdient dabei Herr Prof. Dr. Werner Wetzel, der mit seinem unermüdlichen Einsatz als Systemadministrator des ITP hervorragende Bedingungen für diesen sehr wichtigen Aspekt der täglichen Arbeit geschaffen hat.

Another very influential aspect of the everyday work was the 'Dachzimmer'. I would like to thank all those people who contributed to creating a friendly atmosphere during the many hours under the roof, and more generally at the institute. I enjoyed our discussions on numerous topics, especially during the lunch breaks, a lot. Unfortunately, lack of space prevents me from thanking by name all of the helpful past and present colleagues. Drawing a line somewhere is also difficult. – With confidence that all the many people I am addressing will feel addressed, I wish to say 'Thank you'.

Für die finanzielle Grundlage durch ein Promotionsstipendium im Rahmen des Graduiertenkollegs 'Simulational Methods in Physics' bedanke ich mich bei der Landesgraduiertenförderung Baden-Württemberg.

Nun noch in unangemessener Kürze zu etwas, das sich in den vergangenen Jahren oft brav der Physik untergeordnet hat, nämlich zur Welt jenseits der Institutsmauern.

Bestimmte Freundinnen und Freunde – meist, aber nicht sämtlich aus der Tübinger Zeit des Studiums – haben mir auf viele Weisen geholfen, mich geprägt und mir neue Horizonte eröffnet.

Meiner Freundin Maria Kallenberg möchte ich einen großen Dank sagen für ihre liebevolle Unterstützung, für ihre Geduld auch bei meiner dritten Abschlussarbeit hintereinander und dafür, wie schön die Zeit mit ihr ist.

Zum Schluss, aber keinesfalls zuletzt möchte ich meiner Familie danken. Mein ganz besonderer Dank gilt meinen Eltern für ihr Vertrauen und für ihre außergewöhnliche und mannigfache Unterstützung über all die Jahre.